

The University of Sheffield



**Novel Sensorless Control of
Permanent Magnet Synchronous
Machines**

Jiaming Liu

A thesis submitted for the degree of Doctor of Philosophy

Department of Electronic and Electrical Engineering

University of Sheffield

Mappin Street, Sheffield, S1 3JD, UK

7 November 2013

ABSTRACT

This thesis is focused on the sensorless control of permanent magnet synchronous machine (PMSM) based on high frequency carrier voltage injection for zero and low speed and third harmonic back-EMF for higher speed, respectively.

Differing from the conventional high-frequency carrier signal injection based sensorless controls, a new sensorless control strategy is proposed which injects a pulsating high-frequency carrier voltage into α - (or β -) axis of the stationary reference frame as stable as rotating carrier signal injection method and estimates rotor position information from the amplitude-modulated carrier current response as simple as pulsating carrier signal injection method. By injecting a high frequency square waveform carrier voltage, the bandwidth of the rotor position estimation can be significantly improved due to the higher injected frequency and removal of all filters.

When the rotor speed is sufficiently high, the back-EMF based sensorless control should be applied. Third harmonic back-EMF is usually applied as reference for sensorless control since it is not sensitive to the machine and controller parameters. To improve the dynamic performance due to insufficient resolution, a speed error compensation strategy based on the continuous signal of third harmonic flux-linkage is proposed. This method also can be extended to improve the robustness and rotor position estimation in flux observer based sensorless control. Furthermore, based on Extended Kalman Filter (EKF), rotor position can be derived without considering speed even with poor quality signals for single and dual three-phase PMSM

Third harmonic back-EMF based sensorless control also has some restrictions. In salient pole machines, the winding inductance varies with the rotor position which will introduce estimation error. With imbalanced machine parameters, the measured triplen harmonic back-EMF will contain certain fundamental components which will deteriorate the rotor position estimation. By compensating the contained fundamental distortion in advance, the steady-state and dynamic performance of single and dual three-phase PMSM can be remarkably improved with high robustness.

ACKNOWLEDGEMENTS

I would like to express my sincere gratitude to my supervisor Prof. Z.Q. Zhu. Throughout the whole course of this PhD research, his professional technical guidance and constructive help are valuable and impressive.

I am very grateful to Dr. Zhan-Yuan Wu for his help in many ways. Many thanks go to Dr. Liming Gong and Prof. Jiabing Hu for their support and help in starting point for my PhD study. Discussions with Dr. Weizhong Fei, Dr. Guangjin Li, Dr. Kan Liu and Mr. Tzu-Chi Lin were also very helpful. Further thanks to the other PhD students and staff members in the Electrical Machines and Drives Group at the University of Sheffield, as well as the staff members in Sheffield Siemens Wind Power (S²WP) Research Centre.

Finally, I am very grateful to my wife Qianru Meng. Her love, encouragement and faith throughout my PhD study make me dedicate great efforts on my research. I would also like to thank my whole family for their endless care.

CONTENTS

ABSTRACT.....	II
ACKNOWLEDGEMENTS	III
CONTENTS.....	IV
LIST OF SYMBOLS	IX
LIST OF ABBREVIATIONS	XIII

CHAPTER 1.....1

GENERAL INTRODUCTION

1.1 Introduction.....	1
1.2 Permanent Magnet Synchronous Machines.....	2
1.2.1 Single Three-Phase PMSM.....	2
1.2.2 Dual Three-Phase PMSM	8
1.3. Sensorless Control of PMSM	13
1.3.1 Saliency Based Sensorless Control.....	15
1.3.2 Fundamental Model Based Sensorless Control	21
1.3.3 Sensorless Predictive Torque Control	30
1.3.4 Sensorless Control for Dual Three-Phase PMSM	31
1.4 Outline and Contributions of the Thesis	31

CHAPTER 2.....35

EXPERIMENTAL PERMANENT MAGNET SYNCHRONOUS MACHINES AND DRIVE SYSTEMS

2.1 Introduction.....	35
2.2 dSPACE Based Control System.....	35
2.2.1 CPU Board-DS1006.....	35
2.2.2 ADC board-DS2004.....	36
2.2.3 Encoder board-DS3001.....	37
2.2.4 PWM Board-DS5101.....	38
2.2.5 Software Environment	39

2.3 Test Rigs for Control Strategy Development.....	39
2.3.1 Test Rig I.....	40
2.3.2 Test Rig II.....	41
2.3.3 Test Rig III.....	44
2.3.4 Rotor Position Alignment for Encoder.....	47
2.4 Conclusion.....	49

CHAPTER 3.....50

NEW SENSORLESS CONTROL BASED ON SINUSOIDAL HIGH-FREQUENCY PULSATING CARRIER SIGNAL INJECTION INTO STATIONARY REFERENCE FRAME

3.1 Introduction.....	50
3.2 High Frequency Model of PMSM Accounting for Cross-Saturation Effect...51	
3.2.1 Model in Synchronous Reference Frame.....	51
3.2.2 Current Model in Estimated Synchronous Reference Frame.....	54
3.2.3 Current Model in Stationary Reference Frame.....	55
3.3 Conventional High Frequency Carrier Signal Injection Methods.....	55
3.3.1 Pulsating Carrier Signal Injection.....	55
3.3.2 Rotating Carrier Signal Injection.....	60
3.3.3 Rotor Position Observer.....	65
3.3.4 Steady-state and Dynamic Performance.....	66
3.4 New Proposed Control Strategy with Injection of High Frequency Pulsating Signal into Stationary Reference Frame.....	69
3.4.1 New Proposed High Frequency Carrier Signal Injection Method.....	70
3.4.2 I_p Pre-Detection and Compensation.....	74
3.4.3 Cross-saturation Effect Compensation.....	75
3.4.4 Rotor Position Estimator.....	76
3.4.5 Magnetic Polarity Detection.....	78
3.4.6 Steady-state and Dynamic Performance.....	88
3.4.7 Comparison of Carrier Signal Injection based Sensorless Controls.....	92
3.5 Conclusion.....	93

CHAPTER 4.....94

NEW SENSORLESS CONTROL BASED ON SQUARE WAVEFORM HIGH FREQUENCY PULSATING CARRIER SIGNAL INJECTION INTO STATIONARY REFERENCE FRAME

4.1 Introduction.....	94
4.2 Conventional Square Waveform High Frequency Carrier Signal Injection Methods	95
4.2.1 Square Waveform High Frequency Injection.....	95
4.2.2 Steady-state and Dynamic Performance	98
4.3 New Proposed Control Strategy with Square Waveform High-Frequency Pulsating Signal Injection into Stationary Reference Frame.....	101
4.3.1 Square Waveform Carrier Signal Injection.....	101
4.3.2 I_p^{SQ} Pre-Detection and Compensation.....	106
4.3.3 Rotor Position Estimator.....	109
4.3.4 Steady-state and Dynamic Performance	110
4.3.5 Square waveform Carrier Signal Injection based Sensorless Controls	112
4.4 Application of High Frequency Injection Strategy in Wind Power System .	114
4.5 Conclusion	117

CHAPTER 5..... 119

IMPROVEMENT OF SENSORLESS CONTROL PERFORMANCE BASED ON THIRD HARMONIC BACK-EMF BY SPEED ERROR COMPENSATION

5.1 Introduction.....	119
5.2 Detection of Third Harmonic Back-EMF and Conventional Sensorless Control.....	120
5.2.1 Detection of Third Harmonic Back-EMF.....	120
5.2.2 Conventional Sensorless Control.....	123
5.3 Improved Rotor Position Estimator	127
5.3.1 Rotor Position Estimator based on Zero-Crossing Correction	127
5.3.2 Improved Rotor Position Estimator Based on Speed Compensation..	130

5.4 Comparison and Improvement of Flux Observer based on Third Harmonic Back-EMF by Error Compensation	141
5.4.1 Position Estimation from Flux Observer	141
5.4.2 Position-Error-Based Compensator	146
5.4.3 Improved Speed-Error-Based Compensator	149
5.4.4 Robust Operation Performance	152
5.4.5 Comparison of Third Harmonic Back-EMF and Fundamental Back-EMF Based Sensorless Controls	156
5.5 Conclusion	157

CHAPTER 6.....158

SENSORLESS CONTROL BASED ON THIRD HARMONIC BACK-EMF AND SIMPLIFIED EKF FOR SINGLE AND DUAL THREE-PHASE PMSM

6.1 Introduction.....	158
6.2 EKF and Its Application to Rotor Position Estimation.....	159
6.3 Rotor Position Estimation Based on Third Harmonic Back-EMF and Simplified EKF for Single Three-Phase PMSM Operation.....	161
6.4 Rotor Position Estimation Based on Third Harmonic Back-EMF and Simplified EKF for Dual Three-Phase PMSM	168
6.5 Conclusion	177

CHAPTER 7.....178

INFLUENCE OF MACHINE SALIENCY AND WINDING IMBALANCE ON SENSORLESS CONTROL BASED ON THIRD HARMONIC BACK-EMF

7.1 Introduction.....	178
7.2 Absence of Third Harmonic Back-EMF	179
7.3 Influence of Stator Current and Machine Saliency to Rotor Position Estimation Based on Third Harmonic Back-EMF.....	181
7.3.1 Influence of Stator Current and Machine Saliency.....	181
7.3.2 Experimental Analysis and Estimation Error Compensation.....	183
7.3.3 Summary	191

7.4 Rotor Position Estimation Based on Third Harmonic back-EMF under Imbalanced Situation for Single and Dual Three-Phase PMSM	192
7.4.1 Detection of Third Harmonic back-EMF under Imbalanced Situation	192
7.4.2 Rotor Position Estimation under Imbalanced Situation for Single Three-Phase PMSM operation	195
7.4.3 Rotor Position Estimation under Imbalanced Situation for Dual Three-Phase PMSM operation	203
7.5 Conclusion	210

CHAPTER 8.....212

GENERAL CONCLUSION AND DISCUSSION

8.1 Sensorless Control	213
8.1.1 Sensorless Control Based on Machine Saliency	213
8.1.2 Sensorless Control Based on Third Harmonic Back-EMF	215
8.2 Future Work: Hybrid Sensorless Control with Proper Designed Motor	217

REFERENCES.....219

APPENDICES.....236

Appendix I Specification of Prototype Machines	236
Motor I	236
Motor II	237
Motor III	238
Appendix II Transformation of Phase Vector with Harmonics	239
Appendix III Rotating Carrier Signal Injection into the Estimated Synchronous Reference Frame	240
Appendix IV Patents and Papers during This PhD Study	247
Patents	247
Papers	247

LIST OF SYMBOLS

Symbol	Explanation of Symbol	Units
A_{mp}	Amplitude of ψ_{sn}	wb
B_3	Amplitude of the third-harmonic component of the excitation flux density	wb
$e_a, e_b, \text{ and } e_c$	3-phase back-EMFs	V
$e_d, \text{ and } e_q$	d - and q -axis back-EMFs	V
$e_i, i=1,2,3,\dots$	i th order harmonic back-EMFs	V
$e_{triplen}$	Triplen harmonic back-EMF	V
$e_{\alpha}, \text{ and } e_{\beta}$	α - and β -axis back-EMFs	V
E_{ex}	Extended back-EMF	V
$E_i, i=1,2,3,\dots$	Amplitude of i th order harmonic back-EMF	V
E_m	Amplitude of back-EMF	V
$f(\Delta\theta)$	Position error signal	
$i_a, i_b, \text{ and } i_c$	3-phase currents	A
$i_{ah}, i_{bh}, \text{ and } i_{ch}$	3-phase high frequency carrier currents	A
$i_d, \text{ and } i_q$	d - and q -axis currents	A
$i_d^e, \text{ and } i_q^e$	d - and q -axis currents in estimated reference frame	A
$i_{dh}, \text{ and } i_{qh}$	d - and q -axis high frequency carrier currents	A
$ i_{dqh}^e $	Amplitudes of d - and q -axis high frequency carrier currents in estimated reference frame	A
i_n	Negative sequence current	A
i_{neg}	Negative sequence carrier current	A
$i_{\alpha h}, \text{ and } i_{\beta h}$	α - and β -axis high frequency carrier currents	A
$ i_{\alpha\beta h} $	Amplitudes of α - and β -axis high frequency carrier currents	A
$i_{\alpha\beta h}^{**}$	Alternating components of $ i_{\alpha\beta h} $ without considering θ_m	A

$i_{\alpha\beta h}^*$	Alternating components of $ i_{\alpha\beta h} $ considering θ_m	A
\dot{i}	Current vector	A
I_{dh} , and I_{qh} ,	Amplitude of high frequency carrier currents	A
I_p , and I_n	$I_p = U_c / \omega_c L_p$, and $I_n = U_c / \omega_c L_n$	A
I_p^{SQ} , and I_n^{SQ}	$I_p^{SQ} = U_c \Delta T / L_p$, and $I_n^{SQ} = U_c \Delta T / L_n$	A
I_m	Amplitude of phase current	A
K_3	Third harmonic back-EMF constant	
K_{id} , K_{iq}	d - and q -axis influence factor to third harmonic back-EMF	
K_p	Amplitude unified ratio between u_{sn} and ψ_{sn}	
L_a , L_b , and L_c	3-phase incremental inductances	mH
L_{aa} , L_{bb} , and L_{cc}	3-phase incremental self-inductances	mH
L_d , and L_q	d - and q -axis incremental inductances	mH
L_{dh} , and L_{qh}	d - and q -axis high frequency incremental self-inductances	mH
L_{dqh} and L_{qdh}	High frequency incremental mutual-inductances	mH
L_i , M_i , $i=1,2,3,\dots$	i th order harmonic incremental self- and mutual-inductances	mH
L_p , and L_n	$L_p = (L_{dh}L_{qh} - L_{dqh}^2) / L_{sa}$, and $L_n = (L_{dh}L_{qh} - L_{dqh}^2) / \sqrt{L_{sd}^2 + L_{dqh}^2}$	mH
L_{sa} , and L_{sd}	Average and difference of d - and q -axis incremental inductances	mH
M_{ab} , M_{ac} , M_{bc} , M_{ba} , M_{ca} , and M_{cb} ,	3-phase incremental mutual-inductances	mH
p	Derivative operator, $p=d/dt$	
R_s	Phase resistance	Ω
t_d	Time difference between two zero crossings	s
T_{m_BLAC}	Electromagnetic torque of a BLAC motor	Nm
T_{m_BLDC}	Electromagnetic torque of a BLDC motor	Nm

$u_{an}, u_{bn},$ and u_{cn}	3-phase voltages	V
$u_{as}, u_{bs},$ and u_{cs}	3-phase voltages to the central point “s” of the resistor network	V
u_c	High frequency injection carrier voltage	V
u_f	Fundamental components in u_{sn} due to imbalanced machine parameters, $u_f = A_{p_u} \sin(\omega_r t + \varphi_u)$	V
$u_d,$ and u_q	d - and q -axis voltages	V
$u_{dh},$ and u_{qh}	d - and q -axis high frequency carrier voltages	V
$u_d^e,$ and u_q^e	d - and q -axis voltages in estimated reference frame	V
$u_p,$ and ψ_p	Positive sequence components in u_{sn} and ψ_{sn}	V
$u_{nz},$ and ψ_{nz}	Negative and zero sequence components in u_{sn} and ψ_{sn}	V
u_{sn}	Voltage between central point “s” of resistor network and winding neutral “n” representing third harmonic back-EMF	V
$u_{sn_unified}$	Amplitude-unified u_{sn}	V
$u_{\alpha h},$ and $u_{\beta h}$	α - and β -axis high frequency carrier voltages	V
$u_{\alpha\beta}^*$	Command of SVPWM	V
\dot{U}	Voltage vector	V
U_c	Amplitude of high frequency injection voltage	V
α	Phase angle of injected carrier voltage, $\alpha = \omega_c t + \varphi$	rad
θ_{cor}	Rotor position correction	rad
θ_f	Rotor position estimated from flux observer	rad
θ_m	Cross-saturation angle	rad
θ_r	Electrical rotor position	rad
θ_r^e	Estimated electrical rotor position	rad
λ	Coupling factor $\lambda = L_{dqh}/L_{qh}$	
$\psi_d,$ and ψ_q	d - and q -axis flux-linkages	wb
ψ_{d_act}	Active flux-linkage	wb

ψ_f	Fundamental components in ψ_{sn} due to imbalanced machine parameters, $\psi_f = A_{mp} \cos(\omega_r t + \varphi_\psi)$	wb
$\psi_{f\alpha}$, and $\psi_{f\beta}$	α - and β -axis rotor flux-linkage	wb
ψ_m	Permanent magnet excited flux-linkage	wb
ψ_s	Stator flux-linkage	wb
ψ_{sn}	Integration of u_{sn} representing third harmonic flux-linkage	wb
ψ_{sn}^e	ψ_{sn} estimated from feedback rotor position	wb
ω_{cor}	Speed correction	rad/s
ω_f	Rotor speed estimated from flux observer	rad/s
ω_r	Electrical rotor speed	rad/s
ω_r^e	Estimated electrical rotor speed	rad/s
$\Delta i_{\alpha\beta h}$	α - and β -axis high frequency carrier current difference	A
$\Delta i_{\alpha\beta h}^*$	Envelopes of $\Delta i_{\alpha\beta h}$	A
$\Delta i'_{\alpha\beta h}$	Difference between two sampling instants of $\Delta i_{\alpha\beta h}^*$	A
Δt_s	Time difference between two sampling instants	s
ΔT	Time duration of injected square waveform voltage	s
$\Delta \theta$	Rotor position estimation error	rad
$\Delta \theta_s$	Rotor position difference between two sampling instants	rad
$\dot{\Psi}_f$	Rotor flux-linkage vector	wb
$\dot{\Psi}_{f(0)}$	Integration drift in flux observer	wb
$\dot{\Psi}_s$	Stator flux-linkage vector	wb
Ω	Mechanical rotor speed	rpm

LIST OF ABBREVIATIONS

AC	Alternating current
A/D	Analog to digital
ADC	Analog to digital converter
BLAC	Brushless AC
BLDC	Brushless DC
BPF	Band pass filter
DC	Direct current
DSC	Direct self-control
DSP	Digital signal processor
DTC	Direct torque control
EKF	Extended Kalman filter
EM	Extended modulation
EMF	Electromotive force
HPF	High pass filter
IGBT	Insulated-gate bipolar transistor
INFORM	Indirect flux detection by online reactance measurement
IPM	Interior permanent magnet
LPF	Low pass filter
MBPC	Model based predictive control
MMF	Magnetic motive force
MRAS	Model reference adaptive system
PI	Proportional integral
PID	Proportional integral derivative
PLL	Phase-locked loop

PM	Permanent magnet
PMSM	Permanent magnet synchronous machine
PTC	Predictive torque control
PWM	Pulse width modulation
RPM	Revolutions per minute
SNR	Signal to noise ratio
SPM	Surface-mounted permanent magnet
SRFF	Synchronous reference frame filter
SVPWM	Space vector pulse width modulation
TP-PLL	Two-phase-type Phase-locked loop
VC	Vector control
VSI	Voltage source inverter

CHAPTER 1

GENERAL INTRODUCTION

1.1 Introduction

In the last several decades, the development of permanent magnet (PM) materials, power electronic devices and DSP/microprocessors has made a great contribution to the permanent magnet synchronous machines (PMSM), which have the advantages of high efficiency, high power density, easy maintenance and excellent control performance. Multi-phase motor drives have also remarkably increased, especially for high-power applications such as electric vehicles, wind power generators, etc, where the power can be divided into more inverter legs in order to reduce the current stress of single static switch and the current density instead of adopting parallel and multi-level converter. Furthermore, the torque ripple, the rotor harmonic currents and the harmonic content can be reduced. Also, it has higher reliability, since a multi-phase motor can operate with an asymmetric winding structure in the case of breakdown of one or more inverter legs or machine phases for fault-tolerant usage.

Due to the control flexibility, higher dynamic performance and lower cost, PMSM drives continue to be the subject of research in both academia and industry. The essential requirement in PMSM current control is to get the rotor position information, because the air gap flux-linkage is generated from the PM which is attached to the rotor. Consequently, position sensors such as an absolute/incremental encoder or a resolver located on the shaft of the rotor are needed. However, in certain applications, these sensors cannot be used because of several disadvantages, such as increased complexity of the drive system leading to lower reliability, susceptibility to noise and vibration, additional cost and weight, etc. Hence, sensorless control techniques have been widely researched and applied in industries, and will be the subject of research in this thesis.

1.2 Permanent Magnet Synchronous Machines

1.2.1 Single Three-Phase PMSM

1.2.1.1 Topologies of single three-phase PMSM

There are numerous topologies for PMSM as briefly summarized in Fig. 1.1 [CHE99, pp. 3-9].

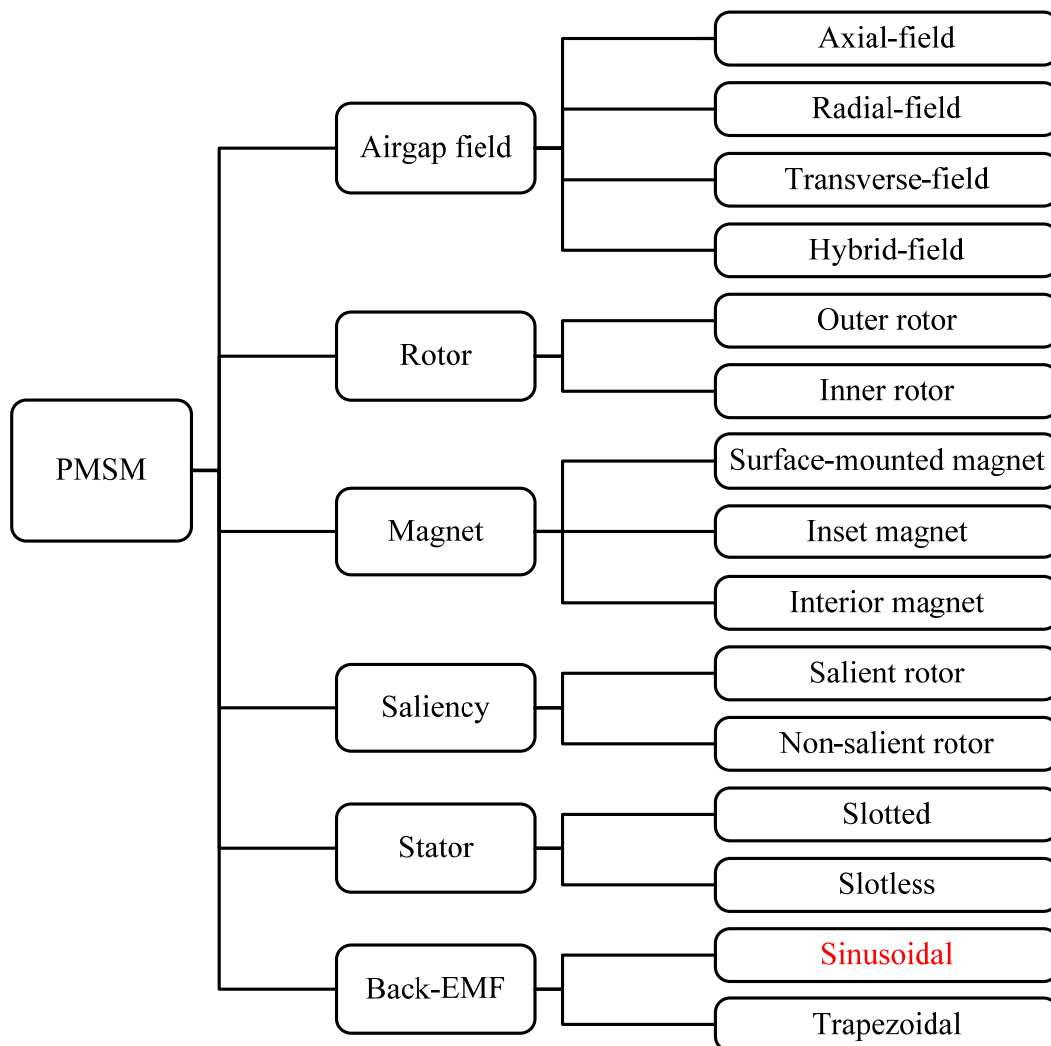


Fig. 1.1. Summary of PMSM topologies [CHE99]

In general, the windings for a typical slotted stator can be classified into non-overlapping winding and overlapping winding, as illustrated in Fig. 1.2. For non-overlapping winding, it is easy for automatic manufacture, and the end winding is short whereas the winding factor is usually smaller than 1. The thermal isolation

between phases can be good depending on the design and the cogging torque is usually low due to the fractional-slot stator. Also the space distribution of stator magnetomotive force (MMF) is usually a square-waveform which makes the back-EMF usually trapezoidal. For overlapping winding, it is difficult for automatic manufacture and thermal isolation. The end winding is long, whereas the winding factor could be up to 1. Due to the integral-slot, the cogging torque may be larger. However, the MMF distribution can be sinusoidal [HEN94].

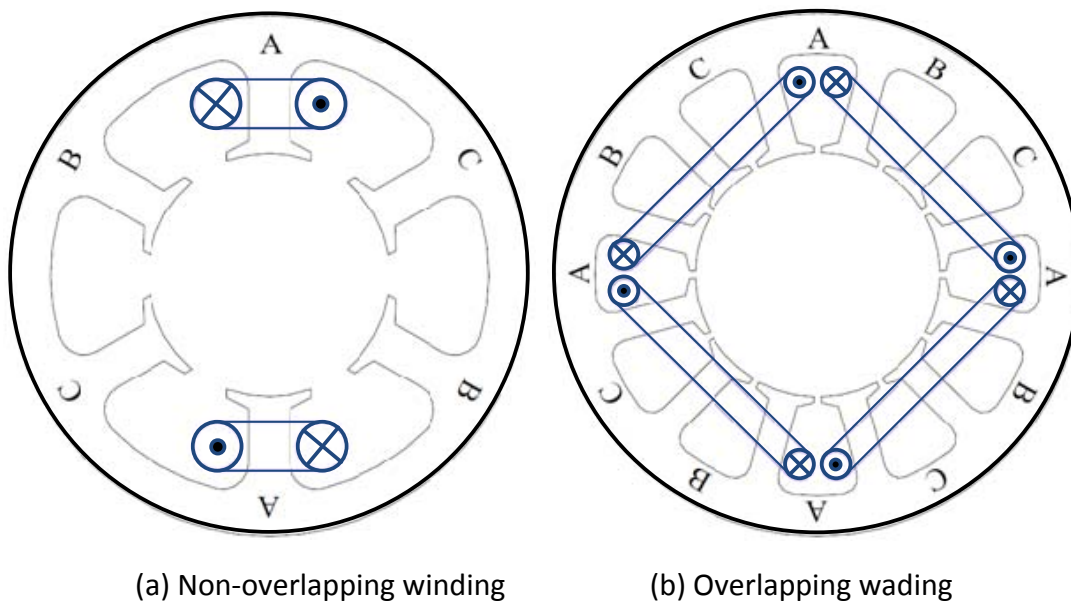


Fig. 1.2. Stator windings [SHE02a].

PMSM can also be characterized by PM on the rotor which produces the air gap flux-linkage. Fig. 1.3 illustrates the typical rotor structures for conventional inner rotor radial field PMSMs [LI09a]. Unlike the lamination with high magnetic permeability, the rare earth PM materials have lower permeability, which is close to the value of air gap. As a consequence, there is negligible geometric saliency for the surface-mounted rotor configuration, whereas, the other three rotor configurations exhibit significant saliency effect resulting from geometric anisotropy. Moreover, motors with interior permanent magnets (IPM) can exhibit good flux-weakening capability which will significantly extend the maximum operation speed due to its larger d -axis inductances, whilst the flux-weakening capability of surface-mounted permanent magnet (SPM) motors is usually limited.

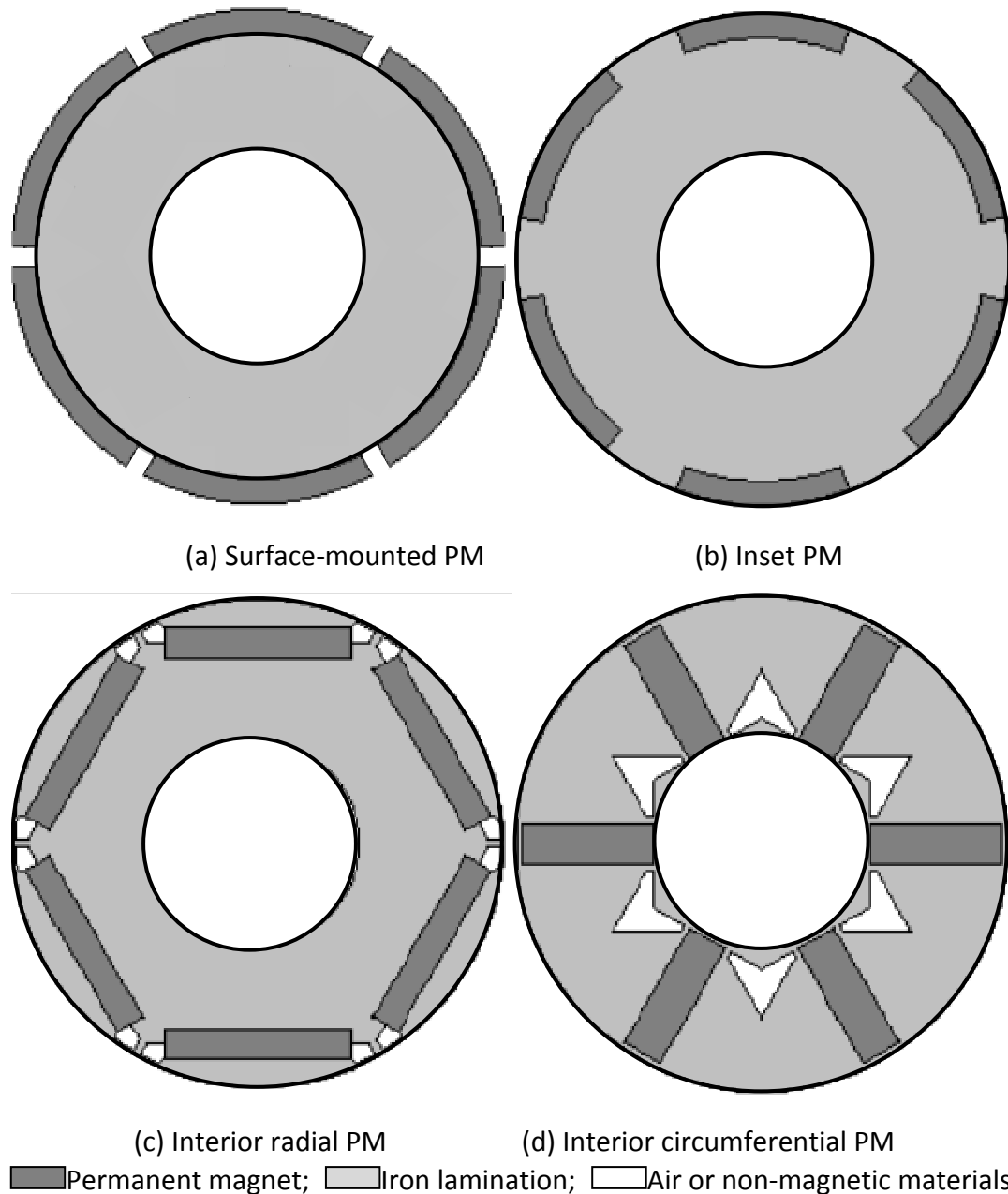
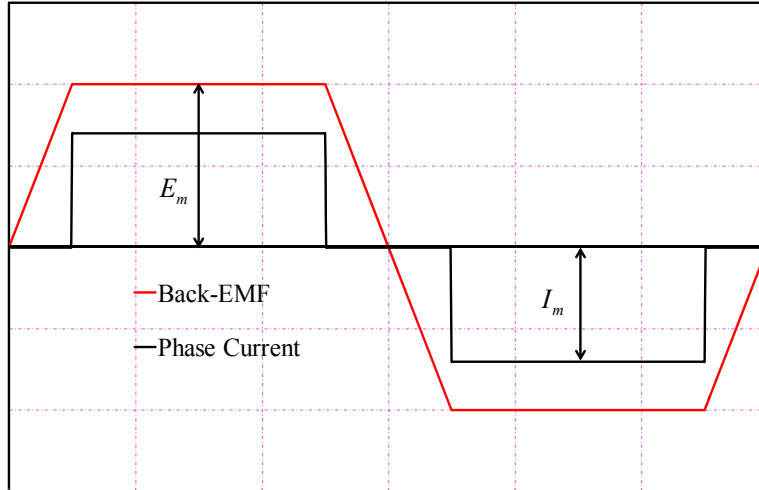
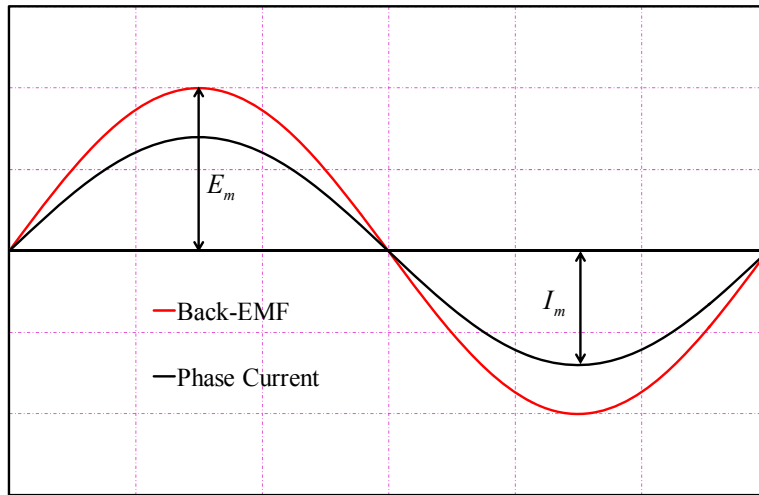


Fig. 1.3. Typical rotor structures of PMSM [CHE99].

According to the type of back-EMF, PMSM can be categorized as brushless DC (BLDC) machines with trapezoidal phase back-EMF and brushless AC (BLAC) machines with sinusoidal back-EMF. Meanwhile, according to the type fundamental excitation, PMSM operation can be categorized as BLDC machines operation mode driven by square wave current excitation, and BLAC operation mode driven by sinusoidal current excitation. Usually, BLDC machine is driven in BLDC operation mode and BLAC machine is driven in BLAC operation mode as shown in Fig. 1.4.



(a) BLDC machine driven by BLDC operation mode



(b) BLAC machine driven by BLAC operation mode

Fig. 1.4. Excitation of BLDC and BLAC machines.

Ideally, a square wave back-EMF motor should be operated in the BLDC mode. If both the phase current and back-EMF are ideal waveforms, as shown in Fig. 1.4(a), i.e. the back-EMF is trapezoidal with a flat top of 120° , while the current waveform is square wave, the electromagnetic torque of a BLDC motor will be free of ripple, and can be expressed as

$$T_{m_BLDC} = \frac{2E_m \cdot I_m}{\Omega} = \frac{2p \cdot E_m \cdot I_m}{\omega_r} \quad (1.1)$$

where p is the number of pole-pairs, and Ω and ω_r are the mechanical and electrical rotor speed, respectively. However, both the phase current and back-EMF are rich in harmonics which may increase the stator and rotor losses.

A sinusoidal wave back-EMF motor should ideally operate in the BLAC mode, where both the phase current and back-EMF are ideal sinusoidal waveforms, as shown in Fig. 1.4(b), and the ripple free electromagnetic torque can be expressed as

$$T_{m_BLAC} = \frac{3E_m \cdot I_m}{2\Omega} = \frac{3p \cdot E_m \cdot I_m}{2\omega_r} \quad (1.2)$$

1.2.1.2 Control of single three-phase PMSM

A PMSM drive consists of a controller, an inverter and a motor, as shown in Fig. 1.5. BLDC machines are usually used in relatively low cost applications, where only discrete rotor position information with low resolution is required. Whereas, BLAC machines are excited by sinusoidal phase current, synchronizing with the PM excited flux-linkage, thus continuous rotor position information with high resolution is required. In this thesis, only the operation of PMSM as a BLAC machine is considered since it is widely applied due to its excellent control performance.

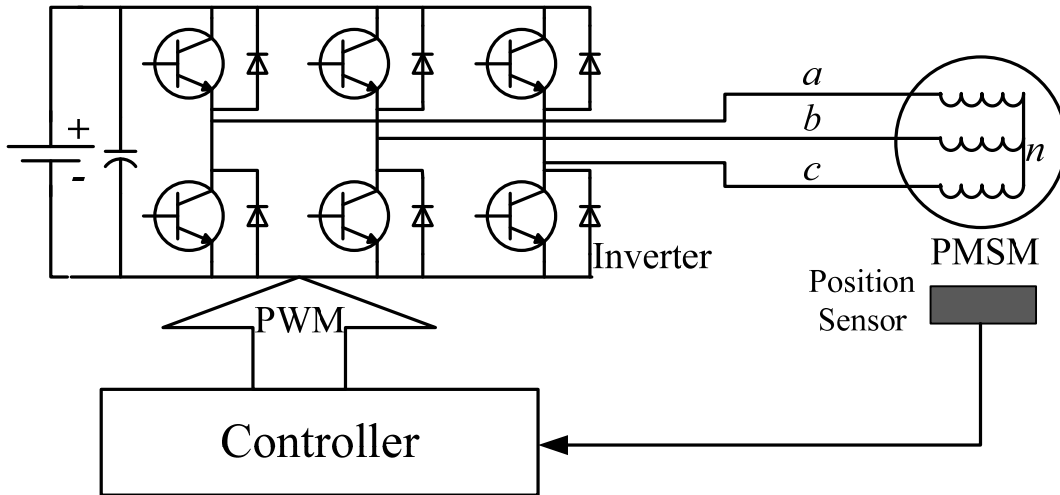


Fig. 1.5. Single three-phase PMSM drive

It is well known that the vector control (VC) by applying the $d-q-0$ reference frame transformation has been used in the analysis and control of three-phase electrical machine successfully for long time. In this system, with the aid of coordinate transformations and specific modulations, the original three-dimensional vector space is decomposed into a $d-q$ subspace and an orthogonal zero sequence subspace. By this decomposition, the parameters which produce rotating MMF and

the parameters of zero sequence which is usually triplen harmonic components are totally decoupled. When the windings of PMSM are Y-connected, the zero sequence components usually neglected. Thus the analysis and control of the motor are simplified. The VC scheme of PMSM is shown Fig. 1.6 where the torque related q -axis current and airgap flux-linkage related d -axis current can be directly controlled individually [VAS03, pp. 87-177].

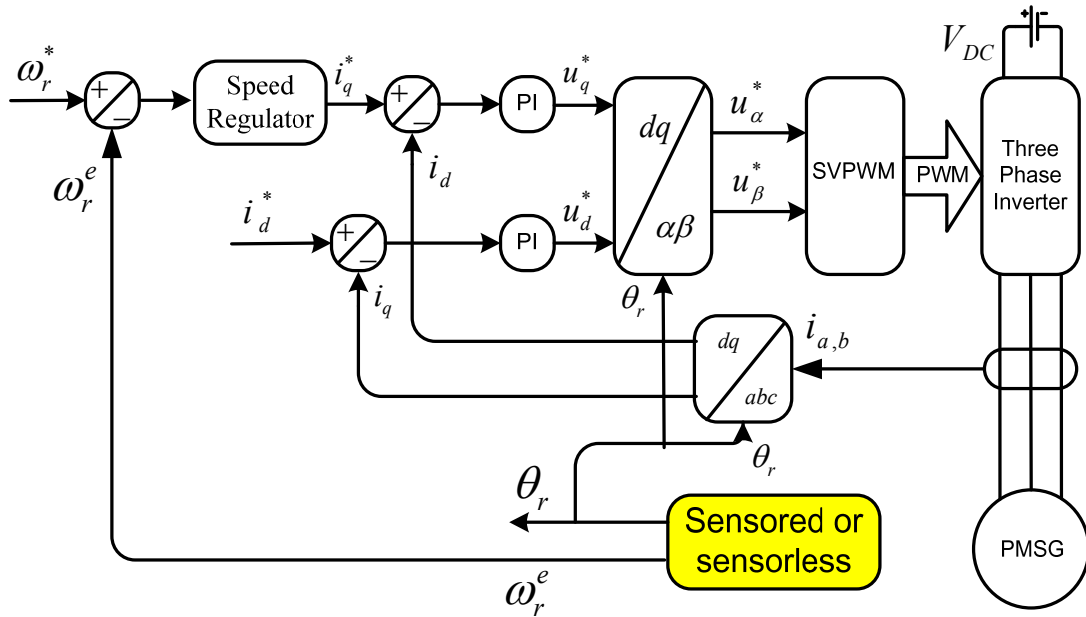


Fig. 1.6. Vector control scheme of PMSM

Direct torque control (DTC) has been developed for PMSM due to simple structure, excellent transient response and good robustness against rotor parameters, DTC was first proposed in [TAK86] and [DEP88] for induction machines, and has now been extended to other machines, such as PMSM [ZHO97] [PAC05] [FOO09a] [ZHA11], BLDC operation [ZHU12], and doubly fed induction machine [ABA08]. Hysteresis regulators are usually implemented in the conventional switching-table based DTC strategy for the regulation of both electromagnetic torque and stator flux as shown in Fig. 1.7. The same as VC, phase voltage which is necessary for torque and flux calculation can be obtained from the regulators. Hence, the voltage sensors are not needed either. Compared to the VC, coordinate transformations and specific modulations are not required. Hence, the transient torque control performance can be significantly improved. However, in a digital controller, the responses of both torque

and stator flux controllers can exceed the predefined hysteresis bands due to the time delay and the fixed sampling frequency, potentially leading to large torque and stator flux ripples.

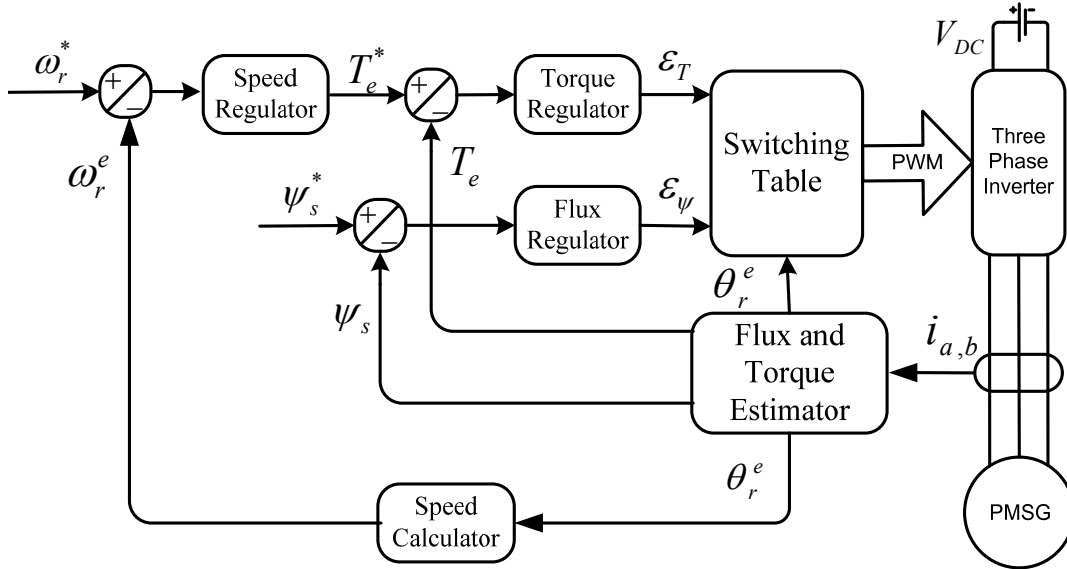


Fig. 1.7. Direct torque control scheme of PMSM

1.2.2 Dual Three-Phase PMSM

During the past decade, interest in multiphase systems with more than three phases has increased. For power system applications, the high phase order transmission system has been investigated as a means of increasing the capacity of overhead electric power transmission rights of way. For motor drive applications, multiphase system could potentially meet the demand for high-power electric drive systems which are both rugged and energy-efficient.

1.2.2.1 Topologies of dual three-phase PMSM

The basic structure of dual three-phase PMSM is similar as single three-phase PMSM as introduced in Section 1.2.1.1 where the windings can be classified into non-overlapping windings and overlapping windings, and the rotor can be categorized as SPM and IPM. Due to multiphase winding structure, the displacement of three-phase winding sets can have different phase shift. Nelson in [NEL74] analyzes multi-phase motor in that it permits an arbitrary displacement between any numbers of

three-phase winding sets. The amplitude of the torque ripple with BLDC operation has been reduced from 25% of the average torque for 0° and 60° displacement to only 5% with 30° displacement. The predominant frequency has also been shifted from six to twelve times supply frequency because it can be seen as a symmetrical twelve-phase motor. Furthermore, the q - and d -axis rotor currents for the 30° case are seen to be more sinusoidal than for the other two cases, which minimises the temperature and the associated sixth harmonic pulsating torque. Hence, two three-phase winding sets displaced by 30° as shown in Fig. 1.8 is the most popular topology.

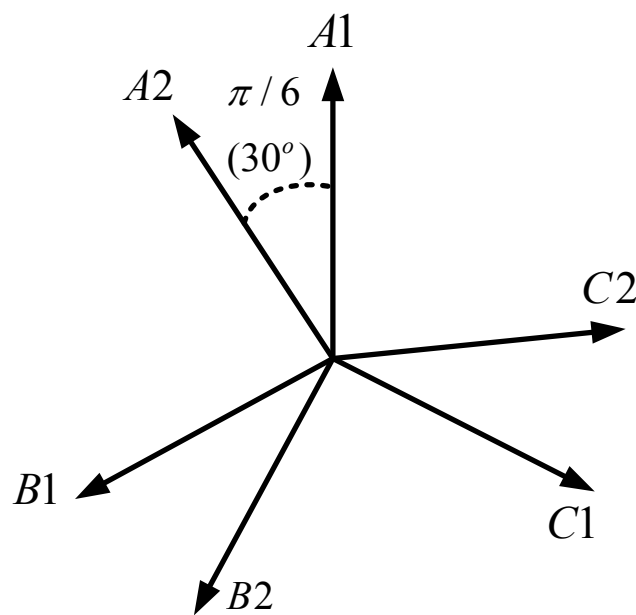


Fig. 1.8. Winding vector of dual three-phase PMSM

Having additional phases to control means additional degrees of freedom available for further improvements in the drive system. For dual three-phase motor, it is usually excited by a full-bridge voltage source inverter as shown in Fig. 1.9. Then the required inverter phase current permits are reduced due to the multiphase inverter instead of a group of devices connected in parallel, and hence, the total system reliability is also improved, whereas the efficiency performance is nearly not affected [BOG06]. However, the increasing of control complexity is significant.

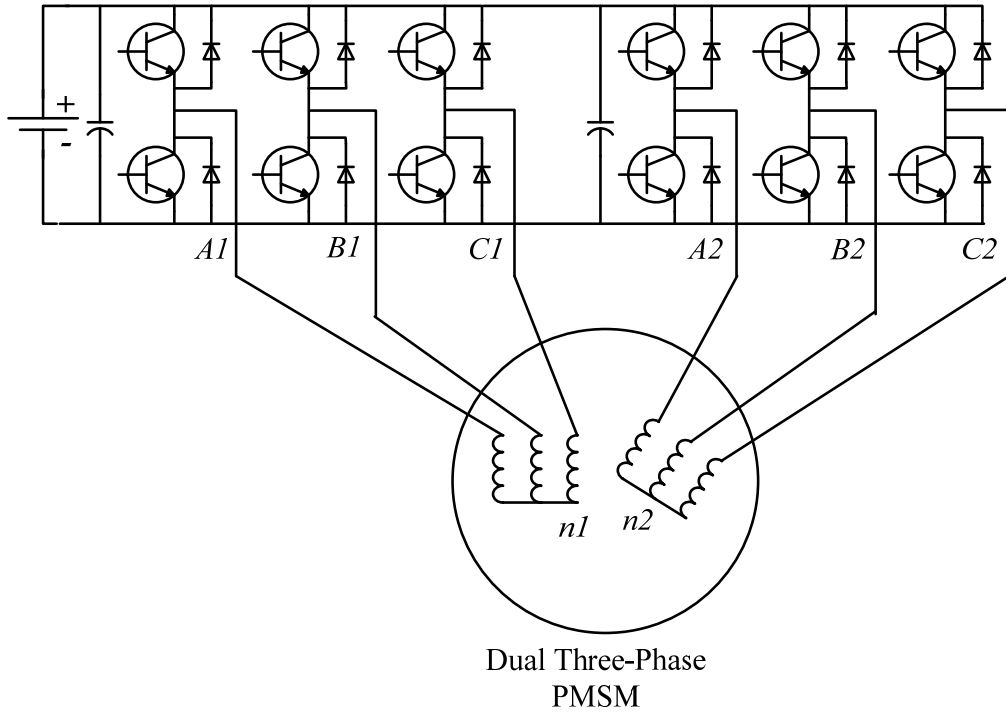


Fig. 1.9. Dual three-phase PMSM drive

1.2.2.2 Control of dual three-phase PMSM

For dual three-phase PMSM control, it can also be categorized into two different techniques as the ones for single three-phase PMSM, i.e. VC and DTC.

VC, i.e. vector control, follows two different approaches, viz. dual $d-q$ reference frame control and six-dimensional control. In both approaches the two zero-sequence components can be omitted from consideration, since the neutral points n_1 and n_2 of the two three-phase windings are isolated as illustrated in Fig. 1.9.

According to the first approach, the machine can be represented with two pairs of $d-q$ windings that represent the two three-phase windings, and be considered as two single three-phase motor with coupling voltage [NEL74] [LIP80]. Then, each original set of three-dimensional vector spaces are decomposed into one $d-q$ subspace and one orthogonal zero sequence subspace. By this decomposition, the parameters which produce rotating MMF and the parameters of zero sequence are totally decoupled within one set. Thus, the analysis and control of the motor are simplified, and the dual three-phase PMSM can be excited by applying the conventional space vector pulse

width modulation (SVPWM) generator. However, the cross-coupling effect between of the two sets of windings which will increase the stator leakage inductance and consequently increase the inverter commutation voltage [KAR12] is nearly not considered. Meanwhile, the generated fifth and seventh harmonic current which will affect the output torque performance are also not easy to eliminate.

According to the second approach, dual three-phase PMSM is seen as a six-dimensional system. Hence, the modelling and control of this system are addressed in a six-dimensional space. Geometrically, the proper control of the dual three-phase machine is equivalent to positioning the vector on a certain surface in the six-dimensional vector space and rotating this vector at a desired speed [WAR69] [ABB84]. Based on vector space decomposition, the machine can be represented with three orthogonal subspaces, viz. a $d-q$ subspace which is related to the electromechanical energy conversion, a z_1-z_2 subspace does not, and a o_1-o_2 which is neglected since the neutral points of the two three-phase windings are isolated and will not affect the operation [ZHA95].

The surface spanned by the fundamental component vector with key importance to the electromechanical energy conversion function of the machine is addressed as $d-q$ subspace and the variables can be controlled by applying VC as single three-phase PMSM. z_1-z_2 subspace is orthogonal to the $d-q$ subspace, and is expected that the variables on this plane will not generate any rotating MMF in the airgap. However, if there is any asymmetry between the two three-phase stator windings or inside each set of winding, stator currents of fundamental frequency will appear in the z_1-z_2 subspace, and should be eliminated to avoid the inherent asymmetry effect of the dual three-phase systems [LYR02] [BOJ03] [HE10] [GRE10].

The transformation has the property to separate harmonics into different groups and to project them into each subspace. Hence, the low-order harmonics such as the fifth and seventh will be projected to z_1-z_2 subspace which results in large stator circulating fifth and seventh harmonic currents [ABB84] [GOP93], especially when dual six-step VSI is used [NEL74] [XU95], because of the small impedance for these harmonics. Therefore, the above-mentioned impedance should be as high as possible.

Furthermore, in [ZHA95] [HAD06], SVPWM for dual three-phase motor to minimize these low-order harmonic is described, where four adjacent voltage vectors are always selected from the vectors which span the outermost polygon on the $d-q$ plane according to the position of the reference voltage vector, and the fifth vector is chosen from the zero vectors located at the $d-q$ plane origin.

DTC, i.e. direct torque control, is normally used in conventional single three-phase PMSM drives when fast electrical dynamic performance is required, and can be extended to multiphase machines. DTC with properly designed switching-table could obtain sinusoidal machine phase currents, by minimizing the current components $x-y$ subspace which is related to the stator flux-linkage [HAT05] [HOA12]. For the asymmetric dual three-phase machine, phase current distortion will appear, which can be solved by keeping the switching frequency constant, imposing the direct mean torque control approach, and applying PWM-DTC strategy [BOJ05] [FAR06]. By using the voltage vectors corresponding to the external layer of the dodecagon in the $\alpha-\beta$ subspace which is related rotor flux-linkage [BOJ06], the direct self-control (DSC) imposing a 12-sided polygonal trajectory of the stator flux is applied to minimize the fifth and seventh voltage harmonics which will in turn produce large current harmonics in $x-y$ subspace. Also, the utility of a predictive torque control (PTC) scheme in [BAR09] [BAR11a] for asymmetric dual three-phase AC drives could reduce the harmonic content of the stator current to improve the control performance.

A dual three-phase motor has a higher reliability at the system level, since it can operate with an asymmetric winding structure in the case of broken down of one or more inverter legs or machine phases for fault-tolerant usage [JAH80] [APS06] [BAR11b] [ALB12]. [BAR09] applies PTC in a fractional-slot PMSM with dual windings which is supplied by two parallel converters to increase the drive fault tolerance. [BAR10a] investigates the PMSM with dual three-phase windings and its capabilities during faulty operating condition. A fractional-slot interior PMSM with 12 slots and 10 poles is discussed in [BAR10b] according to different winding configurations, where the torque behaviour, overload capability, and thermal limits

are evaluated under open-circuit and short-circuit fault.

1.3. Sensorless Control of PMSM

As mentioned in Sector 1.2, the rotor position information is a critical concern for both BLDC and BLAC machines. Generally, this rotor position information can be obtained from high-resolution sensors mounted on a motor shaft. However, these sensors not only increase system cost and size but also tend to reduce the system reliability. To overcome these drawbacks, on-line rotor position estimation rather than direct measurement from physical position sensor, which is referred as sensorless, has been of considerable interest. Recently, various sensorless techniques have been developed which can be categorized into the methods for BLDC and for BLAC. BLDC machines are usually used in relatively low cost applications, where only discrete rotor position information with low resolution is required. Whereas, continuous rotor position information with high resolution is required for BLAC with sinusoidal phase current excitation. In this thesis, only sensorless control for BLAC operation is considered.

Various sensorless techniques for BLAC operation have been widely developed which can be categorized into the methods based on machine saliency and fundamental model as shown in Fig. 1.10. However, it is well known that none of the sensorless methods can guarantee the performance for all applications. Since the machine saliency which is the anisotropic property of PMSM is independent on the speed, the saliency based sensorless methods are expected to be reliable in zero and low speed range, but suffer at higher speed due to the weaker signal to noise ratio (SNR) of position dependent signal caused by the lower ratio between the injected and fundamental current. However, the algorithms based on fundamental model, which tend to fail at zero and low speed operations due to unobserved machine model, will show good performances over middle and high speed ranges since the machine model can be more accurately established over that speed ranges.

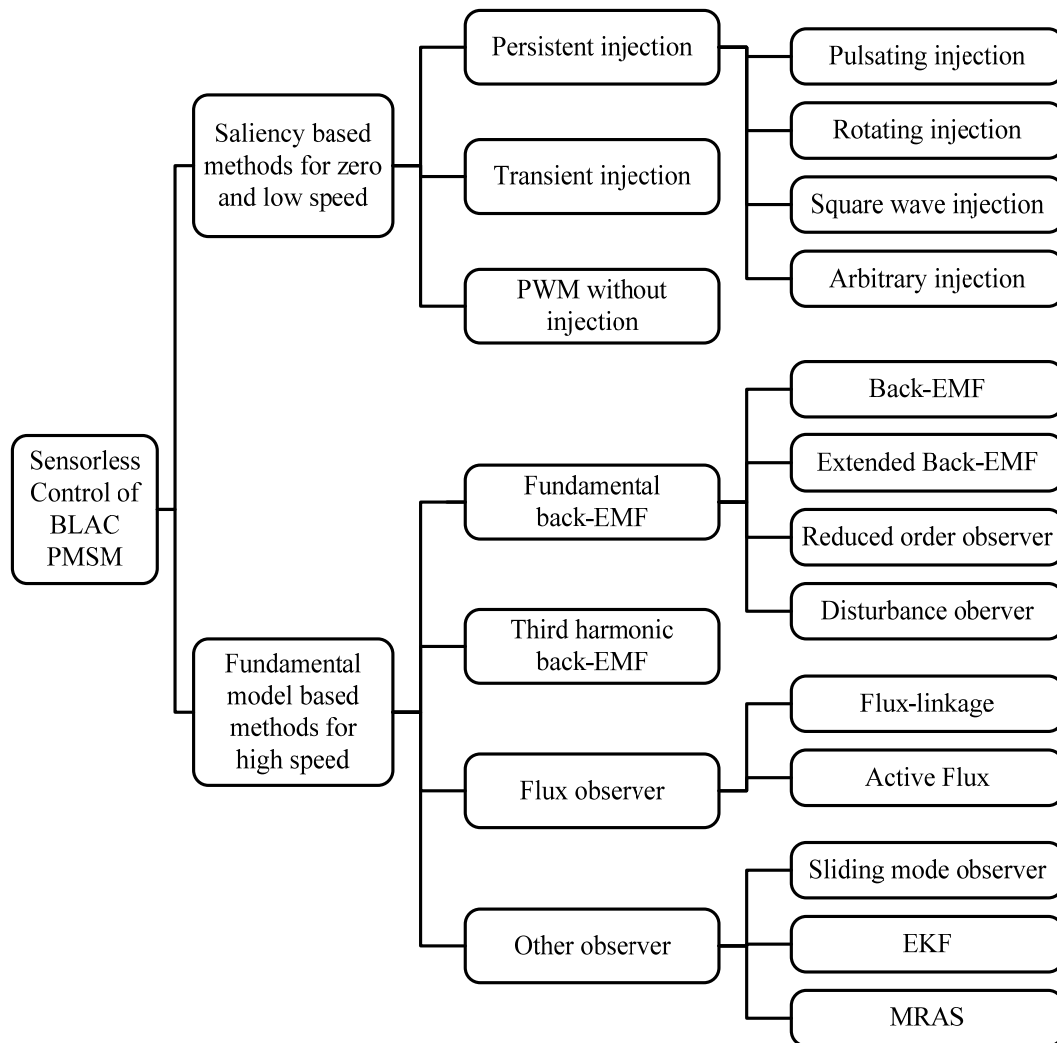


Fig. 1.10. Categories of sensorless control strategies for PMSM

To evaluate the sensorless control methods, rotor position error needs to be analyzed in detail. Usually, the estimation error can be categorized into AC, DC, and transient errors.

- An AC estimation error is a fluctuation and noise component which will introduce a ripple into the coordinate transformation. In position or speed control applications, the consequent current and torque ripples will increase, and the controlled position and speed will also contain certain fluctuation and noise, which will deteriorate the performance. Hence, AC estimation error should be minimized.

- A DC estimation error is the constant component which will lead the estimated rotor position a constant shift. Hence, the fundamental current will increase due to the consequent flux-enhancing or flux-weakening operation, which may result

in problems depending on the application. However, in some applications, such as cooling fan and water pump, where the energy conservation is the critical concern, the optimal efficiency of the machine and drive system is selected to be the objective for sensorless operation, and thus accurate rotor position without DC error is not required.

- A transient estimation error occurs during the dynamic operation such as speed or load step change. Differing from the AC and DC estimation errors, it is a short time duration error caused by improper closed-loop bandwidth of the rotor position estimator. This transient estimation error will increase the current and torque disturbance, as well as the risk of the divergence of the rotor position estimator and sensorless control system under dynamic operation. Hence, it must be minimized carefully.

1.3.1 Saliency Based Sensorless Control

The anisotropic property of PMSM, resulting from either geometric rotor or magnetic saliency, can be exploited in rotor position estimation for sensorless control and expected to be reliable in zero and low speed range, since the machine saliency behaviour is independent on the speed.

Fig. 1.11 illustrates the measured Inductance variation according to electrical rotor position for a salient PMSM [KAN10]. It confirms that the machine inductance is modulated by the position dependent spatial saliency. Hence, the rotor position can be deduced from this inductance variation.

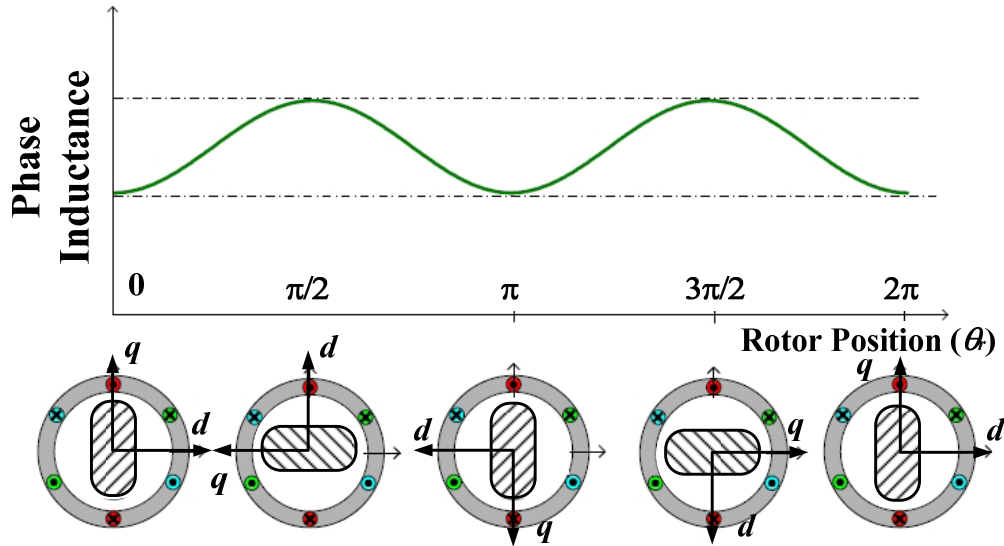


Fig. 1.11. Inductance variation according to electrical rotor position [KAN10].

In order to estimate the rotor position from the machine saliency, high frequency carrier signal injection is necessary to derive the position dependent response. According to the types of injected signal, the saliency based sensorless techniques can be classified into persistent carrier signal injection, transient voltage vector injection and PWM excitation without injection.

1.3.1.1 Persistent carrier signal injection

The persistent carrier signal injection continuously injects some extra voltage or current signals into the motor winding superimposed on the fundamental excitation. Then, the injected carrier signal interacts with machine saliency and the corresponding signal could be applied to deduce the rotor position. However, in carrier current injection [LIU11b], the current regulator with sufficiently high bandwidth is used to guarantee that the injected high frequency carrier current follows the reference command. For carrier voltage injection, although the injected carrier voltage signal may be disturbed by the current regulator and inverter nonlinearity effect, it is still acceptable to use the carrier voltage reference signal in the control algorithm with appropriate compensation techniques. Furthermore, the current sensors which are already present for current vector control can be used for the carrier current measurement, which would simplify the hardware design and decrease the system

cost. Consequently, carrier voltage signal injection is preferred. According to the type of injected carrier voltage signal, it consists of rotating sinusoidal signal injection [JAN95] [DEG98] [GAR07] [RAC08a] [RAC10], pulsating sinusoidal signal injection [COR98] [HA00] [LIN02] [JAN03] [LI09B], square wave signal injection [YOO09] [HAM10], and arbitrary injection [PAU11].

Rotating signal injection schemes inject a balanced three phase voltage into the stationary reference frame to form a rotating excitation superimposed on the fundamental excitation. The interaction between the carrier voltage vector and the machine saliency in the interior PMSM produces a carrier current signal response that contains rotor position information [JAN95] [JOE05]. It is clearly shown that the carrier current response consists of two components. The first term is a positive sequence component, which has the same rotating speed as the injected carrier voltage vector, and the second term is the negative sequence component, which contains the rotor position information in its phase angle. In order to extract the position dependent negative sequence carrier current, a synchronous reference frame filter (SRFF) is the typical solution [DEG98] [GAR07] [RAC10]. SRFF uses the frame transformation to centre the spectral component of interest at DC. With the aid of a low pass filter (LPF), this DC component can be easily obtained without phase lag. Conversely, a HPF can be used to eliminate this DC component. In general, the high-pass cut-off frequency is chosen to be sufficiently low so that negligible distortion occurs in the desired content, and the rotor position can be obtained by using a demodulator [JAN95]. Furthermore, the multiple saliencies [RAC08b], inverter dead-time effects [GUE05] [CHO07] [GON11a], and cross-coupling magnetic saturation [GUG06] [ZHU07] [BIA07] [LI09B] [GON11b] are considered since they will all affect the rotor position estimation.

For pulsating signal injection methods, a high frequency pulsating carrier voltage is injected into the d - [COR98] [JAN03] [LI09b] or q -axis [LIN03] [YAN11] in the estimated synchronous reference frame, which can be seen as the superposition of two rotating carrier vectors with opposite rotating direction. Then, the carrier current response will be amplitude modulated by the rotor position information, and the rotor

position could be estimated through minimization of the amplitude signal along the axis orthogonal to the injection axis which is derived by using the synchronous detection technique [MAD95] [RAC10]. [HA00] explores physical understanding of the phenomenon of high frequency signal injection method to differentiate between the d - and the q -axis under no or heavy load condition. D -axis injection is sensitive to the inverter nonlinearity effect, whereas more current ripple by using the q -axis injection can be generated, which would generate substantial torque ripple even the position estimation error is zero. Consequently, injection of pulsating carrier voltage along the d -axis is preferred in terms of torque ripple.

Rotating and pulsating sinusoidal carrier signal injection based sensorless methods have the advantage of simple physical principles and low implementation cost. However, the common problem of the conventional sensorless control is that it is not easy to be applied to the sensorless drive of a SPM motor with small machine saliency under heavy-load condition [LIN02] [JAN03]. Since rotating and pulsating carrier signal injection methods utilize the sinusoidal high frequency signal, the dynamic characteristics and dynamic bandwidth of system are restricted in relation to the frequency of the injected signal. In this case, square waveform signal injection is a better solution. In [YOO11], square waveform signal is applied to inject into the estimated d -axis, which eliminates the requirement of LPFs for demodulation, and hence sensorless dynamic performance is remarkably enhanced. In [HAM10], an effective solution with integration of pulsating square wave injection and current control loop is proposed for sensorless control of low salient surface-mounted PMSM.

The information of the injected carrier signal is of great importance for the aforementioned methods, i.e., the injected carrier signal should be predefined. Instead, an arbitrary injection with half PWM frequency square wave is presented in [PAU11], which relies on the presence of current derivative rather than the certain shape of injected signal. The current progression can be predicted using an isotropic machine model, whilst, it can also be calculated from two consecutive current measurement. From the difference between them, the saliency position information can be directly extracted. The major advantages of this scheme are higher dynamic bandwidth and the

independence from machine parameters, whereas the SNR of the signal demodulation is usually low which could lead to large estimation noise.

1.3.1.2 Transient voltage vector injection

Differing from persistent injection based sensorless control methods, the rotor position information can also be derived from current transient response against an impulse voltage vector, which is decided by rotor position modulated inductance.

The Indirect Flux Detection by On-line Reactance Measurement (INFORM) method [SCH96] [OVR03] [ROB04] is a typical technique. Additional impulse voltage vectors are superimposed during zero vectors dwelling for standard PWM within three successive PWM cycles. Since the methods detect the inductance of the motor using voltage signals in a short time, they might be insignificant to the parameter variation and measurement noise. However, due to the injected signal being a periodic signal, a compensation scheme, such as a Kalman filter, is required.

The major problem for the standard INFORM method is the introduced current disturbance due to additional transient voltage vectors. Furthermore, the rotor position is assumed to be constant during the successive three PWM cycles, which is reasonable for standstill and low speed operation rather than at higher speed. Hence, compensation using double transient injection is proposed in [ROB04] to improve the sensorless performance at higher speed. On the other hand, with additional transient voltage vectors, the resultant zero sequence voltage for star-connection [HOL98] and zero sequence current derivatives for delta-connection [STA06] which would contain saliency position information can also be applied for rotor position estimation.

1.3.1.3 PWM excitation without injection

The voltage vectors used in transient voltage vector injection methods also exist in standard PWM for normal operation. Therefore, it should be possible to measure the current transient response introduced by the inherent PWM, so as to extract the rotor position information. The major advantage of PWM excitation is eliminating the requirement of additional transient voltage vector injection which may cause some

problems, including additional current ripple, higher switching loss, and limited dwelling time of zero voltage vectors.

Different combinations of measured current derivative in response to specific voltage vectors can be used to construct the position vector, from which, the rotor position information can be obtained [HOL05] [GAO07] [BOL11] [HUA11]. In [HOL05], an extended modulation (EM) scheme is presented to obtain the saliency information using the current transient response introduced by modifying the PWM excitation. Compared to EM techniques, the standard PWM can also be exploited for saliency based position estimation [GAO07] [BOL11] [HUA11]. In each PWM period, the active voltage vectors occur twice, centred from the middle of the PWM cycle, therefore, second PWM harmonic which has the largest amplitude will appear in α - and β -axis. Hence, this second harmonic can be considered as a pulsating vector to estimate the rotor position information [RAU10]. The zero sequence excitation introduced by standard PWM is also proven to be effective for saliency based position estimation [LEI11].

1.3.1.4 Magnetic polarity detection

As illustrated in Fig. 1.11, the variation of inductance with rotor position undergoes two cycles per single electrical cycle, leading to an ambiguity of π in the estimated rotor position. Hence, all the saliency tracking based sensorless technique suffers the magnetic polarity identification.

The basic principle for magnetic polarity identification is utilizing the saturation effect of machine. Considering the magnetic saturation, some methods utilize the inductance measurement by monitoring the di/dt of winding current to obtain the initial rotor position information including magnetic polarity information [NAK00] [BOU05]. However, these kinds of methods require dedicated voltage generation and current measurement, which are quite different from the conventional one.

Alternatively, the magnetic polarity information can be obtained based on transient short pulses injection [NOG98] [AIH99] [HAQ03] [HOL08] [WAN12a] or secondary harmonics due to magnetic saturation effect [HA03] [KIM04] [JEO05]

[HAR05] [RAC08a]. Although the short pulses injection method has robust and reliable identification performance due to good SNR, the magnetic polarity identification should be performed as an independent process, which stops the position estimation during the polarity identification process [HOL08]. The secondary harmonics based methods have the advantage of quick convergence [HAR05], whereas the procedure is very slow, which limits the robustness of the magnetic polarity identification. To solve this problem, increasing the magnitude of injected signal or decreasing the carrier frequency [JEO05] and employing hysteresis controller for noise attenuation [RAC08a] are implemented. Considering the limitations of existing methods, [GON13] develops a initial rotor position estimation scheme from the variation of d -axis carrier current, which is not useful in conventional pulsating d -axis injection sensorless control, against d -axis fundamental current. This method can be seamlessly integrated with a conventional carrier signal injection based sensorless algorithm, which implies that this initial rotor position estimation method is valid for the both standstill and free-running.

1.3.2 Fundamental Model Based Sensorless Control

At higher speed, due to the lower ratio between the injected and fundamental current, the SNR of position dependent signals of saliency based sensorless control methods would become lower, which will deteriorate the rotor position estimation. However, the fundamental model based sensorless methods are expected to show good performance at that speed range since the machine model which tends to fail to be observed at zero and low speed can be accurately described.

The basic idea of fundamental model based sensorless methods is to estimate the fundamental or harmonic back-EMF, or flux-linkage according to the machine model, which contain the rotor position information. Position estimation can be performed through open-loop calculation or close-loop observer. Additionally, observers including the sliding mode observer (SMO), extended Kalman filter (EKF) and model reference adaptive system (MRAS) provide other options to estimate the rotor position directly from machine fundamental model without considering the back-EMF

or flux-linkage.

1.3.2.1 Fundamental back-EMF model based methods

The back-EMF is a voltage that occurs in electrical machine where there is relative motion between the armature of the machine and the airgap magnetic field generated by PM, and hence, is directly related to the rotor position. The fundamental mathematical model of PMSM in synchronous reference frame can be expressed as

$$\begin{bmatrix} u_d \\ u_q \end{bmatrix} = \begin{bmatrix} R_s & 0 \\ 0 & R_s \end{bmatrix} \begin{bmatrix} i_d \\ i_q \end{bmatrix} + p \begin{bmatrix} \psi_d \\ \psi_q \end{bmatrix} + \omega_r \begin{bmatrix} -\psi_q \\ \psi_d \end{bmatrix} \quad (1.3)$$

where p is the differential operator, R_s is the phase resistance, ω_r denotes the electrical angular speed, and ψ_d and ψ_q indicate the d - and q -axis flux-linkages. Assuming the flux-linkage is sinusoidal without distortion of saturation and cross-saturation effects, (1.3) can be re-written as

$$\begin{bmatrix} u_d \\ u_q \end{bmatrix} = \begin{bmatrix} R_s + pL_d & -\omega_r L_q \\ \omega_r L_d & R_s + pL_q \end{bmatrix} \begin{bmatrix} i_d \\ i_q \end{bmatrix} + \begin{bmatrix} 0 \\ \omega_r \psi_m \end{bmatrix} \quad (1.4)$$

where L_d and L_q are the d - and q -axis inductances, and ψ_m is the PM excited flux-linkage. For non-salient PMSM, $L_d = L_q = L$, which indicates that the impedance matrix in (1.4) is symmetrical. Then, with the aid of transformation matrix $T(\Delta\theta)$ which is

$$T(\Delta\theta) = \begin{bmatrix} \cos(\Delta\theta) & -\sin(\Delta\theta) \\ \sin(\Delta\theta) & \cos(\Delta\theta) \end{bmatrix} \quad (1.5)$$

where $\Delta\theta$ is the estimation error of rotor position, i.e. $\Delta\theta = \theta_r - \theta_r^e$, the fundamental voltage model of PMSM in estimated synchronous reference frame can be derived as

$$\begin{bmatrix} u_d^e \\ u_q^e \end{bmatrix} = T(\Delta\theta) \begin{bmatrix} u_d \\ u_q \end{bmatrix} T^{-1}(\Delta\theta) = \begin{bmatrix} R_s + pL & -\omega_r L \\ \omega_r L & R_s + pL \end{bmatrix} \begin{bmatrix} i_d^e \\ i_q^e \end{bmatrix} + \begin{bmatrix} 0 \\ \omega_r \psi_m \end{bmatrix} \begin{bmatrix} -\sin(\Delta\theta) \\ \cos(\Delta\theta) \end{bmatrix} \quad (1.6)$$

where $\omega_r \psi_m$ indicates the back-EMF. It can be seen that, for a non-salient PMSM, only the back-EMF contains rotor position information.

However, for a salient PMSM such as an interior PMSM, the rotor position information is not only contained in the back-EMF but also in the armature effect due to the asymmetric impedance matrix. Defining the extended back-EMF which

consists of conventional back-EMF generated by the PM and the voltage terms related with machine saliency [CHE00b] [MOR02] [CHE03] as

$$E_{ex} = \omega_r \psi_m + \omega_r (L_d - L_q) i_d + p(L_q - L_d) i_q \quad (1.7)$$

the voltage model for a salient PMSM could be re-written as

$$\begin{bmatrix} u_d \\ u_q \end{bmatrix} = \begin{bmatrix} R_s + pL_d & -\omega_r L_q \\ \omega_r L_q & R_s + pL_d \end{bmatrix} \begin{bmatrix} i_d \\ i_q \end{bmatrix} + \begin{bmatrix} 0 \\ E_{ex} \end{bmatrix} \quad (1.8)$$

Hence, the rotor position information is expected to be fully contained in the extended back-EMF regardless of salient or non-salient machines, since for non-salient machines, the extended back-EMF would be reduced to conventional back-EMF. Furthermore, the extended back-EMF has been improved in [LI07] by accounting for cross-saturation effect between d - and q -axes. Whilst to solve the starting and low speed issue, [WAN12b] develops a new starting method which can work under different load conditions and allow smooth transition from the start up procedure to the back-EMF based sensorless control mode.

To estimate the back-EMF more precisely than the open-loop model, several close-loop observer based strategies considering the parameter variation have been developed. The main idea of the observer is feeding back the error between the estimated outputs and measured inputs of the actual system into the system model to correct the estimated values. The advantage is that all of the states in the system model can be estimated including states that are hard to obtain by measurements.

In [HOS89], a simple reduced order observer named Luenberger observer is developed which has been applied in [KIM95] for sensorless control on the basis of the back-EMF estimation for PMSM, and even in the flux weakening region [KWO05] without any mechanical information of system inertia or load torque. However, in order to stabilize the system, the gains of the observer should be optimized [SOL96], whereas it has difficulties under all operating conditions since the electrical equations are nonlinear. Hence, linear control strategies for determining the nonlinear term in the electrical equations to realize the linearization of the motor model have been considered in [TAT98].

In [SEN95a] [SEN95b], a disturbance voltage observer is used to estimate the back-EMF in PMSM sensorless control. It can also be applied to estimate the extended back-EMF of interior PMSM in [CHE03] and for sensorless control of induction motor in [HOS09]. To improve the robustness against the load torque variation, the disturbance observer based sensorless scheme is adopted to estimate the load torque, generate a compensating signal and cancel the estimation error [LEE11]. The stability of the disturbance observer can be easily guaranteed since it is based on a linear model of the machine.

1.3.2.2 Third harmonic back-EMF based methods

Third harmonic back-EMF is usually contained in windings and synchronously rotates with the fundamental components. When the machine windings are Y-connected, the third harmonic back-EMF presents in the phase back-EMF rather than line back-EMF [MOR92] [PRO94] [TES94] [MOR96]. Hence, the neutral point of the Y-connected windings is essential for detecting the third harmonic back-EMF since the measurement of phase back-EMF is necessary.

With the aid of a Y-connected resistor network as shown in Fig. 1.12, the voltage u_{sn} between the central point “s” of this Y-connected resistor network and the machine winding neutral point “n” could just represent the third harmonic back-EMF irrespective of the operational mode of the PMSM [SHE04].

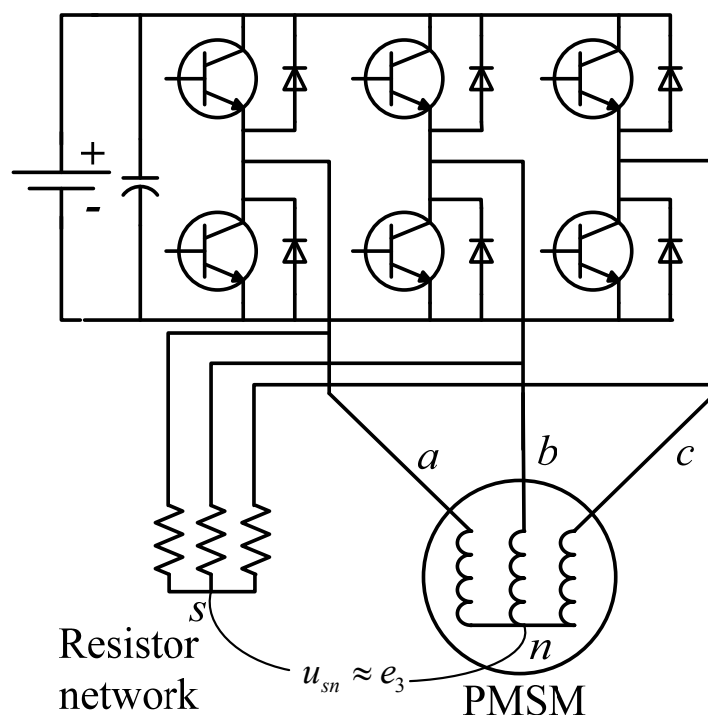


Fig. 1.12. Measurement of third harmonic back-EMF.

The waveforms of u_{sn} and its integration ψ_{sn} which is the third harmonic flux-linkage are demonstrated in Fig. 1.13 compared with the electrical rotor position. Then the six particular commutation points essential for BLDC operation which are $\pi/6, \pi/2, 5\pi/6, 7\pi/6, 3\pi/2, 11\pi/6$ can be detected as shown in Fig. 1.13 as well.

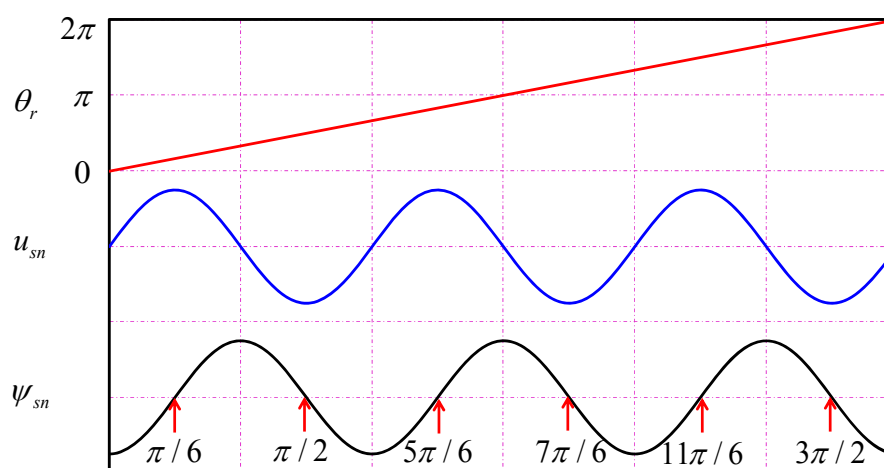


Fig. 1.13. Relationship of u_{sn} , its integration ψ_{sn} and rotor position

However, continuous rotor position information with high resolution is required for BLAC drives or if phase-advancing control is applied in BLDC drives, where

rotor position can be simply estimated by integration of the motor speed by [SHE04]

$$\theta_r^e = \theta_0 + \int_0^t \omega_r^e dt = \theta_0 + \int_0^t \frac{\pi/3}{t_d} dt \quad (1.9)$$

Once the rotor position has been estimated, the instantaneous current in the windings can be controlled to facilitate either BLAC or BLDC operation [KRE94, DWA08]. Shen in [SHE06a] presents some practical issues in the utility of third-harmonic back-EMF in sensorless control including detection and restrictions of the sensorless control. In [SHE06b], application specific integrated circuit ML4425 which integrates the third harmonic back-EMF instead of the terminal voltage is implemented to reduce the commutation retarding and improve the machine performance. In [FAE09], a new software scheme of phase-locked loop (PLL) of third harmonic back-EMF detection in order to accomplish a precise switching strategy is presented and claimed to improve the torque produced during high speed operation. Also, by applying the third harmonic back-EMF, a completely sensorless drive is implemented which can successfully synchronously start the reluctance machine from zero speed in [KRE93]. However, all the sensorless control methods are based on the zero-crossings of ψ_{sn} with insufficient resolution. Hence, the steady-state performance would be good but will be degraded under dynamic situation.

1.3.2.3 Flux-linkage based methods

Flux-linkage based sensorless control technique is widely applied and the rotor position is derived from the observed vector of PM excitation flux-linkage which calculated from the integration of back-EMF under stationary reference frame. Then the relative phase angle and speed between the observed vector and the reference frame are the rotor position and speed, respectively, as demonstrated in Fig. 1.14 [WU91] [XU98] [SHE02b].

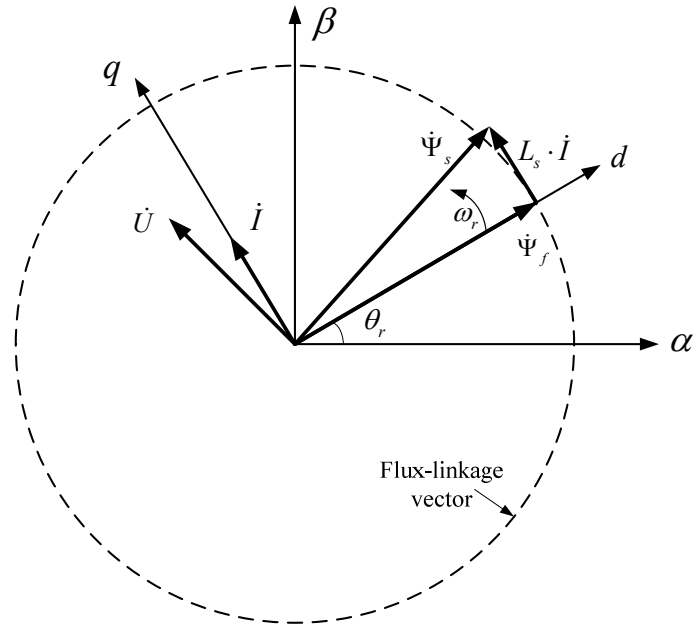


Fig. 1.14. Phasor diagram of PMSM

In order to observe the PM excitation flux-linkage vector, stator flux-linkage which is very important for DTC should be calculated first. In stationary reference frame, the stator flux-linkage can be calculated from the current vector \dot{I} and the voltage vector \dot{U} as

$$\dot{\Psi}_s = \int_{t_0}^{t_1} (\dot{U} - R_s \cdot \dot{I}) dt \quad (1.10)$$

where \dot{I} can be easily obtained from the phase currents which are measured with two or three current transducers, and \dot{U} can be also obtained from the phase voltages measured with voltage transducers. However, in most electrical machines, it is not practicable to measure the phase terminal voltages directly because of isolation issues. Instead, the applied phase voltage is usually estimated from the DC supply voltage and demands of SVPWM, which includes certain error caused by the dead-time between switching off one device in an inverter phase leg and switching on the other device in the same leg. This error would be greatest at output voltages near zero, and has been researched and compensated in [HAR00] [TER01].

The stator flux-linkage calculation in (1.10) is a straightforward open-loop method without considering the stator resistance variation and integration drift. To solve the problems, close-loop methods become more attractive for stator flux-linkage

estimation [HU98] [AND08] [YOO09] [BOL09] [FOO10]. Combining the voltage model and current model estimator, a hybrid flux observer as shown in Fig. 1.15 could be applied over a wider speed range, where the voltage model is dominant at high speed while the current model dominant at low speed. Meanwhile, the integration drift could also be fully compensated since this flux observer behaves as a high pass filter (HPF).

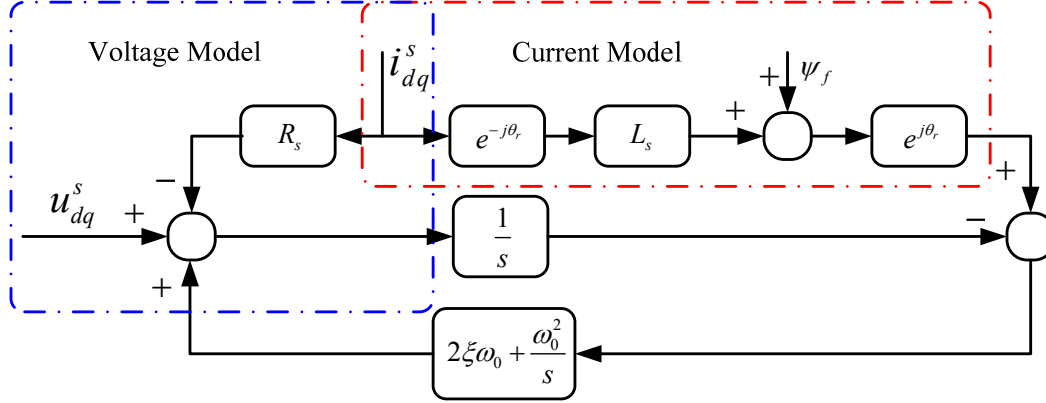


Fig. 1.15. Combined flux-linkage observer [YOO09].

Similar to the extended back-EMF, active flux is applied in [BOL09] [LIU11a] [COR11] to overcome the armature reaction of salient PMSM. With the concept of active flux, which is

$$\psi_{d_act} = \psi_m + (L_d - L_q)i_d = -L_q i_s \quad (1.11)$$

the voltage equation of salient PMSM can be rewritten as

$$\begin{cases} u_d = R_s i_d + L_q \frac{di_d}{dt} - \omega_r L_q i_q + \frac{d\psi_{d_act}}{dt} \\ u_q = R_s i_q + L_q \frac{di_q}{dt} + \omega_r L_d i_d + \omega_r \psi_{d_act} \end{cases} \quad (1.12)$$

which can transform the salient PMSM to a non-salient machine. Consequently, the PM excitation flux vector $\dot{\Psi}_f$ can be derived from the stator flux-linkage as

$$\dot{\Psi}_f = \dot{\Psi}_s - L_q \cdot \dot{I} \quad (1.13)$$

And the rotor position can be estimated from the α - and β - parts of $\dot{\Psi}_f$, i.e.

$$\theta_f = \arctan \frac{\psi_{f\beta}}{\psi_{f\alpha}} \quad (1.14)$$

1.3.2.4 Other observer based sensorless control

Other observers, such as sliding mode observer (SMO), extended Kalman filter (EKF) and model reference adaptive system (MRAS), become more and more attractive for rotor position estimation due to their robustness, quick convergence, immunity to machine parameter variation, and elimination of estimating back-EMF or flux-linkage.

SMO, i.e. sliding mode observer as shown in Fig. 1.16, is an observer with inputs as discontinuous functions of the error between the estimated and measured variables, and the dynamic behaviour of the control system is only decided by the surfaces chosen in the state space but not affected by the matched uncertainty. Hence, it has the advantages of order reduction, disturbance rejection, and strong robustness.

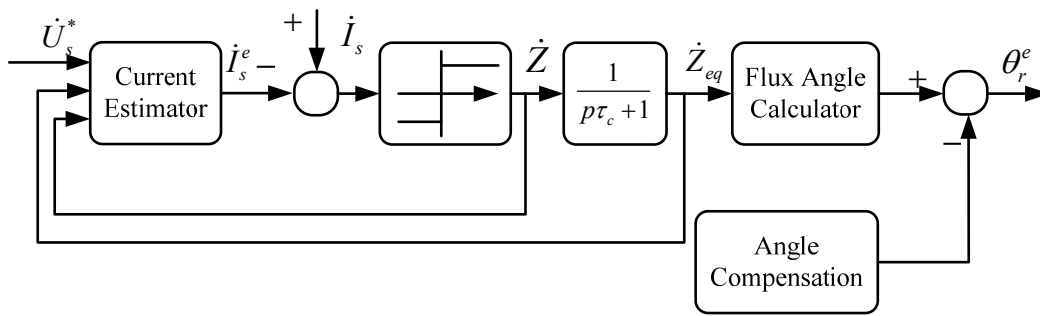


Fig. 1.16. Sliding mode observer [CHI09]

SMO is firstly applied for sensorless control in [FUR92], and afterward, the saturation sign function [ZHA06], d - and q -axis stator currents [PEI95, CHE00a] are also utilized. [CHI09] presents a sensorless control based on SMO over wide speed range, including the deep flux-weakening region. [FOO09b] [FOO10] [WAN10] also propose nonlinear speed controllers for IPMSMs based on SMO theory and high frequency signal injection technique to enhance the dynamic state performance and robustness to load disturbances.

EKF is an extension application in a nonlinear system of a Kalman filter which is an optimal state observation based on least-square variance estimation for a linear system [VAS03]. It is less influenced by measured noise, and parameter inaccuracy is not as critical as in conventional fundamental estimation methods [BOL99] [TER01]

[RIV13]. However, heavy computation burden is obvious and the reduced order EKF is presented with the assumption that some system states are free of noise to enhance the speed control [FUE11].

The MRAS scheme provides another option for sensorless position estimation [PII08] [HE09] [GAD10]. The diagram of MRAS is shown in Fig. 1.17, in which the reference model represents the real machine, while the adjustable model is a fictitious machine based on the fundamental mathematical model. With the same excitation, the difference between the responses from two models yields an estimation error ε , which should be sufficiently small. Then, the behaviour of the adaptive model could be considered the same as that of the actual machine, and hence the machine states including position information can be accessed from the adaptive mathematical model. With regard to the correction controller, it can be realized by the conventional PI [MAT96] [BAE03] or nonlinear controller involving fuzzy logic controller [GAD10].

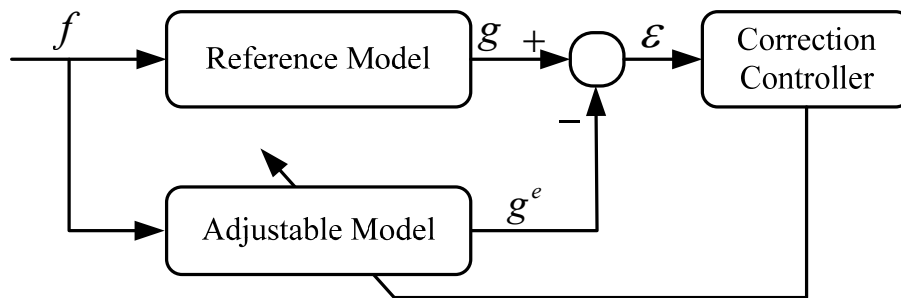


Fig. 1.17. Block diagram of MRAS [PII08].

1.3.3 Sensorless Predictive Torque Control

DTC is an inherent sensorless technique due to its elimination of coordinate transformations and specific modulations. Flux estimation is a critical concern in DTC which is normally obtained by the combined flux observer, in which, the voltage model, dominant at middle and high speed, and the current model requires the position information to estimate the flux at low speed and standstill. Hence, position information is also required in DTC for standstill and very low speed operation.

The integration of saliency based sensorless technique and DTC provides a significant enhancement of torque response for PMSM wide speed operation [SIL06]

[AND08]. As an alternative to VC and DTC, a sensorless PTC scheme is presented in [LAN10]. For a salient machine, the predicted current would deviate from the real one due to additional position dependent part. Hence, the difference between predicted and measured, which contains the position information, can be used to extract the rotor position without any additional voltage injection. However, accurate machine parameters are required for current prediction.

1.3.4 Sensorless Control for Dual Three-Phase PMSM

Theoretically, most of the sensorless techniques for single three-phase PMSM could be easily extended to the dual three-phase applications. Recently, several sensorless techniques particularly for dual three-phase machines are proposed. In [HE09], a sensorless vector control based on MRAS is developed for a dual three-phase PMSM and the system stability is verified by Popov's super stability theory, as well as a new and very simple initial rotor position estimation method by means of DC excitation without any sensors. [BAR12a] [BAR12b] investigate the torque components and the sensorless position detection capability of a dual three-phase IPM machine equipped with two fractional-slot windings by using both finite element simulations and experimental tests. [GRE12] deals with the speed sensorless control of asymmetric dual three-phase induction machines by using an inner loop of Model Based Predictive Control (MBPC), which is obtained from the mathematical model of the machine, using a state-space representation where the two state variables are the stator and rotor currents, respectively.

1.4 Outline and Contributions of the Thesis

The major objective of this thesis is the sensorless control of PMSM based on high frequency carrier voltage injection for zero and low speed region and third harmonic back-EMF for higher speed region. Fig. 1.18 illustrates the research structure and summary of key features of each investigated method.

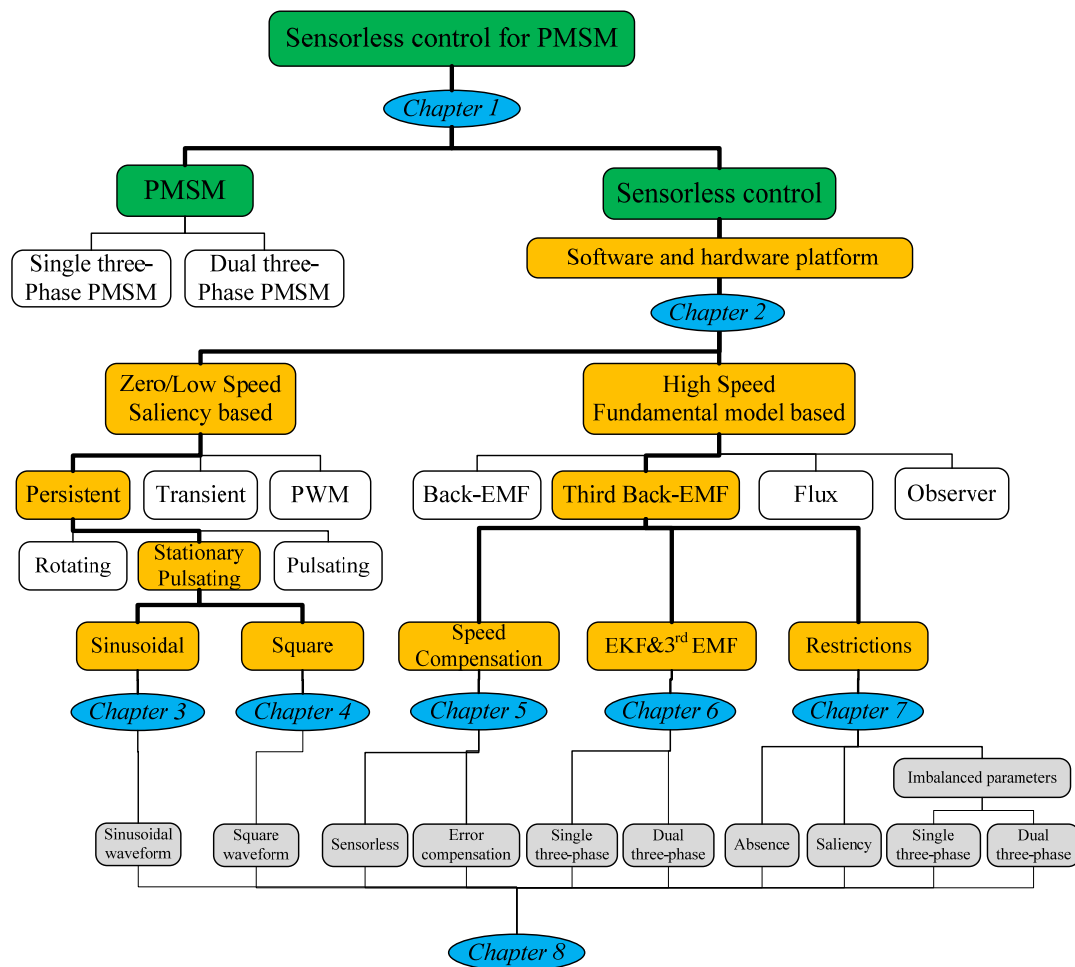


Fig. 1.18. Research structure

This thesis is organized as followed:

Chapter 1 generally reviews both single and dual three-phase PMSM, and the related sensorless control methods including the saliency based and fundamental model based strategies.

Chapter 2 gives a detailed description about the experimental setup based on a dSPACE control system including the hardware platform and software interface, as well as the three test rigs which will be implemented in the following chapters.

Chapter 3 discusses details about commonly used conventional pulsating and rotating carrier signal injection based sensorless control techniques, and proposes a new rotor position estimation strategy by injecting a pulsating high frequency carrier voltage into α - (or β -) axis of stator stationary reference frame.

Chapter 4 applies a higher frequency square waveform pulsating carrier voltage into stator stationary reference frame to retrieve rotor position without any filtering, and hence, the dynamic performance and observe bandwidth can be improved

Chapter 5 applies the continuous signal of third harmonic flux-linkage which is the integration of third harmonic back-EMF to minimize the rotor position error in the conventional method and improve the dynamic performance. Furthermore, a multi-technology fusion technique based on third harmonic flux-linkage is proposed to improve the performance of flux observer and system robustness.

Chapter 6 improves the sensorless control based on third harmonic back-EMF and flux-linkage for single-three-phase PMSM by applying the simplified EKF based rotor position estimator. For dual three-phase PMSM, with the aid of simplified EKF based estimator, the rotor position could be estimated without any filter, which can significantly improve the frequency response and dynamic performance.

Chapter 7 investigates the potential issues with the third harmonic back-EMF based sensorless control, such as absence of third harmonic back-EMF, influence of the stator current and machine saliency to rotor position estimation based on third harmonic, as well as the estimation error compensation due to the machine saliency and imbalanced machine parameters.

Chapter 8 summarizes this research work and gives some discussions about future work.

The major contributions of this thesis are:

- A new strategy by injecting a pulsating high frequency carrier voltage into α - (or β -) axis of stator stationary reference frame, and retrieving rotor position information from the rotor position dependent response current is presented.
- By applying higher frequency square waveform pulsating carrier voltage into stator stationary reference frame, the rotor position information is retrieved without any filtering to improve the dynamic performance and observe bandwidth.
- To improve the dynamic performance in the conventional method based on third

harmonic back-EMF, a speed compensation strategy based on the continuous signal of third harmonic flux-linkage is proposed.

- To improve the performance and system robustness of rotor position estimation in flux observer sensorless control which is sensitive to the machine and controller parameters, a multi-technology fusion technique is proposed.
- Simplified EKF based rotor position estimator is applied with third harmonic back-EMF and flux-linkage for single three-phase PMSM operation for rotor position estimation is proposed to improve the sensorless performance even with poor quality of measured third harmonic back-EMF.
- For dual three-phase PMSM, the two sets of third harmonic back-EMF will be orthogonal under third harmonic reference frame. Consequently, with the aid of simplified EKF estimator, the rotor position could be estimated without any filter to improve the frequency response and dynamic performance.
- The influence of the stator current and machine saliency to rotor position estimation based on third harmonic back-EMF is investigated, as well as estimation error compensation.
- Due to the imbalanced machine parameters, the measured third harmonic back-EMF will contain certain fundamental component distortion which will severely deteriorate the performance of rotor position estimation. An improved rotor position estimation strategy for single- and dual three-phase PMSM under imbalanced situation is proposed.

The publications originating from this PhD research work are listed in Appendix III.

CHAPTER 2

EXPERIMENTAL PERMANENT MAGNET SYNCHRONOUS MACHINES AND DRIVE SYSTEMS

2.1 Introduction

The experimental platform is constructed based on a dSPACE control system. The set up of whole experimental test system is shown in Fig. 2.1. Detailed information of the dSPACE control system and three applied test rigs will be introduced in this chapter.

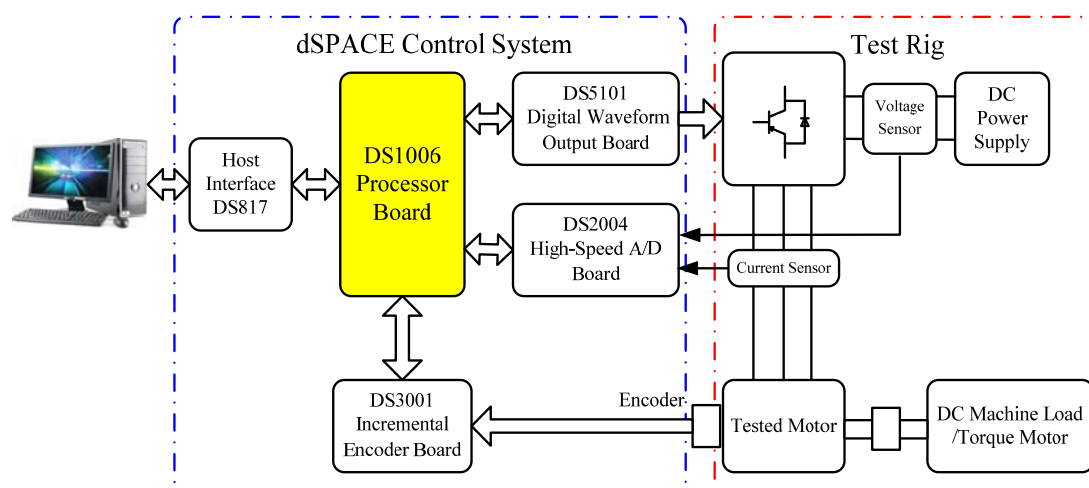


Fig. 2.1. Setup of experimental system

2.2 dSPACE Based Control System

2.2.1 CPU Board-DS1006

The heart of the dSPACE control system applied in this thesis is the DS1006 processor board which is based on a 2.4GHz multi-core AMD Opteron CPU. The main processing unit can access modular I/O boards via its PHS-bus, and multiprocessing capable via the DS911 Giga-link Module. Hence, the real time

application can be running on two or more processor cores of a multi-core DS1006 board, on two or more multi-core DS1006 boards, or a combination of all these.

Each multi-core CPU contains 512KB L2 on-chip cache per core, 6MB L3 cache, 128MB DDR2-267 global memory per core for host data exchange, and 1GB DDR2-800 local memory for the application and dynamic application data as illustrated in Fig. 2.2. The operating frequency of the CPU is 2.4GHz per core. Hence, the control strategy which may be extremely complex for normal DSP control system can be applied on the dSPACE control system. Usually, dSPACE is not only applied for the development of motor control, but also for automotive engineering, aerospace, and industrial control.

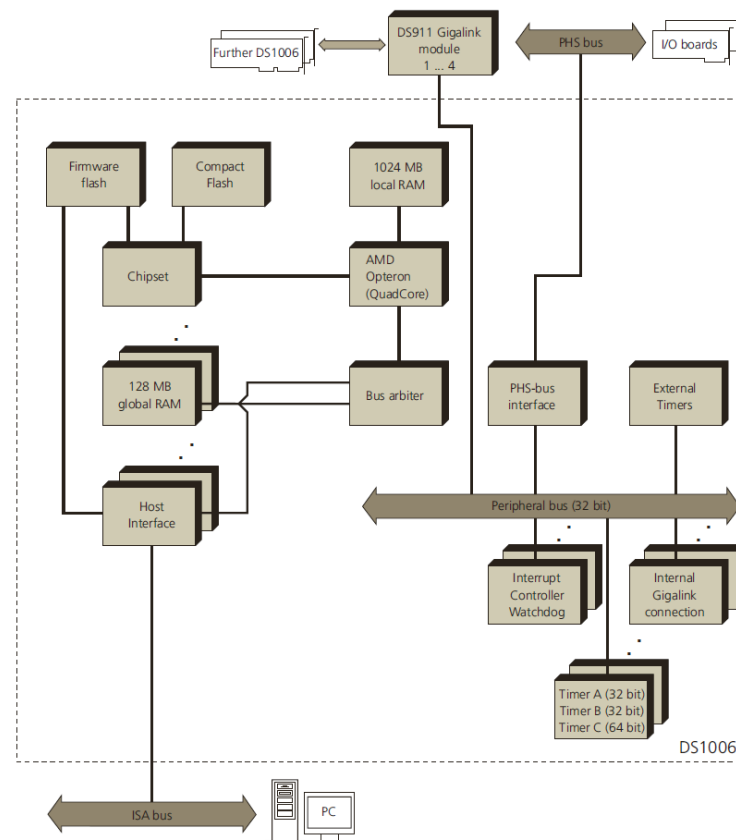


Fig. 2.2. Overview of the functional units of the DS1006 [DSP10]

2.2.2 ADC board-DS2004

A/D conversion is an element of most applications in rapid control prototyping, because sensors, for example, for phase current and DC linkage voltage, provide analogue signals by current and voltage transducers which have to be processed as

digital signals. For the control system in this thesis, the DS2004 High-Speed A/D Board is used in dSPACE modular systems based on processor boards DS1006 for digitizing analogue input signals. The A/D converters of the DS2004 are equipped with differential inputs and particularly meet the requirements for digitizing analogue input signals at high sampling rates.

The DS2004 High-Speed A/D board contains 16 A/D conversion channels, each of which provides a differential input with a sample/hold unit and an A/D converter, and advanced circular swinging buffers for decoupling the conversion process from the read process. The A/D channel applies the successive approximation conversion technique to achieve 16-bit resolution and a maximum conversion time of 800ns. The input voltage range is selectable which is $\pm 5V$ or $\pm 10V$. Meanwhile, the sources for triggering A/D conversions are also selectable, for example, external trigger inputs, channel timer, and software trigger. For the external trigger inputs, four independent hardware interrupts are associated to the each A/D conversion state.

DS2004 A/D board can realize two different modes, i.e. burst mode for digitizing a data set of up to 16384 analogue values per burst including triggered sampling with selectable trigger source for starting the bursts and continuous sampling with automatically started successive bursts, and single A/D conversion mode to use the channel as a standard A/D converter without utilizing its burst capability. If the conversion settings are set to burst conversion mode, the output comprises the A/D conversion results of the last burst of A/D conversions on the selected channel. This is a vector of 1 ... 16384 results depending on the buffer settings. If the conversion settings are set to single conversion mode, the output is the result of the last A/D conversion on the current channel. Then based on the selected input signal range, the output signal in Simulink will be Double Range from -1 to +1.

2.2.3 Encoder board-DS3001

To verify the accuracy of rotor position estimation for sensorless control, an optical incremental encoder with the resolution of 2048PPR is applied on each test rig to supply the actual rotor position. Before the sensorless algorithm development, it is

desirable to implement the sensed current vector control, in which the position information from the encoder is used for forward and inverse park transformation. Afterward, the encoder is also important to be used as reference to evaluate the rotor position estimation in developed sensorless control algorithm. The DS3001 incremental encoder board is specifically designed for the implementation of high speed multivariable digital controllers whose key features are

- 5 fully parallel 24-bit encoder interface channels.
- Fourfold pulse multiplication.
- Differential (RS422) or single ended (TTL) encoder inputs.
- Digital noise pulse filters for the phase lines.
- Regulated 5V encoder power supply with sense line.
- Compatible with the dSPACE PHS-bus

When the input encoder lines are from -2^{21} to $+2^{21}$, the output to Simulink should be from -1 to +1. Hence, to receive the radian angle from the scaled output value of the DS3001 Simulink block, the following calculation must be applied.

$$\theta_r = 2^{21} \cdot \frac{2\pi}{\text{encoder_lines}} \cdot \text{scaled_output} \quad (2.1)$$

For the incremental encoders with the resolution of 2048PPR which are applied in thesis, the derived rotor position should be calculated by

$$\theta_r = 2^{21} \cdot \frac{2\pi}{2048} \cdot \text{scaled_output} \quad (2.2)$$

2.2.4 PWM Board-DS5101

The DS5101 Digital Waveform Output Board is designed to generate complex, high speed digital signals at high resolution. The board can generate a multitude of signals at various frequencies, including incremental encoder signals and PWM waveforms. It is able to vary signal pulse widths on the fly, and through the use of various trigger and interrupt mechanisms, provides a high degree of flexibility. Its main area of deployment is hardware-in-the-loop simulation in automotive applications, for example, simulating sensors or controlling actuators.

DS5101 can generate up to 16 channels of PWM output which can be applied for multi-phase motor control. Generally, the output can be categorized as 1-Phase PWM Signal Generation (PWM1), 3-Phase PWM Signal Generation (PWM3), and 3-Phase PWM Signal Generation with Inverted and Non-Inverted Outputs (PWM6).

For PWM1, the timing I/O unit of the DS5101 provides generation of 1-phase PWM signals with run-time adjustable PWM period and duty cycle on up to 16 channels. For PWM3, the timing I/O unit provides 3-phase PWM signals with run-time adjustable PWM period, duty cycles, and interrupt shift. Up to 4 control units can be used for controlling 4 three-phase inverters, e.g. the back-to-back inverters control of wind power generation. For PWM6, The timing I/O unit of the DS5101 provides 3-phase/6-channel PWM signals with 3 inverted outputs and 3 non-inverted outputs. The two sets of PWM output could be applied to control two three-phase motors or a dual three-phase motor.

2.2.5 Software Environment

The dSPACE based control system is working with diagram block built by Simulink/MATLAB. Hence, the simulation blocks in Simulink can be easily applied into dSPACE platform with minor modification, which can significantly reduce the burden of coding and improve the efficiency of control strategy development.

Due to the connection between dSPACE and host PC is optical fibre cable, the communication speed is up to 100MB/s which can transmit the real-time data from real-time control platform to PC interface software. Then all the data generated in the dSPACE controller can be captured and monitored during the operation which makes the optimization of strategy and data capture much easier than DSP based platform. Hence, digital to analogue converter is not needed in this thesis.

2.3 Test Rigs for Control Strategy Development

To develop the control strategy, three test rigs are employed in this thesis, i.e. Test rig I based on Motor I which is an interior PMSM working as a torque motor, Test rig II based on Motor II which is outer rotor surface mounted PMSM working as

a generator, and Test rig III based on Motor III which is a surface-mounted dual three-phase PMSM. The details will be introduced in this section.

2.3.1 Test Rig I

Test Rig I is based on Motor I which is a 600W 3-phase PMSM with interior circumferential rotor configuration. The machine is made by Control Techniques Ltd., while the rotor is re-designed by Chen in [CHE99]. The major parameters of the prototype machine are shown in Table 2.1, and the cross-section is shown in Fig. 2.3. Due to interior structure, the machine saliency is significant. Hence, Motor I will be applied in Chapter 3 to develop the high frequency carrier voltage injection based sensorless control.

TABLE 2.1
SPECIFICATION AND PARAMETERS OF TESTING MACHINE

Rated voltage (peak)	158	V
Rated current (peak)	4.0	A
Rated power	600	W
Rated speed	1000	rpm
Rated torque	4.0	Nm
Pole number	6	
Stator phase resistance	6.0	Ω
D-axis inductance (@ 0A)	29.1	mH
Q-axis inductance (@ 0A)	41.3	mH

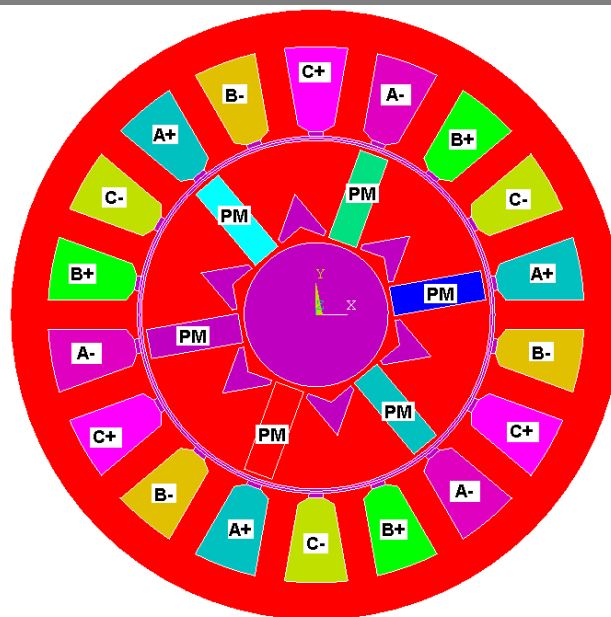


Fig. 2.3. Cross-section of Motor I [CHE99]

The power converter as shown in Fig. 2.4 is constructed based on a PS21255, an intelligent power module from Mitsubishi, which is located underneath the PCB board. It integrates a 600V, 20A, 3-phase IGBT Inverter Bridge with gate drive and related protection functions. The operating frequency is 10kHz, and the dead-time is 2 μ s. This integration structure significantly simplifies the external circuits, and increases overall reliability of the drive system. For galvanic isolation between control system and power stage, the opto-coupler, HCPL-4506, is used to pass the gate drive signals from the DS5101 Digital Waveform Output Board to the power converter. Meanwhile, two transformers with four channels of isolated DC voltage output (+15V) provide power supply for the gate drive circuits.

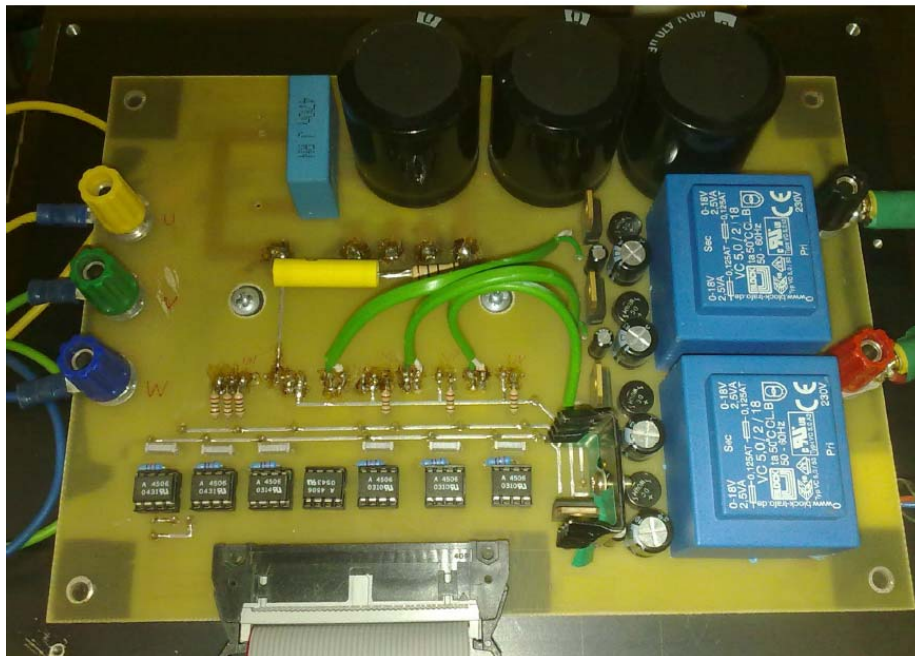


Fig. 2.4. Power converter working with Motor I

A Bushed DC generator is directly coupled to Motor I as a mechanical load. A power resistor is used to dissipate the generated power from the generator. The magnetic field of the DC generator is externally excited by a DC power supply. Therefore, the load condition can be adjusted by changing the field excitation current or the power resistance.

2.3.2 Test Rig II

Test Rig II is based on Motor II which is a 3kW laboratory surface-mounted

PMSM working as a generator. Its major specification and parameters are listed in Table 2.2. The motor is the laboratory prototype of a 3MW wind power generator for control strategy development. It is a 14 pole-pairs outer rotor PMSM, and the segment cross-section of Motor II is shown in Fig. 2.5. Due to the shape of PM, third harmonic is contained in the air-gap flux linkage as well as phase back-EMF. Hence, Motor II will be applied for the development of sensorless control based on third harmonic back-EMF as introduced in Chapter 5 and Chapter 6.

TABLE 2.2
SPECIFICATION AND PARAMETERS OF TESTING MACHINE

Phase EMF (RMS) @ 170rpm	199.44	V
Machine mechanical rated speed	170	rpm
Pole number	28	
Electrical frequency	39.667	Hz
Rated phase current (RMS)	5.83	A
Rated torque	195.84	Nm
Rated input power	3486.41	W
Phase resistance	1754.9	m Ω
Rated output power	3194.48	W
L_s (exclude the end winding)	13.04	mH
PM flux per pole	1.1315	Wb

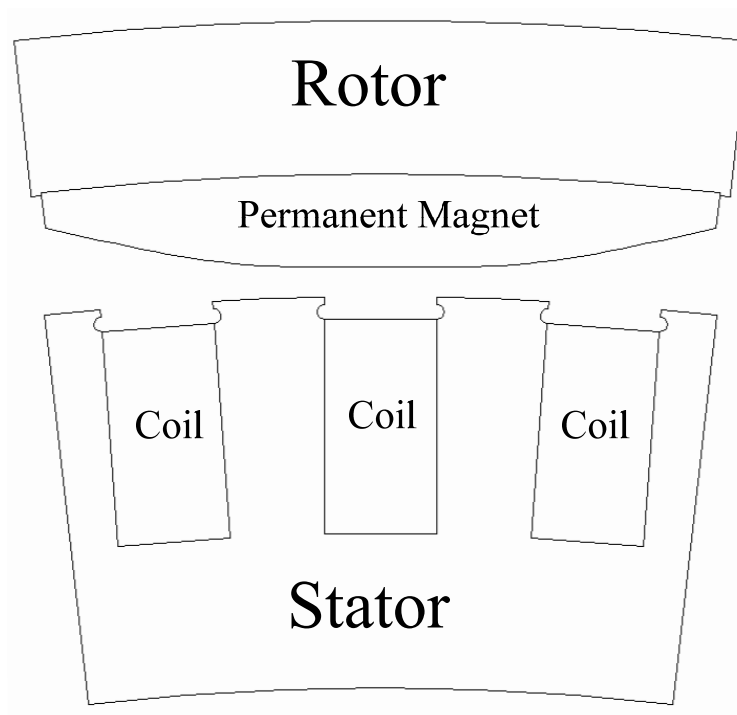
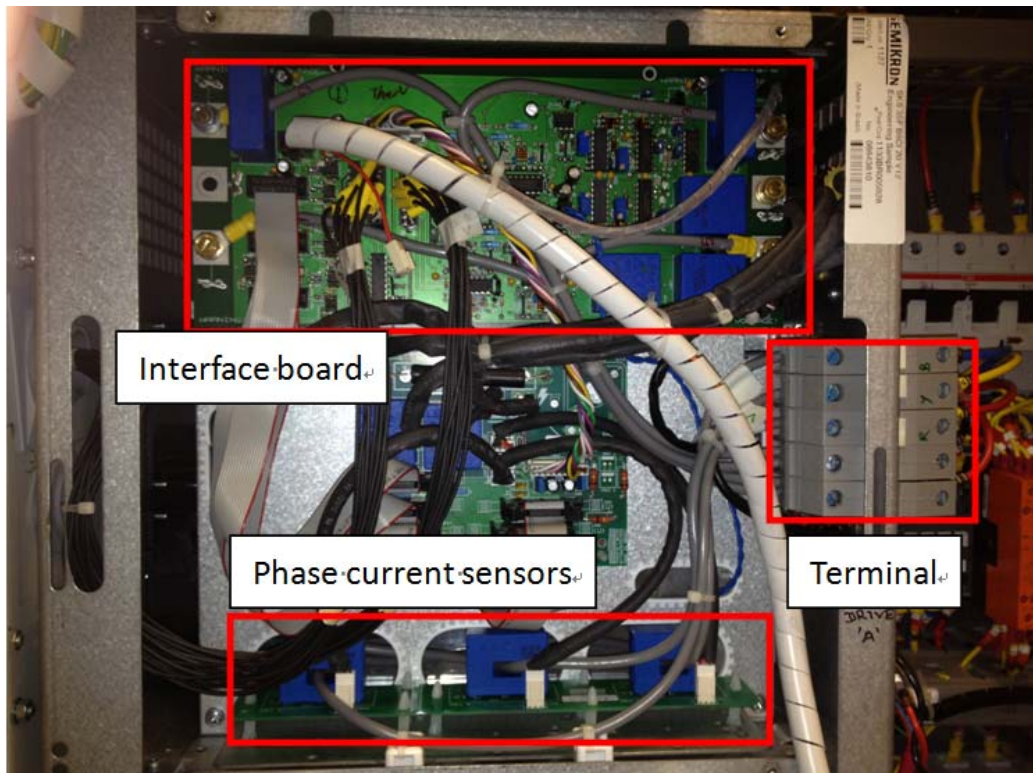
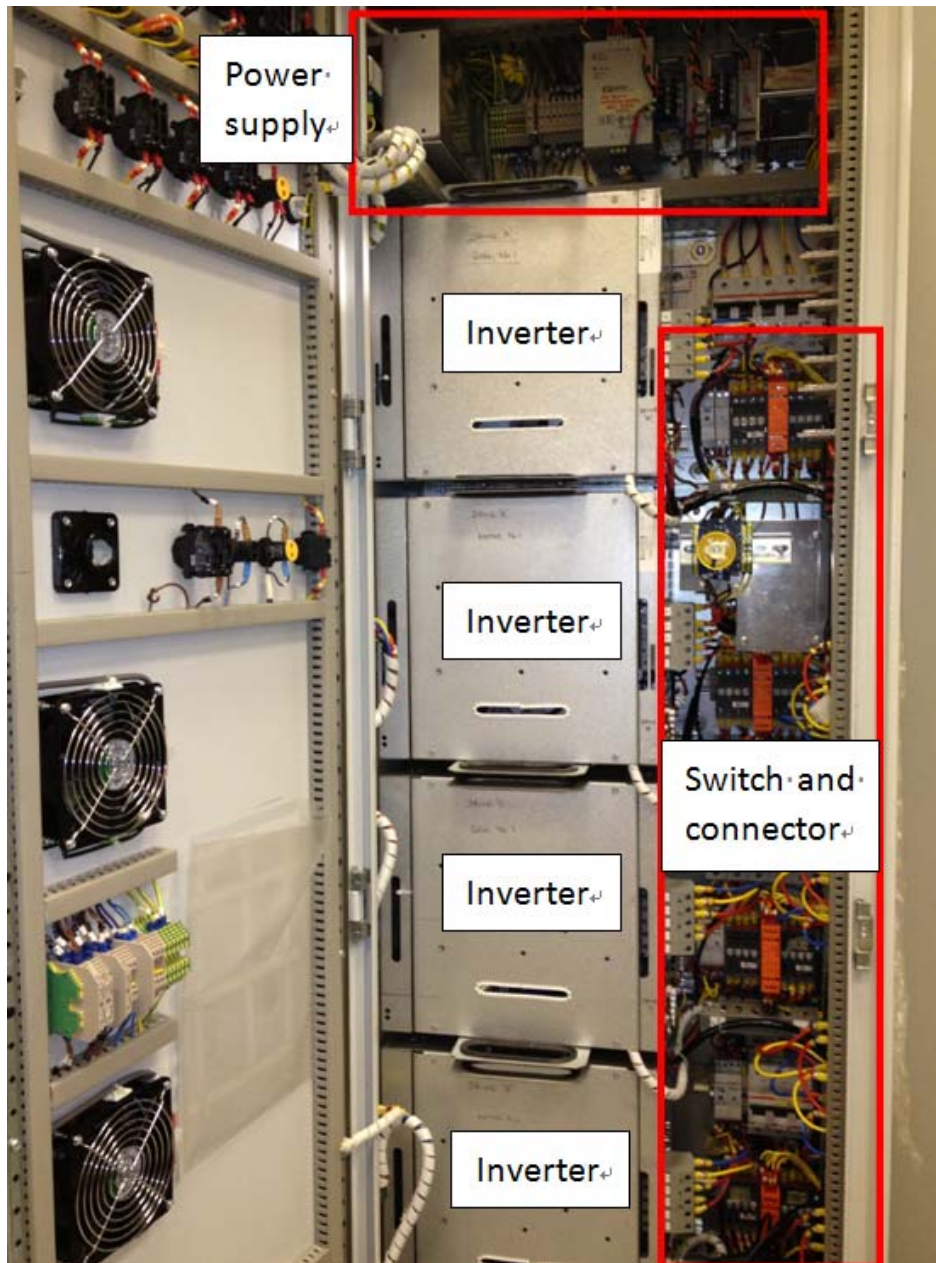


Fig. 2.5. Segment cross-section of Motor II

The inverter is a commercial power unit produced by Semikron as shown in Fig. 2.6(a). The power converter is constructed based on SEMiX71GD12E4s, an intelligent power module from Semikron. The rated voltage is 650VDC and the current can be up to 35Arms, and the voltage drop is 0.8V@25°C. The PWM frequency is set to 2.5 kHz to minimize the switching loss, and the dead-time is fixed as 4 μ s. An interface board is used to pass the gate drive signals from the DS5101 Digital Waveform Output Board to the power converter and to feedback the measured DC voltage and phase current signals to DS2004 High-Speed A/D Board. The overall control cabinet is shown in Fig. 2.6(b). The electric load of the system is a power resistor. The torque machine of driving system is a commercial drive unit with individual Starter series controller produced by Siemens.



(a) Semikron inverter



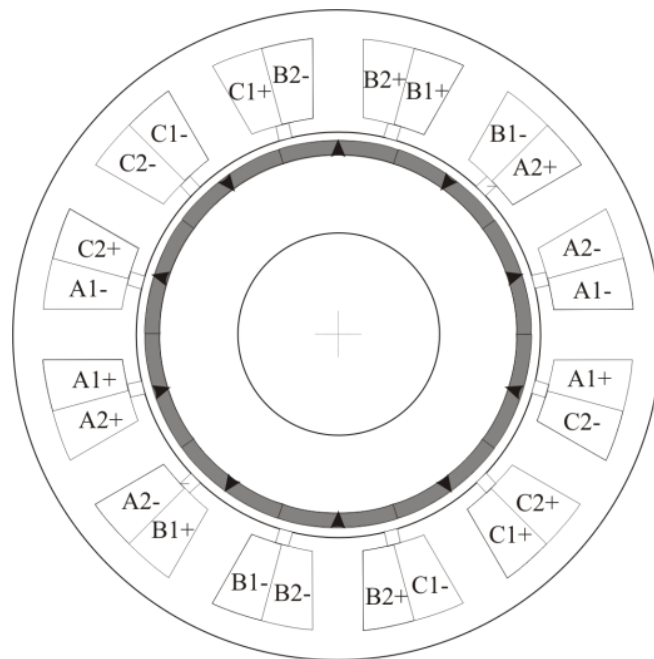
(b) Control cabinet

Fig. 2.6. Power converter working with Motor II

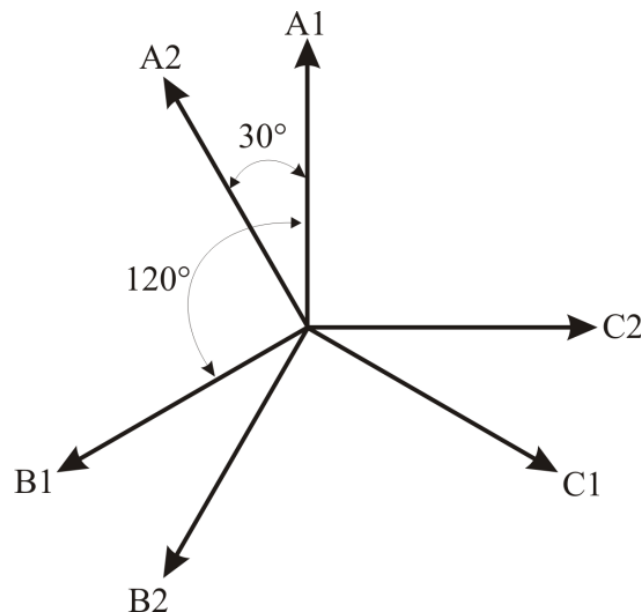
2.3.3 Test Rig III

Test Rig III is based on Motor III which is a 230W dual three-phase laboratory surface-mounted PMSM. Its specification and parameters are listed in Table 2.3. The cross-section and winding configuration of this 12/10 PMSM is shown in the Fig. 2.7. The original design of Motor III is a single three-phase PMSM, and apply alternative winding structure to form a dual three-phase PMSM. Differing from the classic

three-phase PMSM, each phase is formed by two coils which are connected in series. Phases A1, B1 and C1 are connected in Y forming the star1 while phases A2, B2 and C2 are connected in Y forming the star2. Moreover, there is a phase angle between phase A1 and A2, the value of which is 30 electrical degrees. This the same case for the phases B1 and B2, phases C1 and C2. However, the higher harmonic components such as fifth and seventh and so on, which could be minimized by single three-phase winding configuration, will exit is dual three-phase configuration windings.



(a) Cross-section



(b) Phase vector

Fig. 2.7. Cross-section and winding configuration as well as phase vector of Motor III

TABLE 2.3
SPECIFICATION AND PARAMETERS OF TESTING MACHINE

Rated power	230	W
Rated torque	5.5	Nm
Rated phase current (RMS)	5.11	A
Machine mechanical rated speed	400	rpm
Phase back-EMF (Amp) @ 400rpm	15.5	V
Slot number	12	
Pole number	10	
Phase resistance	300	m Ω
Self inductance L_s	3.03	mH
Number of series turns per phase	132	

Furthermore, even though the rotor structure is surface mounted, the machine saliency is large enough due to saturation effect caused by the dual three-phase winding configuration on a single three-phase PMSM. Meanwhile, in terms of winding turns error, the impedances and three phase back-EMFs of the two sets are imbalanced. Hence, Motor III is applied to develop the sensorless control based on third harmonic back-EMF of dual three-phase PMSM as introduced in Chapter 5 and investigate the influence of machine saliency and imbalanced parameters as introduced in Chapter 6.

The dual three-phase motor drive as shown in Fig. 2.8 is based on STEVAL-IHM027V1 which is a 1kW, three-phase motor control demonstration board produced by STMicroelectronics. The power module of the power board is STGIPS10K60A featuring the 600V, 10A IGBT intelligent power module which is also from STMicroelectronics. The voltage drop is 2.1V@25°C. The operating frequency is 10kHz and the dead-time is set as 2 μ s. It is designed to be compatible with single-phase AC supply from 90 to 220 V, or DC supply from 125 to 350 V. An interface board is used to pass the gate drive signals from the DS5101 Digital Waveform Output Board to the power converter and to measure DC voltage and phase current and feedback the measured signals to DS2004 High-Speed A/D Board.

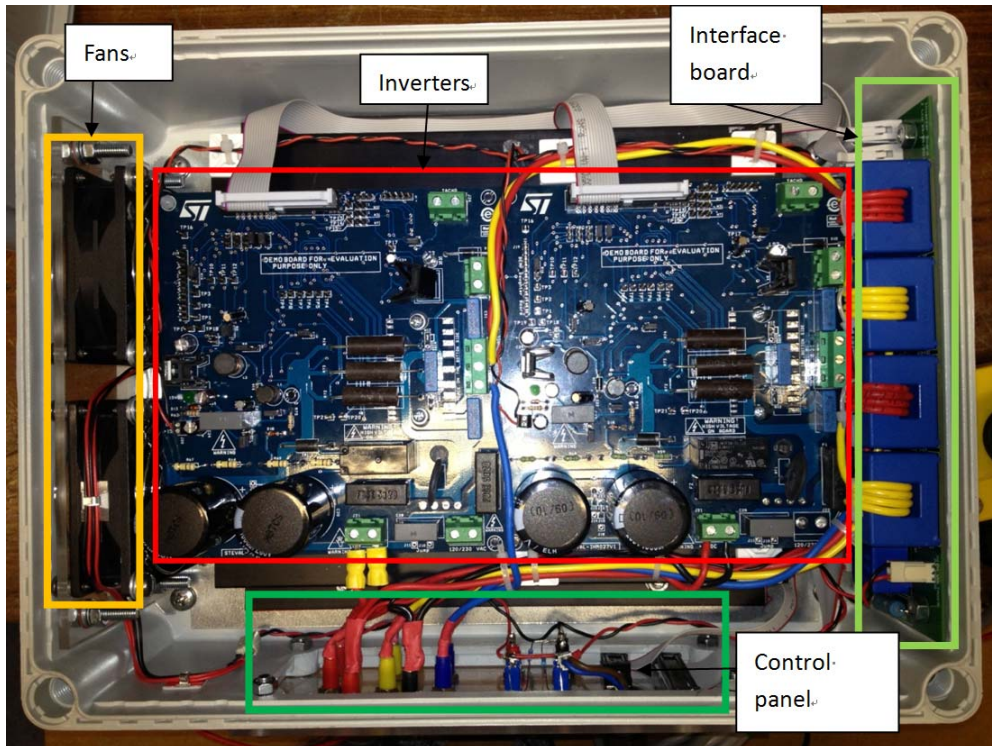


Fig. 2.8. Dual three-phase power converter working with Motor III

A 500W PM brushed DC machine with rated 3000rpm is directly coupled to this dual three-phase PMSM as a mechanical load. A power resistor is used to dissipate the generated power from the generator. The magnet field of the DC generator is excited by PM. Therefore, the load condition should be adjusted by changing the value of power resistance.

2.3.4 Rotor Position Alignment for Encoder

Each test rig contains an incremental encoder to provide actual rotor position to the control system. DS3001 incremental encoder board is applied to detect the rotor position. However, it is necessary to align the zero position of position sensor to the magnet axis (d -axis), as shown in Fig. 2.9. Typically, the three-phase back-EMF is a good reference for initial position alignment.

Spun by load machine, the three-phase back-EMF of PMSM can be measured from the machine winding terminals. For the case where a machine neutral point could not be accessed, the phase back-EMF can be calculated from the measured line back-EMF. Without consideration of harmonic components, the back-EMF in

stationary reference frame can be expressed as

$$\begin{bmatrix} e_a \\ e_b \\ e_c \end{bmatrix} = \begin{bmatrix} -\sin \theta_r \\ -\sin(\theta_r - 2\pi/3) \\ -\sin(\theta_r + 2\pi/3) \end{bmatrix} \omega_r \psi_m \quad (2.3)$$

From (2.3), it can be found that with positive rotation, the fundamental phase-A back-EMF should cross zero in the negative direction when the electrical rotor position is zero. By way of example, the position information can be well aligned for Motor I as an example, as shown in Fig. 2.10.

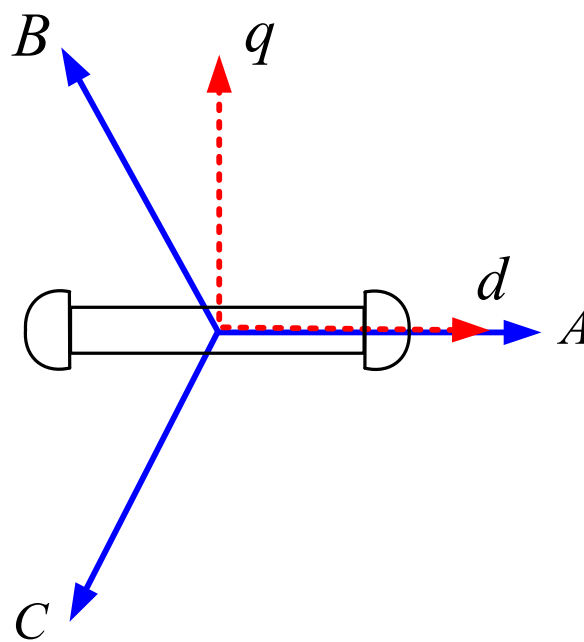


Fig. 2.9. Rotor position alignment.

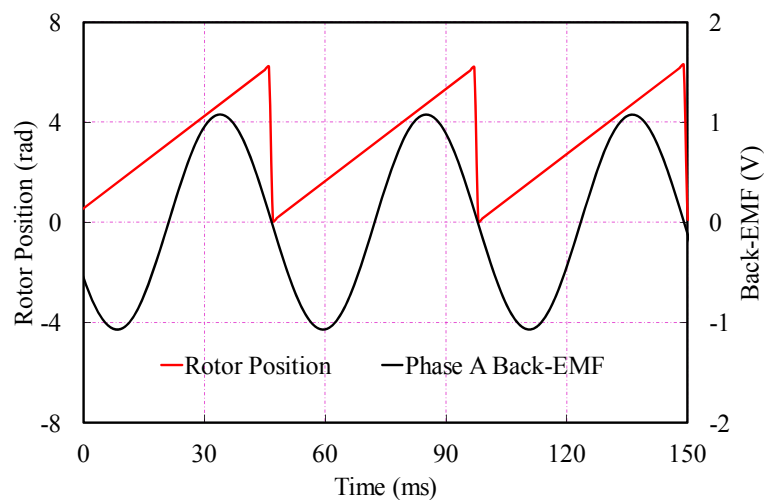


Fig. 2.10. Aligned rotor position against Phase-A back-EMF

2.4 Conclusion

This chapter gives a detailed description about the experimental setup based on a dSPACE control system, including the hardware platform and software interface. Three test rigs which will be implemented in this thesis are also introduced in this chapter. Since the function, character, structures and specifications of the three test rigs are all different, the applied control strategies are also different from each other which will be detailed introduced in each related chapter.

CHAPTER 3

NEW SENSORLESS CONTROL BASED ON SINUSOIDAL HIGH-FREQUENCY PULSATING CARRIER SIGNAL INJECTION INTO STATIONARY REFERENCE FRAME

3.1 Introduction

Sensorless control methods based on carrier signal injection are well developed due to their effectiveness at zero and low speed region. A high frequency carrier voltage signal (pulsating or rotating conventionally) is persistently superimposed on the fundamental excitation, and then the position-dependant carrier current response, which results from the interaction between the injected carrier voltage signal and the machine saliency, can be used to extract rotor position information. Alternatively, it is possible to inject a high frequency carrier current signal, and extract rotor position from the carrier voltage response. However, due to the simpler injection algorithm and hardware design, high frequency carrier voltage signal injection is preferred.

This chapter firstly provides a detailed discussion about most commonly used conventional pulsating and rotating carrier signal injection based sensorless control techniques, i.e. pulsating signal into d - or q -axis of the estimated synchronous reference frame and rotating signal which generated by two orthogonal pulsating signals into α - and β -axis stationary reference frame. Differing from these two high frequency injection methods, a new strategy with injection of a pulsating high frequency carrier voltage into α - (or β -) axis of stator stationary reference frame, and retrieving rotor position information from the carrier current response which is amplitude-modulated by rotor position is presented. The algorithm of the proposed

strategy, compensation of cross-saturation effect and magnetic polarity detection will be fully discussed and analyzed in this chapter.

3.2 High Frequency Model of PMSM Accounting for Cross-Saturation Effect

In the high frequency carrier voltage signal injection based sensorless control methods, the position-dependent carrier current response is subject to the impedance of the machine. Hence the high frequency model of a PMSM machine needs to be analyzed first.

3.2.1 Model in Synchronous Reference Frame

The voltage equation of PMSM in the synchronous reference frame is given by

$$\begin{bmatrix} u_d \\ u_q \end{bmatrix} = \begin{bmatrix} R_s & 0 \\ 0 & R_s \end{bmatrix} \cdot \begin{bmatrix} i_d \\ i_q \end{bmatrix} + p \begin{bmatrix} \psi_d \\ \psi_q \end{bmatrix} + \begin{bmatrix} -\omega_r \psi_q \\ \omega_r \psi_d \end{bmatrix} \quad (3.1)$$

where p is the differential operator, and ψ_d , ψ_q represent the d - and q -axis flux linkage respectively. Assuming that the machine reluctances have pure sinusoidal spatial distribution along the rotor circumference, they are only determined by load condition rather than rotor position.

If the injected carrier frequency is sufficiently higher than the fundamental excitation frequency normally at zero and low speed region, the back-EMF and resistive voltage drop can be negligible and the PMSM can be seen as a pure inductive load [RAC08a]. Since the injected voltage and response current are high frequency, and the amplitude are small, the incremental inductance which is defined as $\Delta\psi/\Delta i$ and used to describe the AC inductance should be employed. If the cross-saturation effect is considered [LI09a], the high frequency voltage equation of a PMSM in the synchronous reference frame is given by

$$\begin{bmatrix} u_{dh} \\ u_{qh} \end{bmatrix} = \begin{bmatrix} L_{dh} & L_{dqh} \\ L_{qdh} & L_{qh} \end{bmatrix} \cdot p \begin{bmatrix} i_{dh} \\ i_{qh} \end{bmatrix} \quad (3.2)$$

where L_{dh} and L_{qh} are the high frequency incremental d - and q -axis self-inductances

which are different from each other due to the machine saliency. L_{dqh} and L_{qdh} are the high frequency incremental mutual-inductances which are related with cross-saturation effect. Normally, L_{dqh} is not the same as L_{qdh} , however, the difference between is only about 1% which is difficult to differentiate [LI07]. Hence, for simplicity, $L_{dqh}=L_{qdh}$ is usually considered [LIN02] [REI08], and so does in this thesis.

From (3.2), it can be seen that only incremental inductances are contained in the high frequency voltage model. These incremental inductances can be measured by injecting the high frequency voltage signal into the d - and q -axes, respectively, when the machine is equipped with an encoder [LI09a]. The high frequency voltage signal, $u_c=U_c\cos(\omega_c t)$, is injected into the d -axis to obtain the relevant d -axis high frequency current responses, i.e. i_{dh1} and i_{qh1} , and then applied to the q -axis to record i_{dh2} and i_{qh2} . These voltages and currents are applied to (3.2), then

$$\begin{bmatrix} u_c & 0 \\ 0 & u_c \end{bmatrix} = \begin{bmatrix} L_{dh} & L_{dqh} \\ L_{qdh} & L_{qh} \end{bmatrix} \cdot p \begin{bmatrix} i_{dh1} & i_{dh2} \\ i_{qh1} & i_{qh2} \end{bmatrix} \quad (3.3)$$

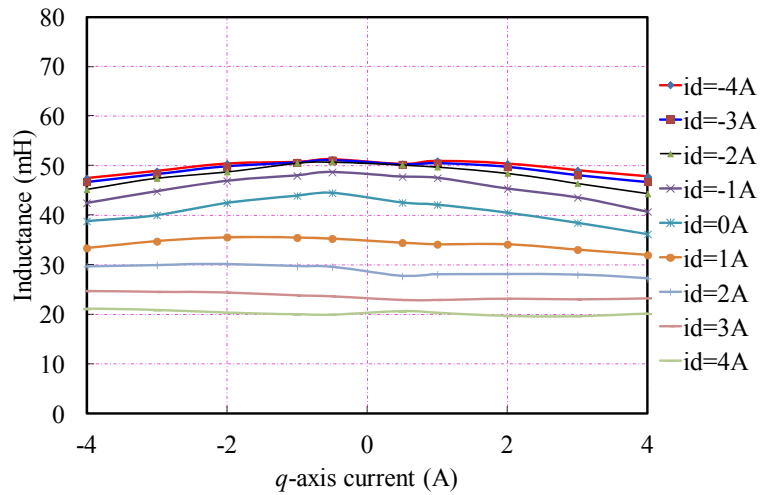
Both sides of (3.3) are multiplied by $2\cos(\omega_c t)$ and applied to a LPF to give

$$\begin{bmatrix} U_c & 0 \\ 0 & U_c \end{bmatrix} = \omega_c \begin{bmatrix} L_{dh} & L_{dqh} \\ L_{qdh} & L_{qh} \end{bmatrix} \cdot \begin{bmatrix} I_{dh1} & I_{dh2} \\ I_{qh1} & I_{qh2} \end{bmatrix} \quad (3.4)$$

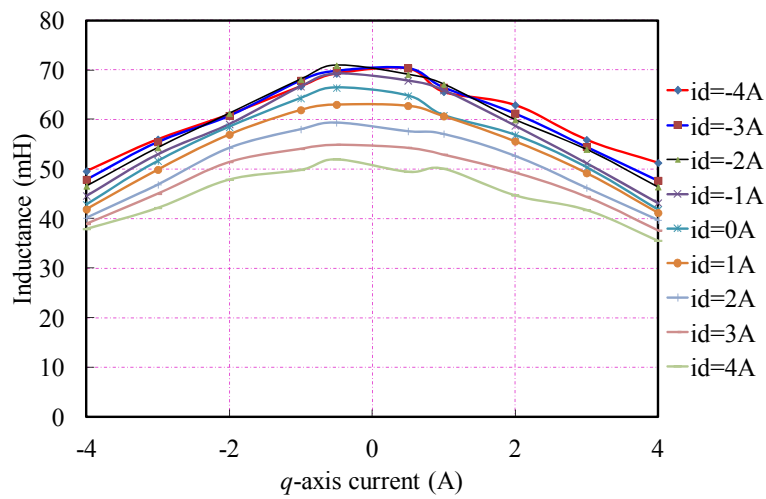
where I_{dh1} , I_{qh1} , I_{dh2} and I_{qh2} are the amplitude of corresponding high frequency currents. Then, the incremental self- and mutual-inductances of d - and q -axis are obtained by solving (3.4) as

$$\begin{bmatrix} L_{dh} & L_{dqh} \\ L_{qdh} & L_{qh} \end{bmatrix} = \frac{1}{\omega_c} \begin{bmatrix} U_c & 0 \\ 0 & U_c \end{bmatrix} \begin{bmatrix} I_{dh1} & I_{dh2} \\ I_{qh1} & I_{qh2} \end{bmatrix}^{-1} \quad (3.5)$$

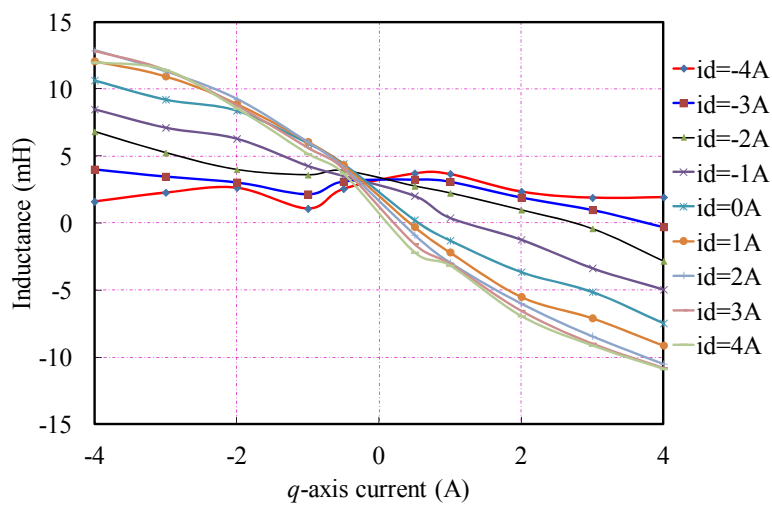
For the prototype machine Motor I which is used in this chapter, when the injected high frequency voltage signal is $u_c=10\times\cos(2\pi\times 400t)$ V, the self- and mutual-inductances are shown in Fig. 3.1 [LI09a], from which it could be found due to magnetic saturation, L_{dh} , L_{qh} and L_{dqh} vary with fundamental excitation.



(a) d -axis self-inductance, L_{dh}



(b) q -axis self-inductance, L_{qh}



(c) dq -axis mutual-inductance, L_{dqh}

Fig. 3.1. Measured incremental inductances for the prototype machine

3.2.2 Current Model in Estimated Synchronous Reference Frame

Since in the sensorless operation, the accurate rotor position is unknown, the estimated rotor position is usually used in the control algorithm. Hence, with the aid of transformation matrix $T(\Delta\theta)$ which is

$$T(\Delta\theta) = \begin{bmatrix} \cos(\Delta\theta) & -\sin(\Delta\theta) \\ \sin(\Delta\theta) & \cos(\Delta\theta) \end{bmatrix} \quad (3.6)$$

where $\Delta\theta$ is the estimation error of rotor position, i.e. $\Delta\theta = \theta_r - \theta_r^e$, the high frequency voltage model of PMSM in estimated synchronous reference frame can be derived as

$$\begin{aligned} \begin{bmatrix} u_{dh}^e \\ u_{qh}^e \end{bmatrix} &= T(\Delta\theta) \begin{bmatrix} L_{dh} & L_{dqh} \\ L_{dqh} & L_{qh} \end{bmatrix} T^{-1}(\Delta\theta) \cdot p \begin{bmatrix} i_{dh}^e \\ i_{qh}^e \end{bmatrix} \\ &= \begin{bmatrix} \cos(\Delta\theta) & -\sin(\Delta\theta) \\ \sin(\Delta\theta) & \cos(\Delta\theta) \end{bmatrix} \cdot \begin{bmatrix} L_{dh} & L_{dqh} \\ L_{dqh} & L_{qh} \end{bmatrix} \cdot \begin{bmatrix} \cos(\Delta\theta) & \sin(\Delta\theta) \\ -\sin(\Delta\theta) & \cos(\Delta\theta) \end{bmatrix} \cdot p \begin{bmatrix} i_{dh}^e \\ i_{qh}^e \end{bmatrix} \\ &= \begin{bmatrix} L_{sa} - L_{sd} \cos 2\Delta\theta - L_{dqh} \sin 2\Delta\theta & -L_{sd} \sin 2\Delta\theta + L_{dqh} \cos 2\Delta\theta \\ -L_{sd} \sin 2\Delta\theta - L_{dqh} \cos 2\Delta\theta & L_{sa} + L_{sd} \cos 2\Delta\theta + L_{dqh} \sin 2\Delta\theta \end{bmatrix} \cdot p \begin{bmatrix} i_{dh}^e \\ i_{qh}^e \end{bmatrix} \end{aligned} \quad (3.7)$$

where L_{sa} and L_{sd} are the average and difference of d - and q -axis incremental inductances, i.e.

$$\begin{cases} L_{sa} = (L_{qh} + L_{dh}) / 2 \\ L_{sd} = (L_{qh} - L_{dh}) / 2 \end{cases} \quad (3.8)$$

Solving (3.7), the differential of the high frequency carrier current response in estimated synchronous reference frame will be

$$\begin{aligned} p \begin{bmatrix} i_{dh}^e \\ i_{qh}^e \end{bmatrix} &= \begin{bmatrix} \frac{L_{sa} + \sqrt{L_{sd}^2 + L_{dqh}^2} \cos(2\Delta\theta + \theta_m)}{L_{dh}L_{qh} - L_{dqh}^2} & \frac{\sqrt{L_{sd}^2 + L_{dqh}^2} \sin(2\Delta\theta + \theta_m)}{L_{dh}L_{qh} - L_{dqh}^2} \\ \frac{\sqrt{L_{sd}^2 + L_{dqh}^2} \sin(2\Delta\theta + \theta_m)}{L_{dh}L_{qh} - L_{dqh}^2} & \frac{L_{sa} - \sqrt{L_{sd}^2 + L_{dqh}^2} \cos(2\Delta\theta + \theta_m)}{L_{dh}L_{qh} - L_{dqh}^2} \end{bmatrix} \cdot \begin{bmatrix} u_{dh}^e \\ u_{qh}^e \end{bmatrix} \\ &= \begin{bmatrix} \frac{1}{L_p} + \frac{1}{L_n} \cos(2\Delta\theta + \theta_m) & \frac{1}{L_n} \sin(2\Delta\theta + \theta_m) \\ \frac{1}{L_n} \sin(2\Delta\theta + \theta_m) & \frac{1}{L_p} - \frac{1}{L_n} \cos(2\Delta\theta + \theta_m) \end{bmatrix} \cdot \begin{bmatrix} u_{dh}^e \\ u_{qh}^e \end{bmatrix} \end{aligned} \quad (3.9)$$

where

$$\theta_m = \tan^{-1}\left(\frac{-L_{dqh}}{L_{sd}}\right), \quad L_p = \frac{L_{dh}L_{qh} - L_{dqh}^2}{L_{sa}}, \quad L_n = \frac{L_{dh}L_{qh} - L_{dqh}^2}{\sqrt{L_{sd}^2 + L_{dqh}^2}} \quad (3.10)$$

θ_m is the cross-saturation angle which is caused by cross coupling saturation effect and will cause a constant estimation error in the estimated rotor position, which will be introduced in detail in Section 3.4.3.

3.2.3 Current Model in Stationary Reference Frame

With the aid of transformation matrix $T(\theta_r)$ which is

$$T(\theta_r) = \begin{bmatrix} \cos(\theta_r) & -\sin(\theta_r) \\ \sin(\theta_r) & \cos(\theta_r) \end{bmatrix} \quad (3.11)$$

the high frequency model of PMSM in stationary reference frame can be derived as

$$\begin{aligned} \begin{bmatrix} u_{\alpha h} \\ u_{\beta h} \end{bmatrix} &= T(\theta_r) \begin{bmatrix} L_{dh} & L_{dqh} \\ L_{dqh} & L_{qh} \end{bmatrix} T^{-1}(\theta_r) \cdot p \begin{bmatrix} i_{\alpha h} \\ i_{\beta h} \end{bmatrix} \\ &= \begin{bmatrix} L_{sa} - L_{sd} \cos 2\theta_r - L_{dqh} \sin 2\theta_r & -L_{sd} \sin 2\theta_r + L_{dqh} \cos 2\theta_r \\ -L_{sd} \sin 2\theta_r - L_{dqh} \cos 2\theta_r & L_{sa} + L_{sd} \cos 2\theta_r + L_{dqh} \sin 2\theta_r \end{bmatrix} \cdot p \begin{bmatrix} i_{\alpha h} \\ i_{\beta h} \end{bmatrix} \end{aligned} \quad (3.12)$$

Similar as in estimated synchronous reference frame, solving (3.12), the differential of the high frequency carrier current response in stationary reference frame can be derived as

$$p \begin{bmatrix} i_{\alpha h} \\ i_{\beta h} \end{bmatrix} = \begin{bmatrix} \frac{1}{L_p} + \frac{1}{L_n} \cos(2\theta_r + \theta_m) & \frac{1}{L_n} \sin(2\theta_r + \theta_m) \\ \frac{1}{L_n} \sin(2\theta_r + \theta_m) & \frac{1}{L_p} - \frac{1}{L_n} \cos(2\theta_r + \theta_m) \end{bmatrix} \cdot \begin{bmatrix} u_{\alpha h} \\ u_{\beta h} \end{bmatrix} \quad (3.13)$$

3.3 Conventional High Frequency Carrier Signal Injection

Methods

According to the type of injected carrier signal, the two most popular methods are rotating sinusoidal signal injection [JAN95] [DEG98] [GAR07] [RAC08a] [RAC10] and pulsating sinusoidal signal injection [COR98] [HA00] [LIN02] [JAN03] [LI09B].

3.3.1 Pulsating Carrier Signal Injection

For pulsating signal injection methods, a high frequency pulsating carrier signal which is also normally a voltage is injected into the d - (or q -axis) in the estimated synchronous reference frame, which can be seen as the superposition of two rotating

carrier vectors with opposite rotating direction as illustrated in Fig. 3.2. That the reason why it is called pulsating carrier signal. Position could be estimated through minimization of the amplitude modulated carrier frequency response signal measured along the axis orthogonal to the injection axis.

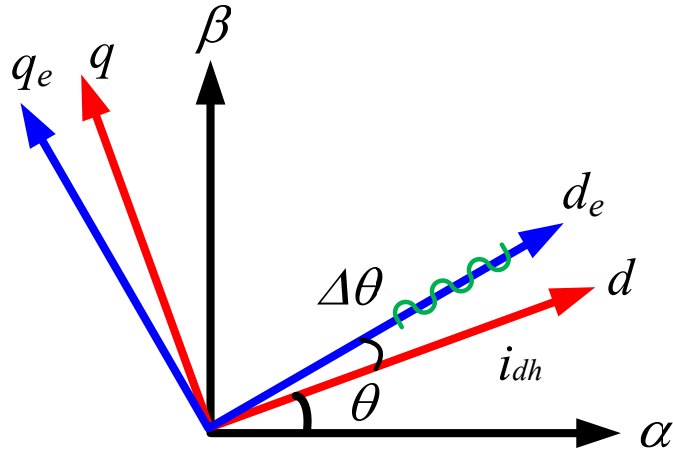


Fig. 3.2. Conventional pulsating signal injection

For d -axis pulsating carrier signal injection, the high frequency pulsating carrier voltage vector (3.14) which is illustrated in Fig. 3.3 is injected on the estimated d -axis [COR98][JAN03]LI09b].

$$\begin{bmatrix} u_{dh}^e \\ u_{qh}^e \end{bmatrix} = U_c \begin{bmatrix} \cos \alpha \\ 0 \end{bmatrix}, \alpha = \omega_c t + \varphi \quad (3.14)$$

where U_c , ω_c and φ are the amplitude, angular speed and the initial phase angle of the injected pulsating high frequency voltage, respectively.

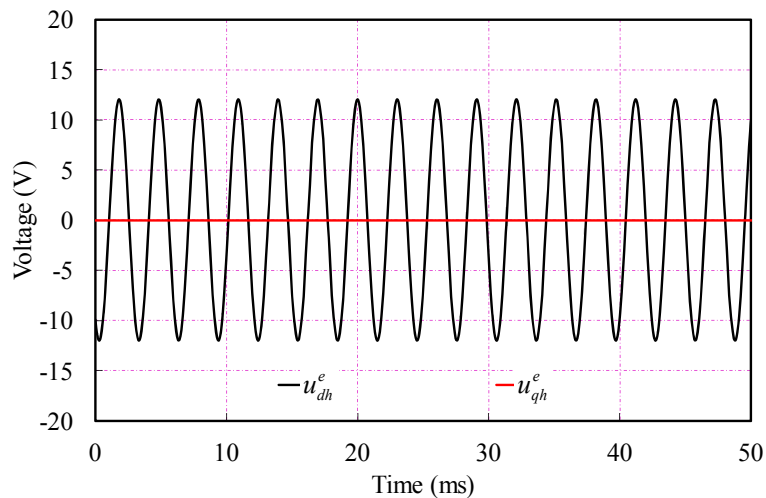


Fig. 3.3. Injected pulsating carrier voltage ($U_c=12V, f=330Hz$)

Then the Phase-A current response is shown in Fig. 3.4 where the rotor position is contained in the carrier current response.

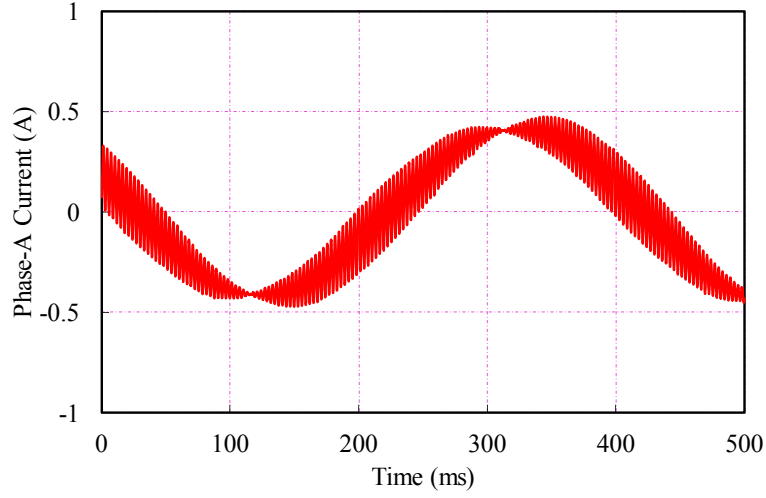


Fig. 3.4. Phase-A current response

Then, the differential of the carrier current in the estimated synchronous reference frame as shown in (3.9) can be expressed as

$$p \begin{bmatrix} i_{dh}^e \\ i_{qh}^e \end{bmatrix} = \begin{bmatrix} \frac{1}{L_p} + \frac{1}{L_n} \cos(2\Delta\theta + \theta_m) & \frac{1}{L_n} \sin(2\Delta\theta + \theta_m) \\ \frac{1}{L_n} \sin(2\Delta\theta + \theta_m) & \frac{1}{L_p} - \frac{1}{L_n} \cos(2\Delta\theta + \theta_m) \end{bmatrix} \cdot U_c \begin{bmatrix} \cos \alpha \\ 0 \end{bmatrix} \quad (3.15)$$

Therefore, the resultant carrier current response in the estimated synchronous reference frame can be expressed as:

$$\begin{bmatrix} i_{dh}^e \\ i_{qh}^e \end{bmatrix} = \begin{bmatrix} \frac{U_c}{\omega_c L_p} + \frac{U_c}{\omega_c L_n} \cos(\Delta\theta + \theta_m) \\ \frac{U_c}{\omega_c L_n} \sin(2\Delta\theta + \theta_m) \end{bmatrix} \cdot \sin \alpha = \begin{bmatrix} I_p + I_n \cos(\Delta\theta + \theta_m) \\ I_n \sin(2\Delta\theta + \theta_m) \end{bmatrix} \cdot \sin \alpha \quad (3.16)$$

where

$$I_p = \frac{U_c}{\omega_c L_p}, \quad I_n = \frac{U_c}{\omega_c L_n} \quad (3.17)$$

It is clearly shown that the carrier current response is amplitude modulated by the rotor position information (for given load condition, cross-saturation angle θ_m is constant). When the estimated position error $\Delta\theta$ is sufficiently small, i_{qh}^e becomes very small, therefore, the q -axis carrier current response is usually used to extract the rotor

position information. Since the introduced current ripple on the q -axis is limited, less torque ripple would be generated.

For q -axis pulsating carrier signal injection, the high frequency pulsating carrier voltage vector (3.18) is injected on the estimated q -axis [LIN03] [YAN11].

$$\begin{bmatrix} u_{dh}^e \\ u_{qh}^e \end{bmatrix} = U_c \begin{bmatrix} 0 \\ \cos \alpha \end{bmatrix}, \alpha = \omega_c + \varphi \quad (3.18)$$

Then the resultant carrier current in the estimated synchronous reference frame as shown in (3.9) can be expressed as

$$\begin{bmatrix} i_{dh}^e \\ i_{qh}^e \end{bmatrix} = \begin{bmatrix} \frac{U_c}{\omega_c L_n} \sin(\Delta\theta + \theta_m) \\ \frac{U_c}{\omega_c L_p} - \frac{U_c}{\omega_c L_n} \cos(2\Delta\theta + \theta_m) \end{bmatrix} \cdot \sin \alpha = \begin{bmatrix} I_n \sin(\Delta\theta + \theta_m) \\ I_p - I_n \cos(2\Delta\theta + \theta_m) \end{bmatrix} \cdot \sin \alpha \quad (3.19)$$

Similar to the d -axis injection, the carrier current response is amplitude modulated by the rotor position information, and the d -axis carrier current response is usually used to extract the rotor position information. q -axis injection is a good choice for zero d -axis current vector control, since it is less sensitive to the inverter nonlinearity effect. Compared to d -axis injection, however, more current ripple on the q -axis can be generated. It would generate substantial torque ripple even the position estimation error is zero. Consequently, injection of pulsating carrier voltage along the d -axis is preferred in terms of torque ripple [HA00].

In order to demodulate the position dependent amplitude from the carrier current response, the synchronous detection technique is applied [MAD95] [RAC10]. Both sides of (3.16) are multiplied by $2\sin\alpha$, and then applying the signal to a LPF, the amplitude of the carrier current, e.g. with d -axis pulsating injection based sensorless method, can be obtained with noise suppression as shown in (3.20) and Fig. 3.5.

$$\left| i_{dqh}^e \right| = \begin{bmatrix} i_{dh}^e \\ i_{qh}^e \end{bmatrix} = LPF \left(\begin{bmatrix} i_{dh}^e \\ i_{qh}^e \end{bmatrix} \cdot 2\sin \alpha \right) = \begin{bmatrix} I_p + I_n \cos(\Delta\theta + \theta_m) \\ I_n \sin(2\Delta\theta + \theta_m) \end{bmatrix} \quad (3.20)$$

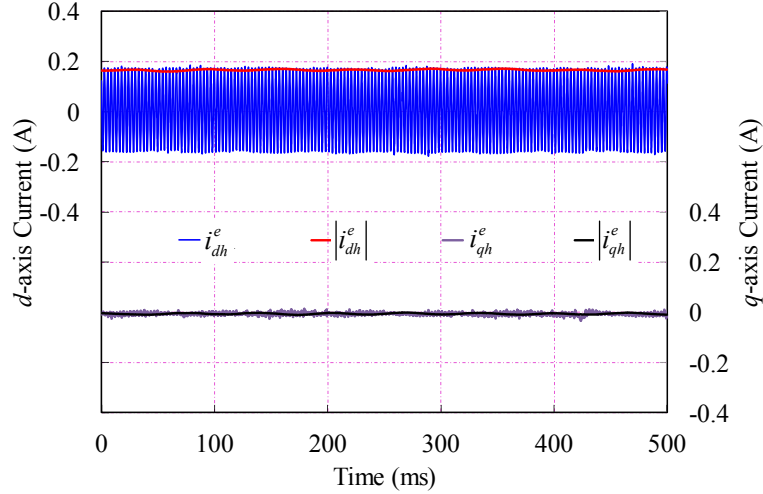


Fig. 3.5. Amplitude demodulation from carrier current response

Then the amplitude of q -axis carrier current response is regarded to be the signal input to the position observer,

$$f(\Delta\theta) = |i_{qh}^e| = I_n \sin(2\Delta\theta + \theta_m) \quad (3.21)$$

In steady-state, $f(\Delta\theta)$ is forced to be zero due to the position observer, and hence, rotor position can be derived with the load-dependent position estimation error ($-\theta_m/2$) due to cross-saturation effect.

In order to compensate the estimated position error resulting from cross-saturation effect, either proper machine design or compensation control can be employed. Many efforts have been made on the control aspect. When the rotor position estimation error $\Delta\theta$ is sufficiently small, (3.22) can be further derived as,

$$\begin{bmatrix} |i_{dh}^e| \\ |i_{qh}^e| \end{bmatrix} = \begin{bmatrix} I_p + I_n \cos(\Delta\theta + \theta_m) \\ I_n \sin(2\Delta\theta + \theta_m) \end{bmatrix} \approx \begin{bmatrix} I_p + I_n \cos(\Delta\theta + \theta_m) \\ 2I_n \cos \theta_m \cdot \Delta\theta + I_n \sin \theta_m \end{bmatrix} \quad (3.22)$$

Defining a coupling factor $\lambda = L_{dqh}/L_{qh}$, then $f(\Delta\theta)$ can be re-defined as

$$f(\Delta\theta) = |i_{qh}^e| + \lambda |i_{dh}^e| \approx 2I_n \cos \theta_m \cdot \Delta\theta \quad (3.23)$$

Then, the new $f(\Delta\theta)$ is forced to be zero by the position observer. Obviously, in this way no position estimation error would be generated by the cross-saturation effect.

The overall control strategy is shown in Fig. 3.6

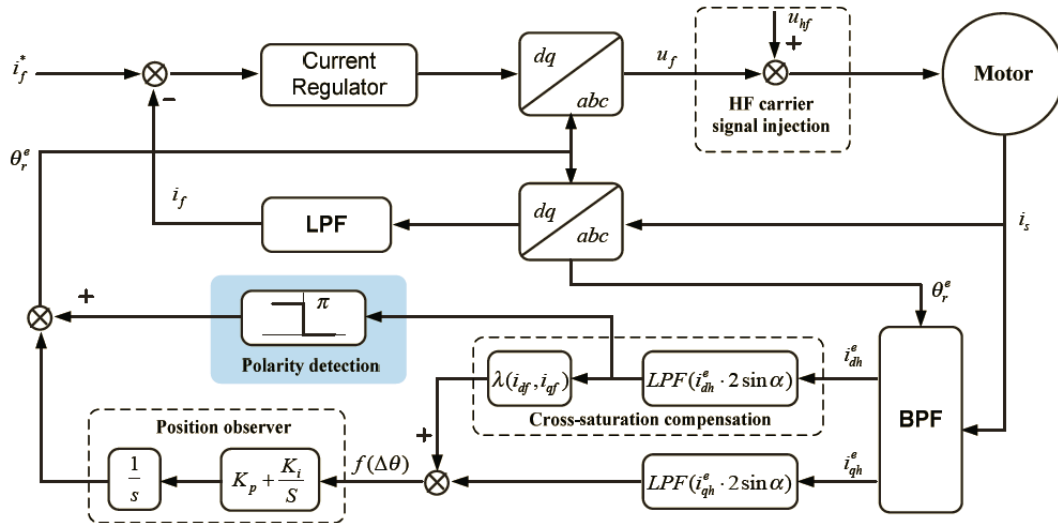


Fig. 3.6. Block diagram of d -axis pulsating injection based sensorless control [GON12]

3.3.2 Rotating Carrier Signal Injection

Rotating signal injection schemes inject a balanced three phase voltage (or current) carrier signal which normally is a voltage into the stationary reference frame superimposed on the fundamental excitation as demonstrated in Fig. 3.7. The injected voltage can form a rotating excitation, and that is the reason why this method is called rotating carrier signal injection. The rotor position information can be obtained from the rotor position modulated response current [JAN95] [JOE05].

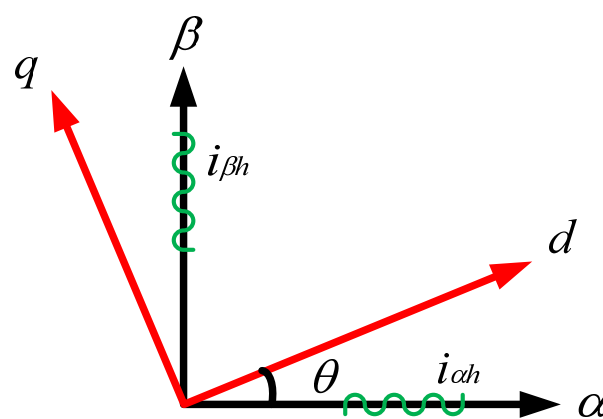


Fig. 3.7. Conventional rotating signal injection

For rotating carrier signal injection, a balanced rotating carrier voltage vector (3.24) which is shown in Fig. 3.8 is injected into stationary reference frame,

$$\begin{bmatrix} u_{\alpha h} \\ u_{\beta h} \end{bmatrix} = U_c \begin{bmatrix} \cos \alpha \\ \sin \alpha \end{bmatrix}, \alpha = \omega_c t + \varphi \quad (3.24)$$

where U_c , ω_c and φ are the amplitude, angular speed and the initial phase angle of the injected pulsating high frequency voltage, respectively. Then the Phase-A current response is shown in Fig. 3.9 where the rotor position is contained in the carrier current response.

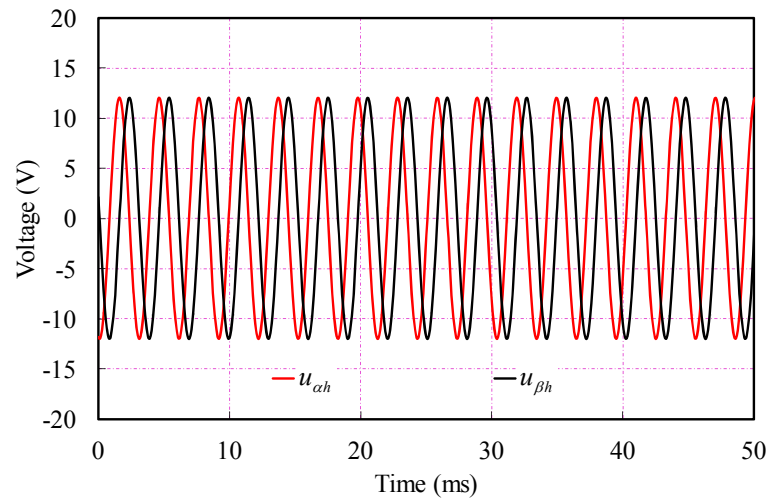


Fig. 3.8. Injected rotating carrier voltage ($U_c=12V$, $f=330Hz$)

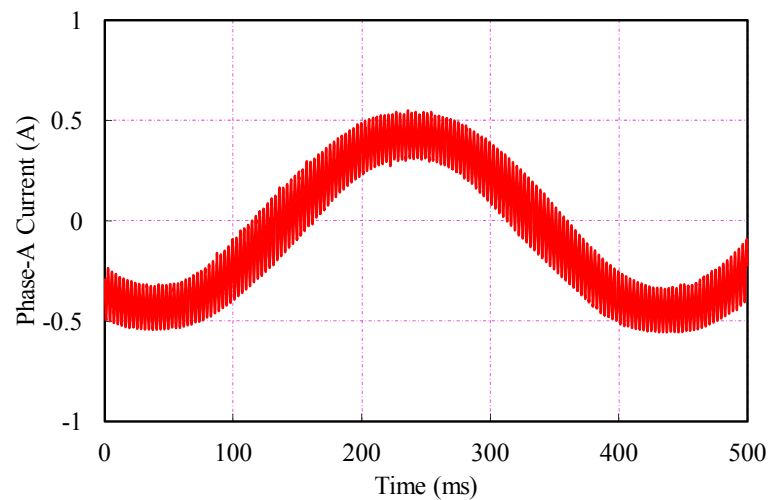


Fig. 3.9. Phase-A current response

The differential of the carrier current in the stationary reference frame as shown in (3.13) can be expressed as

$$p \begin{bmatrix} i_{\alpha h} \\ i_{\beta h} \end{bmatrix} = \begin{bmatrix} \frac{1}{L_p} + \frac{1}{L_n} \cos(2\theta_r + \theta_m) & \frac{1}{L_n} \sin(2\theta_r + \theta_m) \\ \frac{1}{L_n} \sin(2\theta_r + \theta_m) & \frac{1}{L_p} - \frac{1}{L_n} \cos(2\theta_r + \theta_m) \end{bmatrix} \cdot U_c \begin{bmatrix} \cos \alpha \\ \sin \alpha \end{bmatrix} \quad (3.25)$$

Then, the resultant carrier current response in the stationary reference frame can be shown in (3.26) and Fig. 3.10.

$$\begin{aligned} \begin{bmatrix} i_{\alpha h} \\ i_{\beta h} \end{bmatrix} &= \frac{U_c}{\omega_c} \begin{bmatrix} \frac{1}{L_p} + \frac{1}{L_n} \cos(2\theta_r + \theta_m) & \frac{1}{L_n} \sin(2\theta_r + \theta_m) \\ \frac{1}{L_n} \sin(2\theta_r + \theta_m) & \frac{1}{L_p} - \frac{1}{L_n} \cos(2\theta_r + \theta_m) \end{bmatrix} \cdot \begin{bmatrix} \sin \alpha \\ -\cos \alpha \end{bmatrix} \\ &= \begin{bmatrix} I_p \cos(\alpha - \frac{\pi}{2}) \\ I_p \sin(\alpha - \frac{\pi}{2}) \end{bmatrix} + \begin{bmatrix} I_n \cos(-\alpha + 2\theta_r + \theta_m + \frac{\pi}{2}) \\ I_n \sin(-\alpha + 2\theta_r + \theta_m + \frac{\pi}{2}) \end{bmatrix} \end{aligned} \quad (3.26)$$

and by using complex vector as

$$i_h = I_p \cdot e^{j(\alpha - \pi/2)} + I_n \cdot e^{j(-\alpha + 2\theta_r + \theta_m + \pi/2)} \quad (3.27)$$

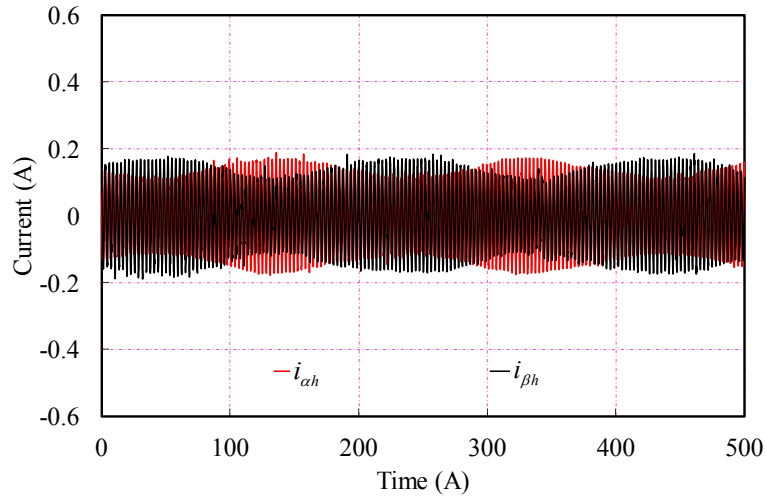


Fig. 3.10. Carrier current response of rotating signal injection

Clearly, the carrier current response consists of two components. The first term is a positive sequence component, which has the same angular speed as the injected carrier voltage vector, and the second term is referred to as the negative sequence component, which contains the rotor position information in phase angle [RAC08a]. Consequently, the negative sequence component is used to track the rotor position.

In order to extract the position dependent negative sequence carrier current from the total current response, SRFF, i.e. synchronous reference frame filter, is the typical solution [DEG98] [RAC10] [GAR07]. Firstly, SRFF uses the frame transformation based on feedback estimated rotor position to transform the fundamental current to DC. With the aid of a LPF which is a second order with 50Hz cut-off frequency, this DC component is obtained without phase lag. Then with the reverse frame transformation, this fundamental current can be easily obtained. By employing the same procedure with the phase angle of the injected carrier voltage, the positive sequence current can be derived. Then subtracting them from the total current response, the negative sequence current can be obtained. By applying the signal demodulation with SRFF as shown in Fig. 3.11, we can obtain the negative sequence signal as

$$i_n = I_n \cdot e^{j(-\alpha+2\theta_r+\theta_m+\pi/2)} \quad (3.28)$$

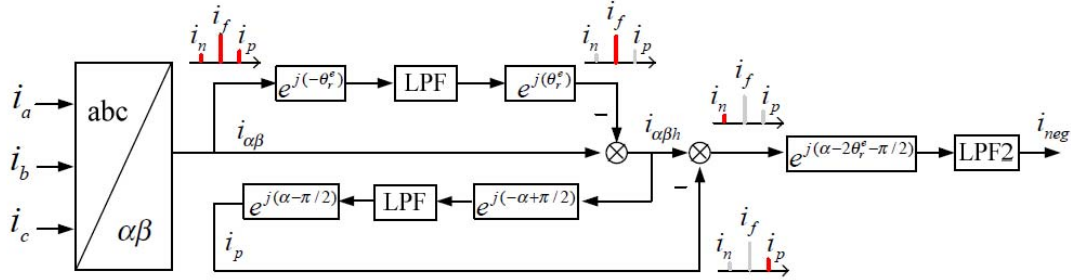


Fig. 3.11. Signal demodulation for rotating injection [GON12]

Then i_n in the reference frame synchronous with estimated negative sequence carrier frequency, can be expressed as shown in (3.29) and Fig. 3.12.

$$i_{neg} = I_n \cdot e^{j(-\alpha+2\theta_r+\theta_m+\pi/2)} \cdot e^{j(\alpha-2\theta_r-\pi/2)} = I_n \cdot e^{j(2\Delta\theta+\theta_m)} = I_n \cdot e^{j\theta_{neg}} \quad (3.29)$$

where θ_{neg} is the angular offset of negative sequence carrier current. (3.29) can be rewritten as

$$\begin{bmatrix} i_{neg_d} \\ i_{neg_q} \end{bmatrix} = \begin{bmatrix} I_n \cos(2\Delta\theta + \theta_m) \\ I_n \sin(2\Delta\theta + \theta_m) \end{bmatrix} \quad (3.30)$$

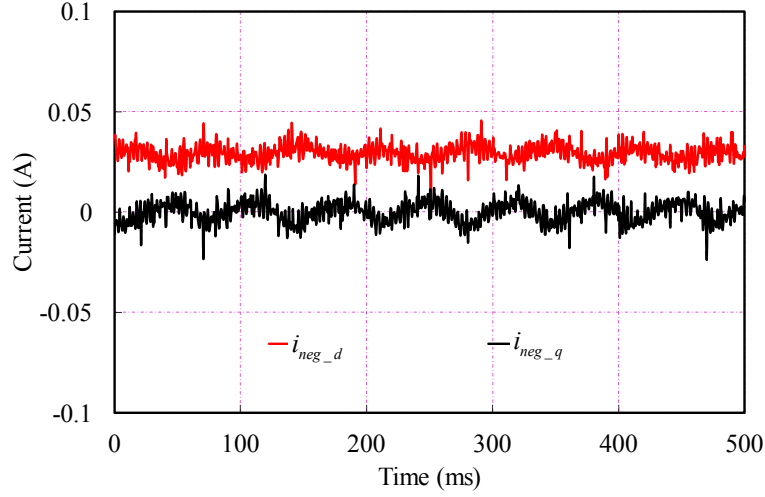


Fig. 3.12. Demodulated negative sequence carrier current response in estimated negative sequence reference frame

Normally, the q -axis component is regarded as the error signal $f(\Delta\theta)$ input to the position observer [JAN95] [DEG98], i.e.

$$f(\Delta\theta) = i_{neg_q} = I_n \sin(2\Delta\theta + \theta_m) \quad (3.31)$$

It is identical to (3.21) for conventional d -axis pulsating injection. Therefore, it is expected that the same position estimation error ($-\theta_m/2$) due to cross-saturation effect would be introduced for rotating injection. To compensate the cross-saturation angle, the phase angle of injected carrier voltage is modified as

$$\alpha' = \alpha + \theta_m \quad (3.32)$$

Then the carrier current response can be derived as

$$i = i_f + I_p \cdot e^{j(\alpha+\theta_m-\pi/2)} + I_n \cdot e^{j(-\alpha+2\theta_r+\pi/2)} \quad (3.33)$$

It can be seen that the cross-saturation angle θ_m has been transferred from the negative sequence carrier current to the positive sequence carrier current. Therefore, the rotor position is expected to be accurately estimated from the negative sequence carrier current. Then, (3.30) can be re-written as

$$\begin{bmatrix} i_{neg_d} \\ i_{neg_q} \end{bmatrix} = \begin{bmatrix} I_n \cos(2\Delta\theta) \\ I_n \sin(2\Delta\theta) \end{bmatrix} \quad (3.34)$$

Therefore, $f(\Delta\theta)$ can be updated as

$$f(\Delta\theta) = i_{neg_q} = I_n \sin(2\Delta\theta) \quad (3.35)$$

With cross-saturation effect compensation, the block diagram of rotating carrier voltage signal injection based sensorless control is shown in Fig. 3.13.

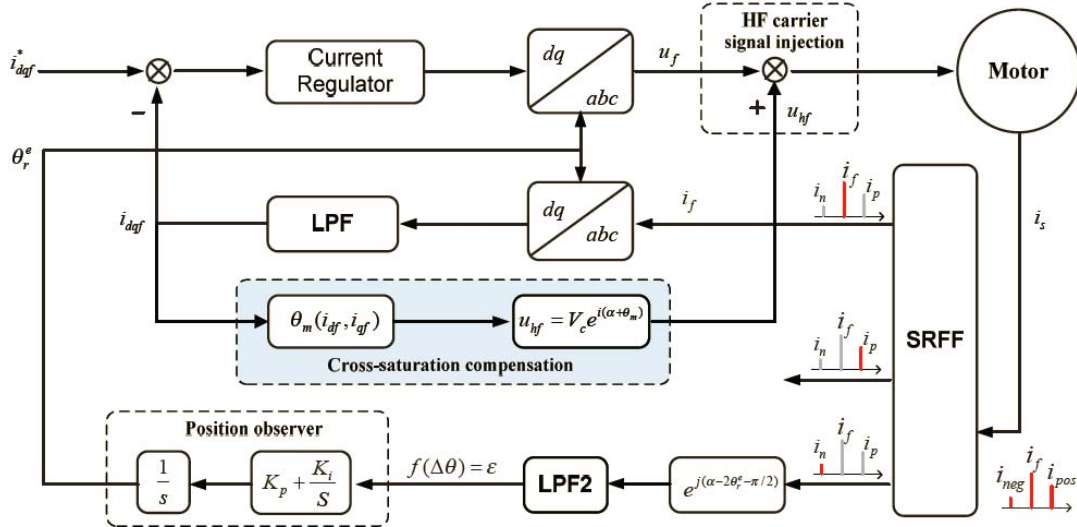


Fig. 3.13. Block diagram of rotating injection based sensorless control [GON12]

3.3.3 Rotor Position Observer

Position tracking observer is much more popular than arc-tangent function (\tan^{-1}) calculation [TES03] in sensorless position estimation due to the good immunity to disturbance harmonics while keeping the dynamic performance of position tracking. Although some nonlinear controllers such as bang-bang controllers can be used in position observer to enhance the dynamic characteristics [JAN04], they have the disadvantage of resulting in an unclear steady-state response. Therefore, linear PI controllers prevail in sensorless position observer [HAR00] [CUP10].

Considering the signal $f(\Delta\theta)$ input to the position observer for conventional pulsating and rotating injection, the block diagram of position observer including PI regulator is shown in Fig. 3.14.

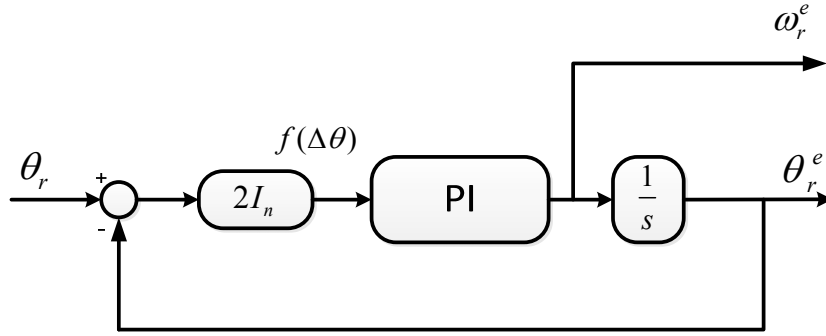


Fig. 3.14. Block diagram of rotor position observer

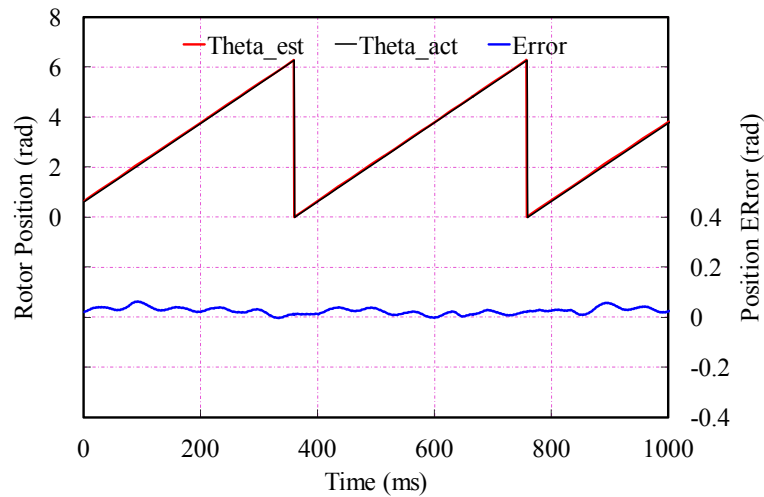
According to the diagram, the closed loop transfer function between the actual rotor position information and the estimated one can be expressed as,

$$\frac{\theta_r^e}{\theta_r} = \frac{2I_n k_p \cdot s + 2I_n k_i}{s^2 + 2I_n k_p \cdot s + 2I_n k_i} \quad (3.36)$$

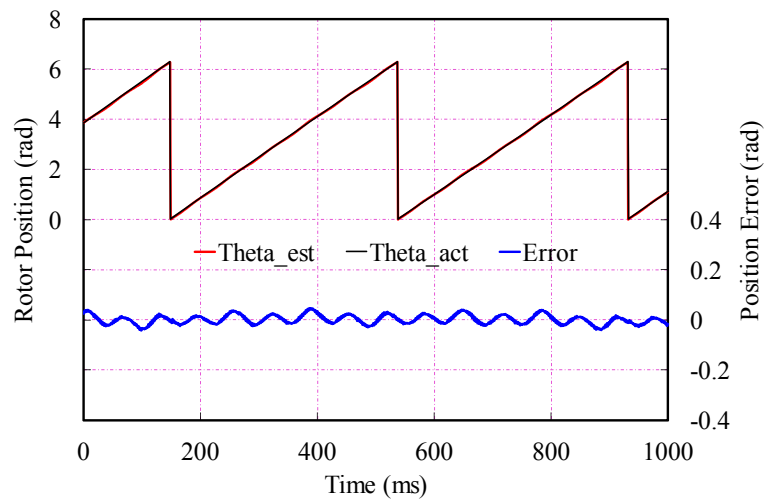
Based on (3.10) and (3.17), it could be seen that I_n is load-dependent. Hence, k_p and k_i of PI controller should be on-line varied with I_n to maintain the constant bandwidth. For simplicity in practical implementation, k_p and k_i could be selected based on the typical value of I_n at no load condition.

3.3.4 Steady-state and Dynamic Performance

The steady-state tests for pulsating and rotating carrier signal injection methods are carried out at the condition of 70V DC bus voltage, 50rpm rotor speed with about 1A q -axis current, and the estimated rotor positions considering the cross-saturation effect are shown in Fig. 3.15 compared with the actual value from encoder. The experimental results of pulsating signal injection are shown in Fig. 3.15 (a) and the ones of rotating signal injection are shown in Fig. 3.15 (b). It can be seen that the estimation errors of both methods are sufficiently small and the estimated rotor position are with high accuracy.



(a) Pulsating signal injection



(b) Rotating signal injection

Fig. 3.15. Steady-state errors from pulsating and rotating injection methods

(Θ_{est} : Estimated rotor position, Θ_{act} : Actual rotor position,

$Error$: Rotor position estimation error)

The dynamic performance tests are carried out when the rotor mechanical initial speed is zero and step change to 25rpm and then 50rpm as demonstrated in Fig. 3.16, and the estimated and actual rotor positions, as well as the estimation error of pulsating signal injection are shown in Fig. 3.17(a) and the ones of rotating signal injection are shown in Fig. 3.17(b). The experimental results prove that the two conventional high frequency injection methods have outstanding dynamic performances.

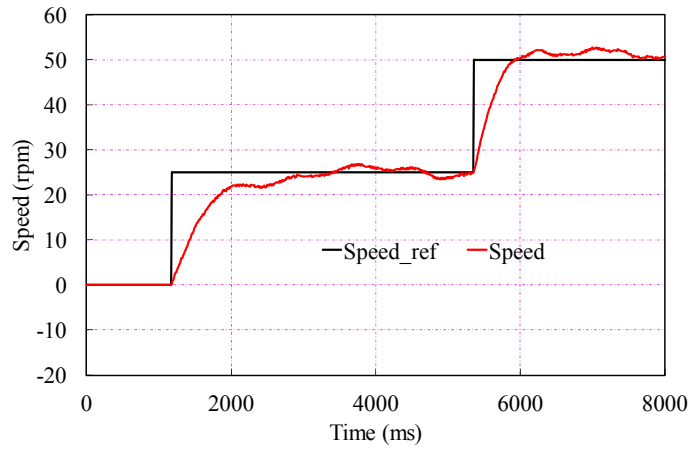
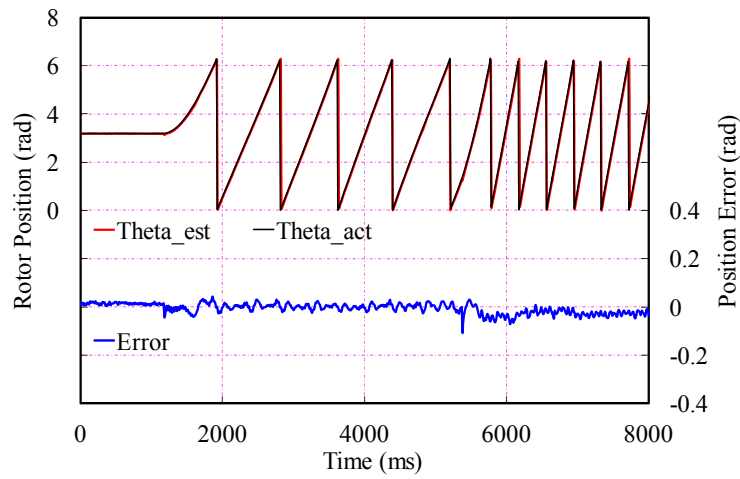
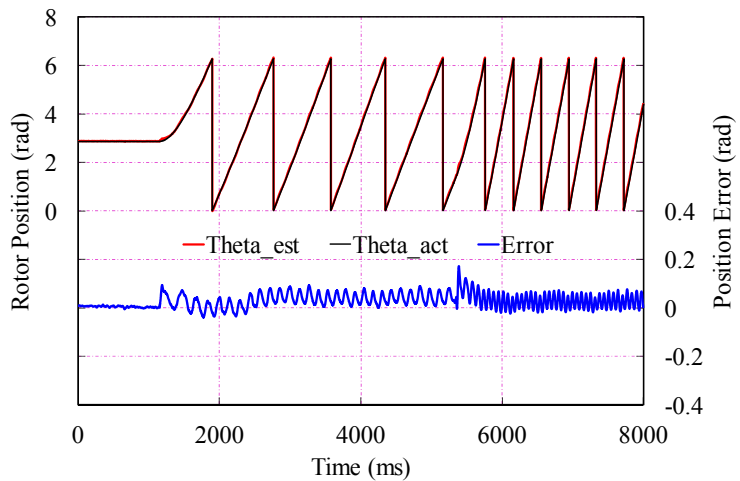


Fig. 3.16. Dynamic test situation
(*Speed_ref*: Speed reference, *Speed*: Actual rotor speed)



(a) Pulsating signal injection



(b) Rotating signal injection

Fig. 3.17. Dynamic performance from pulsating and rotating injection methods

(*Theta_est*: Estimated rotor position, *Theta_act*: Actual rotor position,
Error: Rotor position estimation error)

3.4 New Proposed Control Strategy with Injection of High Frequency Pulsating Signal into Stationary Reference Frame

For the conventional pulsating signal injection methods, a high frequency fluctuating carrier voltage signal is injected into the estimated synchronous reference frame as shown in Fig. 3.2. This method has simple physical principle. However, since the carrier voltage is injected into the estimated synchronous reference frame, the risk of divergence at the starting stage of sensorless control is the drawback. The conventional rotating signal injection schemes inject a balanced three phase voltage in the stationary reference frame to form a rotating excitation as shown in Fig. 3.7. It has stable performance of carrier signal injection since the carrier voltage is injected into the stationary reference frame. However, the signal demodulation procedure with SRF is relatively complicated to implement, and the two more LPFs will deteriorate the dynamic performance. Differing from the conventional high-frequency carrier signal injection methods, a new strategy injects a pulsating high frequency carrier voltage into α - (or β -) axis of stator stationary reference frame, Fig. 3.18. Since the high-frequency carrier current response is amplitude-modulated as same as pulsating carrier signal injection method, the synchronous detection technique with one step of filtering is employed for signal demodulation.

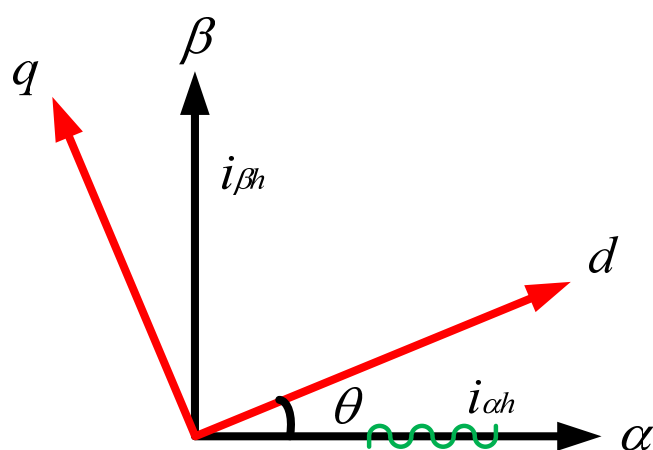


Fig. 3.18. New proposed high frequency injection

3.4.1 New Proposed High Frequency Carrier Signal Injection Method

The new strategy is based on the stationary reference frame with the pulsating high frequency carrier voltage injection, which can be regarded as the superposition of two rotating carrier vectors with opposite rotating direction.

For the new proposed strategy, an α -axis pulsating carrier voltage signal (3.37) which is shown in Fig. 3.19 is injected into stationary reference frame,

$$\begin{bmatrix} u_{\alpha h} \\ u_{\beta h} \end{bmatrix} = U_c \begin{bmatrix} \cos \alpha \\ 0 \end{bmatrix}, \quad \alpha = \omega_c t + \varphi \quad (3.37)$$

Then the Phase-A response current is shown in Fig. 3.20.

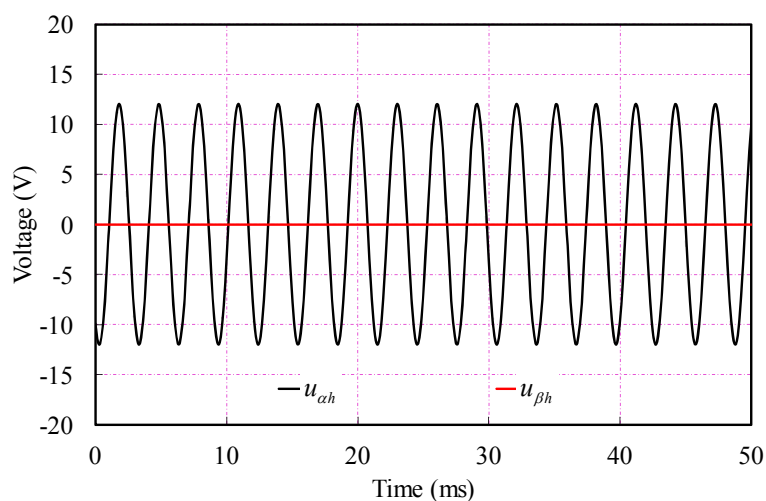


Fig. 3.19. Injected pulsating carrier voltage ($U_c=12V$, $f=330Hz$)

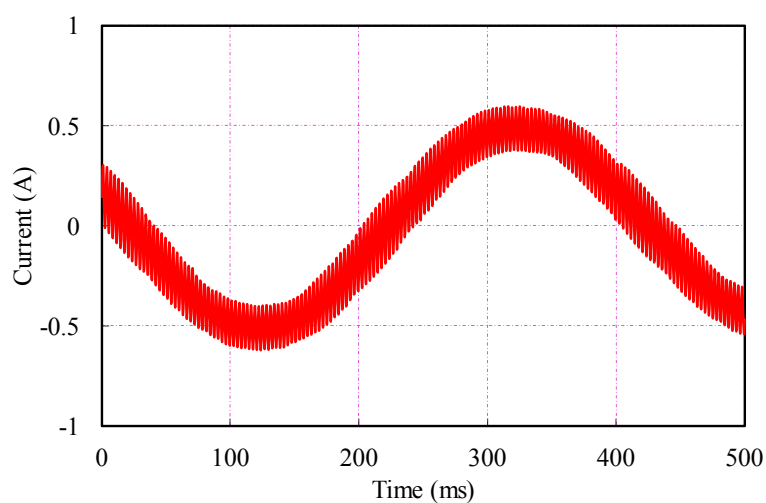


Fig. 3.20. Phase-A current response

The differential of the carrier current in the stationary reference frame can be expressed as

$$p \begin{bmatrix} i_{\alpha h} \\ i_{\beta h} \end{bmatrix} = \begin{bmatrix} \frac{1}{L_p} + \frac{1}{L_n} \cos(2\theta_r + \theta_m) & \frac{1}{L_n} \sin(2\theta_r + \theta_m) \\ \frac{1}{L_n} \sin(2\theta_r + \theta_m) & \frac{1}{L_p} - \frac{1}{L_n} \cos(2\theta_r + \theta_m) \end{bmatrix} \cdot U_c \begin{bmatrix} \cos \alpha \\ 0 \end{bmatrix} \quad (3.38)$$

Then, the resultant carrier current response can be derived as:

$$\begin{bmatrix} i_{\alpha h} \\ i_{\beta h} \end{bmatrix} = \begin{bmatrix} \frac{U_c}{\omega_c L_p} + \frac{U_c}{\omega_c L_n} \cos(2\theta_r + \theta_m) \\ \frac{U_c}{\omega_c L_n} \sin(2\theta_r + \theta_m) \end{bmatrix} \cdot \sin \alpha = \begin{bmatrix} I_p + I_n \cos(2\theta_r + \theta_m) \\ I_n \sin(2\theta_r + \theta_m) \end{bmatrix} \cdot \sin \alpha \quad (3.39)$$

where

$$I_p = \frac{U_c}{\omega_c L_p}, \quad I_n = \frac{U_c}{\omega_c L_n} \quad (3.40)$$

It is clearly shown that the carrier current response is amplitude modulated by the rotor position θ_r and the cross-saturation angle θ_m which is constant at the given load condition. From the response current, the rotor position could be retrieved precisely considering the cross-saturation effect.

In order to demodulate the position dependent amplitude from the carrier current response, the synchronous detection technique [MAD95] [RAC10] which is the same as in pulsating carrier signal injection method, is applied. Both sides of (3.39) are multiplied by $2\sin \alpha$, and then applying the signal to a LPF, the amplitude of the carrier current can be obtained with noise suppression as expressed in (3.41), and the measured carrier current responses and their amplitude in stationary reference frame are shown in Fig. 3.21.

$$\begin{bmatrix} |i_{\alpha h}| \\ |i_{\beta h}| \end{bmatrix} = LPF \left(\begin{bmatrix} i_{\alpha h} \\ i_{\beta h} \end{bmatrix} \cdot 2\sin \alpha \right) = \begin{bmatrix} I_p + I_n \cos(2\theta_r + \theta_m) \\ I_n \sin(2\theta_r + \theta_m) \end{bmatrix} = \begin{bmatrix} I_p \\ 0 \end{bmatrix} + \begin{bmatrix} i_{\alpha h}^{**} \\ i_{\beta h}^{**} \end{bmatrix} \quad (3.41)$$

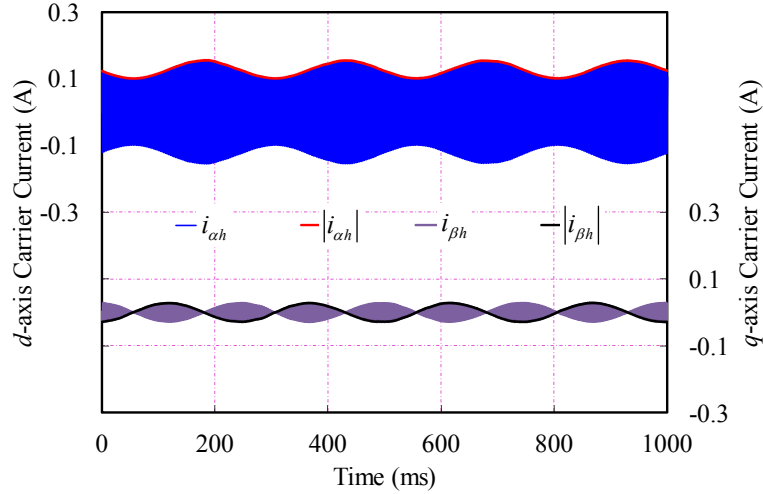


Fig. 3.21. Measured carrier current responses and their amplitudes

With the aid of encoder to provide the actual rotor position, the cross-saturation angle and the amplitude of response current with rotor position of the Motor I are shown in Fig. 3.22(a). The amplitude loci of carrier current response without and with full load are shown in Fig. 3.22(b), where the radius of the locus, I_n , has a significant change due to the variation of inductances versus fundamental excitation, whilst the change of the DC offset, I_p , is much less since it is more robust to the inductance variation.

If I_p and θ_m could be pre-detected and compensated, then

$$\begin{bmatrix} i_{\alpha h}^* \\ i_{\beta h}^* \end{bmatrix} = \begin{bmatrix} I_n \cos(2\theta_r) \\ I_n \sin(2\theta_r) \end{bmatrix} \quad (3.42)$$

From (3.42), the rotor position could be derived easily by proper position estimator.

If a β -axis pulsating carrier voltage signal (3.43) is injected into in the stationary reference frame,

$$\begin{bmatrix} u_{\alpha h} \\ u_{\beta h} \end{bmatrix} = U_c \begin{bmatrix} 0 \\ \cos \alpha \end{bmatrix}, \quad \alpha = \omega_c t + \varphi \quad (3.43)$$

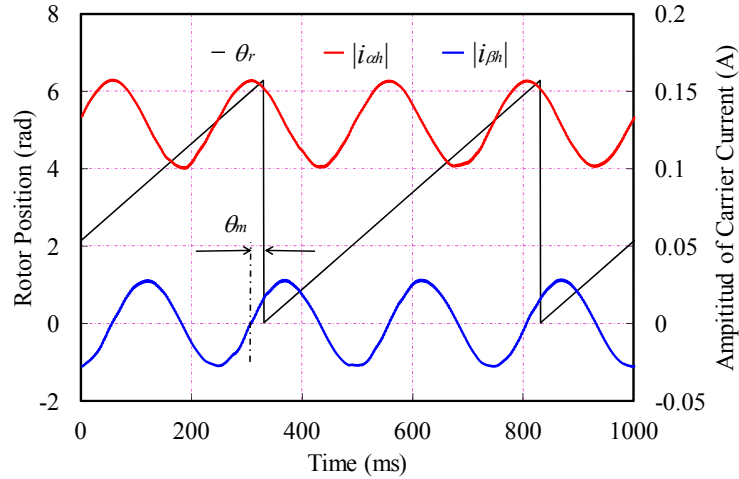
then, the differential of the carrier current in the stationary reference frame can be expressed as

$$p \begin{bmatrix} i_{\alpha h} \\ i_{\beta h} \end{bmatrix} = \begin{bmatrix} \frac{1}{L_p} + \frac{1}{L_n} \cos(2\theta_r + \theta_m) & \frac{1}{L_n} \sin(2\theta_r + \theta_m) \\ \frac{1}{L_n} \sin(2\theta_r + \theta_m) & \frac{1}{L_p} - \frac{1}{L_n} \cos(2\theta_r + \theta_m) \end{bmatrix} \cdot U_c \begin{bmatrix} 0 \\ \cos \alpha \end{bmatrix} \quad (3.44)$$

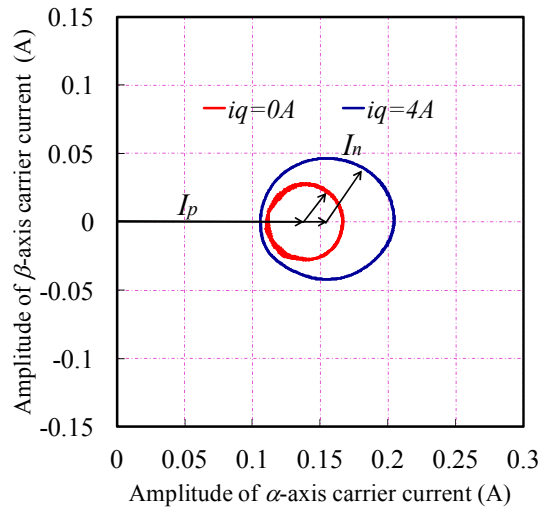
Then, the resultant carrier current response can be derived as:

$$\begin{bmatrix} i_{\alpha h} \\ i_{\beta h} \end{bmatrix} = \begin{bmatrix} I_n \sin(2\theta_r + \theta_m) \\ I_p - I_n \cos(2\theta_r + \theta_m) \end{bmatrix} \cdot \sin \alpha = \left(\begin{bmatrix} 0 \\ I_p \end{bmatrix} + \begin{bmatrix} i_{\beta h}^{**} \\ -i_{\alpha h}^{**} \end{bmatrix} \right) \cdot \sin \alpha \quad (3.45)$$

Similar to the α -axis injection, the carrier current response is also amplitude-modulated by the rotor position and the demodulation process will be the same. However, I_p locates at β -axis current, whilst the phase sequence of $i_{\alpha h}^{**}$ and $i_{\beta h}^{**}$ is different. Hence, the I_p compensation and position estimation will be slightly different.



(a) Amplitude of response carrier current compared with actual rotor position.



(b) Current loci with no load and full load.

Fig. 3.22. Amplitude of response carrier current

3.4.2 I_p Pre-Detection and Compensation

As described above, e.g. with α -axis pulsating injection, I_p should be subtracted from $|i_{\alpha h}|$ to get $i_{\alpha h}^{**}$ in (3.41) for tracking the rotor position.

Based on (3.10) and (3.17), I_p could be expressed as

$$I_p = \frac{U_c}{\omega_c \cdot L_p} = \frac{U_c \cdot L_{sa}}{\omega_c \cdot (L_{dh}L_{qh} - L_{dqh}^2)} \quad (3.46)$$

As shown in (3.46) and Fig. 3.1, I_p is machine parameter dependent and proportional to the ratio of U_c/ω_c . Since the parameter value of L_p is almost not affected by i_q , on the condition of fixed U_c and ω_c , the value of I_p can be eliminated by a look-up table designed based on the pre-measured inductances theoretically. The measured I_p against different fundamental current in sensored mode is shown in Fig. 3.23, from which I_p could be treated as constant at different q -axis current for simplicity.

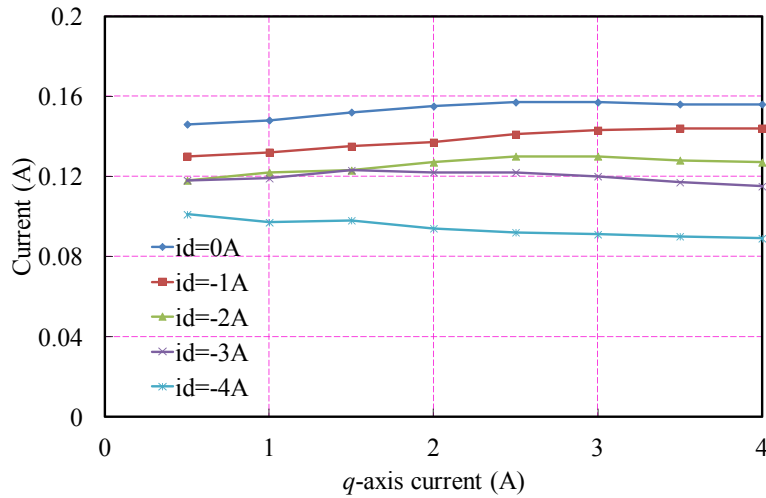


Fig. 3.23. Measured I_p versus different fundamental current.

For general applications at zero and very low speed, i_d is usually set as negative and kept the same. Hence, it is possible to derive I_p from the look-up table under that condition, and apply it for starting.

However, when the rotor speed is higher than a certain value, e.g. 10rpm in this thesis, various i_d may be applied. Due to the variation of the self- and mutual-inductances at different i_d , it is impractical to calculate every I_p at all different current conditions.

However, $i_{\alpha h}^{**}$ in (3.41) will appear as sinusoidal signal where I_p is the constant DC offset. Therefore, if $|i_{\alpha h}|$ signal goes through a LPF, the output should be I_p . To effectively filter the contained AC components which are 1Hz minimally without phase lag, the cut-off frequency should be online adjusted with the feedback rotor speed, where the maximum cut-off frequency is 20% of the AC component frequency.

Since the derived I_p by LPF will maintain the same value with fixed i_d , the value derived at the starting condition could be used, stored into controller memory and applied as I_p during starting from zero to very low speed. The obtaining procedure is machine parameter free, which makes it superior to calculation from pre-tested data.

After deriving I_p , we can have

$$\begin{bmatrix} i_{\alpha h}^{**} \\ i_{\beta h}^{**} \end{bmatrix} = \begin{bmatrix} I_n \cos(2\theta_r + \theta_m) \\ I_n \sin(2\theta_r + \theta_m) \end{bmatrix} \quad (3.47)$$

As shown in (3.47), the phase angle of $i_{\alpha\beta h}^{**}$ is modulated by rotor position θ_r and cross-saturation angle θ_m . Hence, rotor position can be derived with the load-dependent position estimation error ($-\theta_m/2$) due to cross-saturation effect.

3.4.3 Cross-saturation Effect Compensation

Due to the nonlinear behavior of cross-saturation effect, the compensation methods depend considerably on the machine parameters, which can be acquired from finite element calculation, off-line self-commissioning, or on-line parameter identification. A relatively straightforward method is used in [ZHU07] [DEK09]. A self-commissioning procedure was presented in [TES00] to obtain the information of harmonics due to cross-saturation, which can be used for on-line compensation. A more adaptive compensation method based on parameter identification is developed in [REI08], although it is more computationally intensive. Alternatively, neural network structure is used for cross-saturation compensation [GAR07]. In this thesis, the compensation of cross-saturation effect follows the method in [ZHU07] [DEK09], where the angular error is obtained from the experimental measurement in sensed

operation, and directly used to compensate the estimated position error on-line.

The error in the estimated rotor position can be compensated by employing (3.10) with pre-tested data as shown in Fig. 3.1 using the experimental results. However, from both the cross-saturation angles which are calculated from machine parameters and measured in sensed operation as shown in Fig. 3.24, it can be seen that the cross-saturation angle is approximately proportional to the q -axis current, i.e. $\theta_m \approx K_r i_q$. Thus, by applying this compensation factor K_r , θ_m can be predicted with measured q -axis current, which significantly simplifies the implementation of error compensation scheme. The predicted θ_m by the feedback i_q is also shown in Fig. 3.24. Then, after compensation of the cross-saturation effect, equation (3.42) could be derived, and the rotor position could be retrieved by applying rotor position estimator.

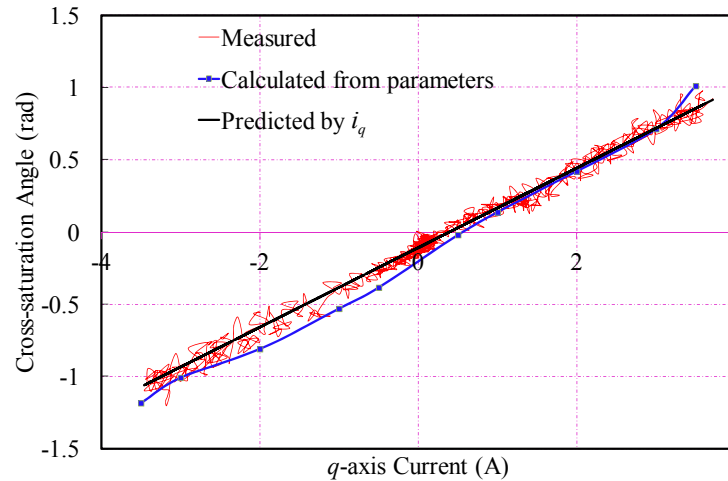


Fig. 3.24. Comparison of cross-saturation angles measured in sensed operation, calculated from parameters, and predicted based on i_q

3.4.4 Rotor Position Estimator

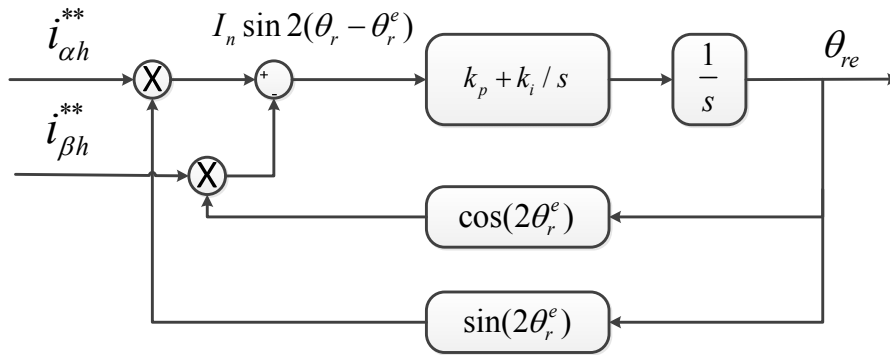
To obtain the rotor position from (3.42), the Two-Phase-Type Phase-Locked Loop (TP-PLL) is applied. TP-PLL was first proposed by Takashi Emura in [EMU00] and has been widely applied in the accurate position interpolation for servo controllers and modern resolver to digital (RD) conversion. The theoretical principle can be simply described in Fig. 3.25(a) and has the similar structure of simplified extended Kalman-filter (EKF) as will be introduced in Section 6.2. According to the diagram, the

closed loop transfer function between the actual and estimated rotor positions can be expressed as

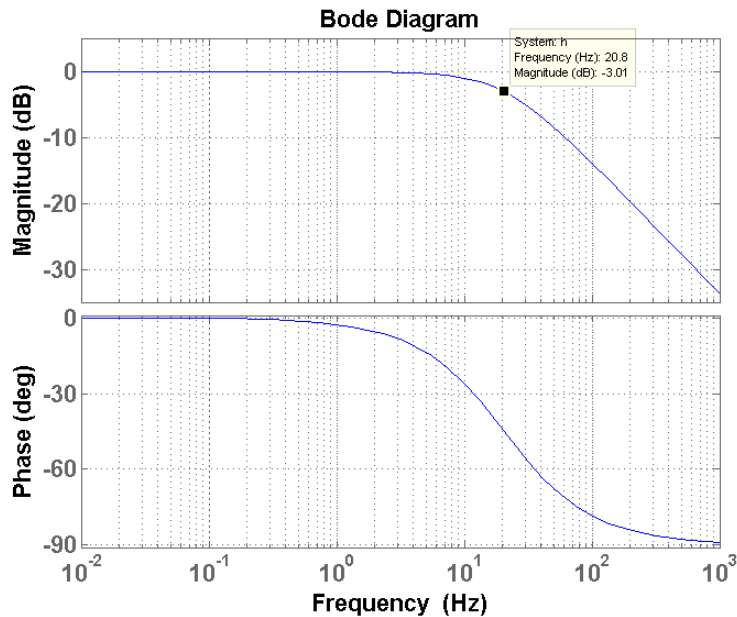
$$\frac{\theta_r^e}{\theta_r} = \frac{2I_n k_p \cdot s + 2I_n k_i}{s^2 + 2I_n k_p \cdot s + 2I_n k_i} \quad (3.48)$$

Based on (3.10) and (3.17), I_n is load-dependent. Hence, k_p and k_i of PI controller should be on-line varied with I_n to maintain the constant bandwidth. For simplicity in practical implementation, k_p and k_i could be selected based on the typical value of I_n at no load condition.

For the prototype system, the typical value of I_n is $130mA$, and the parameters of TP-PLL are $k_p=500$ and $k_i=1000$. The Bode plot of the position estimator are shown in Fig. 3.25(b), it can be seen that the loop bandwidth is around 20.8Hz.



(a) Block diagram of TP-PLL



(b) Bode chart of the TP-PLL

Fig. 3.25. Block diagram and bode chart of position estimator.

3.4.5 Magnetic Polarity Detection

Since the machine saliency varies periodically as a second spatial harmonic without magnetic polarity information, the estimated rotor position has an angle ambiguity of π . If the estimated rotor direction which should align at the north magnetic pole position, is aligned at the south magnetic pole position and regarded as the rotor position, the sign of output torque will be changed and the system will be unstable. Therefore, it is important to identify the magnetic polarity before the drive is put into operation. The initial rotor direction can be estimated from carrier current response and can be used to calculate the initial rotor position. Once the polarity information before start-up is obtained, it can be latched. Generally, the polarity could be detected from saturation effect of the air gap flux. Short pulses injection, secondary harmonics based, and response high frequency current against different fundamental current methods have been proposed.

3.4.5.1 Conventional magnetic polarity detection methods

Method A. Short pulses injection method

Magnetic polarity detection can be performed by injecting the specified transient pulse signal along the estimated d -axis, which gives rise to stator iron saturation. Different transient signals can be utilized, such as AC current [NOG98], dual short voltage pulses [AIH99] [HOL08] [WAN12a] and so on. Among them, dual voltage pulses injection proposed in [AIH99] is the simplest. One of the pulses aligns with the positive direction of the magnet flux, thus increasing the magnetization of the stator iron and driving the d -axis incremental inductance into lower value. The other pulse, aligning with the negative direction of the magnet flux, tends to de-saturate the stator iron and leads to increasing d -axis incremental inductance. The injected short voltage pulses have identical volt-second values (identical $\Delta\psi$), hence the current pulse having higher magnitude indicates the positive direction of d -axis, as shown in Fig. 3.26.

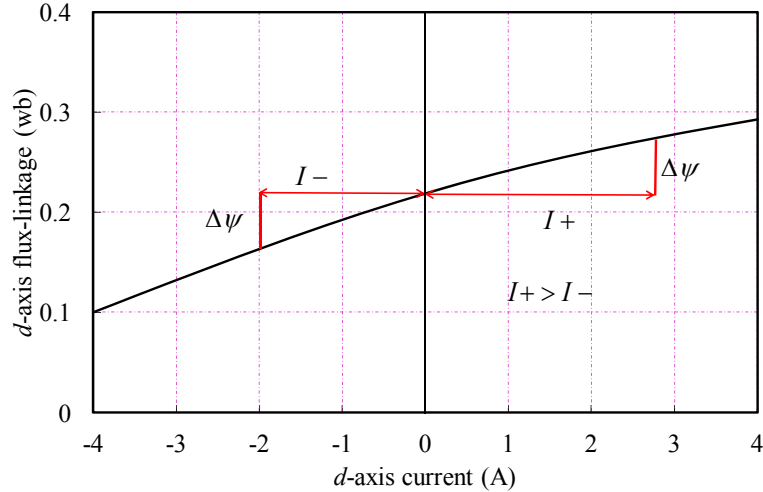


Fig. 3.26. Magnetic polarity detection using dual voltage pulses injection [GON13].

Fig. 3.27 shows the magnetic polarity detection for the Machine I with dual voltage pulses method. If initially estimated rotor direction from machine saliency property is equal to the real rotor position ($\Delta\theta=0\text{rad}$), the applied positive d -axis voltage pulse would result in higher d -axis current pulse, as shown in Fig. 3.27(a). On the other hand, lower amplitude current response to the positive d -axis voltage pulse suggests that the estimated rotor direction has an angle shift of π with respect to the real rotor position information, as shown in Fig. 3.27(b).

Although short pulses injection method has robust and reliable identification performance due to good SNR, the magnetic polarity identification should be performed as an independent process, which means that the rotor position estimation is stopped when the magnetic polarity identification is active [HOL08]. If the rotor is free running due to coupled mechanical load, it would fail to do so. For the free-running rotor application, the rotor position is always changing, thus applying short voltage pulses along the direction of the magnet flux could not be guaranteed.

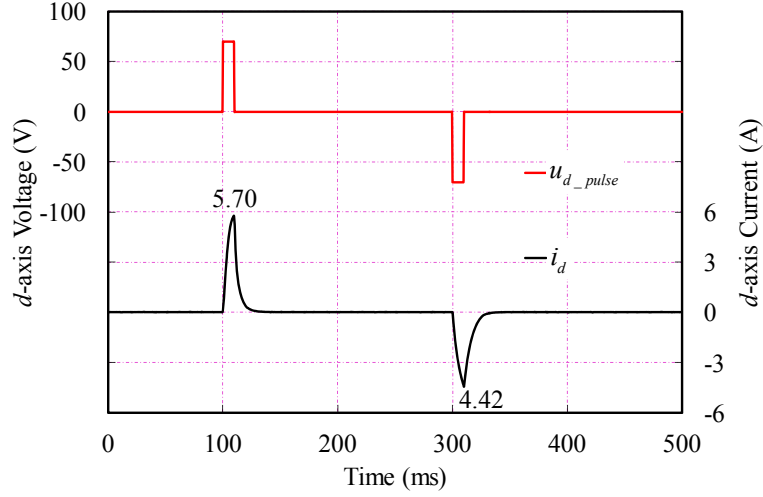
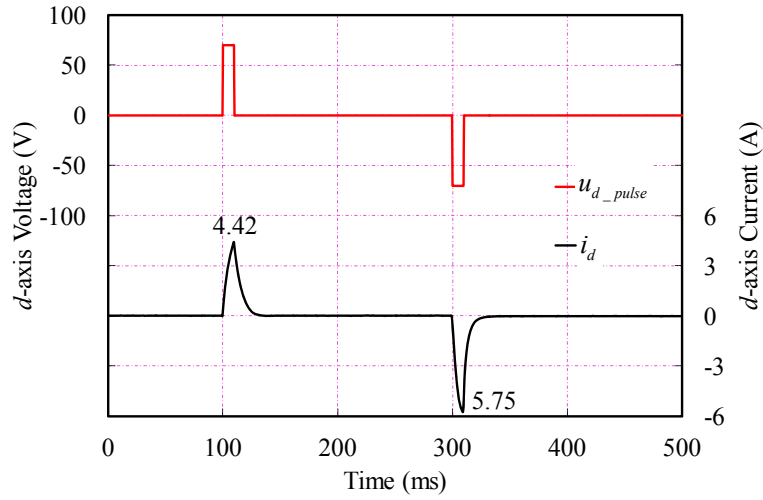
(a) Magnetic polarity detection ($\Delta\theta=0$ rad).(b) Magnetic polarity detection ($\Delta\theta=\pi$ rad).

Fig. 3.27. Magnetic polarity detection with dual voltage pulses.

Method B. Secondary harmonics based method

Without consideration of magnetic saturation effect, magnetic polarity information cannot be extracted from the carrier current response; however, the actual machine is subject to saturation effect, and the carrier current response should contain the related information. When the machine saturation property is considered in the machine model, the resultant carrier current response to the d -axis pulsating carrier signal injection can be simplified as [JEO05],

$$\begin{bmatrix} i_{dh}^e \\ i_{qh}^e \end{bmatrix} = \begin{bmatrix} I_p + I_n \cos(2\Delta\theta) \\ I_n \sin(2\Delta\theta) \end{bmatrix} \cdot \sin \alpha + \begin{bmatrix} I_{sat} \cos^2 \Delta\theta \cos \Delta\theta \\ I_{sat} \cos^2 \Delta\theta \sin \Delta\theta \end{bmatrix} \cdot \sin^2 \alpha \quad (3.49)$$

$$I_{sat} = \frac{U_c^2}{2\omega_c^2} \frac{d^2 i_d}{d\psi_d^2} \psi_m > 0 \quad (3.50)$$

where i_d is the d -axis current, ψ_d is the d -axis flux linkage, ψ_m is the permanent magnet flux linkage without stator current. The additional term with $\sin^2\alpha$ in (3.50), resulting from the interaction between the injected carrier voltage and the saturation saliency, is referred to as the secondary carrier current component. It can be used to identify the magnetic polarity information [HA03] [KIM04] [JEO05] [HAR05] [RAC08a]. From (3.50), the signals corresponding to magnetic polarity detection can be calculated as follows,

$$\begin{cases} I_{d \sin 2\alpha} = LPF(i_{dh}^e \cdot \sin 2\alpha) = 0 \\ I_{d \cos 2\alpha} = LPF(i_{dh}^e \cdot \cos 2\alpha) = -\frac{I_{sat} \cos^2 \Delta\theta \cos \Delta\theta}{4} \end{cases} \quad (3.51)$$

Obviously, the magnetic polarity information can be detected from the sign of $I_{d \cos 2\alpha}$. In this way, carrier current component due to primary spatial saliency ($\sin\alpha$) is used to estimate the rotor direction information, while the additional carrier current component due to magnetic saturation ($\sin^2\alpha$) is used to detect the magnetic polarity information. Although this kind of method has the advantage of quick convergence [HAR05], the major problem is that the magnitude of secondary carrier current component for magnetic polarity detection is very low, leading to lower SNR for the magnetic polarity identification. The magnetic polarity detection fails to be implemented on Machine I due the too low SNR.

Method C. Integrated with pulsating injection considering magnetic saturation

For a conventional d -axis pulsating carrier signal injection based sensorless method, the amplitude of d -axis carrier current has not been used in the control algorithm. However, it will be proven to be very useful in magnetic polarity detection [GON13]. Providing the estimated rotor direction is sufficiently correct, the amplitude of d -axis carrier current in the estimated synchronous reference frame can be derived as

$$\left| i_{dh}^e \right| = I_p + I_n \cos(2\Delta\theta) \approx I_p + I_n = \frac{U_c}{\omega_c} \cdot \frac{1}{L_{dh}} \quad (3.52)$$

For given injected carrier voltage signal (U_c/ω_c), the above equation indicates that the amplitude of d -axis carrier current is only determined by L_{dh} . Due to magnetic saturation, L_{dh} is significantly depended on the d -axis fundamental current, as shown in Fig. 3.28 for the prototype machine.

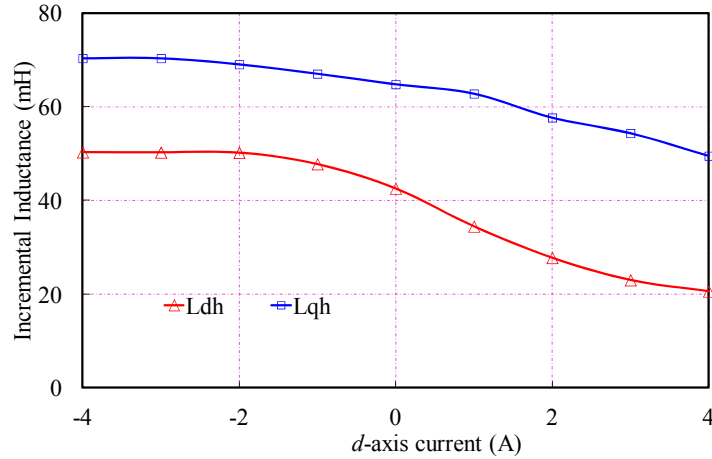


Fig. 3.28. Incremental self-inductance at different fundamental excitations.

Consequently, it is possible to identify the magnetic polarity from the variation of $\left| i_{dh}^e \right|$ against d -axis fundamental current. The initial $\left| i_{dh}^e \right|$ without fundamental d -axis current is stored as $I_{dh(k)}$. A given d -axis fundamental current is applied and $\left| i_{dh}^e \right|$ under this load condition is stored as $I_{dh(k+1)}$. And then the machine is returned back to initial operating state. Finally, $\left| i_{dh}^e \right|$ at different load condition is compared. The increase of amplitude ($I_{dh(k+1)} > I_{dh(k)}$) indicates the estimated rotor direction is equal to the correct rotor position, Fig. 3.29(a), otherwise, the phase shift of π should be added, Fig. 3.29(b).

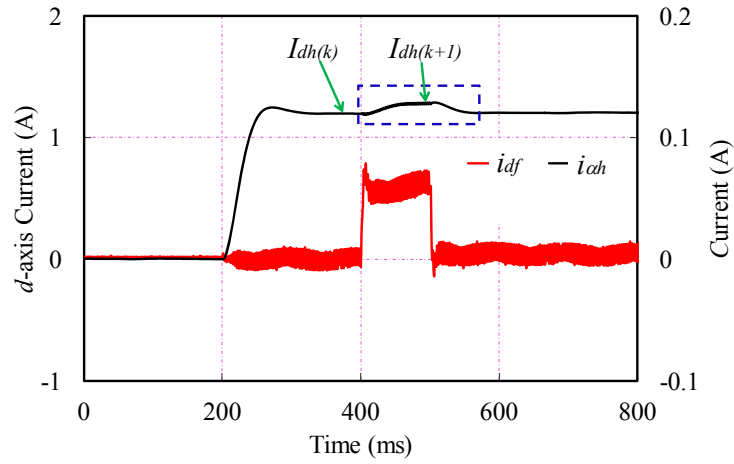
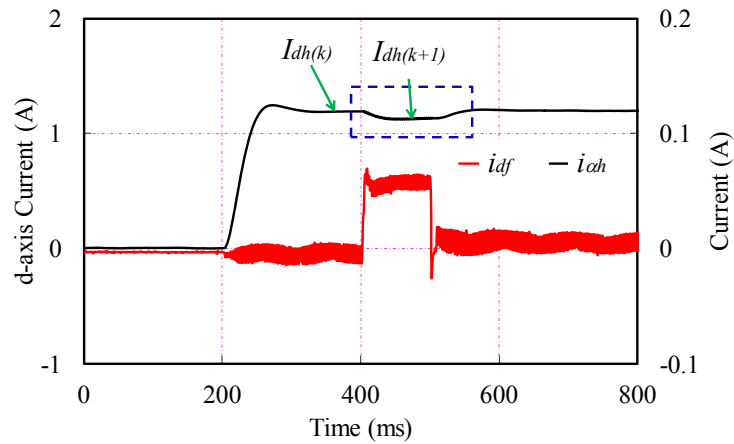
(a) Magnetic polarity detection ($\Delta\theta=0$ rad).(b) Magnetic polarity detection ($\Delta\theta=\pi$ rad).

Fig. 3.29. Magnetic polarity detection with fundamental current

If the rotor is free running or working as a generator, the estimated rotor position is updated real time, thus the fundamental current is guaranteed to be applied along d -axis. Hence, unlike the short pulses injection method, the proposed scheme never stops the sensorless position estimation due to the integration with conventional pulsating carrier signal injection based sensorless algorithm. This method is also applicable to rotating carrier signal injection based sensorless technique. The difference is that the comparable parameter turns out to be the amplitude of the positive sequence carrier current, instead of the amplitude of the d -axis carrier current for pulsating injection.

3.4.5.2 Polarity detection for stationary frame pulsating injection

Detailed experimental comparison among these three conventional polarity detection methods has been made in [GONG13]. Method A for polarity detection cannot be employed when the motor is free-running or working as a generator, whilst Method B has too low SNR which makes the robustness the lowest among these methods. Although Method C has the best performance, it only can be adopted with conventional high frequency injection strategies. Hence, in this new proposed strategy with injection of pulsating carrier signal into stationary reference frame, alternative method for polarity detection with high robustness should be developed.

The phase angle of $i_{\alpha\beta h}^{**}$ in (3.41) is used to extract the rotor direction information, while I_p has not been used in control algorithm and should be eliminated. However, in this section it will be very useful in magnetic polarity detection. Based on (3.10) and (3.17), and considering the mutual inductance is sufficiently small, i.e. $L_{dqh}^2 \ll L_{dh}L_{qh}$, equation (3.41) could be simplified as,

$$\begin{aligned} |i_{\alpha h}| &= I_p + i_{\alpha h}^{**} = I_p + I_n \cos(2\theta + \theta_m) \\ &= \frac{U_c}{2\omega_c L_{dh}} + \frac{U_c}{2\omega_c L_{qh}} + \left(\frac{U_c}{2\omega_c L_{qh}} - \frac{U_c}{2\omega_c L_{dh}} \right) \cos(2\theta + \theta_m) \end{aligned} \quad (3.53)$$

For a given injected carrier voltage signal (U_c/ω_c), equation (3.53) indicates that the α -axis amplitude of response current is determined by L_{dh} and L_{qh} . Due to magnetic saturation, L_{dh} is significantly dependant on d -axis fundamental current, at the same time, L_{qh} has the same trend but less significant as shown in Fig. 3.28 for Motor I. Consequently, it is possible to identify the magnetic polarity from the variation of $|i_{\alpha h}|$ against d -axis fundamental current which is similarly as [GON13] for pulsating carrier voltage signal injection based method.

With the aid of accurate rotor position information from the encoder, $|i_{\alpha h}|$ current can be measured at different fundamental excitations, as shown in Fig. 3.30. From the experimental results, it can be concluded that the magnetic polarity can be reliably detected based on the comparison of $|i_{\alpha h}|$ at different d -axis fundamental current levels.

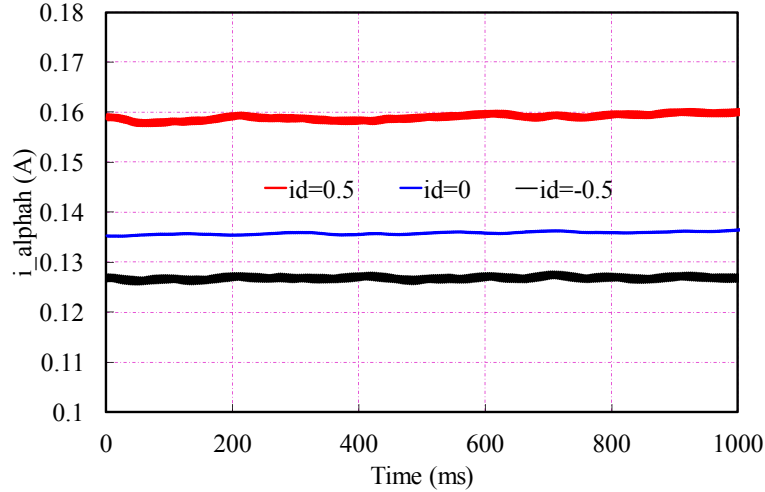


Fig. 3.30. $|i_{oh}|$ at different fundamental excitations.

The procedure is described as follows:

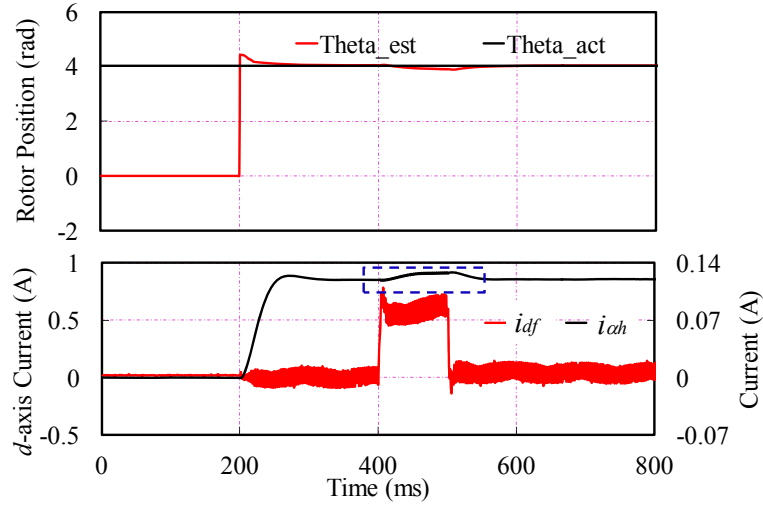
Step 1: Before the motor is initially started, the rotor direction information can be obtained from the proposed sensorless strategy without fundamental excitation ($i_d^e = i_q^e = 0A$), meanwhile, the value of $|i_{oh}|$ at this condition is recorded. The estimated rotor direction either indicates the correct one, or shifted by π .

Step 2: Referring to the estimated rotor direction, a given d -axis fundamental current reference is applied to the machine. The fundamental current reference of ($i_d^e = 0.5A$, $i_q^e = 0A$) is selected for the prototype machine. At the same time, the value of $|i_{oh}|$ at this load condition is also stored into processor memory.

Step 3: After that, the fundamental current reference is set back to ($i_d^e = i_q^e = 0A$).

Finally, the values of $|i_{oh}|$ at different load conditions (with and without fundamental current) are compared. The amplitude increase indicates the estimated rotor direction is at the correct, otherwise, the phase shift of π should be added.

The experimental results shown in Fig. 3.31 validate the effectiveness of the magnetic polarity detection method at zero speed. By the magnetic saturation effect of d -axis fundamental current, the magnitude of $|i_{oh}|$ in (3.53) will change as shown in Fig. 3.31(a) and (b). Compared the magnitude before and after applying the fundamental current, the increase of $|i_{oh}|$ suggests that the estimated rotor position is correct, Fig. 3.31(a), otherwise, a phase shift of π is added, Fig. 3.31(b).



(a) Rotor direction without ambiguity

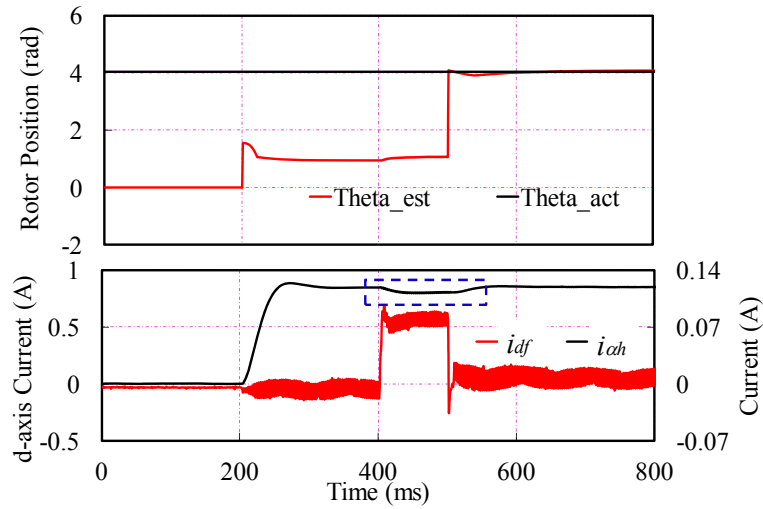
(b) Rotor direction with ambiguity of π

Fig. 3.31. Detection of magnetic polarity at zero speed.

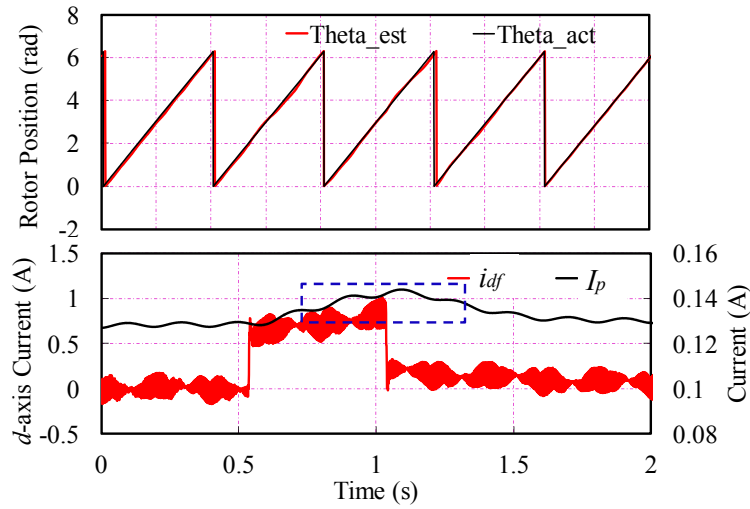
(Θ_{est} : Estimated rotor position, Θ_{act} : Actual rotor position)

However, if the motor is free-running or working as a generator, before the whole control system enables, the rotor speed is already higher than certain value. Then, i_{ch}^{**} in (3.53) will appear as sinusoidal signal, which leads the method described above fail to work. If $|i_{ch}|$ signal goes through a LPF, the output should be I_p . Considering $L_{dq}^2 \ll L_{dh}L_{qh}$, we can get

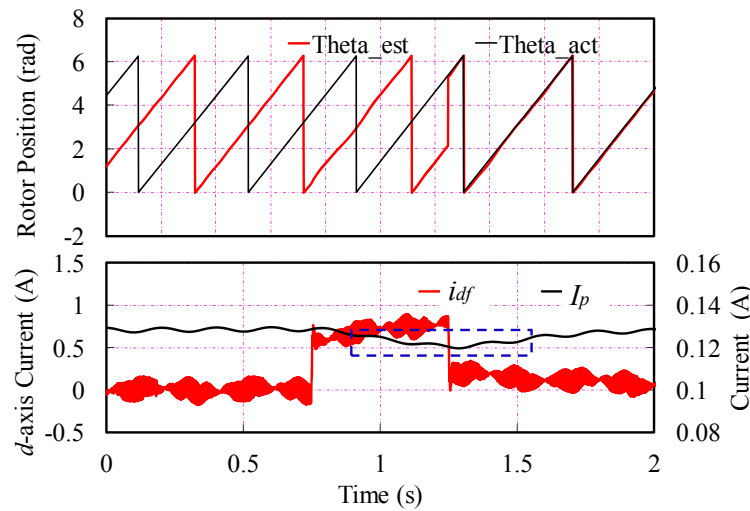
$$I_p = \frac{U_c}{2\omega_c L_{dh}} + \frac{U_c}{2\omega_c L_{qh}} \quad (3.54)$$

Similarly, for a given injected carrier voltage signal (U_c/ω_c), I_p is determined by

L_{dh} and L_{qh} . Consequently, it is possible to identify the magnetic polarity from I_p instead of $|i_{\alpha h}|$ by applying the same comparison and detection method. However, applying the LPF may slow the detection procedure but the reliability is not affected. The experimental results shown in Fig. 3.32 validate the effectiveness of the magnetic polarity detection method when the rotor speed is already higher than certain value. By the magnetic saturation effect of d -axis fundamental current, the value of I_p in (3.54) will change as shown in Fig. 3.32(a) and (b). Compared the magnitude before and after applying the fundamental current, the increase of I_p suggests that the estimated rotor position is correct, Fig. 3.32(a), otherwise, a phase shift of π is added, Fig. 3.32(b).



(a) Rotor direction without ambiguity



(b) Rotor direction with ambiguity of π

Fig. 3.32. Detection of magnetic polarity at certain speed.

(Θ_{est} : Estimated rotor position, Θ_{act} : Actual rotor position)

Based on the d -axis magnetic saturation effect which is similar to Method C, the proposed magnetic polarity identification scheme can be easily integrated with the new proposed strategy with injection of pulsating carrier voltage into stationary reference frame. Hence unlike the short pulses injection Method A, the proposed scheme never stops the sensorless position estimation even while free-running. Furthermore, the proposed method has the advantage of robust detection due to higher SNR and less computational intensity compared with secondary harmonics based Method B. Different kinds of magnetic polarity detection methods are compared in Table 3.1.

TABLE 3.1
COMPARISON OF MAGNETIC POLARITY DETECTION

	Method A	Method B	Method C	Proposed
Convergence speed	High	Low	Medium	Medium
Conceptual simplicity	High	Low	High	High
Computational burden	Low	High	Low	Low
Reliability	High	Low	High	High
SNR	High	Low	High	High
Integration availability	Low	Medium	High	High

3.4.6 Steady-state and Dynamic Performance

Several experiments have been performed to validate the new proposed high frequency sinusoidal pulsating signal injection method based on the stationary reference frame. The overall control scheme including the new proposed strategy is shown in Fig. 3.33 which has been implemented on a dSPACE platform. The Test Rig I with Motor I is applied for test. The DC bus voltage is 70V, and the magnitude of injected carrier voltage is set as 12V. In general, the frequency of carrier signal is typically between 250-850Hz since the operating speed is only within the low and zero speed range [JAN95] [DEG98] [JAN03]. Here the maximum speed for sensorless control based on high-frequency carrier signal injection is limited within 50rpm which is equivalent as 2.5Hz of the fundamental current. Hence, the carrier frequency is selected as 330Hz which is sufficiently larger than 2.5Hz.

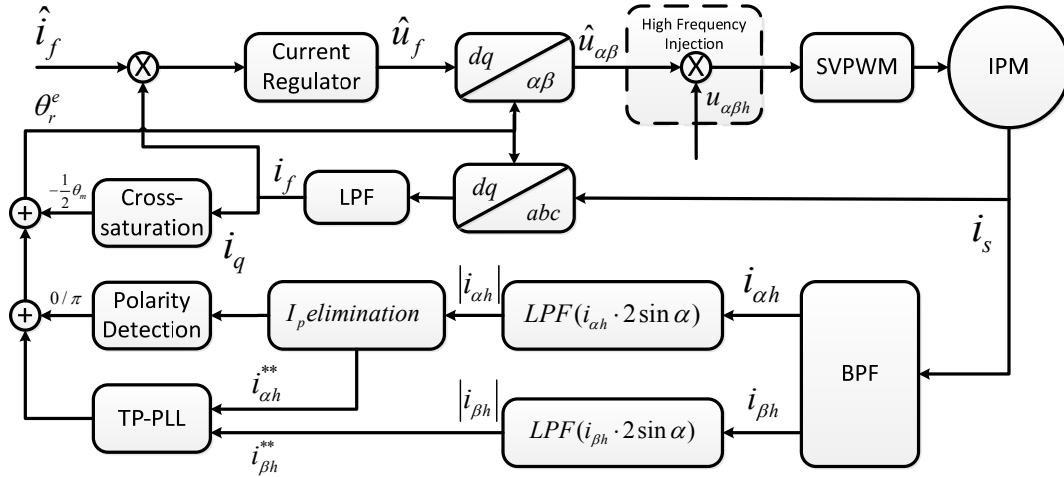


Fig. 3.33. Block diagram of overall control system.

With the proposed strategy, the amplitude of the carrier current response before and after I_p elimination, the estimated rotor position before cross-saturation effect compensation compared with the actual value from encoder are shown in Fig. 3.34. It could be seen that, without cross-saturation effect compensation, there is a significant error between estimated and actual rotor position. Based on the predicted cross-saturation angle in Fig. 3.24, the estimated rotor positions before and after compensation under steady-state at 50rpm with about 1A q -axis current are shown in Fig. 3.35(a), and Fig. 3.35(b) shows the dynamic performance when rotor speed changes from -50rpm to 50rpm and then back to -50rpm. It can be found that there are significant errors before compensation, whilst after compensation, the estimated rotor positions can match the actual rotor position well and the errors are close to zero.

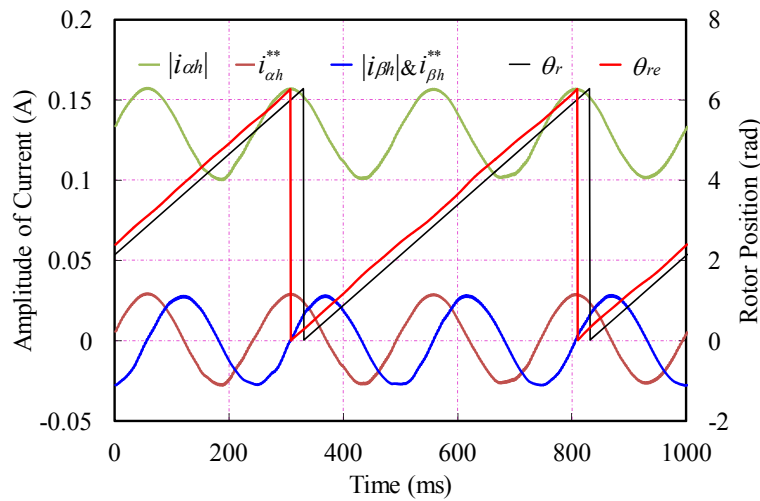
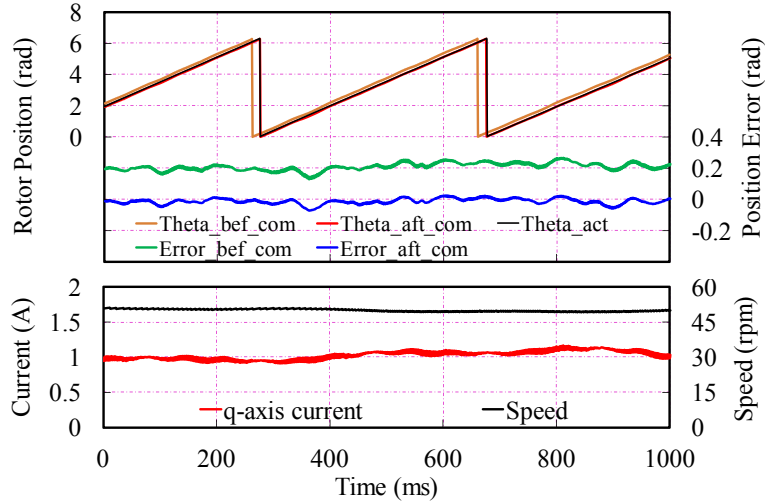
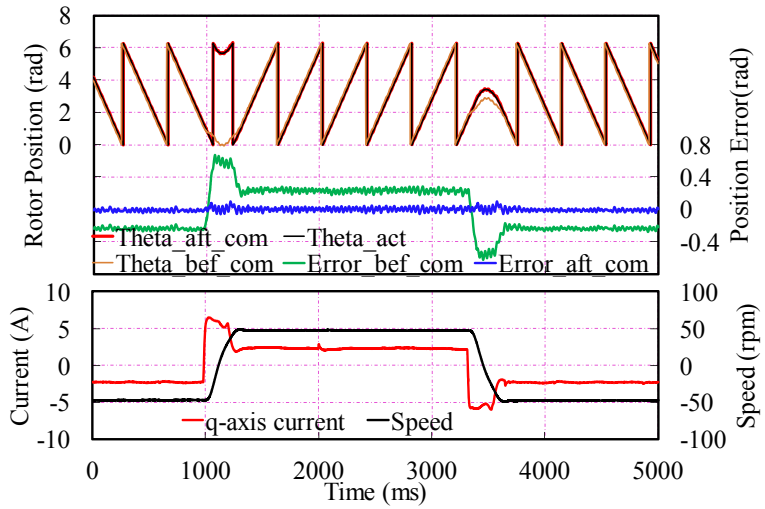


Fig. 3.34. Related signals of the proposed HF sensorless injection method.



(a) Steady-state



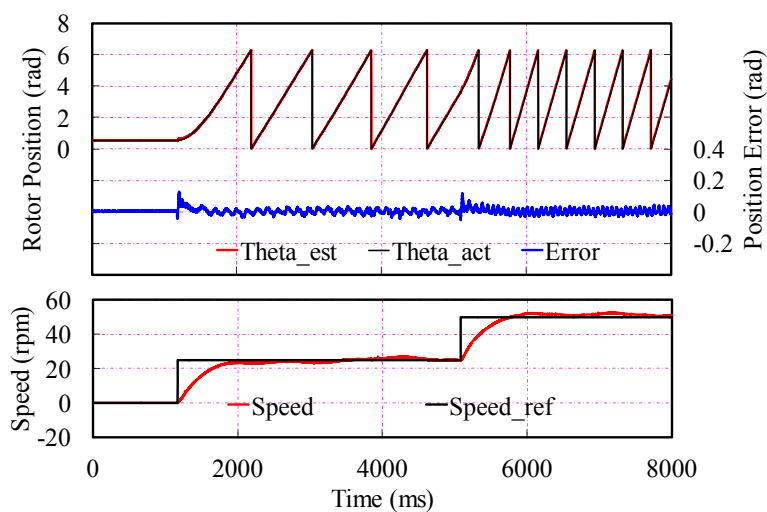
(b) Dynamic

Fig. 3.35. Cross-saturation effect compensation.

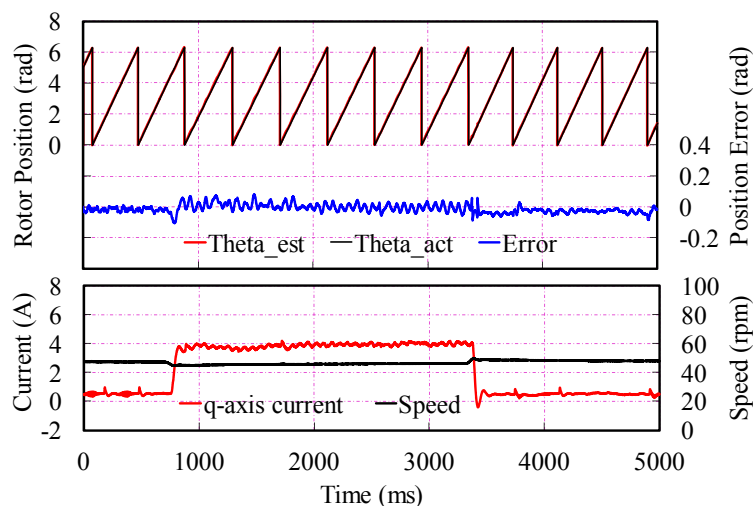
(*Theta_aft_com*: Estimated rotor position after cross saturation compensation,
Theta_bef_com: Estimated rotor position before cross saturation compensation,
Error_aft_com: Estimation error after cross saturation compensation,
Theta_bef_com: Estimation error before cross saturation compensation,
Theta_act: Actual rotor position)

The dynamic performance test is carried out when the rotor mechanical initial speed is zero and step change to 25rpm and then 50rpm which is the same as in Fig. 3.16, and the estimated and actual rotor positions and the estimation error are shown in Fig. 3.36(a). Compared with the dynamic performances of pulsating signal injection, Fig. 3.17(a), and rotating signal injection, Fig. 3.17(b), it can be conclude that, the

new proposed stationary pulsating signal injection strategy has the similar dynamic performance as pulsating signal injection one, and better performance than rotating signal injection strategy. The dynamic performance under the step load condition where the q -axis current step change from 0.5A to full load which is 4A and then back to 0.5A at 50rpm is shown in Fig. 3.36 (b). From the experimental results, it can be concluded that the new proposed stationary pulsating signal injection strategy has the outstanding dynamic performance against different speed and load condition.



(a) Dynamic performance of step speed



(b) Dynamic performance of step load

Fig. 3.36. Dynamic performance of the new proposed strategy.

(Θ_{est} : Estimated rotor position, Θ_{act} : Actual rotor position, $Error$: Rotor Position estimation error)

3.4.7 Comparison of Carrier Signal Injection based Sensorless Controls

Controls

Although a similar principle is exploited to estimate the rotor position information for conventional pulsating and rotating carrier signal injection, and the new proposed strategy, they have different characteristics due to different carrier signal injection and demodulation processes. The comparative results are shown in Table 3.2.

TABLE 3.2

COMPARISON OF CARRIER SIGNAL INJECTION BASED SENSORLESS CONTROLS

	Pulsating	Rotating	Proposed
Signal injection			
Reference frame	Estimated synchronous	Stationary	Stationary
Carrier voltage injection	Pulsating carrier voltage	Rotating carrier voltage	Pulsating carrier voltage
Carrier current response	Amplitude-modulated	Phase-modulated	Amplitude-modulated
Torque ripple	Small	Large	Medium
Cross-saturation angle	$-\theta_m/2$	$-\theta_m/2$	$-\theta_m/2$
Stability of signal injection	Medium	Good	Good
Signal demodulation	Simple	Complex	Simple
Dynamic performance	Good	Medium	Good

3.5 Conclusion

After detailed discussion of commonly used conventional high frequency carrier signal injection based sensorless control techniques, i.e. pulsating voltage into estimated synchronous rotating reference frame and rotating voltage into stationary reference frame, a new strategy with injection of a pulsating sinusoidal waveform high frequency carrier voltage into α - (or β -) axis of stator stationary reference frame is proposed. Then the rotor position information can be retrieved from carrier current response which is amplitude-modulated by rotor position. Considering the cross-saturation effect compensation, employing the TP-PLL based rotor position estimator, the rotor position can be estimated however with ambiguity of π . Then, by the magnetic saturation effect of d -axis fundamental current, the change of the response current magnitude can be used to detect the magnetic polarity.

The new strategy has stable performance of signal injection as rotating carrier signal injection method, and the rotor position information estimation from the amplitude-modulated carrier current response is as simple as pulsating carrier signal injection method. However, to eliminate I_p and cross-saturation effect which are parameter-dependant, look-up table and LPF are employed, which may increase the complexity of the control strategy optimization. By applying proper detection and compensation procedure, the strategy can achieve robust magnetic polarity detection, and accurate rotor position estimation with outstanding steady-state and dynamic performances which have been validated by experiments.

CHAPTER 4

NEW SENSORLESS CONTROL BASED ON SQUARE WAVEFORM HIGH FREQUENCY PULSATING CARRIER SIGNAL INJECTION INTO STATIONARY REFERENCE FRAME

4.1 Introduction

The sensorless control algorithms introduced in Chapter 3 can be adopted in general-purpose inverters to drive interior PMSM. However, the performances of these sinusoidal waveform injection based sensorless controls are usually insufficient for some applications, since the bandwidths of rotor position estimation are limited by the LPFs which are applied in the carrier current response demodulation. Meanwhile, only when the carrier frequency is sufficiently higher than the fundamental excitation, PMSM can be seen as a pure inductive load, and the resistance can be ignored. However, in order to form a proper sinusoidal high frequency injected voltage, the frequency of injected voltage cannot be too high due to the limitation of PWM frequency. Hence, with larger machine resistance and smaller inductance, the influence of the resistance may deteriorate the rotor position estimation. Therefore, in some areas, a position sensor has to be used in normal operations due to the limitation of the performance of the sensorless control, and sensorless algorithms are just utilized as the backup system for emergency when the position sensor fails.

To improve the bandwidth of rotor position estimation, in [YOO11], and [HAM10], square waveform signal is applied in d -axis based pulsating carrier voltage signal injection method, which eliminates the requirement of LPFs for demodulation, and hence sensorless dynamic performance is remarkably enhanced even with a low salient surface-mounted PMSM. Based on the analysis of conventional d -axis square waveform signal injection method and the new proposed sensorless control strategy

based on sinusoidal waveform high frequency pulsating signal injection into the stationary reference frame as introduced in Section 3.4, high frequency square waveform pulsating carrier voltage will be employed to improve the dynamic performance and extend the observe bandwidth. The algorithm of the proposed strategy will be fully discussed and analyzed in this chapter.

4.2 Conventional Square Waveform High Frequency Carrier Signal Injection Methods

Rotating carrier signal injection schemes inject a balanced three phase voltage carrier signal into the stationary reference frame to form a rotating excitation superimposed on the fundamental excitation, which makes it difficult to employ square waveform injection. However, for pulsating carrier signal injection methods, high frequency sinusoidal pulsating carrier signal could be replaced by square waveform carrier signal [YOO11].

4.2.1 Square Waveform High Frequency Injection

For d -axis pulsating carrier signal injection, the high frequency pulsating carrier voltage (4.1) which is demonstrated as in Fig. 4.1 is injected on the estimated d -axis.

$$\begin{bmatrix} u_{dh}^e \\ u_{qh}^e \end{bmatrix} = \begin{cases} \begin{bmatrix} U_c \\ 0 \end{bmatrix} & \text{halfduty} \\ \begin{bmatrix} -U_c \\ 0 \end{bmatrix} & \text{other halfduty} \end{cases} \quad (U_c > 0) \quad (4.1)$$

For the square waveform injection, within the half duty of injection, the applied voltage is constant. Hence, for the simplicity in carrier current response demodulation, the differential of resultant carrier current response in the estimated synchronous reference frame as show in (3.9) should be re-expressed as

$$\begin{bmatrix} \Delta i_{dh}^e \\ \Delta i_{qh}^e \end{bmatrix} = \begin{bmatrix} \frac{1}{L_p} + \frac{1}{L_n} \cos(2\Delta\theta + \theta_m) & \frac{1}{L_n} \sin(2\Delta\theta + \theta_m) \\ \frac{1}{L_n} \sin(2\Delta\theta + \theta_m) & \frac{1}{L_p} - \frac{1}{L_n} \cos(2\Delta\theta + \theta_m) \end{bmatrix} \cdot \begin{bmatrix} u_{dh}^e \\ u_{qh}^e \end{bmatrix} \quad (4.2)$$

where Δi_{dqh}^e is current difference between the present and previous values at the edge of u_{dh}^e .

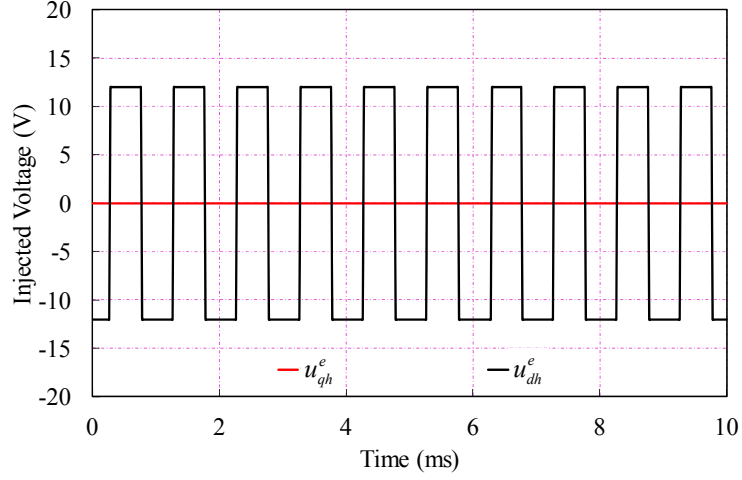


Fig. 4.1. Injected pulsating carrier voltage ($U_c=12V, f=1kHz$)

Then, the resultant difference of d - and q -axis current response Δi_{dqh}^e in the estimated synchronous reference frame between the present and previous value at the edge of u_{dh}^e as shown in (4.3) can be derived and demonstrated in Fig. 4.2. It could be concluded that, the higher injected voltage and lower frequency, the larger difference between the two edges of injected voltage.

$$\begin{bmatrix} \Delta i_{dh}^e \\ \Delta i_{qh}^e \end{bmatrix} = \begin{cases} U_c \Delta T \begin{bmatrix} \frac{1}{L_p} + \frac{1}{L_n} \cos(2\Delta\theta + \theta_m) \\ \frac{1}{L_n} \sin(2\Delta\theta + \theta_m) \end{bmatrix}, & u_{dh}^e > 0 \\ -U_c \Delta T \begin{bmatrix} \frac{1}{L_p} + \frac{1}{L_n} \cos(2\Delta\theta + \theta_m) \\ \frac{1}{L_n} \sin(2\Delta\theta + \theta_m) \end{bmatrix}, & u_{dh}^e < 0 \end{cases} \quad (4.3)$$

where ΔT is the duration time of U_c or $-U_c$ (half period).

Considering the polarity of the injection voltage, i.e.

$$\Delta i_{dqh}^* = \begin{cases} \Delta i_{dqh}, & u_{dh}^e > 0 \\ -\Delta i_{dqh}, & u_{dh}^e < 0 \end{cases} \quad (4.4)$$

(4.3) can be expressed as

$$\begin{bmatrix} \Delta i_{dh}^* \\ \Delta i_{qh}^* \end{bmatrix} = \begin{bmatrix} \frac{U_c \Delta T}{L_p} + \frac{U_c \Delta T}{L_n} \cos(2\Delta\theta + \theta_m) \\ \frac{U_c \Delta T}{L_n} \sin(2\Delta\theta + \theta_m) \end{bmatrix} \quad (4.5)$$

where θ_m is the cross-saturation effect to be compensated. Δi_{dqh}^e , and Δi_{dqh}^* are compared in Fig. 4.3 where Δi_{dqh}^* is actually the envelopes of Δi_{dqh}^e .

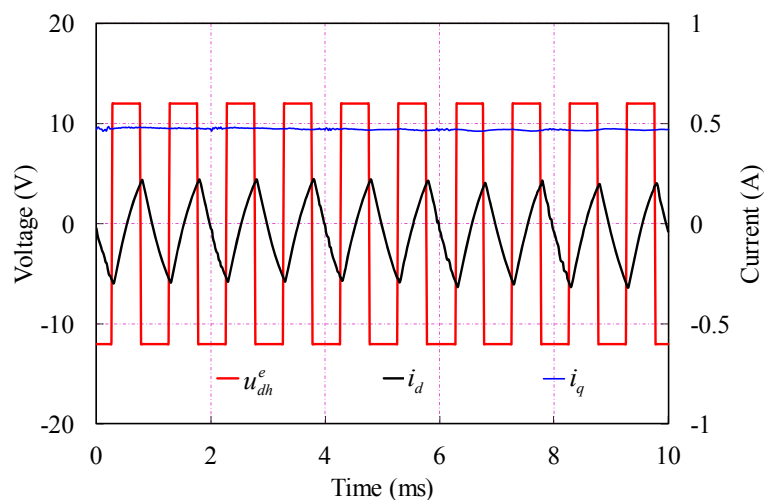


Fig. 4.2. d - and q -axis current compared to the injected voltage

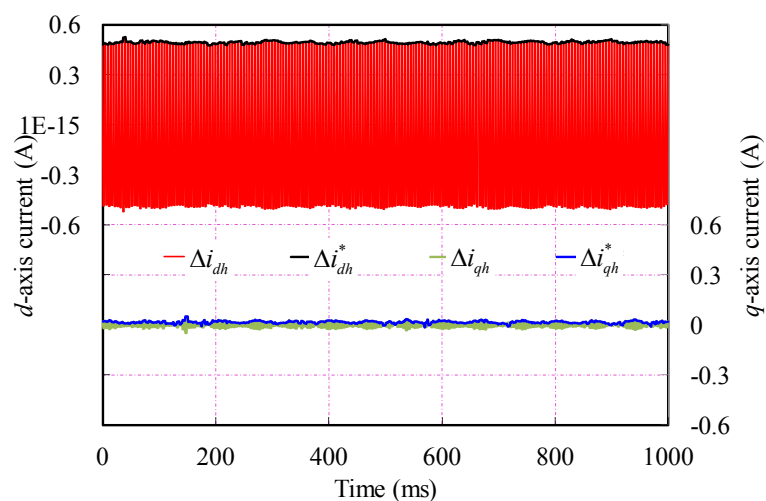


Fig. 4.3. Carrier current differences between the present and previous values at the edge of u_{dh}^e , and their envelopes

Then the envelope of q -axis carrier current response difference is regarded to be the signal input to the position observer,

$$f(\Delta\theta) = \Delta i_{qh}^* = \frac{U_c \Delta T}{L_n} \sin(2\Delta\theta + \theta_m) \quad (4.6)$$

For q -axis square waveform pulsating carrier signal injection, the high frequency pulsating carrier voltage vector (4.7) is injected on the estimated q -axis.

$$\begin{bmatrix} u_{dh}^e \\ u_{qh}^e \end{bmatrix} = \begin{cases} \begin{bmatrix} 0 \\ U_c \end{bmatrix} & \text{halfduty} \\ \begin{bmatrix} 0 \\ -U_c \end{bmatrix} & \text{otherwise} \end{cases} \quad (U_c > 0) \quad (4.7)$$

Then the resultant envelope of carrier current difference in the estimated synchronous reference frame can be expressed as

$$\begin{bmatrix} \Delta i_{dh}^* \\ \Delta i_{qh}^* \end{bmatrix} = \begin{bmatrix} \frac{U_c \Delta T}{L_n} \sin(2\Delta\theta + \theta_m) \\ \frac{U_c \Delta T}{L_p} - \frac{U_c \Delta T}{L_n} \cos(2\Delta\theta + \theta_m) \end{bmatrix} \quad (4.8)$$

Similar to the d -axis pulsating carrier signal injection method, the carrier current response is amplitude modulated by the rotor position information, and the d -axis carrier current response is usually used to extract the rotor position information. Then the envelope of d -axis carrier current response difference which is exactly the same as (4.6) is regarded to be the signal input to the position observer. As introduced in Section 3.3.1, torque ripple can be generated by the current ripple on the q -axis even the position estimation error is zero. Consequently, d -axis injection is preferred in terms of torque ripple.

4.2.2 Steady-state and Dynamic Performance

The steady-state tests for pulsating and rotating carrier signal injection methods are carried out at the condition of 70V DC bus voltage, 50rpm rotor speed with about 1A q -axis current, and the estimated rotor positions considering the cross-saturation

effect are shown in Fig. 3.15 compared with the actual value from encoder. In steady-state, $f(\Delta\theta)$ is forced to be zero due to the position observer which is the same as Fig. 3.14, and hence, rotor position can be derived with the load-dependent position estimation error $(-\theta_m/2)$ due to cross-saturation effect. Then by employing the cross-saturation effect as introduced in Section 3.3.1, the accurate rotor position could be derived. Based on the predicted cross-saturation angle as shown in Fig. 4.4, the estimated rotor positions under steady-state at 50rpm can be estimated. It can be seen that, the estimation error can be kept within 0.03 rad.

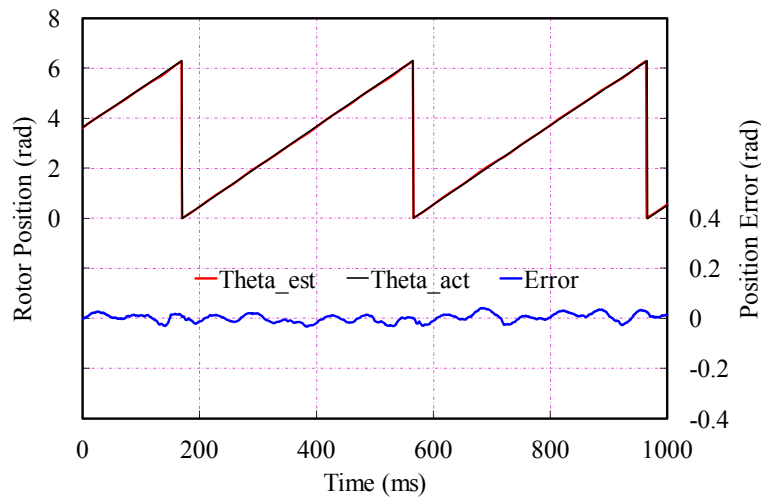
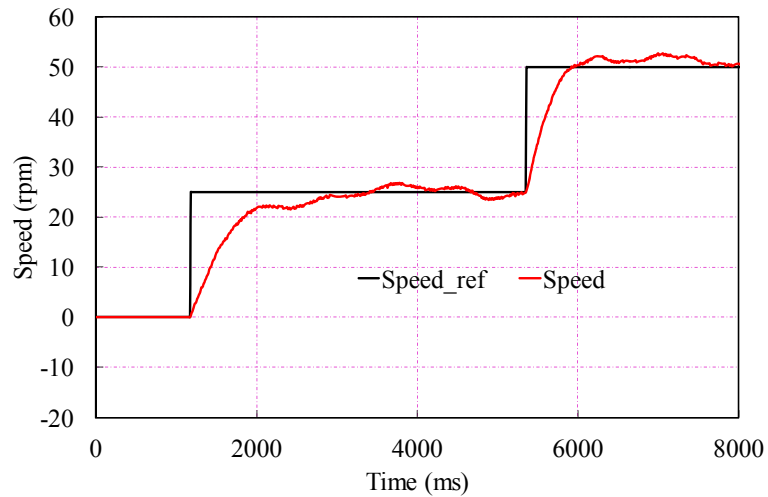
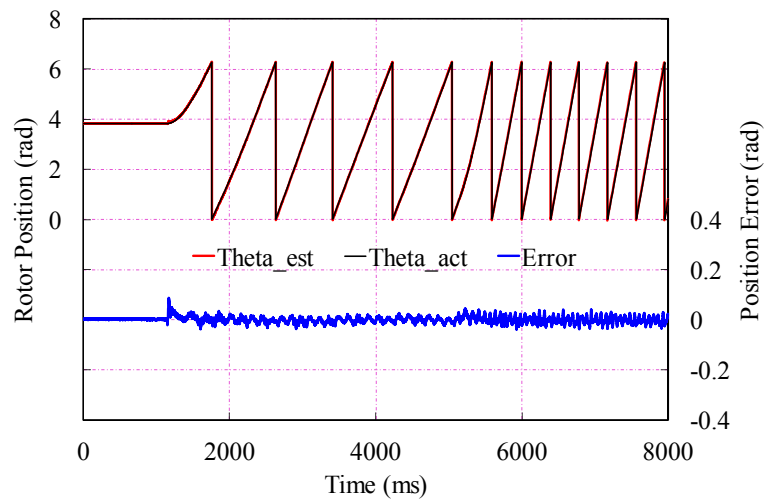


Fig. 4.4. Steady-state performance (θ_{est} : Estimated rotor position, θ_{act} : Actual rotor position, $Error$: Rotor position estimation error)

The dynamic performance test is carried out when the rotor mechanical initial speed is zero and step change to 25rpm and further to 50rpm as illustrated in Fig. 4.5(a). Then the estimated and actual rotor positions and the estimation error are shown in Fig. 4.5(b). Compared with experimental results by applying the sinusoidal waveform injection in Fig. 3.17(a), the proposed square waveform high frequency injection method can achieve better dynamic performance due to higher bandwidth as a result of higher injected frequency and elimination of all filters.



(a) Dynamic test situation



(b) Dynamic performance

Fig. 4.5. Dynamic test of square waveform d -axis injection

($Speed_ref$: Speed reference, $Speed$: Actual rotor speed, $Theta_est$: Estimated rotor position, $Theta_act$: Actual rotor position, $Error$: Rotor position estimation error)

4.3 New Proposed Control Strategy with Square Waveform High-Frequency Pulsating Signal Injection into Stationary Reference Frame

4.3.1 Square Waveform Carrier Signal Injection

To extend the application bandwidth, the concept of square waveform injection which is applied in conventional pulsating carrier signal injection sensorless control can be extended to the strategy with injection of high frequency carrier pulsating signal into stationary reference frame, where the square waveform high frequency pulsating carrier voltage vector (4.9) as shown in Fig. 4.6 is injected on the α -axis.

$$\begin{bmatrix} u_{\alpha h} \\ u_{\beta h} \end{bmatrix} = \begin{cases} \begin{bmatrix} U_c \\ 0 \end{bmatrix} & \text{halfduty} \\ \begin{bmatrix} -U_c \\ 0 \end{bmatrix} & \text{other halfduty} \end{cases} \quad (U_c > 0) \quad (4.9)$$

where U_c is the amplitude which is 12V, and the injected frequency is 1kHz.

Since the injected frequency is sufficiently higher than fundamental excited frequency, the PMSM can be seen as a pure inductive load without influence of machine resistance, and then the response of the α -axis carrier current $i_{\alpha h}$ will be derived as in Fig. 4.7.

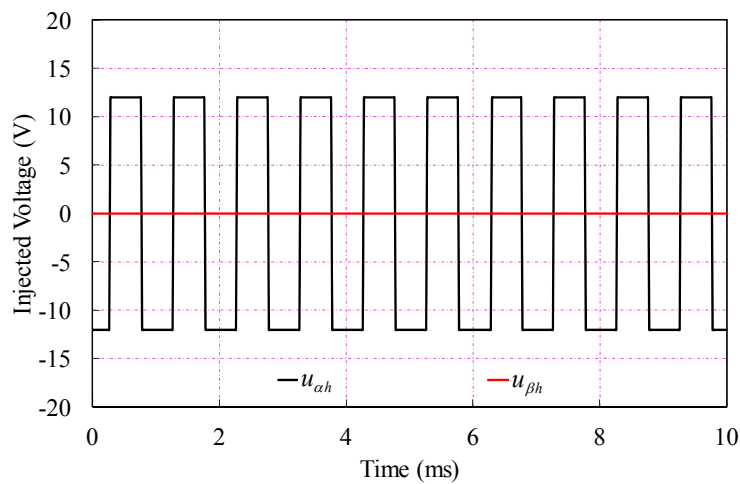


Fig. 4.6. Injected square waveform pulsating voltage ($U_c=12\text{V}$, $f=1\text{kHz}$)

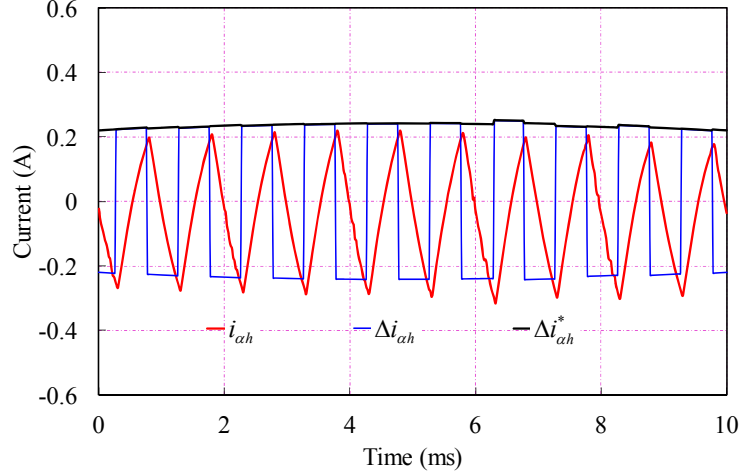


Fig. 4.7. Current response, amplitude difference and its envelope

For the square waveform injection, within the half duty of injection, the applied voltage is constant. Hence, for the simplicity in current response demodulation, the differential of resultant carrier current response in the stationary reference frame as show in (3.13) should be re-expressed as

$$\begin{bmatrix} \Delta i_{\alpha h} \\ \Delta i_{\beta h} \end{bmatrix} = \begin{bmatrix} \frac{1}{L_p} + \frac{1}{L_n} \cos(2\theta_r + \theta_m) & \frac{1}{L_n} \sin(2\theta_r + \theta_m) \\ \frac{1}{L_n} \sin(2\theta_r + \theta_m) & \frac{1}{L_p} - \frac{1}{L_n} \cos(2\theta_r + \theta_m) \end{bmatrix} \begin{bmatrix} u_{\alpha h} \\ u_{\beta h} \end{bmatrix} \quad (4.10)$$

where $\Delta i_{\alpha\beta h}$ is current difference between the present and previous values at the edge of $u_{\alpha h}$. By measuring the response carrier current at each edge of $u_{\alpha h}$, $\Delta i_{\alpha\beta h}$ as shown in (4.11) can be derived and demonstrated in Fig. 4.7.

$$\begin{bmatrix} \Delta i_{\alpha h} \\ \Delta i_{\beta h} \end{bmatrix} = \begin{cases} U_c \Delta T \begin{bmatrix} \frac{1}{L_p} + \frac{1}{L_n} \cos(2\theta_r + \theta_m) \\ \frac{1}{L_n} \sin(2\theta_r + \theta_m) \end{bmatrix}, & u_{\alpha h} > 0 \\ -U_c \Delta T \begin{bmatrix} \frac{1}{L_p} + \frac{1}{L_n} \cos(2\theta_r + \theta_m) \\ \frac{1}{L_n} \sin(2\theta_r + \theta_m) \end{bmatrix}, & u_{\alpha h} < 0 \end{cases} \quad (4.11)$$

From both Fig. 4.7 and (4.11), it can be found that the sign of $\Delta i_{\alpha\beta h}$ is decided by the polarity of injected carrier voltage. Then, the envelopes of $\Delta i_{\alpha\beta h}$ could be

calculated considering the polarity of the injected voltage only, i.e.

$$\begin{aligned}\Delta i_{ah}^* &= \begin{cases} \Delta i_{ah}, & \text{if } u_{ah} > 0 \\ -\Delta i_{ah}, & \text{otherwise} \end{cases} \\ \Delta i_{\beta h}^* &= \begin{cases} \Delta i_{\beta h}, & \text{if } u_{ah} > 0 \\ -\Delta i_{\beta h}, & \text{otherwise} \end{cases}\end{aligned}\quad (4.12)$$

Then, the envelope of the amplitude difference of carrier current can be derived from (4.13), which is also illustrated in Fig. 4.7.

$$\begin{aligned}\begin{bmatrix} \Delta i_{ah}^* \\ \Delta i_{\beta h}^* \end{bmatrix} &= \begin{bmatrix} \frac{U_c \Delta T}{L_p} + \frac{U_c \Delta T}{L_n} \cos(2\theta_r + \theta_m) \\ \frac{V_c \Delta T}{L_n} \sin(2\theta_r + \theta_m) \end{bmatrix} \\ &= \begin{bmatrix} I_p^{SQ} \\ 0 \end{bmatrix} + \begin{bmatrix} I_n^{SQ} \cos(2\theta_r + \theta_m) \\ I_n^{SQ} \sin(2\theta_r + \theta_m) \end{bmatrix} = \begin{bmatrix} I_p^{SQ} \\ 0 \end{bmatrix} + \begin{bmatrix} \Delta i_{\alpha h}^{**} \\ \Delta i_{\beta h}^{**} \end{bmatrix}\end{aligned}\quad (4.13)$$

where

$$I_p^{SQ} = \frac{U_c \Delta T}{L_p}, \quad I_n^{SQ} = \frac{U_c \Delta T}{L_n}\quad (4.14)$$

Then, based on aforementioned analysis and considering the polarity of injected voltage, the α - and β -axis current differences between the present and the previous values at the edge of u_{ah} , and their envelopes could be derived as shown in Fig. 4.8.

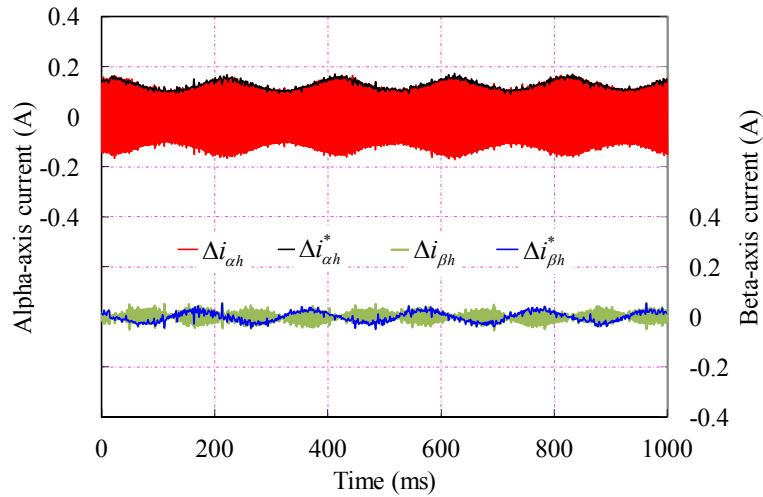


Fig. 4.8. Carrier current differences between the present and previous values at the edge of u_{ah} , and their envelopes

From (4.13) and Fig. 4.8, it is clearly shown that the envelopes of carrier current

response is modulated by the rotor position θ_r and the cross-saturation angle θ_m which is constant at the given load condition. Similar to sinusoidal waveform injection method, if I_p^{SQ} can be compensated and the cross-saturation effect is considered, the rotor position could be retrieved from the response current precisely.

If a β -axis square waveform pulsating carrier voltage signal (4.15) is injected into the stationary reference frame,

$$\begin{bmatrix} u_{\alpha h} \\ u_{\beta h} \end{bmatrix} = \begin{cases} \begin{bmatrix} 0 \\ U_c \end{bmatrix} & \text{halfduty} \\ \begin{bmatrix} 0 \\ -U_c \end{bmatrix} & \text{otherwise} \end{cases} \quad (U_c > 0) \quad (4.15)$$

Then the amplitude difference in the stationary reference frame between the present and the previous values at the edge of $u_{\alpha h}$ can be derived as

$$\begin{bmatrix} \Delta i_{\alpha h} \\ \Delta i_{\beta h} \end{bmatrix} = \begin{cases} U_c \Delta T \begin{bmatrix} \frac{1}{L_n} \sin(2\theta_r + \theta_m) \\ \frac{1}{L_p} - \frac{1}{L_n} \cos(2\theta_r + \theta_m) \end{bmatrix}, & u_{\alpha h} > 0 \\ -U_c \Delta T \begin{bmatrix} \frac{1}{L_n} \sin(2\theta_r + \theta_m) \\ \frac{1}{L_p} - \frac{1}{L_n} \cos(2\theta_r + \theta_m) \end{bmatrix}, & u_{\alpha h} < 0 \end{cases} \quad (4.16)$$

Then, envelopes of the amplitude difference of current can be derived considering the polarity of the injected voltage, i.e.

$$\begin{aligned} \begin{bmatrix} \Delta i_{\alpha h}^* \\ \Delta i_{\beta h}^* \end{bmatrix} &= \begin{bmatrix} \frac{U_c \Delta T}{L_n} \sin(2\theta_r + \theta_m) \\ \frac{U_c \Delta T}{L_p} - \frac{U_c \Delta T}{L_n} \cos(2\theta_r + \theta_m) \end{bmatrix} \\ &= \begin{bmatrix} 0 \\ I_p^{SQ} \end{bmatrix} + \begin{bmatrix} I_n^{SQ} \sin(2\theta_r + \theta_m) \\ -I_n^{SQ} \cos(2\theta_r + \theta_m) \end{bmatrix} = \begin{bmatrix} 0 \\ I_p^{SQ} \end{bmatrix} + \begin{bmatrix} \Delta i_{\beta h}^{**} \\ -\Delta i_{\alpha h}^{**} \end{bmatrix} \end{aligned} \quad (4.17)$$

Similar to the α -axis injection, the carrier current response is also amplitude modulated by the rotor position information and the demodulation process will be the

same. However, I_p^{SQ} locates at β -axis current, whilst the phase sequence of $\Delta i_{\alpha h}^{**}$ and $\Delta i_{\beta h}^{**}$ is different. Hence, I_p^{SQ} compensation and position estimation will be slightly different.

If the frequency of injected voltage is not high enough, the high-frequency induced current will not be properly filtered out by the digital filter which is used for the feedback of the current controller. Then, the output voltage of the current regulator would interfere with the injected voltage, which would degrade the overall performance. Meanwhile, applying higher frequency can also minimize the noise in the induced current due to the sampling delay and/or the non-ideal components in the signal processing [YOO11]. As mentioned above, the sinusoidal waveform injection method needs much more cycles of PWM to form a proper injection voltage, whereas a square waveform injected voltage needs much less. Hence, the maximum injected frequency of square waveform injection can be up to half of the PWM switching frequency and better performance could be deduced theoretically.

However, with higher injected frequency, the carrier current response difference would be smaller due to the shorter duration time ΔT of the injected voltage, and the SNR of the envelopes would also be lower. Then the demodulation process would be induced with higher signal noise which also will deteriorate the rotor position estimation accuracy. Thus, the frequency of the injected voltage should be optimized to compromise the requirement of bandwidth and SNR. The sensorless safety operation area (SSOA) is introduced with due account for the quantization error in the analog to digital conversion [GON11]. The SSOA defines a working area in the d - q plane in which the motor can operate in sensorless mode with a guaranteed performance in steady-state, and then a proper injected carrier signal can be selected for the specific prototype machine and current-measurement resolution. With the aid of SSOA, the injected frequency is set as 1kHz which is much higher than the frequency in sinusoidal waveform injection which is 330Hz to derive higher bandwidth, and the SNR is also not too low to interfere the rotor position estimation.

Hence, even with a surface-mounted PMSM with small machine saliency, a

square waveform high frequency injection sensorless method can also be implemented due to its higher sensitivity to machine saliency with higher injected frequency [HAM10]. Furthermore, the demodulation is proceeded by only considering the polarity of injected voltage without any filtering, which can also extend the bandwidth of the position estimation.

4.3.2 I_p^{SQ} Pre-Detection and Compensation

The same as the sinusoidal waveform injection method, I_p^{SQ} also should be subtracted from Δi_{ah}^* to get Δi_{ah}^{**} for tracking the rotor position. Based on (3.10) and (3.17), I_p^{SQ} could be expressed as

$$I_p^{SQ} = \frac{U_c \Delta T}{L_p} = \frac{U_c \cdot L_{sa} \cdot \Delta T}{L_{dh} L_{qh} - L_{dqh}^2} \quad (4.18)$$

where I_p^{SQ} is parameter-dependent and proportional to the ratio of $U_c \Delta T$ which is nearly the same as I_p in (3.17) of sinusoidal waveform injection. As mentioned above, L_p is almost not affected by i_q , and for general applications at zero and very low speed, i_d is usually set as negative and maintains the same value. Furthermore, it is possible to obtain I_p by LPF with i_d is applied for starting in sensed operation at higher speed. Then, the derived I_p can be stored into a controller memory, and applied for starting from zero to very low speed. Then subtracting the calculated or measured I_p^{SQ} from Δi_{ah}^* , Δi_{ah}^{**} which is modulated by rotor position θ_r and cross-saturation angle θ_m could be derived as (4.19), which is illustrated in Fig. 4.9.

$$\begin{bmatrix} \Delta i_{ah}^{**} \\ \Delta i_{\beta h}^{**} \end{bmatrix} = \begin{bmatrix} I_n^{SQ} \cos(2\theta_r + \theta_m) \\ I_n^{SQ} \sin(2\theta_r + \theta_m) \end{bmatrix} \quad (4.19)$$

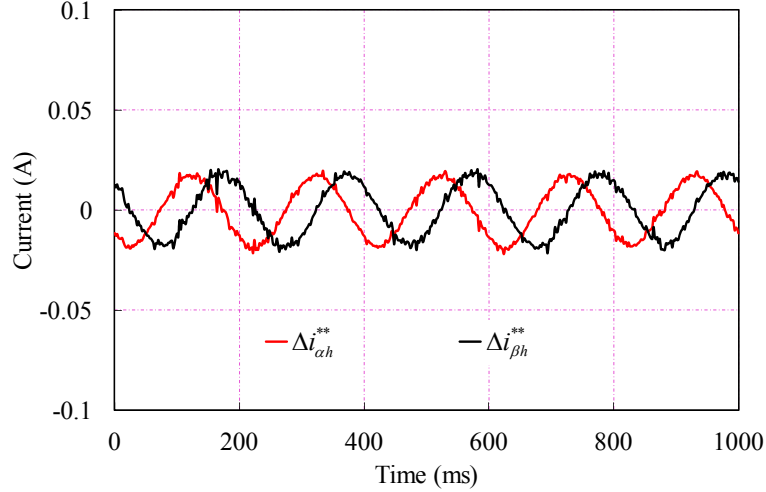


Fig. 4.9. Envelopes of response current difference after subtracting I_p^{SQ}

Once the rotor is rotating at higher speed, different i_d may be applied and L_p will vary. Then, deriving I_p^{SQ} from the pre-tested data at all different operating condition is not practical any more. Meanwhile, applying LPF to detect I_p^{SQ} will degrade sensorless control performances due to the inherent time delay. Hence, alternative solution should be applied instead, where derivation calculation is considered at each sampling instant. Then, the difference value $\Delta i'_{\alpha\beta h}$ of the present and previous sampling instants of $\Delta i^*_{\alpha\beta h}$ can be calculated as

$$\begin{aligned}
 \begin{bmatrix} \Delta i'_{\alpha h} \\ \Delta i'_{\beta h} \end{bmatrix} &= \begin{bmatrix} \frac{I_p^{SQ} + I_n^{SQ} \cos(2\theta_r + \theta_m)}{\Delta t_s} \\ \frac{I_n^{SQ} \sin(2\theta_r + \theta_m)}{\Delta t_s} \end{bmatrix} \Big|_{(k)} - \begin{bmatrix} \frac{I_p^{SQ} + I_n^{SQ} \cos(2\theta_r + \theta_m)}{\Delta t_s} \\ \frac{I_n^{SQ} \sin(2\theta_r + \theta_m)}{\Delta t_s} \end{bmatrix} \Big|_{(k-1)} \\
 &= \begin{bmatrix} \frac{I_p^{SQ} \Big|_{(k)} - I_p^{SQ} \Big|_{(k-1)} + \frac{I_n^{SQ} \cos(2\theta_r + \theta_m) \Big|_{(k)} - I_n^{SQ} \cos(2\theta_r + \theta_m) \Big|_{(k-1)}}{\Delta t_s} \\ \frac{I_n^{SQ} \sin(2\theta_r + \theta_m) \Big|_{(k)} - I_n^{SQ} \sin(2\theta_r + \theta_m) \Big|_{(k-1)}}{\Delta t_s} \end{bmatrix} \quad (4.20)
 \end{aligned}$$

Since I_p^{SQ} could be seen as constant between two sampling instants, the difference of I_p^{SQ} between the two sampling instants could be treated as zero. Hence,

$$\begin{aligned}
\begin{bmatrix} \Delta i'_{\alpha h} \\ \Delta i'_{\beta h} \end{bmatrix} &= \begin{bmatrix} \frac{I_n^{SQ} \cos(2\theta_r + \theta_m)|_{(k)} - I_n^{SQ} \cos(2\theta_r + \theta_m)|_{(k-1)}}{\Delta t_s} \\ \frac{I_n^{SQ} \sin(2\theta_r + \theta_m)|_{(k)} - I_n^{SQ} \sin(2\theta_r + \theta_m)|_{(k-1)}}{\Delta t_s} \end{bmatrix} \\
&= \frac{I_n^{SQ}}{\Delta t_s} \begin{bmatrix} -\sin(2\theta_r + \theta_m) \cdot \sin(2\Delta\theta_s) \\ \cos(2\theta_r + \theta_m) \cdot \sin(2\Delta\theta_s) \end{bmatrix} \\
&= \frac{I_n^{SQ}}{\Delta t_s} \cdot \sin(2\Delta\theta_s) \begin{bmatrix} -\sin(2\theta_r + \theta_m) \\ \cos(2\theta_r + \theta_m) \end{bmatrix}
\end{aligned} \tag{4.21}$$

where $\Delta\theta_s$ is the rotor position difference between two sampling instants and is constant at constant speed.

From (4.21), it can be found that $\Delta i'_{\alpha\beta h}$ is also modulated by rotor position θ_r and cross-saturation angle θ_m with one sampling time delay which is nearly the same as (4.19). Then, apply a proper estimator rotor position can be derived from both (4.19) and (4.21) with the load-dependent position estimation error ($-\theta_m/2$) due to cross-saturation effect at different operation situation. Since the cross-saturation effect is the same as sinusoidal waveform injection method, the compensation method can exactly follow the one in Sector 3.4.3. However, compared the experimental results of $\Delta i'_{\alpha\beta h}$ as shown in Fig. 4.10 and $\Delta i_{\alpha\beta h}^{**}$ in Fig. 4.9, it can be found that the amplitudes are different. Hence, the parameters of rotor position estimator should be different from each other.

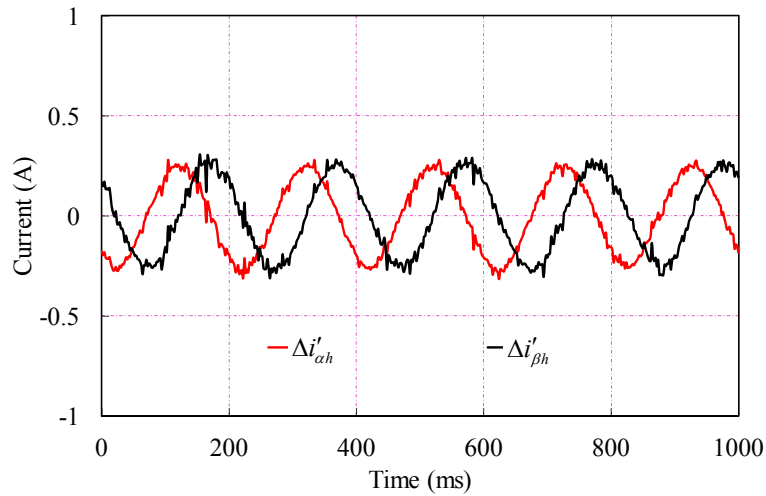


Fig. 4.10. Difference of the present and previous sampling instants of $\Delta i_{\alpha\beta h}^*$

4.3.3 Rotor Position Estimator

To obtain the rotor position from (4.19) and (4.21), the rotor position estimator in Sector 3.4.4 as shown in Fig. 3.25(a) can also be applied. According to the diagram, the closed-loop transfer function between the actual and estimated rotor positions can be expressed as

$$\frac{\theta_{re}}{\theta_r} = \frac{2Ik_p \cdot s + 2Ik_i}{s^2 + 2Ik_p \cdot s + 2Ik_i} \quad (4.22)$$

where I indicates I_n^{SQ} in (4.14), or $I_n^{SQ}/\Delta t_s \cdot \sin(2\Delta\theta_s)$ in (4.21). Based on (3.10), it could be seen that I in the different methods are all different and load-dependent. Hence, k_p and k_i of PI controller should be on-line varied with I in (4.22) to maintain the constant bandwidth. For simplicity in practical implementation, k_p and k_i could be selected based on the typical value of I at no load condition.

Since for square waveform voltage injection, I_n^{SQ} in (4.18), or $I_n^{SQ}/\Delta t_s \cdot \sin(2\Delta\theta_s)$ in (4.21) are different from each other. Hence, the parameters of PI controller also would be different. Furthermore, due to higher injected frequency and elimination of filter, the bandwidth of signal demodulation process would be much higher than sinusoidal waveform injection. Therefore, the loop bandwidth of rotor position estimator can also be enhanced up to 50Hz. Hence, the PI controller could be selected based on the typical value at no load condition and set up at around 44Hz for both estimating from (4.14) and (4.21), and the Bode plot of the position estimator are shown in Fig. 4.11.

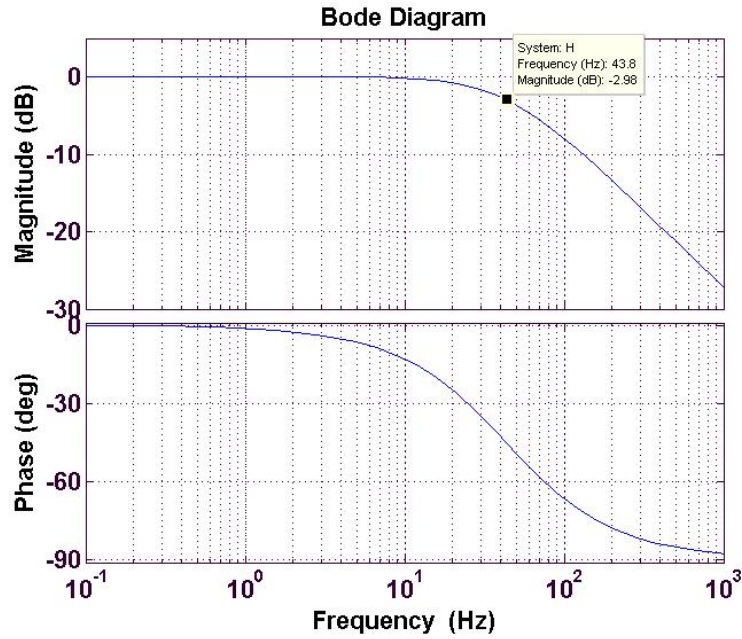


Fig. 4.11. Bode chart of position estimator for square waveform injection

Meanwhile, the machine saliency varies periodically as a second spatial harmonic, hence, the estimated position information based on machine saliency is rotor direction without magnetic polarity information, which has an angle ambiguity of π . Since the injection voltage of the square and sinusoidal waveforms are both pulsating carrier voltage signal into the stationary reference frame, the magnetic polarity detection method for square waveform injection can follow the one as introduced in Sector 3.4.5 exactly.

4.3.4 Steady-state and Dynamic Performance

Several experiments have been performed to validate the new proposed high frequency sinusoidal pulsating signal injection method based on the stationary reference frame. The overall control scheme including the new proposed strategy is shown in Fig. 4.12 which has been implemented on a dSPACE platform. The Test Rig I with Motor I is applied for test, and the DC bus voltage is 70V. Inject a square waveform with 12V magnitude and 1kHz frequency, Fig. 4.6, into α -axis of stationary reference frame.

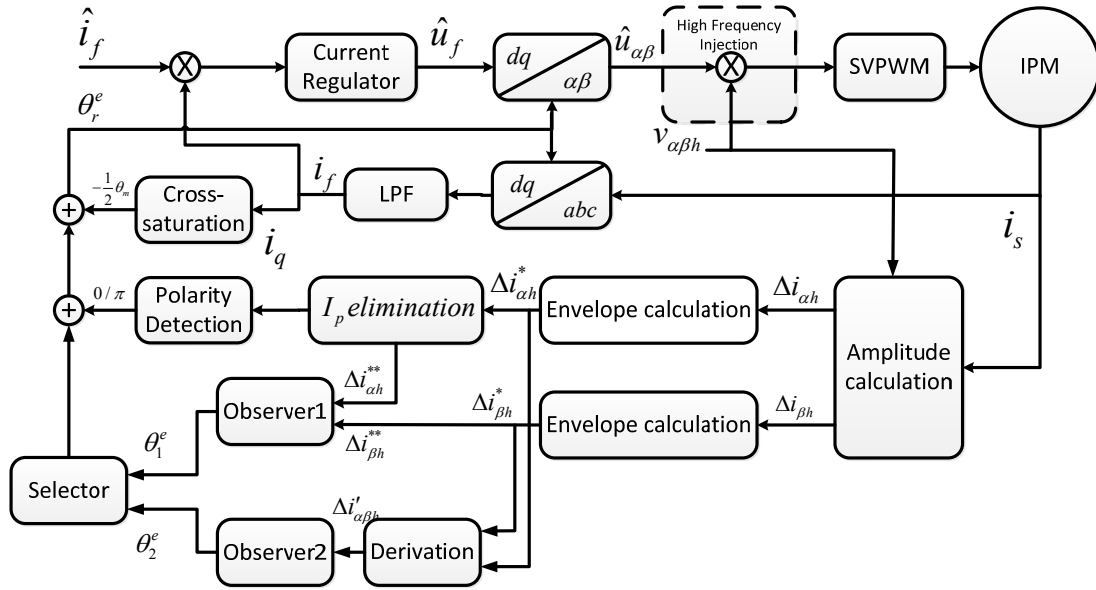


Fig. 4.12. Block diagram of overall control system.

Based on the predicted cross-saturation angle as shown in Fig. 3.24, the estimated rotor positions before and after compensation under steady-state at 50rpm can be estimated by the rotor position estimator are shown in Fig. 4.13. It can be seen that, before compensation, there exists an approximate 0.1rad estimation error, and after compensation, the error can be kept within 0.01 rad. Even though the estimated position has a little high frequency noise, the accuracy is much higher.

The dynamic performance test is carried out when the rotor mechanical initial speed is zero and step change to 25rpm and further to 50rpm as illustrated in Fig. 4.5(a). Then the estimated and actual rotor positions and the estimation error are shown in Fig. 4.14. Compared with experimental results by applying the sinusoidal waveform injection in Fig. 3.36(a), the proposed square waveform high frequency injection method can achieve better dynamic performance due to higher bandwidth caused by the higher injected frequency and elimination of all filters.

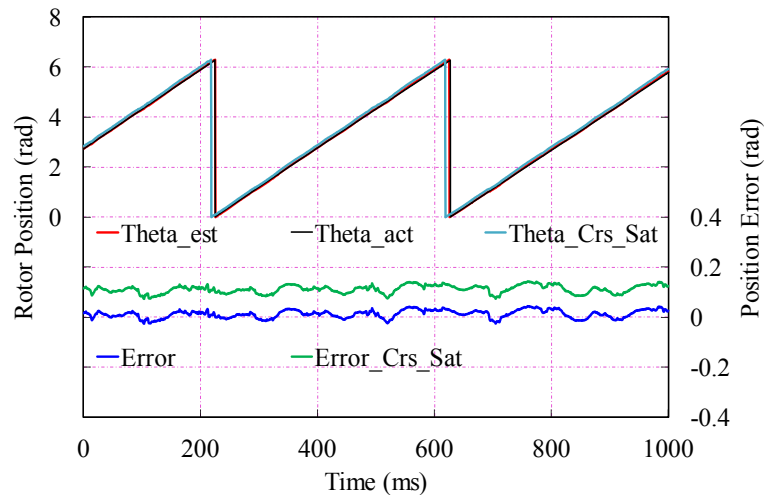


Fig. 4.13. Steady-state performance of the square waveform injection (θ_{est} : Estimated rotor position after cross saturation compensation, θ_{act} : Actual rotor position, θ_{Crs_Sat} : Estimated rotor position before cross saturation compensation, $Error$: Position estimation error after cross saturation compensation, $Error_Crs_Sat$: Position estimation error before cross saturation compensation)

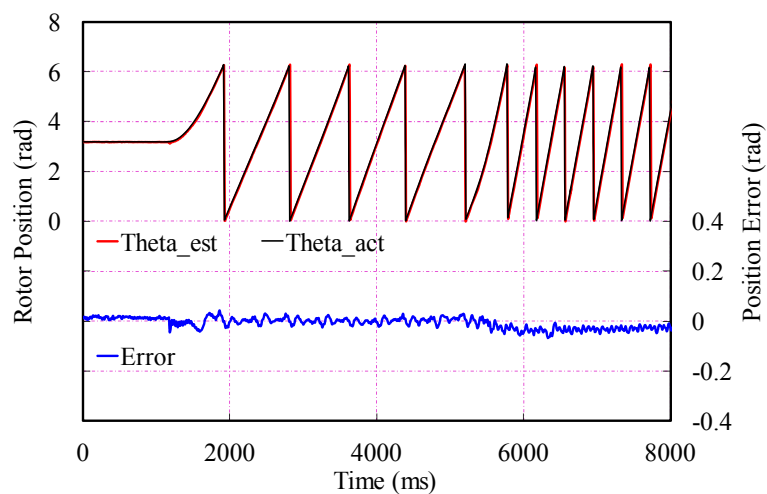


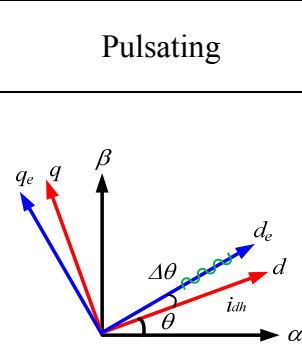
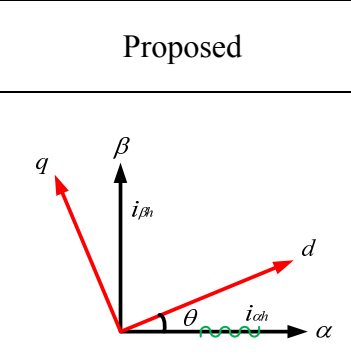
Fig. 4.14. Dynamic performance of the square waveform injection (θ_{est} : Estimated rotor position, θ_{act} : Actual rotor position, $Error$: Rotor position estimation error)

4.3.5 Square waveform Carrier Signal Injection based Sensorless Controls

Similar principle is exploited to estimate the rotor position information for square

waveform carrier signal injection based strategy, where they have different characteristics due to different carrier signal injection and demodulation processes. The new strategy has stable performance of signal injection as rotating carrier signal injection method, and the rotor position information estimation from the amplitude-modulated carrier current response is as simple as pulsating carrier signal injection method. Since the pulsating carrier signal injection based sensorless control cannot be employed with square waveform injection, the comparative results between the pulsating carrier signal injection method and the new proposed one are shown in Table 4.1.

TABLE 4.1
COMPARISON OF SQUARE WAVEFORM CARRIER SIGNAL INJECTION BASED SENSORLESS CONTROLS

	Pulsating	Proposed
Signal Injection		
Reference frame	Estimated synchronous	Stationary
Carrier voltage injection	Pulsating carrier voltage	Pulsating carrier voltage
Carrier current response	Amplitude-modulated	Amplitude-modulated
Torque ripple	Small	Medium
Cross-saturation angle	$-\theta_M/2$	$-\theta_m/2$
Stability of signal injection	Medium	Good
Signal demodulation	Simple	Medium
Dynamic performance	Good	Good

4.4 Application of High Frequency Injection Strategy in Wind Power System

For most wind power applications, zero and low speed region is not operated. Hence, the main sensorless control method is usually applying flux-observer based technique which is widely applied for PMSM drives. Rotor position is derived from the observed vector of PM excitation flux-linkage which is calculated from the integration of back-EMF under stationary reference frame. Then, the relative phase angle and speed between the observed vector and the reference frame are the rotor position and speed, respectively.

In order to observe the PM excitation flux-linkage vector, the current vector \dot{I} and the voltage vector \dot{U} in the PMSM is necessary. Then, the PM excitation flux vector $\dot{\Psi}_f$ can be derived as

$$\dot{\Psi}_f = \int_{t_0}^{t_1} (\dot{U} - R_s \cdot \dot{I}) dt + \dot{\Psi}_{f(0)} - L_s \cdot \dot{I} \quad (4.23)$$

Then, the rotor position can be estimated from the α - and β - parts of $\dot{\Psi}_f$, i.e.

$$\theta_f = \arctan \frac{\Psi_{f\beta}}{\Psi_{f\alpha}} \quad (4.24)$$

However, in this method, \dot{I} is usually obtained directly from current Hall sensors, and \dot{U} from the command of the SVPWM generator which is $u_{\alpha\beta}^*$ instead of from the voltage Hall sensors, as shown in Fig. 4.15. However, to obtain $u_{\alpha\beta}^*$, current closed-loop control is needed, which makes the rotor position necessary and creates a difficulty for starting the whole control system due to lack of the initial rotor position.

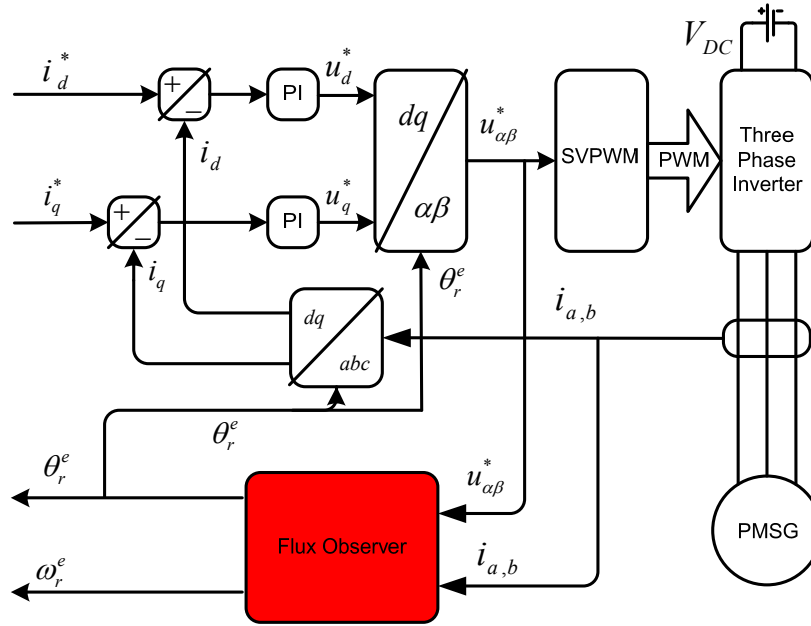


Fig. 4.15. Control diagram of wind power system

To solve the problem of starting the generator control system, the voltage sensors are usually added in the system to obtain the phase voltage. However, the phase voltage is not needed in normal VC operation, as this will increase the complexity of the control system. Hence, the rotor position should be obtained from a separate sensorless method.

In wind power applications, operation of zero and low speed region is not required. Hence, the high frequency carrier signal injection based sensorless control is usually not applied in wind power. However, it can be used for initial rotor position detection of flux observer without the voltage sensors. The PWM frequency is usually set as 2kHz or 2.25kHz which is lower than the common industrial application. As mentioned above, the sinusoidal waveform injection method needs much more cycles of PWM to form a proper injection voltage, whereas a square waveform injected voltage needs much less. Hence, square waveform carrier voltage injection strategy is a better solution for initial rotor position detection.

Step 1: When the generator rotates at steady-state with the generator current control system disabled, firstly make $u_{\alpha\beta}^* = 0$ and inject the high frequency voltage signal $u_{\alpha\beta h}^*$ to the command of the SVPWM. Then enable estimate the rotor position

θ_{hf} based on high frequency injection method as shown in Fig. 4.16.

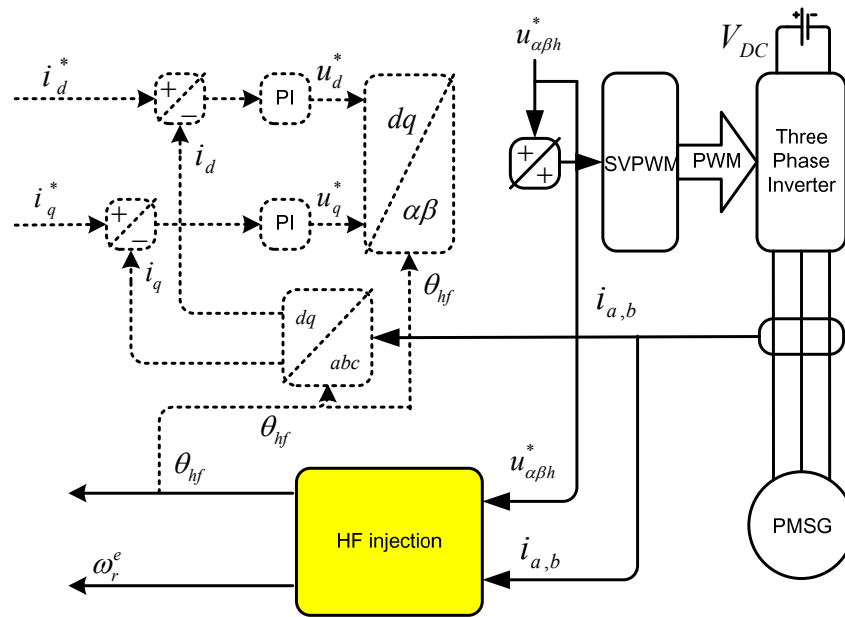


Fig. 4.16. Diagram with HF injection

Step 2: Enable the current control system with use of estimated rotor position θ_{hf} , whilst the current commands are maintained at zero. Thus, $u_{\alpha\beta}^*$ will be obtained together with $i_{\alpha\beta}$. These two signals can be used to derive the rotor position θ_f by using a flux observer, Fig. 4.17.

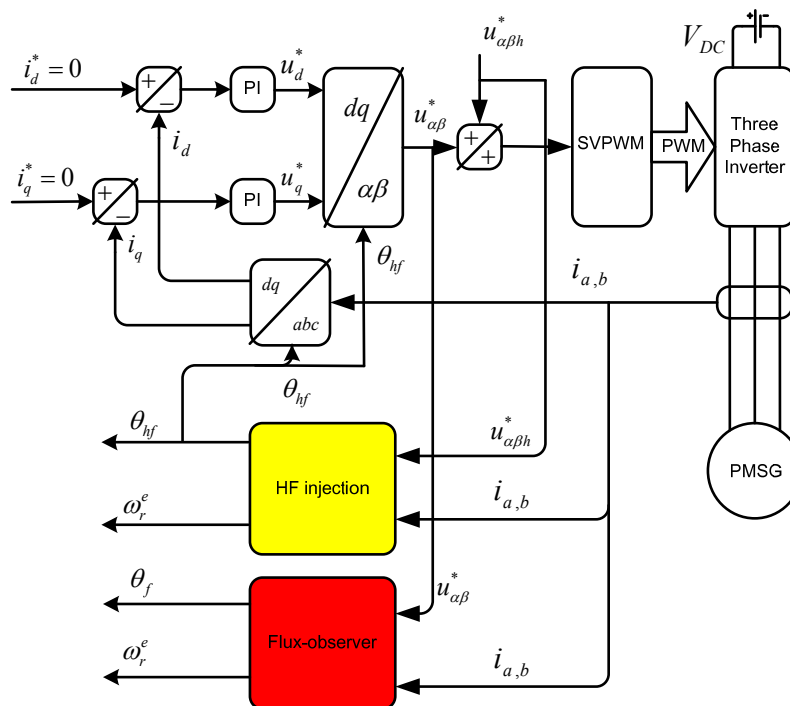


Fig. 4.17. Diagram with HF injection and flux observer

Step 3: Close the control loop with both θ_f which is obtained from a flux observer and the estimated position θ_{hf} from high frequency injection. Then, smoothly transfer the feedback rotor position information from θ_f to θ_{hf} , and disable the high frequency injection voltage. Up to this point enabling of the control system has been completed and the control system works under normal sensorless control with flux-observer as shown in Fig. 4.15.

As the described method is only applied for a very short period of time prior to start of the control system, there is no implication of effects to generator normal operation in terms of torque, speed and efficiency, etc. The high frequency injection sensorless could be applied to estimate the initial rotor position and solve the problem of generator control start in the wind turbine applications. With this technique the phase voltage sensors, which have to be used in the normal sensorless control, will not be required. Thus, the hardware system can be simplified.

4.5 Conclusion

Based on detailed discussion of conventional square waveform high frequency carrier signal injection based sensorless control technique, and the new high frequency injection method introduced in Chapter 3, a new strategy with injection of a pulsating square waveform high frequency carrier voltage into α - (or β -) axis of stator stationary reference frame is proposed, and then the rotor position information is retrieved from the carrier current response which is amplitude-modulated by rotor position. Then the bandwidth of the position estimation can be significantly improved due to the higher injected frequency and removal of all filters in the demodulation process. Meanwhile, since the injected frequency is much higher even than the fundamental frequency at rated speed, the square waveform injection method is possible to be applied at wider range of speed and deduce the higher performance. Considering the cross-saturation effect compensation, applying the TP-PLL based rotor position estimator, the rotor position can be estimated. Similar to the strategy with injection of sinusoidal pulsating carrier signal injection into stationary reference frame, the new strategy has stable performance of signal injection as rotating carrier signal injection method, and the

rotor position information estimation from the amplitude-modulated carrier current response is as simple as pulsating carrier signal injection method.

For most wind power applications, since operation of zero and low speed region is not required, the main sensorless control method is usually applying flux observer based technique which has the difficulty of starting without voltage sensor and lacking of initial rotor position. Whereas the square waveform high frequency injection based sensorless control strategy could be applied to estimate the initial rotor position and solve the problem of generator control start in the wind turbine applications without additional sensors, and can achieve more effect than the sinusoidal waveform injection due to the lower PWM frequency. Meanwhile, it is only applied for a very short period of time prior to start of the control system, thus there is no implication of effects to generator normal operation in terms of torque, speed and efficiency, etc.

CHAPTER 5

IMPROVEMENT OF SENSORLESS CONTROL PERFORMANCE BASED ON THIRD HARMONIC BACK-EMF BY SPEED ERROR COMPENSATION

5.1 Introduction

The back-EMF is a voltage that occurs in a permanent magnet machine when there is relative motion between the armature of the machine and the air gap magnetic field generated by permanent magnet, and hence, is directly related to the rotor position. Since the back-EMF voltage is proportional to rotor speed, all back-EMF based sensorless controls show good performance above certain speed but suffer at low and zero speed. When rotor speed is higher than certain speed, the back-EMF based sensorless control strategies would be superior to high frequency carrier signal injection based strategies which is introduced in Chapter 3 and Chapter 4. Hence, when PMSM has started from zero speed as a torque motor or has identified the initial rotor position as a generator by high frequency carrier signal injection based strategies, the control technique based back-EMF should be applied instead.

Moreira in [MOR92] introduced the third harmonic zero sequence back-EMF in the stator phase voltages which is usually significant due to the heavy saturation and/or character of designed PM excited flux-linkage which contains third harmonic on purpose. Hence, the zero-crossings of third harmonic flux-linkage which results from integration of third harmonic back-EMF are usually detected and the related discrete positions are utilized for sensorless control of brushless DC machine [PRO92] [KER93] [KER94] [MOR96] [SHE04] [SHE06a] [SHE06b]. Although it also suffers at very low and zero speed region as all the other EMF based strategy and the access to neutral point of the Y-connected stator winding is required, it still has several advantages superior to the widely applied fundamental back-EMF based strategies, such as

theoretically free of PWM noise, not distorted by the free-wheel diode conduction and not affected by the inaccurate measurements of winding resistance, inductance and the other parameters [WU91] [XU98] [SHE02b].

In this chapter, the detection of third harmonic back-EMF and conventional sensorless control strategy based on zero-crossings of third harmonic flux-linkage, which is the integration of third harmonic back-EMF which suffers at dynamic situation due to the insufficient precise rotor position reference points, are to be introduced. To minimize the rotor position error in the conventional method and improve the dynamic performance, a speed error compensation strategy based on the continuous signal of third harmonic flux-linkage is proposed. Furthermore, to improve the performance of rotor position estimation in flux observer sensorless control which is sensitive to the machine and controller parameters, a multi-technology fusion technique based on the error compensation of rotor position or speed to improve the performance and the robustness is also proposed in this chapter.

5.2 Detection of Third Harmonic Back-EMF and Conventional Sensorless Control

5.2.1 Detection of Third Harmonic Back-EMF

Third harmonic back-EMF is usually contained in windings irrespective of the operational mode and synchronously rotates with the fundamental components. When the machine windings are Y-connected, the third harmonic back-EMF presents in the phase back-EMF rather than line back-EMF. Hence, the neutral point of the Y-connected windings is essential for detecting the third harmonic back-EMF since the measurement of phase back-EMF is necessary. However, the neutral point leading wire can be thin as a signal cable without the need of power current in it [SHE04].

Assuming the inductances of the PMSM are constant with rotor position, the motor phase voltages and currents can be expressed as

$$\begin{cases} u_{an} = R_a i_a + (L_a - M) p i_a + e_a \\ u_{bn} = R_b i_b + (L_b - M) p i_b + e_b \\ u_{cn} = R_c i_c + (L_c - M) p i_c + e_c \end{cases} \quad (5.1)$$

$$i_a + i_b + i_c = 0 \quad (5.2)$$

On the condition of balanced phase impedance, irrespective of the operation mode of either BLDC or BLAC, with or without PWM, we can have

$$\begin{aligned} u_{an} + u_{bn} + u_{cn} &= \{[R_{sa} + p(L_a - M)] \cdot i_a + [R_{sb} + p(L_b - M)] \cdot i_b \\ &\quad + [R_{sc} + p(L_c - M)] \cdot i_c\} + (e_a + e_b + e_c) \\ &= e_a + e_b + e_c \end{aligned} \quad (5.3)$$

Usually, based on Fourier analysis, the phase back-EMF waveform contains the fundamental and odd harmonics, i.e.

$$\begin{cases} e_a = e_{a1} + e_3 + e_{a5} + e_{a7} + e_9 + \dots \\ \quad = -E_1 \sin \theta_r - E_3 \sin 3\theta_r - E_5 \sin 5\theta_r \\ \quad \quad - E_7 \sin 7\theta_r - E_9 \sin 9\theta_r - \dots \\ e_b = e_{b1} + e_3 + e_{b5} + e_{b7} + e_9 + \dots \\ \quad = -E_1 \sin(\theta_r - 2\pi/3) - E_3 \sin 3\theta_r - E_5 \sin 5(\theta_r - 2\pi/3) \\ \quad \quad - E_7 \sin 7(\theta_r - 2\pi/3) - E_9 \sin 9(\theta_r - 2\pi/3) - \dots \\ e_c = e_{c1} + e_3 + e_{c5} + e_{c7} + e_9 + \dots \\ \quad = -E_1 \sin(\theta_r + 2\pi/3) - E_3 \sin 3\theta_r - E_5 \sin 5(\theta_r + 2\pi/3) \\ \quad \quad - E_7 \sin 7(\theta_r + 2\pi/3) - E_9 \sin 9(\theta_r + 2\pi/3) - \dots \end{cases} \quad (5.4)$$

where θ_r is the rotor position. Then, assuming the fundamental back-EMF is also balanced, the following equation is derived from (5.3) and (5.4)

$$\begin{aligned} u_{an} + u_{bn} + u_{cn} &= e_a + e_b + e_c \\ &= (e_{a1} + e_{b1} + e_{c1}) + 3(e_3 + e_9 + e_{15} + \dots) \\ &= 3(e_3 + e_9 + e_{15} + \dots) \end{aligned} \quad (5.5)$$

Then, with the aid of the Y-connected resistor network as shown in Fig. 5.1, (5.6) could be derived as

$$\begin{cases} u_{as} + u_{bs} + u_{cs} = i_{as} R_1 + i_{bs} R_2 + i_{cs} R_3 \\ u_{as} = u_{an} - u_{sn} \\ u_{bs} = u_{bn} - u_{sn} \\ u_{cs} = u_{cn} - u_{sn} \end{cases} \quad (5.6)$$

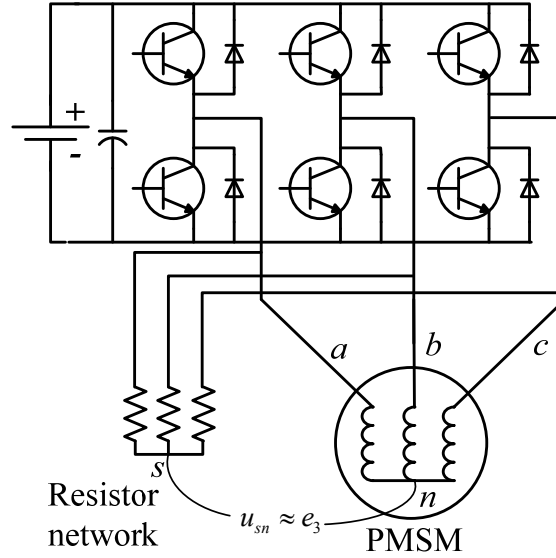


Fig. 5.1. Measurement of third harmonic back-EMF

When the resistor network is balanced, the voltage between the central point “s” of the resistor network and the machine winding neutral point “n” could be expressed as

$$\begin{aligned}
 u_{sn} &= \frac{(u_{an} + u_{bn} + u_{cn})}{3} - \frac{(u_{as} + u_{bs} + u_{cs})}{3} \\
 &= \frac{(u_{an} + u_{bn} + u_{cn})}{3} - \frac{(i_{as}R_1 + i_{bs}R_2 + i_{cs}R_3)}{3} \\
 &= \frac{(u_{an} + u_{bn} + u_{cn})}{3}
 \end{aligned} \tag{5.7}$$

From (5.5) and (5.7), u_{sn} is derived as

$$u_{sn} = e_3 + e_9 + e_{15} + \dots = e_{triplen} \tag{5.8}$$

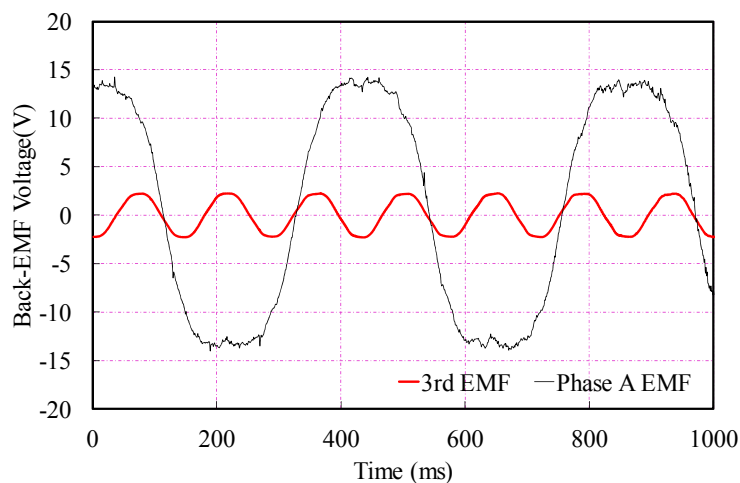
Usually, $e_3 \gg (e_9 + e_{15} + \dots)$, hence

$$u_{sn} = e_{triplen} \approx e_3 \tag{5.9}$$

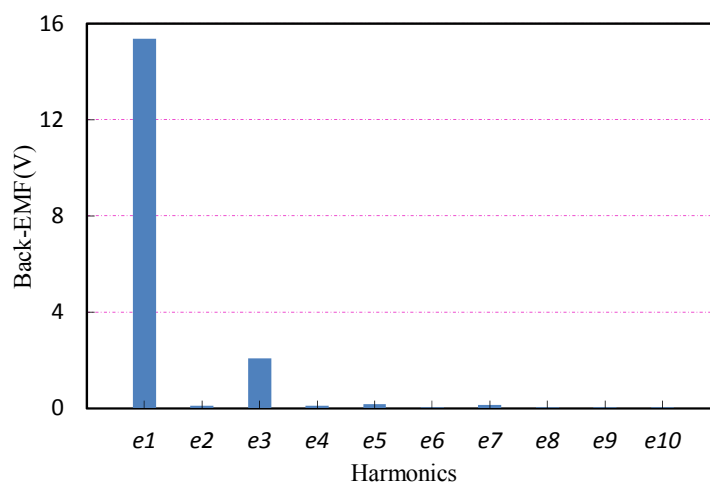
Clearly, on the condition of third harmonic much bigger than other higher order triplen harmonics, the voltage u_{sn} could just represent third harmonic back-EMF irrespective of the operational mode of the PMSM. It is theoretically free of noise and has the advantage of insensitivity to machine and controller parameters than many other sensorless control strategies.

u_{sn} of Motor II which is a 3kW laboratory surface-mounted PMSM can be measured with the aid of 10kΩ sensing resistor network at 10rpm when the windings

are open-circuit, are shown in Fig. 5.2(a) compared with the corresponding phase-A back-EMF. FFT analysis of the measured phase-A back-EMF in Fig. 5.2(b) shows that the third harmonic back-EMF e_3 is predominant compared with other harmonics. Hence, it can be seen that u_{sn} contains third harmonic back-EMF only.



(a) Phase Back-EMF and measured u_{sn}



(b) Spectrum of phase back-EMF

Fig. 5.2. Phase A and third harmonic back-EMF and harmonic analysis.

5.2.2 Conventional Sensorless Control

The waveforms of u_{sn} and its integration ψ_{sn} which is the third harmonic flux-linkage are demonstrated in Fig. 5.3 compared with the electrical rotor position. However, one electrical period contains three identical cycles of third harmonic back-EMF. Hence, with the aid of the zero-crossing of u_{a} , the first related rotor position

θ_0 of zero-crossings of ψ_{sn} which is $\pi/6$ can be located. Once the first θ_0 is obtained, it can be latched, and the followed discrete positions which are $\pi/2$, $5\pi/6$, $7\pi/6$, $11\pi/6$, $3\pi/2$ could also be located as shown in Fig. 5.4. These discrete rotor positions can be directly employed for BLDC PM Machine control. However, continuous rotor position information with high resolution is required for PMSM drives or if phase-advancing control is applied in BLDC drives.

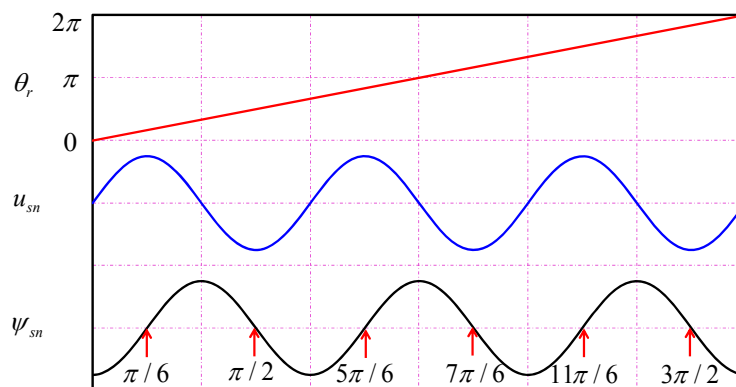


Fig. 5.3. Relationship of u_{sn} , its integration ψ_{sn} and rotor position

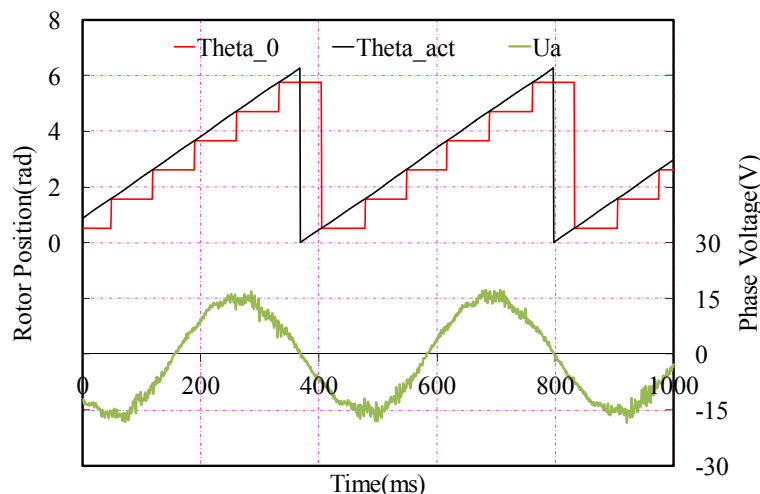


Fig. 5.4. Related rotor positions θ_0 and phase voltage

(θ_0 : Initial rotor position of each zero-crossing of ψ_{sn} , θ_{act} : Actual rotor position, U_a : Measured phase terminal voltage)

Then, the high resolution estimated rotor position θ_r^e can be calculated by simple integration as

$$\theta_r^e = \theta_0 + \int_0^t \omega_{ra}^e dt \quad (5.10)$$

where ω_r^e is the estimated rotor speed which can be calculated by

$$\omega_{ra}^e = \frac{\pi/3}{t_d} \quad (5.11)$$

where t_d is the time interval of the previous half cycle between two zero-crossings of ψ_{sn} [SHE04].

ω_{ra}^e in (5.10) is actually the estimated average speed between the last two zero-crossings of ψ_{sn} rather than the instantaneous speed during the rotor position estimation. The rotor position will be accurate during the steady-state (10rpm with 1A load current), Fig. 5.5, since the rotor speed would not change ideally. Furthermore, on each zero-crossing point, the estimated rotor position which contains some error due to the inaccurate speed estimation will be forcedly set as the related θ_0 . Hence, the rotor position estimation error will not be accumulated.

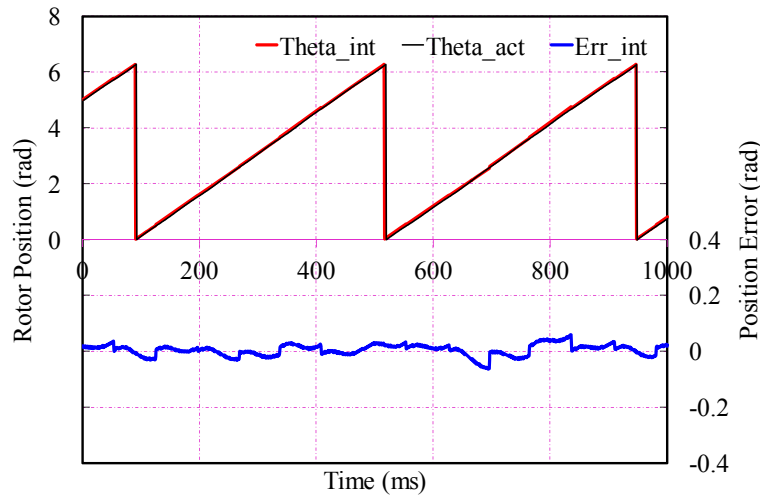
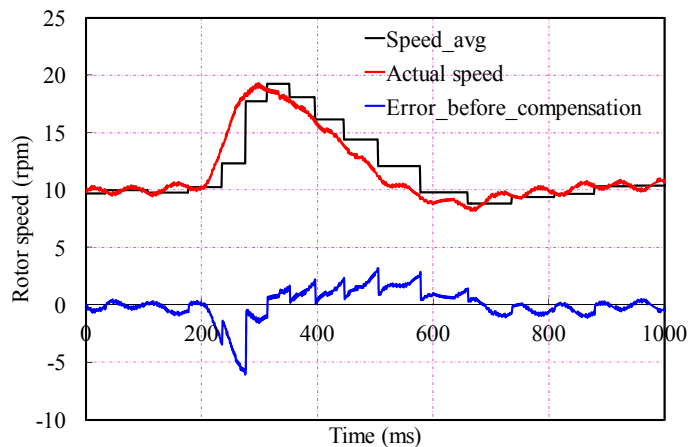


Fig. 5.5. Rotor position at steady-state

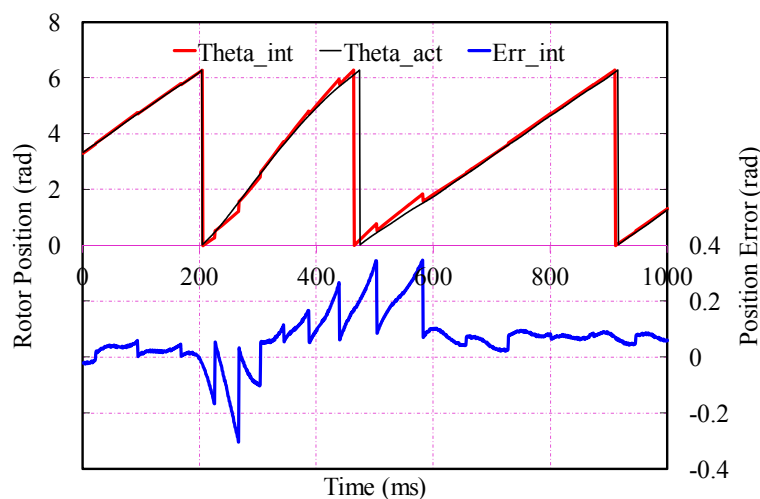
(θ_{int} : Estimated rotor position by integration, θ_{act} : Actual rotor position, Err_{int} : Position estimation error by integration)

However, during variable speed operation, the estimated average speed ω_{ra}^e is not fast enough to reflect the speed change, e.g. with the calculated rotor speed which

have an interruption as shown in Fig. 5.6(a) when the rotor initial speed is 10rpm with the load current changing from 1A to 3A. Hence, the estimated rotor position will appear with sharp changes at each zero-crossing, Fig. 5.6(b).



(a) Rotor speed calculated by zero-crossings



(b) Dynamic rotor position

Fig. 5.6. Dynamic performance (*Speed_avg*: Average speed ω_{ra}^e , *Actual_Speed*: Actual rotor speed, *Error_before_compensation*: Rotor speed estimation error, *Theta_int*: Estimated rotor position by integration, *Theta_act*: Actual rotor position, *Err_int*: Position estimation error by integration)

If the rotor speed is high enough, and the speed variation is not too much, the error accumulation will not be great, and will be reset to zero when zero-crossing is detected. However, with the low speed, the sharp change of the estimated rotor

position will be significant and degrade the operating performance such as current distortion and torque pulsation. Employing the Phase-locked loop (PLL) based rotor speed observer can improve the speed estimation performance, whereas the insufficient discrete rotor positions from zero-crossings of ψ_{sn} will limit the performance. Hence, to improve the dynamic performance, these rotor errors should be compensated.

5.3 Improved Rotor Position Estimator

5.3.1 Rotor Position Estimator based on Zero-Crossing Correction

As mentioned in Section 5.2, the estimated rotor position will appear with sharp changes at each zero-crossing under dynamic situation which will degrade the operating performance. To avoid this sharp change, the rotor position estimator based on zero-crossing correction shown in Fig. 5.7 is implemented. Similarly, with the aid of the zero-crossing of the phase-A terminal voltage u_a , the related rotor position θ_0 of each zero-crossing could be located and applied as reference. And then, on each zero-crossing, rotor position difference between the estimated rotor position and the related reference θ_0 can be calculated and equivalent as the estimation error between the estimated and actual rotor positions. Then, a speed correction ω_{cor} can be obtained by the following PI controller as

$$\omega_{cor} = -\left(k_p + \frac{k_i \cdot \Delta t_s}{1 + z^{-1}}\right) \cdot [\Delta\theta \cdot \text{sign}(\omega_r^e)] \quad (5.12)$$

where the sign function $\text{sign}(\omega_r^e)$ is to reflect the rotor rotation direction, Δt_s is the sampling interval, and k_p and k_i represent the proportional and integral gains, respectively.

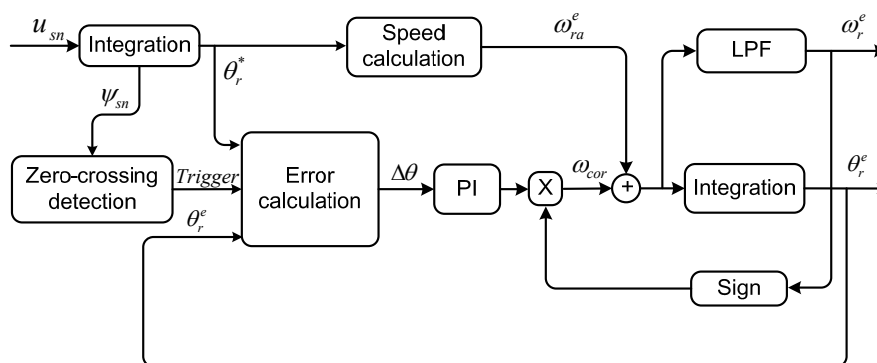


Fig. 5.7. Zero-crossing based position estimator.

In (5.12) speed correction ω_{cor} is corresponding to the position estimation error, i.e. the rotor position difference between the estimated and related reference θ_0 on each zero-crossing. Then, the average rotor speed ω_{ra}^e calculated from the zero-crossings of ψ_{sn} will be appropriately corrected, and the estimated rotor speed ω_r^e is converged to the actual value. Therefore, the high resolution rotor position can be estimated by simple integration.

The overall control scheme with the proposed rotor position estimator based on third harmonic back-EMF is shown in Fig. 5.8 which has been implemented on the dSPACE platform with Test Rig II. Then, the estimated and actual rotor positions and the errors between them shown in Fig. 5.9 shows steady-state performance is nearly as good as conventional sensorless method.

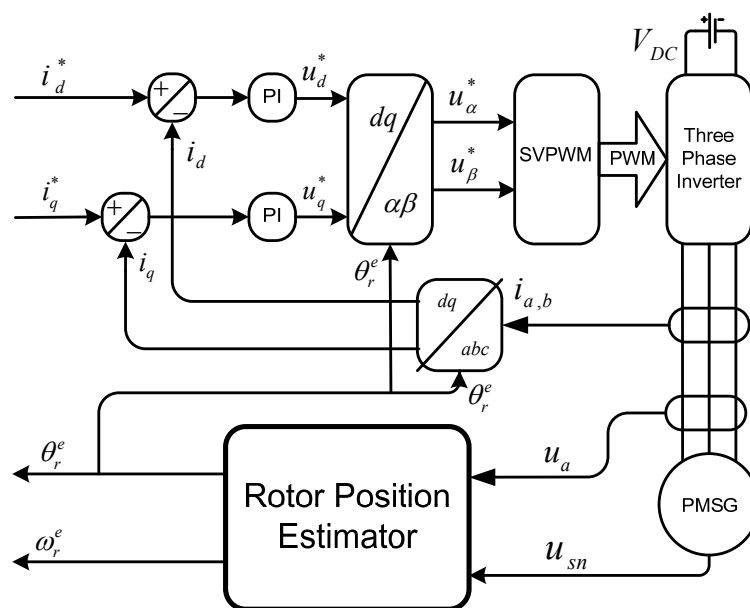


Fig. 5.8. Overall control scheme

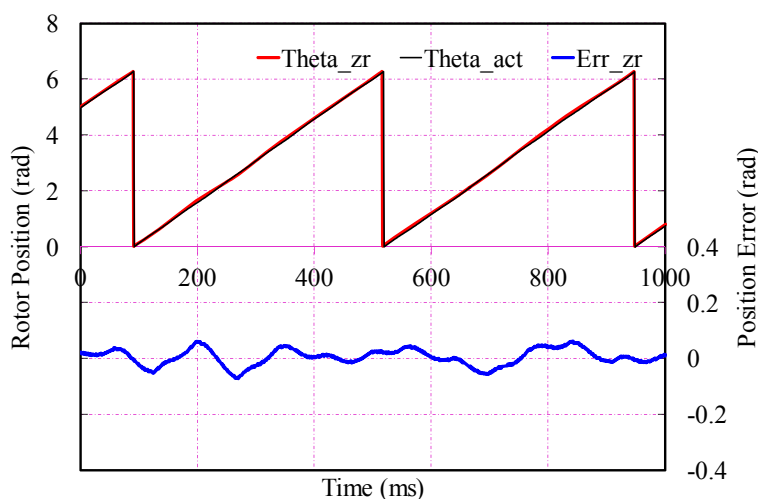


Fig. 5.9. Steady-state performance of the estimator based on zero-crossings
 (θ_{zr} : Estimated rotor position, θ_{act} : Actual rotor position, Err_{zr} : Position estimation error)

Similar to the rotor position estimator based on integration, as long as the rotor speed is not too low, and varies not too significantly, the error accumulation will not be great, and will be reset to zero when zero-crossing is detected. However, for low speed application with dynamic performance requirement, the speed calculation error cannot be neglected. Powered by the estimator, speed error during expected speed change could be compensated. However, ω_{cor} will only refresh on each zero-crossing.

Consequently, the proportional gain k_p and integral gain k_i in PI controller cannot be big enough in order to avoid divergence. Hence, under the situation of random speed change with low speed, the PI controller cannot follow the speed variation due to the insufficient resolution of only six accurate rotor position references. Thus the dynamic performance will still not be good enough. Applying with the same dynamic situation as in Fig. 5.6(a), experimental results from the estimator based on zero-crossings as shown in Fig. 5.10 illustrates that the method could avoid these sharp changes. However, the estimation error is still too big to be satisfied for dynamic control.

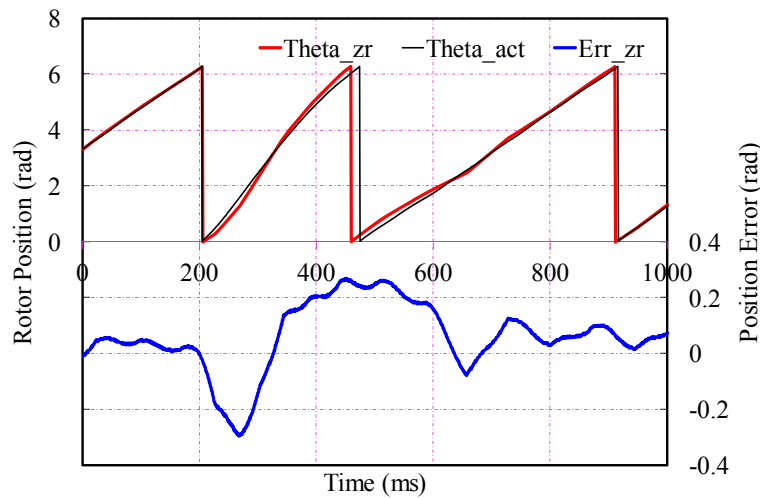


Fig. 5.10. Dynamic performance of the estimator based on zero-crossings (θ_{zr} : Estimated rotor position, θ_{act} : Actual rotor position, err_{zr} : Position estimation error)

5.3.2 Improved Rotor Position Estimator Based on Speed Compensation

5.3.2.1 Improved rotor position estimator

As mentioned above, ω_{ra}^e is the estimated average speed between the last two zero-crossings of ψ_{sn} . The estimated rotor position based on that average speed will be accurate during the steady-state operation and inaccurate during variable-speed operation. Therefore, to improve the dynamic performance, the speed compensation is of great importance.

Considering that the third harmonic back-EMF is much bigger than any other triplen harmonics, and then the measured u_{sn} will contain third harmonic back-EMF only. Therefore, its integration ψ_{sn} will be a continuous sinusoidal signal with constant amplitude. Consequently, the continuous sinusoidal signal of ψ_{sn} can be used as reference to compensate the estimation error of the calculated average speed and furthermore to extract the high resolution rotor position at each sampling time for sensorless control.

The block diagram of improved rotor position estimator based on continuous signal of ψ_{sn} is shown in Fig. 5.11 where ψ_{sn}^e is the virtual third harmonic flux-linkage calculated from the estimated rotor position. If the estimated rotor position and speed are the same as the actual values, ψ_{sn} and ψ_{sn}^e should be in-phase with each other. In contrast, they will be out of phase when there is estimation error between the estimated and actual values. And the phase difference between the two signals could be used to estimate the rotor position.

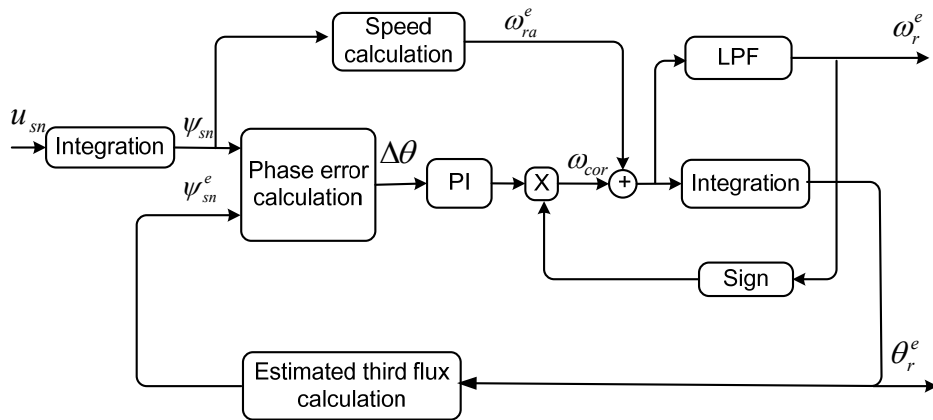


Fig. 5.11. Improved rotor position estimator based on speed compensation

ψ_{sn} can be defined as

$$\psi_{sn} = -A_{mp} \cos(3 \times \theta_r) \quad (5.13)$$

where A_{mp} is the amplitude of ψ_{sn} which could be obtained from the absolute value of ψ_{sn} when its differential is close to zero. Although A_{mp} is normally constant, it also

should be detected in every few cycles to avoid the amplitude variation caused by the temperature effect of PM.

To estimate the rotor position, the related orthogonal signal of ψ_{sn} also should be calculated as supplementary signal based on u_{sn} . However, since the amplitude of u_{sn} varies with rotor speed, it should be unified as A_{mp} considering the feedback estimated rotor speed ω_r^e as

$$u_{sn_unified} = \frac{K_p}{\omega_r^e} E_3 \sin(3 \times \theta_r) = A_{mp} \sin(3 \times \theta_r) \quad (5.14)$$

where K_p is the unify-ratio of the amplitudes of the third harmonic flux-linkage and back-EMF. The measured ψ_{sn} and $u_{sn_unified}$ are shown in Fig. 5.12.

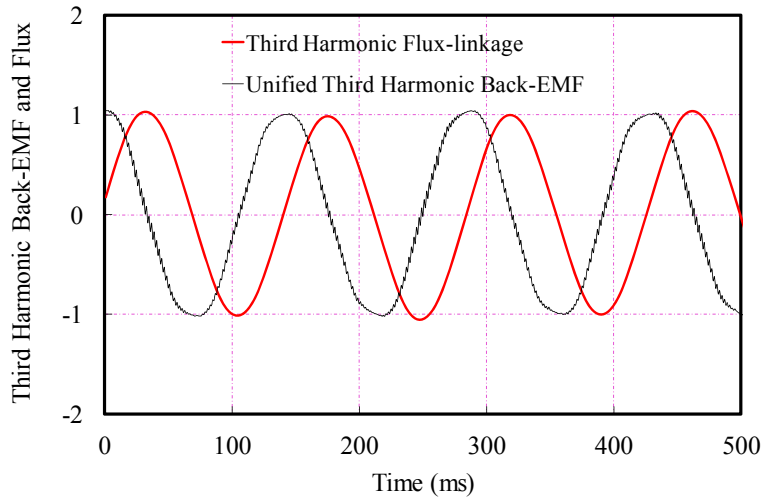


Fig. 5.12. ψ_{sn} and $u_{sn_unified}$ by experiment

Consequently, $\Delta\theta$ between the actual and estimated third harmonic flux-linkages can be derived as

$$\Delta\theta = -A_{mp} \arcsin[\psi_{sn} \times \sin(3 \times \theta_r^e) + u_{sn_unified} \times \cos(3 \times \theta_r^e)] \quad (5.15)$$

The phase difference $\Delta\theta$ is also equivalent to three times of the rotor position estimation error between the estimated and actual rotor positions. Then, the speed correction ω_{cor} which corresponds to the speed estimation error can be derived by the following PI controller as a loop filter as same as the one in (5.12) from the phase difference $\Delta\theta$. Then, the rotor speed derived from zero-crossings or by PLL both

including the intrinsic speed errors, is appropriately corrected, and the estimated rotor speed ω_{ra}^e including the intrinsic speed error can be appropriately corrected, and the estimated rotor speed ω_r^e will converge to the actual value. Consequently, the high resolution rotor position can be estimated by simple integration with high accuracy from the compensated speed. Even though the source signals may contain certain noise and high order harmonic components such as ninth, fifteenth and so far, it can be eliminated by the proposed estimator and will almost not affect the accuracy of rotor speed estimation.

However, one cycle of back-EMF contains three identical cycles of third harmonic back-EMF and the estimated rotor position may align to the other two cycles of third harmonics rather than the correct one. Therefore, the phase-A back-EMF should be considered to avoid the mis-alignment. On the zero-crossing point of Phase-A back-EMF calculated by a rough flux observer, the estimated rotor position should be located between $-\pi/3$ and $\pi/3$. If the rotor position is out of range, then based on the rotor position estimation error, a rotor position bias which is $-2\pi/3$ or $2\pi/3$ needs to be added to the estimated rotor position. Hence, the accurate rotor position can be derived.

5.3.2.2 Performance evaluation of improved estimator

The improved rotor position estimator based on continuous signal of ψ_{sn} can be equivalently transformed to a linear model as shown in Fig. 5.13 from which the open-loop transfer function of the estimator is derived as

$$G(s) = \frac{\theta_r^e}{\theta_r^*} = 3 \times A_p (G_1 + G_2) G_3 = 3(G_1 + k_p + \frac{k_i}{s}) \frac{1}{s} \quad (5.16)$$

where G_1 is the rotor speed calculation block which normally is the differential operator s . However, since the rotor speed ω_r can be calculated from the zero-crossings of ψ_{sn} or by PLL based speed observer rather than differential operation, G_1 will be different. Hence, the estimator cannot be treated as a typical second order linear model nor evaluated by conventional analysis method.

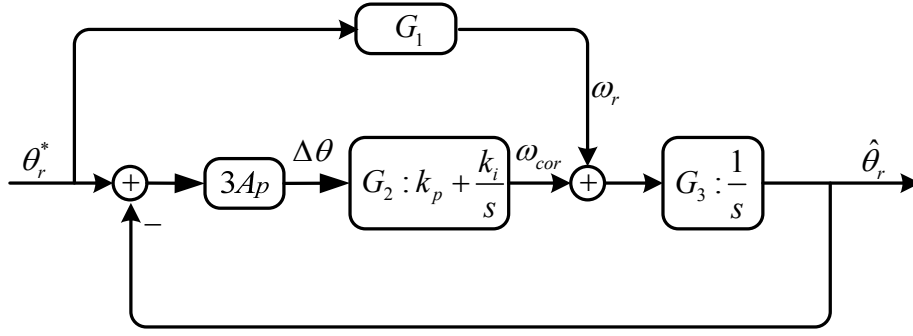


Fig. 5.13. Equivalent linear model.

For the speed calculation from zero-crossings of ψ_{sn} , the time interval t_d of the previous cycle between the zero-crossings of ψ_{sn} is equivalently seen as the speed calculation sampling time and can be calculated as

$$t_d = \frac{2\pi}{\omega} \cdot \frac{1}{6} \quad (5.17)$$

Compared with the system sampling time t_s which is $4e-4$ s in the testing system, G_1 can be equivalently shown as

$$G_1 = \frac{t_s}{t_d} s = \frac{4 \times 10^{-4}}{\left(\frac{2\pi}{\omega} \cdot \frac{1}{6}\right)} s = (12 \times 10^{-4}) \times \frac{\omega}{\pi} s \quad (5.18)$$

Then, the open-loop transfer function of the estimator will be

$$G(s) = \frac{\theta_r^e}{\theta_r^*} = 3 \times A_p \left((12 \times 10^{-4}) \frac{\omega}{\pi} s + k_p + \frac{k_i}{s} \right) \frac{1}{s} \quad (5.19)$$

Since $s=j\omega$, (5.19) can be rewritten as

$$G(\omega) = \frac{\theta_r^e}{\theta_r^*} = -j \frac{3A_p k_p}{\omega} + \left[3A_p (12 \times 10^{-4}) \frac{\omega}{\pi} - \frac{3A_p k_i}{\omega^2} \right] \quad (5.20)$$

To make sure the estimator can achieve accurate estimation performance, the magnitude of the frequency response must be larger than -3dB over the entire speed range with about 200% margin. Based on the unified amplitude A_p , the parameters of PI controller are selected as $k_p=500$ and $k_i=200$. Then, the open loop frequency response of the improved rotor position estimator can be derived as shown in Fig. 5.14, where the frequency with -3dB magnitude attenuation is about 107Hz.

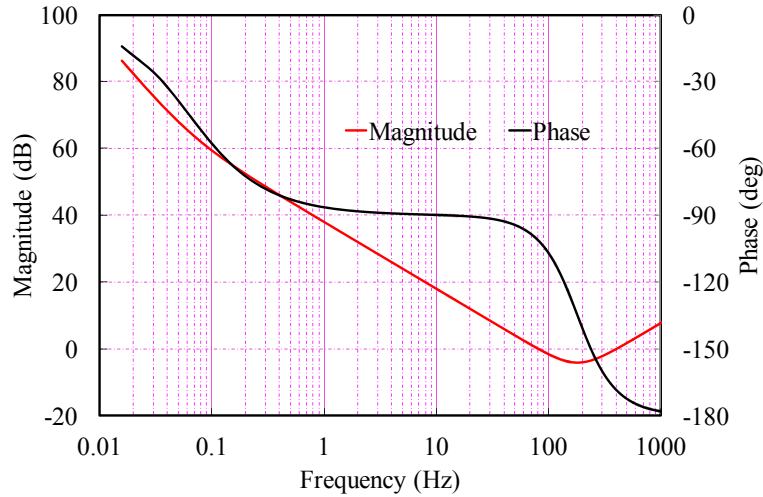


Fig. 5.14. Frequency response of the estimator with zero-crossings based speed estimation.

For the speed calculation by PLL based speed observer which can be equivalent as a second order linear model as

$$G(s)_{PLL} = \frac{(2\xi\omega_n s + \omega_n^2) \cdot s}{s^2 + 2\xi\omega_n s + \omega_n^2} \quad (5.21)$$

The overall open loop transfer function can be written as

$$G(s) = \frac{\theta_r^e}{\theta_r^*} = 3 \times A_p \left[\frac{(2\xi\omega_n s + \omega_n^2) \cdot s}{s^2 + 2\xi\omega_n s + \omega_n^2} \cdot k_p + \frac{k_i}{s} \right] \cdot \frac{1}{s} \quad (5.22)$$

Referring to the standard second order system, the parameters of PLL based observer are configured with a damping factor ξ of 0.707 and ω_n of 300rad/s (about 200rpm). Then, by using the same PI controller parameters which are selected as $k_p=500$ and $k_i=200$, the open-loop frequency response can be derived as shown in Fig. 5.15. From the frequency response analysis, it can be found that with the same PI parameters, the estimator based on the PLL can achieve the same magnitude attenuation as the one based on zero-crossings. For the phase response, the high frequency performance of estimator with the speed estimation based on the PLL is expected to be better than the one with zero-crossing based speed estimation, whereas the low frequency performance is worse.

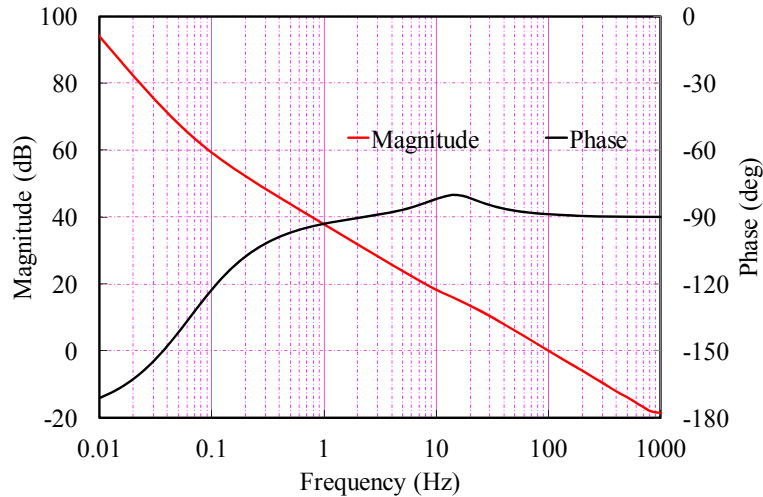


Fig. 5.15. Frequency response of the estimator with PLL based speed estimation.

From these frequency response analyses, it can be found that the estimator has good frequency response over a wide frequency range from 0.2 to 100Hz which are equivalent from 0.85 to 428 rpm of mechanical speed. In the real testing system, the rated speed is 170rpm. Hence, over the whole operation range of speed, the improved rotor position estimator can achieve good frequency response with low magnitude attenuation and phase delay.

It can be found that, several PI or PID regulators are contained in the rotor position estimation algorithm, and each regulator should be tuned to achieve the specified close-loop bandwidth in order to reach optimum control performance. Each closed-loop control algorithm can be equivalently seen as a linear model. With different types of regulator, the equivalent linear model has different order and frequency response. Usually, an equivalent second order linear model with a damping factor ξ of 0.707 is preferred since it has very good dynamic performance without overshooting. However, at different operating condition, the optimum parameters are also different, which makes the optimization process with significant difficulty. Meanwhile, the risk of unstable situation of the whole control system with unsuitable parameters of any regulator is also obvious. Hence, the parameter tuning is of great importance, and should be treated very carefully.

5.3.2.3 Steady-state and dynamic performance

Several experiments have been carried out to validate the proposed rotor position estimator and the overall control scheme is the same as in Fig. 5.8. The estimated and actual rotor positions and the errors between them from the improved rotor position estimator based on continuous signal of ψ_{sn} at 10rpm rotor speed with 1A load current are shown in Fig. 5.16. Compared result with the ones shown in Fig. 5.5 and Fig. 5.9, the improved estimator has better steady-state performance with lower phase error than the other two methods.

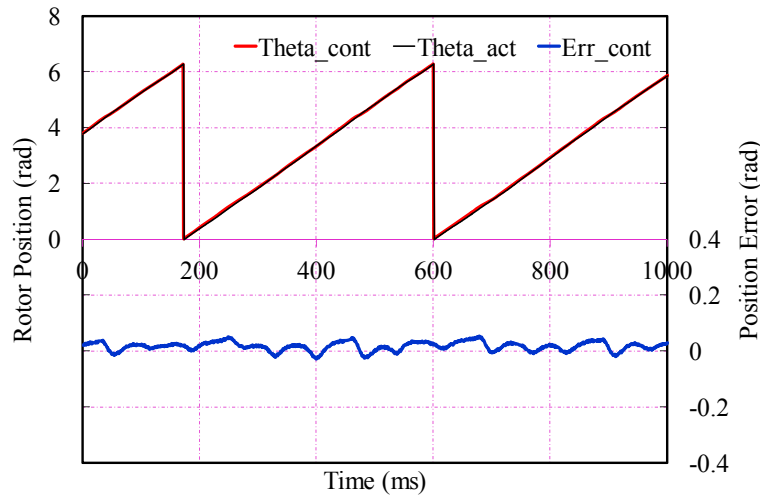
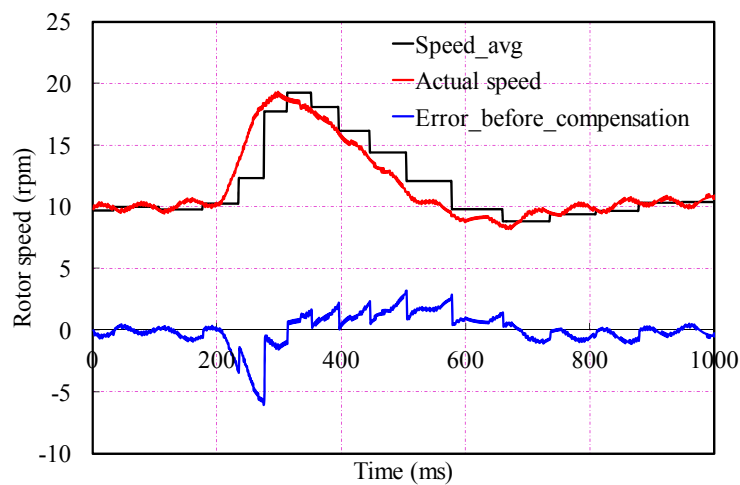


Fig. 5.16. Rotor positions and the error based on the improved estimator (*Theta_cont*: Estimated rotor position, *Theta_act*: Actual rotor position, *Err_cont*: Position estimation error)

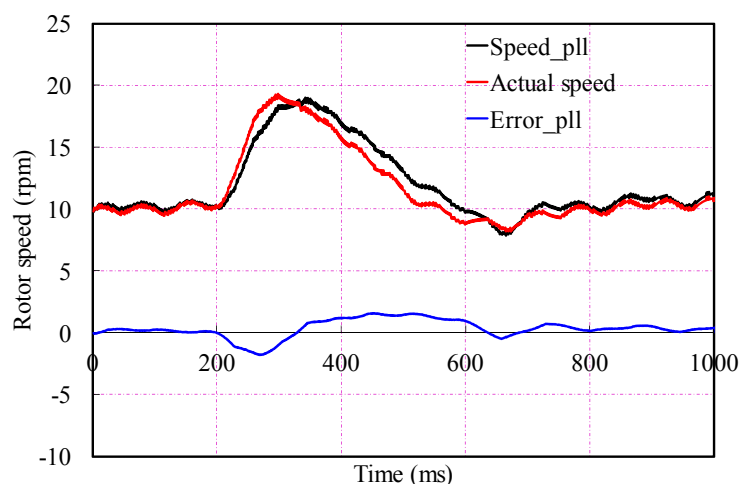
Applying with the same dynamic situation as in Fig. 5.6(a), Fig. 5.17 (a) and (b) show the rotor positions from the estimators based on integration and zero-crossing correction, respectively, and the estimation errors compared with the actual rotor position from the encoder. The sharp changes of the estimated rotor position in Fig. 5.17(a) which will degrade the operating performance with current and torque pulsation is compensated by the estimator based on zero-crossing correction, Fig. 5.17(b). However, the estimation error is still too large to be satisfied for machine dynamic control. Fig. 5.17(c) shows the rotor positions and the error from the improved rotor position estimator based on continuous signal of ψ_{sn} , where the rotor position error is

significantly reduced by the improved estimator. Hence, better dynamic performance compared with the other estimators is expected to be achieved.

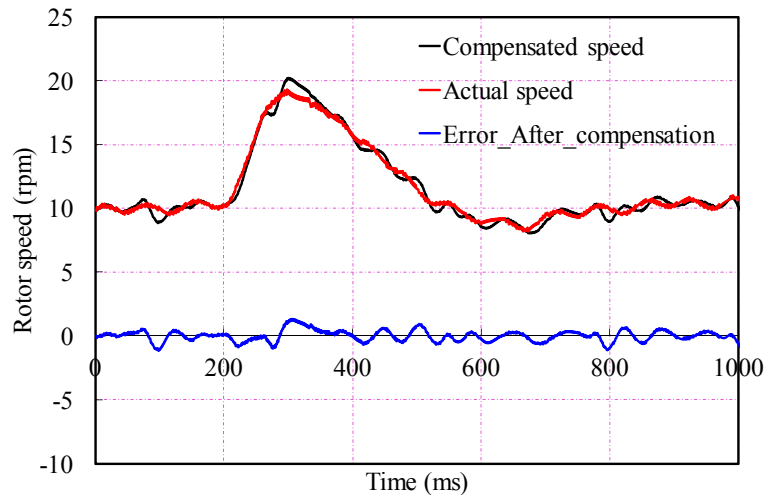
Fig. 5.18 shows the rotor positions and the error from the improved rotor position estimator based on continuous signal of ψ_{sn} for speed compensation. It can be seen that the rotor position error is significantly reduced by the improved estimator and can achieve much better dynamic performance than the performance of the other estimators as shown in Fig. 5.6(b) and Fig. 5.10.



(a) Rotor speed calculated by zero-crossings (*Speed_avg*: Average speed ω_{ra}^e , *Actual_Speed*: Actual rotor speed, *Error_before_compensation*: Rotor speed estimation error before compensation)



(b) Rotor speed derived by PLL observer (*Speed_pll*: speed estimated by PLL observer, *Actual_Speed*: Actual rotor speed, *Error_pll*: Compensated rotor speed error by PLL observer)



(c) Compensated rotor speed by improved estimator (*Compensated Speed*: Compensated rotor speed, *Actual Speed*: Actual rotor speed, *Error_After_Compensation*: compensated rotor speed error)

Fig. 5.17. Rotor speed responses.

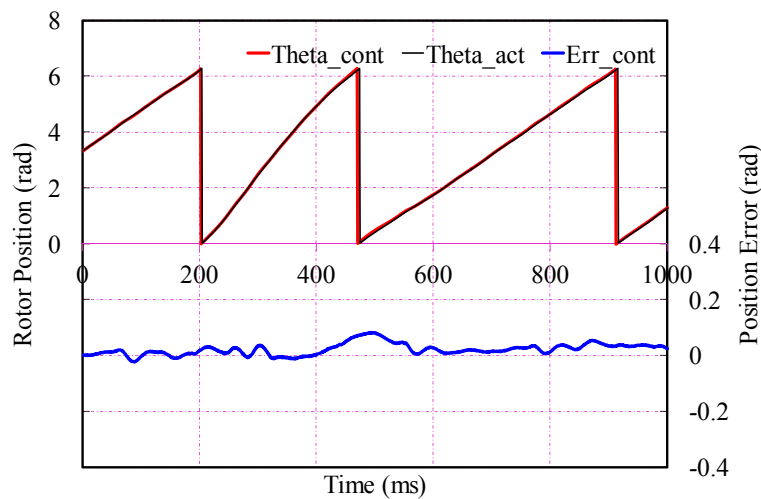
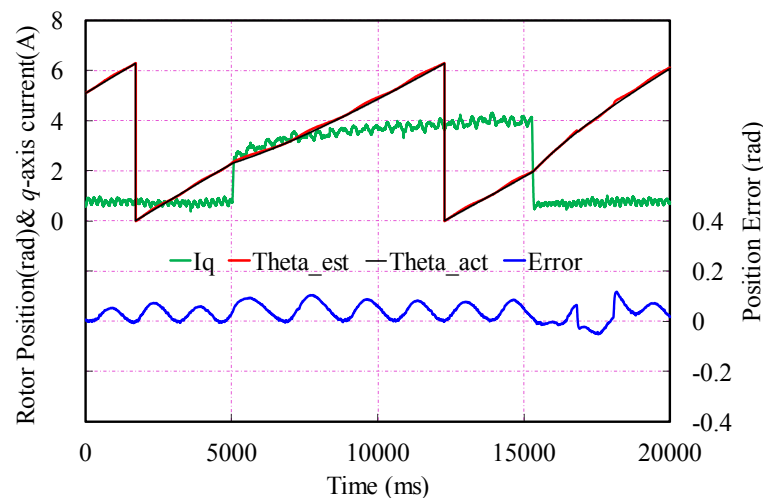


Fig. 5.18. Rotor positions and error based on improved estimator.

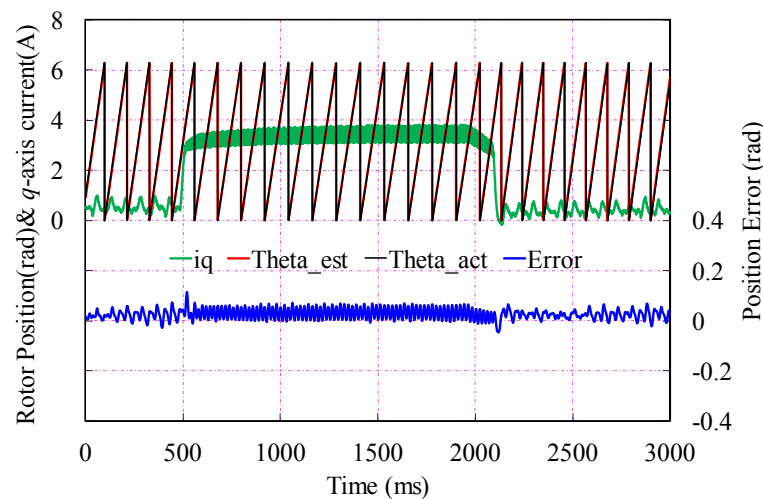
(*Theta_cont*: Estimated rotor position, *Theta_act*: Actual rotor position, *Err_cont*: Position estimation error)

To investigate the influence of speed and load to the proposed improved estimator, several experiments at different speeds with step load change are executed. When the rotor speed is lower than 1rpm (0.25Hz), the proposed improved estimator fails to estimate the rotor position due to the too low signal to noise ratio of the measured third harmonic back-EMF. If the rotor speed is higher than 2rpm (0.5Hz),

the estimator can exhibit good performance with accepted estimation error. The experimental results when the rotor speed is about 2rpm and the load current step change from 0.5A to 4A and then back to 0.5A are shown in Fig. 5.19(a). When the rotor speed is 170rpm which is the rated speed with the same step load change, the experimental results are shown in Fig. 5.19(b). From the experimental results, it can be concluded that the improved estimator can achieve good performance at different speed condition against step load change.



(a) Step load test at 2rpm



(b) Step load test at rated 170rpm

Fig. 5.19. Step load tests at different speed.

(*iq*: *q*-axis current, *Theta_est*: Estimated rotor position, *Theta_act*: Actual rotor position, *Error*: Position estimation error)

When the rotor speed starts from -20rpm with about 110rad/s² acceleration to the

rated speed 170rpm, the estimated rotor position and estimation error are shown in Fig. 5.20. It can be found that the improved estimator can achieve good performance over nearly whole range of operating speed except when the speed is closed to zero.

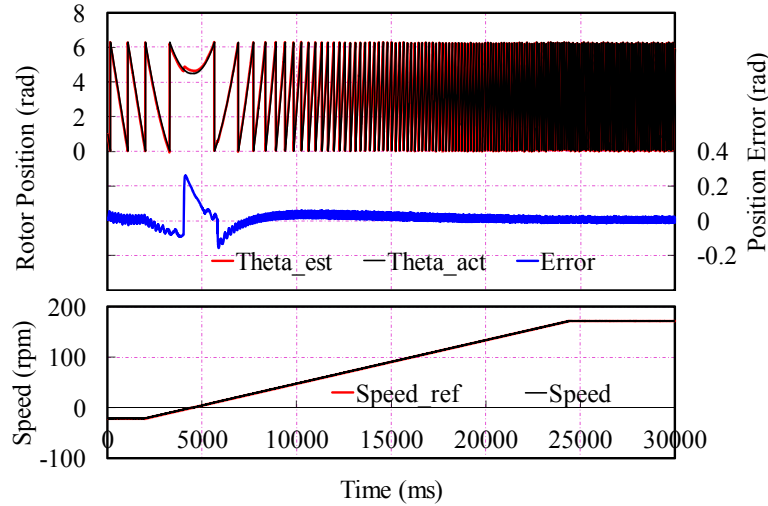


Fig. 5.20. Test with speed acceleration.

(θ_{est} : Estimated rotor position, θ_{act} : Actual rotor position, $Error$: Position estimation error, $Speed_{ref}$: reference speed, $Speed$: Actual rotor speed)

5.4 Comparison and Improvement of Flux Observer based on Third Harmonic Back-EMF by Error Compensation

Flux observer based sensorless control technique is widely applied for PMSM drives. However, this technique is highly sensitive to the accuracy of machine and controller parameters. However, the third harmonic back-EMF is not affected by the accuracy of machine and controller parameters. Hence, to improve the performance and the robustness, a multi-technology fusion technique is proposed based on concept of error compensation of rotor position or speed which has been introduced in Section 5.3.

5.4.1 Position Estimation from Flux Observer

For the flux observer, the rotor position is derived from the observed vector of PM excitation flux-linkage which is calculated from the integration of back-EMF under stationary reference frame. Then the relative phase angle and speed between the observed vector and the reference frame are the rotor position and speed, respectively,

as shown in Fig. 5.21.

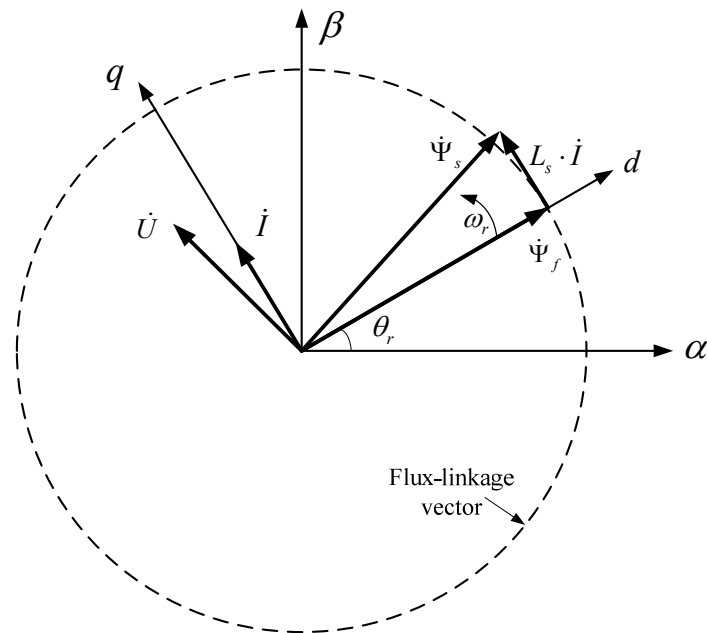
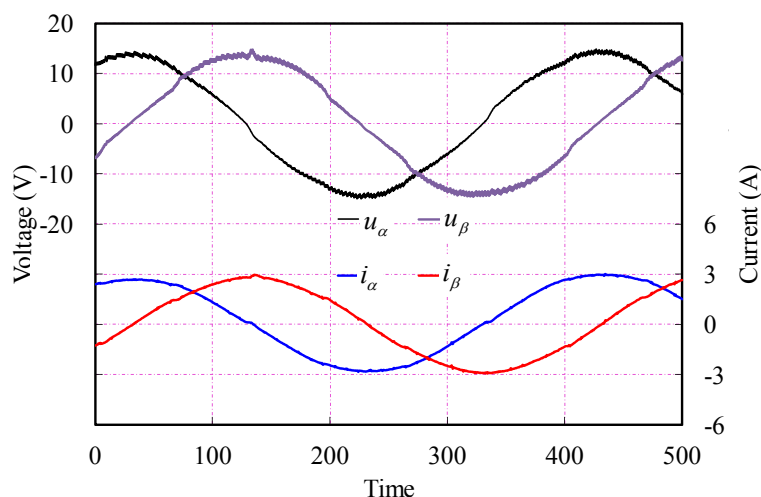


Fig. 5.21. Phasor diagram of PMSM

In order to observe the PM excitation flux-linkage vector, the current vector \dot{I} and the voltage vector \dot{U} in the PMSM is necessary. \dot{I} can be easily obtained from the phase currents which are measured with two or three current transducers. Similarly, \dot{U} can be also obtained from the phase voltages measured with three voltage transducers. However, \dot{U} are usually obtained from the command of the SVPWM generator instead, and to obtain \dot{U} , current closed-loop control is needed, which makes the rotor position information necessary and creates a difficulty for starting the whole control system due to lack of the initial rotor position. And this situation can be solved by the method as introduced in Sector 4.4. The α - and β -axis voltages which are obtained from the command of the SVPWM and the measured α - and β -axis currents are shown in Fig. 5.22.

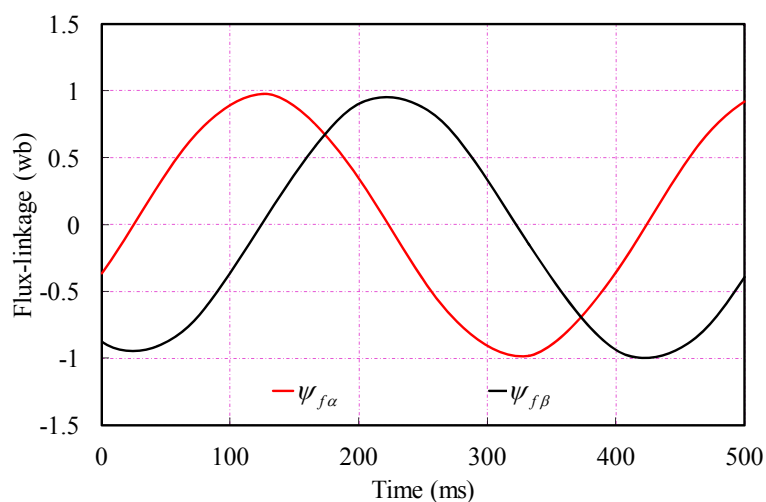
Fig. 5.22. α - and β -axis voltages and currents

Then, the PM excitation flux vector $\dot{\Psi}_f$ can be derived as

$$\dot{\Psi}_f = \int_{t_0}^{t_1} (\dot{U} - R_s \cdot \dot{I}) dt + \dot{\Psi}_{f(0)} - L_s \cdot \dot{I} \quad (5.23)$$

where R_s is the winding resistance, and L_s is the winding inductance. Then, the rotor position can be estimated from the α - and β -parts of $\dot{\Psi}_f$ which is shown in Fig. 5.23, i.e.

$$\theta_f = \arctan \frac{\Psi_{f\beta}}{\Psi_{f\alpha}} \quad (5.24)$$

Fig. 5.23. α - and β -axis flux-linkages

If the rotor is aligned to a certain position before the flux observer begins to work,

$\dot{\Psi}_{f(0)}$ is pre-known. Otherwise, a HPF should be used for minimizing the effect of $\dot{\Psi}_{f(0)}$ [SHE02], or combining the voltage model and current model estimator since this flux observer behaves as a HPF [YOO09].

However, this technique is highly sensitive to the accuracy of machine and controller parameters especially the winding resistance R_s and inductance L_s . Meanwhile, R_s and L_s usually vary when the winding temperature and operating conditions change, and the actual values are very difficult to obtain real-time during operation. In addition, the measured terminal voltage contains PWM components which should be filtered by LPF. Hence, the cut-off frequency of LPF should be low enough, where it will cause unexpected phase delay, whilst the cut-off frequency of HPF also needs to be optimized at different speed. If \dot{U} is obtained from the command of the SVPWM generator it also may differ from actual value due to the inverter dead-time [HAR00] [TER01]. All these issues may deteriorate the position and speed estimation performance.

Fig. 5.24 shows the estimated rotor position obtained from flux observer and the estimation error compared with the actual value at the steady-state of 10rpm speed with 3A load. It can be seen that there is a significant error due to the inaccurate parameters of machine and controller. The dynamic performance test is carried out when the rotor mechanical initial speed is 10rpm and the load current changes from 1A to 3A, Fig. 5.25. The experimental results from flux observer are shown in Fig. 5.26 where the position error shows two obvious step changes. The first change is at approximate 200ms induced by the sudden change of load current, and the inaccurate machine and controller parameters. There is also a second significant step increase around 80ms after the load current increase due to the improper cut-off frequencies of the applied LPF and HPF for rotor position estimation.

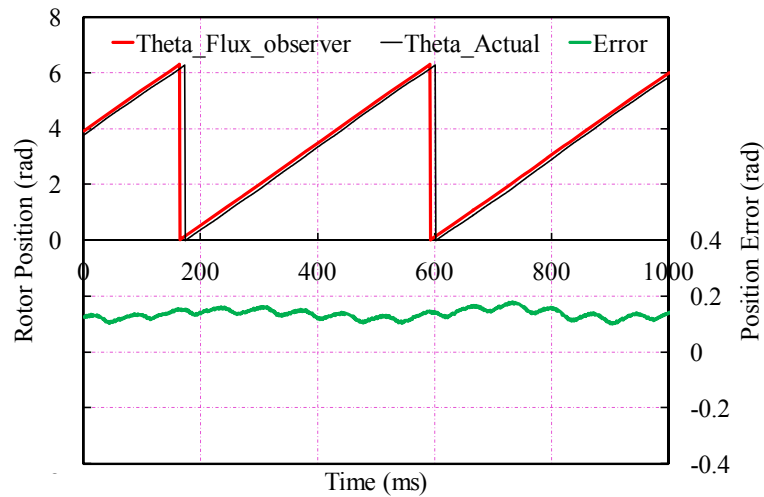


Fig. 5.24. Steady-state performance of flux observer before compensation
 (*Theta_Flux_observer*: Estimated rotor position from flux observer, *Theta_act*: Actual rotor position, *Error*: Position estimation error in flux observer)

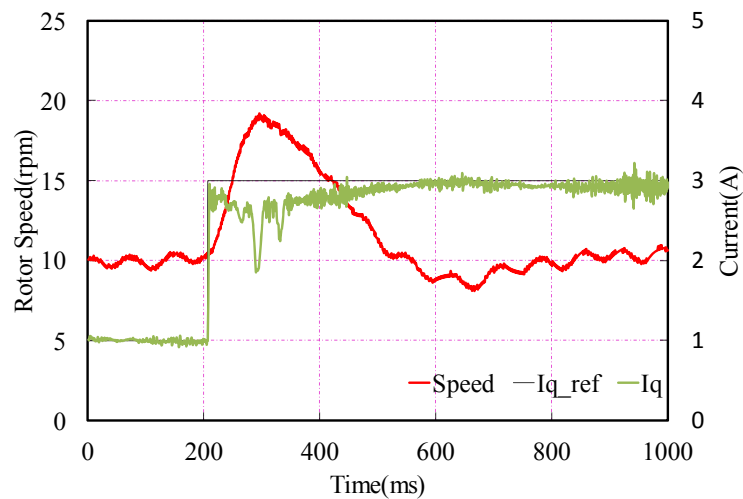


Fig. 5.25. Dynamic test situation
 (*Speed*: Actual rotor speed, *Iq_ref*: *q*-axis current reference, *Iq*: *q*-axis current)

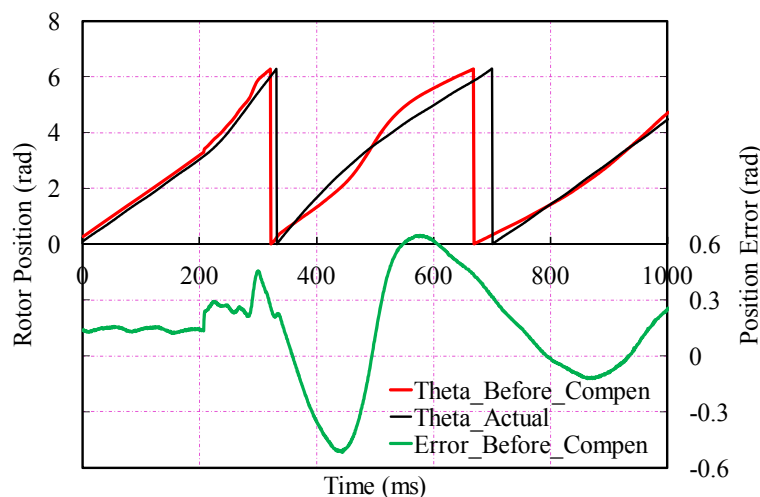


Fig. 5.26. Dynamic performance of flux observer

(*Theta_Before_Compen*: Estimated rotor position from flux observer before error compensation, *Theta_act*: Actual rotor position, *Error_Before_Compen*: Position estimation error in flux observer before error compensation)

5.4.2 Position-Error-Based Compensator

The continuous signal of third-harmonic flux-linkage ψ_{sn} not only can be used for rotor position estimation as discussed in detail in Section 5.2, but also can be employed as reference for rotor position error compensation.

The block diagram of position-error-based compensator is shown in Fig. 5.27 where ψ_{sn}^e is the virtual third harmonic flux-linkage calculated from the estimated rotor position, which is the same as in Fig. 5.11.

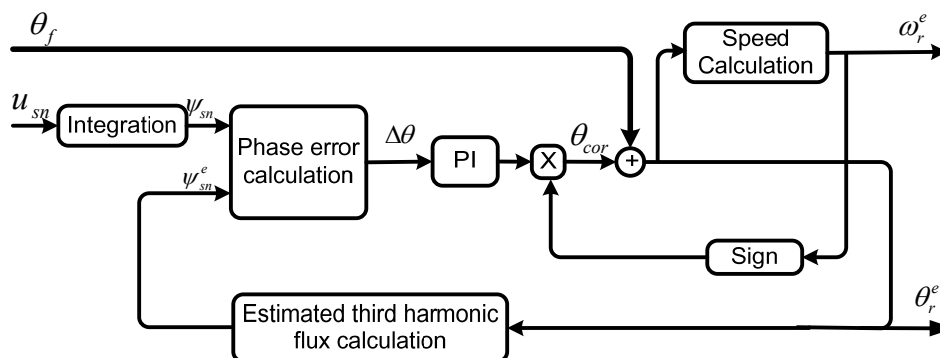


Fig. 5.27. Block diagram of position-error-based compensator

Then, if the estimated rotor position and speed are the same as the actual values, ψ_{sn} and ψ_{sn}^e should be in-phase with each other. In contrast, they will be out of phase as shown in Fig. 5.28 and the phase difference between the two signals can be used for error compensation.

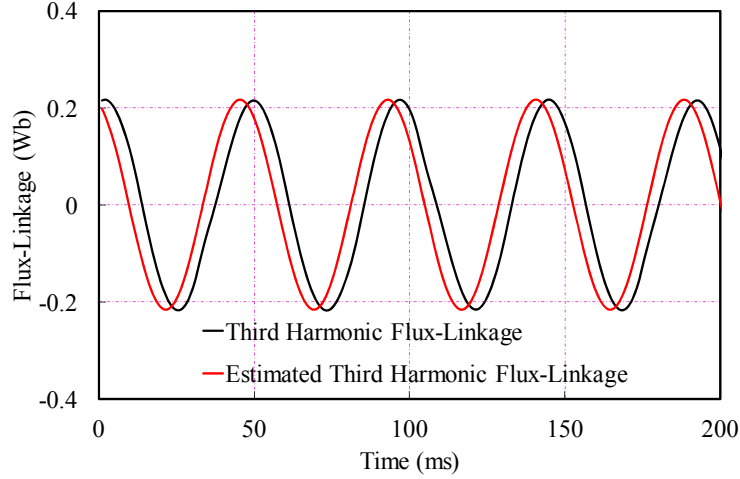


Fig. 5.28. Measured ψ_{sn} and ψ_{sn}^e

To calculate the phase difference, the related orthogonal signal of ψ_{sn} also should be calculated as supplementary signal based on u_{sn} . However, since the amplitude of u_{sn} varies with rotor speed, it should be unified as A_{mp} considering the feedback estimated rotor speed ω_r^e as the same as (5.14). Consequently,

$$\Delta\theta = 1/3 \arcsin[\cos(3 \times \theta_r) \times \sin(3 \times \theta_r^e) - \sin(3 \times \theta_r) \times \cos(3 \times \theta_r^e)] \quad (5.25)$$

Thus, the phase difference $\Delta\theta$ between the estimated and actual third harmonic flux-linkages is derived and can be seen as the rotor position estimation error between the estimated and actual rotor positions. Then, the position correction θ_{cor} which is corresponding to this estimation error can be obtained by the following PI controller as a loop filter of the proposed compensator as

$$\theta_{cor} = -(k_p + \frac{k_i \cdot \Delta t_s}{1+z^{-1}}) \cdot [\Delta\theta \cdot \text{sign}(\omega_r^e)] \quad (5.26)$$

Then, after the system reaches steady-state, the resultant value of (5.26) which is θ_{cor} will converge to zero. Then, the estimated rotor position from flux observer including intrinsic position error is appropriately compensated and converged to the

actual value. Hence, rotor position is derived with high resolution and accuracy. However, one cycle of fundamental back-EMF contains three identical cycles of third harmonic back-EMF. Therefore, the phase-A back-EMF should be considered to avoid the mis-alignment as used by the method in Section 5.3.2.1.

The overall control scheme in Fig. 5.29 has been implemented on a dSPACE platform when Motor II is operating at the steady-state of 10 rpm speed with 3A load.

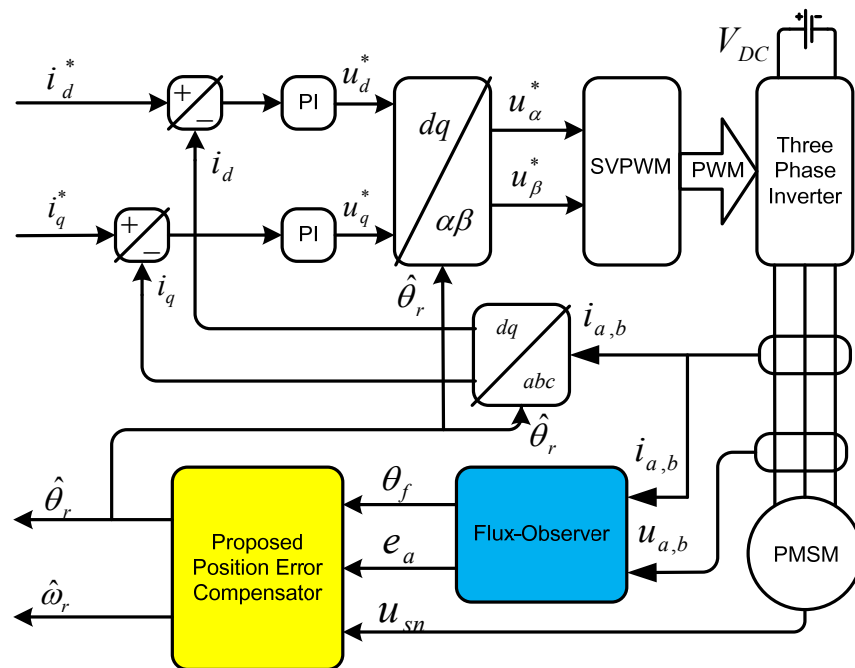
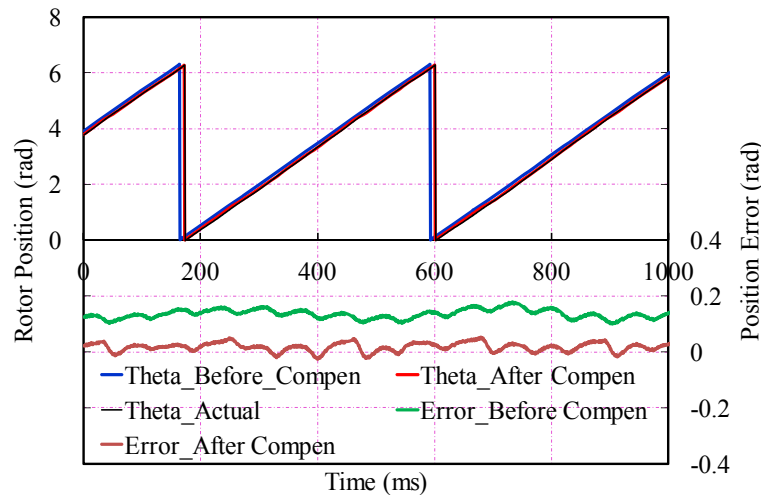
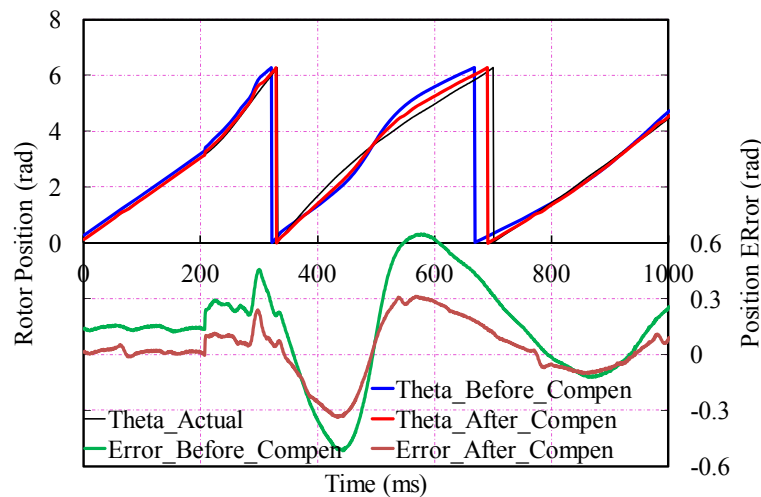


Fig. 5.29. Overall control scheme of PMSM

Then, the estimated rotor positions and the estimation errors before and after compensation from the position-error-based compensator compared with the actual rotor position are shown in Fig. 5.30(a). When the compensator is implemented at the same dynamic as shown in Fig. 5.25, experimental results are shown in Fig. 5.30(b). It is clearly shown that the steady-state estimation error can be significantly minimized; however, the dynamic performance is not so satisfactory.



(a) Steady-state performance



(b) Dynamic performance

Fig. 5.30. Performance of position-error-based compensator

(θ_{act} : Actual rotor position, θ_{Before_Comp} : Estimated rotor position from flux observer before error compensation, e_{Before_Comp} : Position estimation error in flux observer before error compensation, θ_{After_Comp} : Estimated rotor position after error compensation, e_{After_Comp} : Position estimation error after error compensation,)

5.4.3 Improved Speed-Error-Based Compensator

The position-error-based compensator proposed in Section 5.4.2 focuses on the compensation of the rotor position error in flux observer, and the speed is calculated from the compensated rotor position. Therefore, the steady-state rotor position

estimation is usually with high accuracy, whilst, it is not fast enough to yield good dynamic response for speed control. In contrast, rotor speed error based compensation could result in a fast dynamic response with slightly lower accuracy. Hence, the development of improved speed-error-based compensator is of considerable interest and proposed in Fig. 5.31 to improve the dynamic performance.

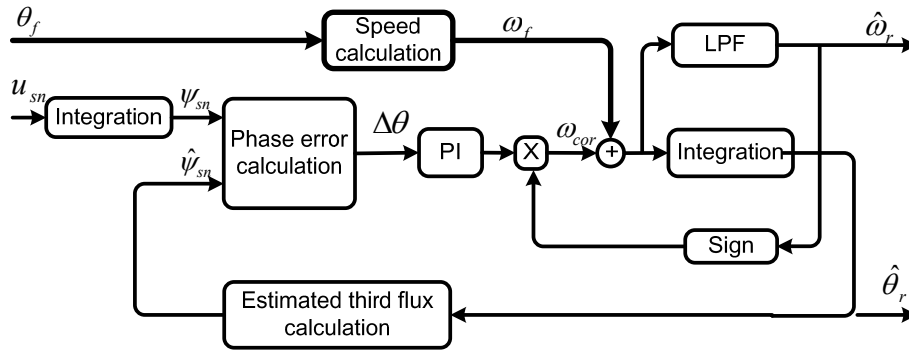


Fig. 5.31. Block diagram of improved speed-error-based compensator

The rotor speed of flux observer can be calculated from rotor position as

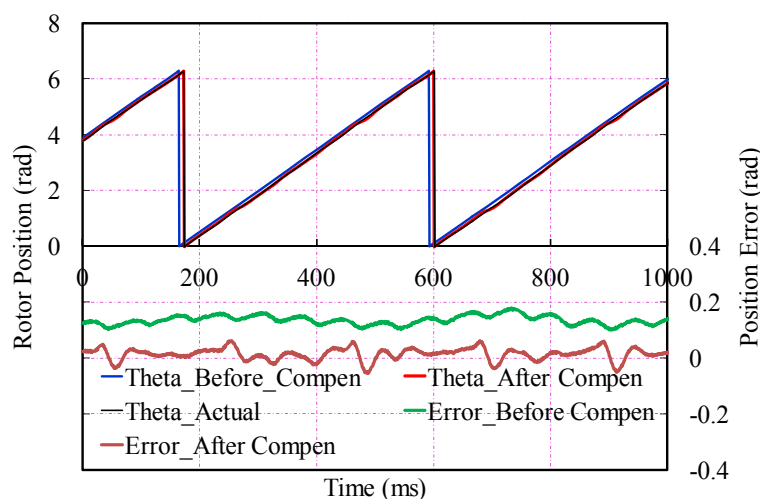
$$\omega_f = [\theta_f(k) - \theta_f(k-1)] / \Delta t_s \quad (5.27)$$

where k is the sampling instant and Δt_s is the duration-time between the previous two sampling points. Usually, Δt_s equals to the PWM period which is 5e-6s in this system. Hence, the calculated rotor speed has high resolution and can reflect the change of calculated rotor position by the flux observer.

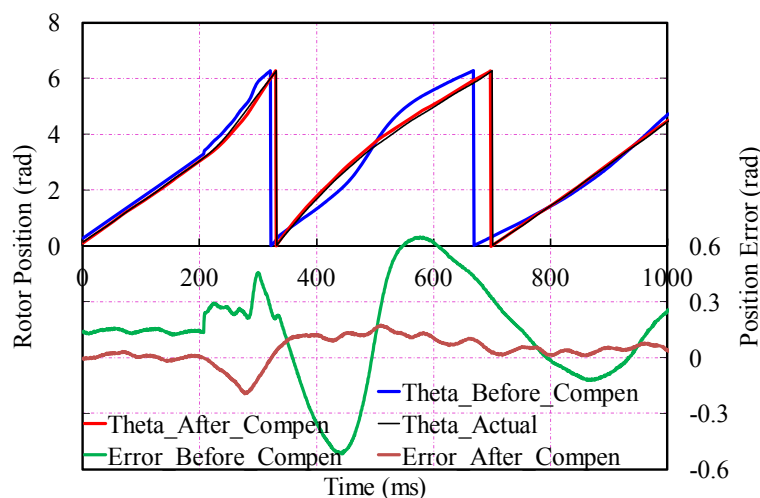
The speed correction ω_{cor} corresponding to the speed estimation error is obtained from the phase difference $\Delta\theta$ calculated in (5.26) by the following PI controller, which is the same as (5.12). Therefore, the estimated speed error rather than position error in flux observer can be directly compensated. Then, after the compensator becoming steady-state, the average rotor speed ω_f from flux observer including the intrinsic speed error is appropriately compensated, and the estimated rotor speed ω_r^e will converge to the actual value. Thus, high resolution rotor position can be estimated with high accuracy by simple integration. The same as the position-error-based compensator, the phase-A back-EMF should be considered to avoid mis-alignment.

The overall control scheme is the same as in Fig. 5.29. When Motor II is working

at the same steady-state and dynamic as in Section 5.4.1, the estimated rotor positions and the estimation errors before and after compensation from the speed-error-based compensator compared with the actual rotor position are shown in Fig. 5.32. It is clearly shown that the steady-state estimation error can be significantly minimized however with larger fluctuation than the position-error-based compensator.



(a) Steady-state performance



(b) Dynamic performance

Fig. 5.32. Performance of speed-error-based compensator

(θ_{act} : Actual rotor position, θ_{Before_Compen} : Estimated rotor position from flux observer before error compensation, e_{Before_Compen} : Position estimation error in flux observer before error compensation, θ_{After_Compen} : Estimated rotor position after error compensation, e_{After_Compen} : Position estimation error after error compensation)

The experimental results prove that the position-error-based compensator is not sensitive enough to the dynamic change of the estimation error since the step error at 200ms and 280ms are still there and the maximum estimation error is around 0.3rad which is also too large to accept for dynamic operation. However, since any estimated speed error in dynamic speed control can be directly compensated, even though the accuracy of the rotor position estimation may be slightly lower, the dynamic speed response is much better than the position-error-based compensator and the estimation error can be limited within 0.1rad.

Back-EMF is proportional to the rotor speed, and theoretically the larger amplitude of the source signal of third harmonic back-EMF would lead to the better sensorless performance. Hence, if the sensorless performance at low speed which is 10rpm can achieve good performance, the higher speed performance would be as good as low speed application or even better.

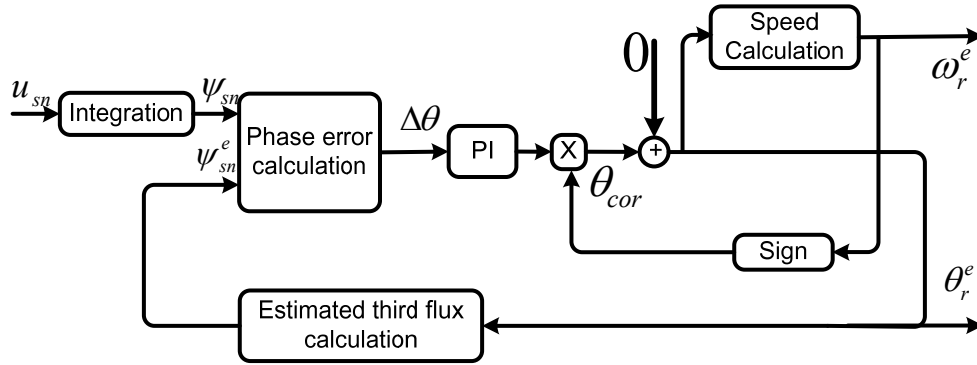
5.4.4 Robust Operation Performance

PMSM control system highly depends on the rotor position information. If sensorless control fails, the whole system will break down and a serious problem may occur. Hence, application of fault tolerant technique in sensorless control is of great importance due to the improvement of robustness for saving cost and planning maintenance procedures in advance.

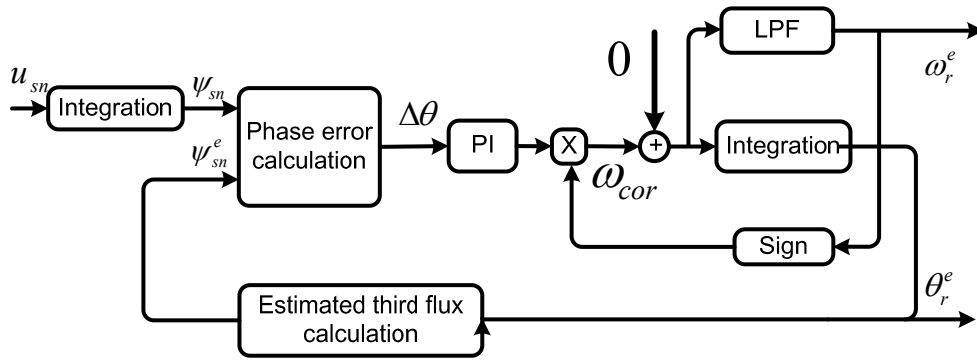
In the proposed sensorless control method as shown in Fig. 5.29, flux observer and the proposed compensator based on third harmonic back-EMF can be seen as mutually complementary. If one of the two sources, viz., flux observer signals or third harmonic back-EMF fails, the other would be able to provide position to the control system.

In first case, if the measurement of third harmonic back-EMF has problem and can no longer be used as reference, then the compensator proposed above will be bypassed, and the rotor position information will be directly obtained from flux observer. Although the estimated rotor position may contain certain error, it can maintain the stability of the control system. In second case, when the flux observer has problem, large estimation error could be compensated by the proposed compensators. The

extreme situation is that all outputs of flux observer are set as zero, and cannot provide any the rotor position information to the compensators, and then the block diagrams of compensators shown in Fig. 5.27 and Fig. 5.31 will be modified to Fig. 5.33.



(a) Position-error-based compensator



(b) Speed-error-based compensator

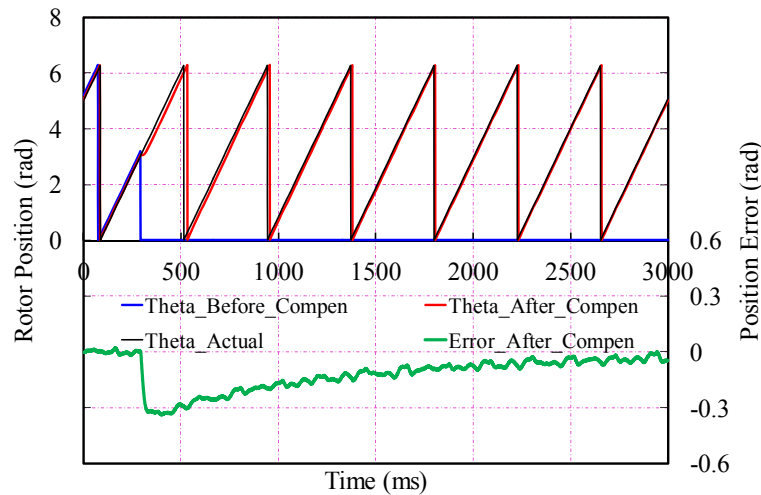
Fig. 5.33. Block diagram of compensators when flux observer fails

For the position-error-based compensator, Fig. 5.33(a), θ_{cor} calculated in (5.26) which represents the rotor position correction corresponding to the position estimation error should be equal to the estimated rotor position θ_r^e . However, θ_r^e is a ramp function with sharp change at the point of 2π elec-rad rotor position, and a regular PI controller cannot track this kind of signal. Hence, θ_{cor} cannot be converged to the actual rotor position. Thus, this compensator cannot provide rotor position information to the control system when the flux observer fails.

For speed-error-based compensator, Fig. 5.33(b), since ω_f is already set as zero, ω_{cor} calculated by (5.12) not only represents the rotor speed correction corresponding to

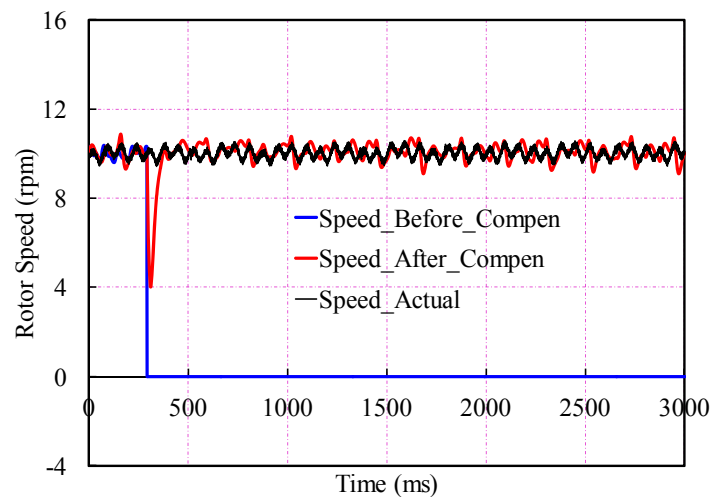
the position estimation error but also will be converged to the actual rotor speed ω_r when the system reaches to the steady-state. Thus, after being corrected by phase-A back-EMF or by phase-A voltage instead, rotor position can be estimated from ω_{cor} by integration with high accuracy to avoid the failure of the control system.

Fig. 5.34 shows the relevant dynamic performance when flux observer has an extreme failure in which all the outputs are suddenly set as zero. The rotor positions from the flux observer before and after compensation compared with the actual value from the encoder, and the compensated estimation error are shown in Fig. 5.34(a). Fig. 5.34(b) shows the rotor speeds calculated from flux observer before and after compensation compared with the actual value calculated from encoder. Although the estimated rotor position and speed derived by the compensator have interruption due to the failure of flux observer, they can reflect the actual values well and maintain the stability of the control system.



(a) Positions before and after compensation and estimated error

(θ_{act} : Actual rotor position, θ_{Before_Comp} : Estimated rotor position from flux observer before error compensation, θ_{After_Comp} : Estimated rotor position after error compensation, e_{Before_Comp} : Position estimation error in flux observer before error compensation, e_{After_Comp} : Position estimation error after error compensation)



(b) Rotor speeds before and after compensation

(ω_{Actual} : Actual rotor speed, ω_{Before_Comp} : Estimated rotor speed before error compensation, ω_{After_Comp} : Estimated rotor speed after error compensation)

Fig. 5.34. Robust performance of speed-error-based compensator

5.4.5 Comparison of Third Harmonic Back-EMF and Fundamental Back-EMF Based Sensorless Controls

Fundamental and third harmonic back-EMF based sensorless both depend on the machine back-EMF which is proportional to rotor speed. However, there are several differences between the two kinds of methods and the comparison results of them are shown in Table 5.1.

TABLE 5.1

COMPARISON OF BACK-EMF BASED SENSORLESS CONTROLS

	Fundamental back-EMF based flux observer	Third harmonic back-EMF
Applicability	SPM and IPM(with extend back-EMF or active flux)	SPM and IPM(To be introduced in Section 7.2)
Zero and very low speed	Not applicable	Not applicable
Cost	Medium	Medium
Implementation complexity	Medium	Medium
Sensitivity to parameters	High	Low
Sensitivity to imbalance	Low	Medium (To be improved in Section 7.3)
Sensitivity to PWM	Medium	Low
Sensitivity to high order harmonic back-EMF	Low	Medium (To be improved in Chapter 6)
Flux weakening	No limit	No limit for SPM/Available for IPM (To be introduced in Section 7.2)
SNR	High	Medium
Dynamic performance	Medium	High

5.5 Conclusion

In this chapter, the detection of third harmonic back-EMF and conventional sensorless control strategy based on zero-crossings third harmonic flux-linkage, which is the integration of third harmonic back-EMF, are introduced. However, the conventional strategy suffers dynamically due to inaccurate average rotor speed calculated from the insufficient precise rotor position reference.

Hence, to minimize the rotor position error and improve the dynamic performance, a speed compensation strategy based on the continuous signal of third harmonic flux-linkage, is proposed. Taking the continuous sinusoidal signal, rather than zero-crossings of third harmonic flux-linkage, as reference, the estimation error in the speed calculated from zero-crossings could be compensated at each sampling time. Then, the high resolution estimated rotor position will be derived from the compensated rotor speed with high accuracy.

Furthermore, to improve the performance of rotor position estimation in flux observer sensorless control which is sensitive to the machine and controller parameters, position-error-based and speed-error-based compensators based on the continuous sinusoidal signal of third harmonic back-EMF are also proposed in this chapter. Meanwhile, the robust performance can also be enhanced due to the mutually complementary between the compensators and flux observer.

The experimental results carried on a PMSM validate that the improved rotor position estimator based on the continuous signal of third harmonic flux-linkage could achieve accurate rotor position estimation and outstanding dynamic performances, whilst the rotor position-error-based compensator has more accurate rotor position estimation under steady-state, and the speed-error-based compensator is outstanding under dynamic situation and has much better robust performance.

CHAPTER 6

SENSORLESS CONTROL BASED ON THIRD HARMONIC BACK-EMF AND SIMPLIFIED EKF FOR SINGLE AND DUAL THREE-PHASE PMSM

6.1 Introduction

The improvement of dynamic performance of conventional sensorless control and the performance and robustness of flux observer by speed error compensation based on third harmonic back-EMF are introduced in Chapter 5. However, in these proposed methods, the source signal quality which is third harmonic back-EMF is of great importance. If the higher order harmonic components contained in the source signal are not too large, they could be eliminated by the proposed estimator. Otherwise, the speed calculation and the rotor position estimation may also be deteriorated. In extreme case, the speed calculation based on zero-crossings of third harmonic flux-linkage may fail due to the absence of zero-crossings or large phase shift. Hence, sensorless control without speed calculation should be considered to solve the signal quality issue.

Extended Kalman filter (EKF) is a recursive optimum-state estimator which can be used in a non-linear dynamic system using random noise distributed signals. Hence, in the rotor position estimation, even though the measured third harmonic back-EMF contains too much high frequency PWM noise or higher order triplen harmonic back-EMF such as ninth, fifteenth, etc, the EKF based estimator could be applied to achieve accurate estimation with noise suppression.

In this chapter, EKF and the application of simplified EKF for rotor position estimation will be introduced. Then, the sensorless control based on third harmonic back-EMF and flux-linkage for single three-phase PMSM operation by employing simplified EKF will be presented. For dual three-phase PMSM, there are two sets of

windings, and they usually have a spatial $\pi/6$ elec-rad shift. Hence, the two sets of third harmonic back-EMF will be orthogonal under third harmonic reference frame. Consequently, with the aid of simplified EKF based estimator, the rotor position could be estimated without any filtering. All these strategies will be introduced in detail.

6.2 EKF and Its Application to Rotor Position Estimation

EKF is a recursive optimum-state estimator used for the joint state and parameter estimation of a non-linear dynamic system in real-time by using noisy monitored signals that are distributed by random noise. The noise source takes account of measurement and modelling inaccuracies. In the first stage of the calculations, the states are predicted by using a mathematical model which contains previous estimates, and in the second stage, the predicted states are continuously corrected by using a feedback correction scheme. This scheme makes use of actual measured states, by adding a term to the predicted state which is obtained in the first stage. The additional term contains the weighted difference of the measured and estimated output signals. Based on the deviation from the estimated value, the EKF provides an optimum output value at the next input instant. In a PMSM drive, the EKF can be used for the real-time estimation of the rotor position and speed. This is possible since a mathematical dynamical model of the machine is sufficiently well known. For this purpose the stator voltages and currents are measured and for example, the speed and position of the machine can be obtained by the EKF quickly and accurately [VAS03, pp. 480-490].

To be more specific, the goal of EKF is to obtain immeasurable states, e.g. speed and rotor position by using measured states, and also statistics of the noise and measurement. In general, by means of the noise inputs, it is possible to take account of computational inaccuracies, modelling errors, and the errors in the measurements. A discrete-time, non-linear dynamic system can be expressed in state-space form as

$$\begin{aligned}x(k+1) &= f(x(k), k) + g(u(k), k) + w(k) \\ y(k) &= h(x(k), k) + v(k)\end{aligned}\tag{6.1}$$

where $u(k)$ and $y(k)$ are the input and output signals, respectively, and $w(k)$ and $v(k)$

are the process noise and measurement noise, respectively. $x(k)$ is the state vector, which can be estimated by the EKF and is given by

$$\hat{x}(k+1) = f(\hat{x}(k), k) + g(u(k), k) + K_k[y(k) - h(\hat{x}(k), k)] \quad (6.2)$$

The Kalman gain K_k is determined through the Riccati difference equation. However, it requires relatively complex matrix calculations, and therefore, takes a significant computing time [LIU04]. In a PMSM with third harmonic back-EMF, the output variables of the EKF may be chosen as the third harmonic flux-linkage integrated from third harmonic back-EMF, i.e.

$$\begin{bmatrix} y_1(k) \\ y_2(k) \end{bmatrix} = \begin{bmatrix} \psi_{3rd_cos} \\ \psi_{3rd_sin} \end{bmatrix} \quad (6.3)$$

while the state variables are chosen as the rotor speed ω_r and position θ_r , and the double integration of the noise, w . The speed identification model based on the EKF can then be established. In order to simplify the model, in particular the computation of the Kalman gain, the output variables, equation are expressed as

$$\begin{bmatrix} y_1(k) \\ y_2(k) \end{bmatrix} = \begin{bmatrix} \cos(3 \times \theta_r(k)) \\ \sin(3 \times \theta_r(k)) \end{bmatrix} + \begin{bmatrix} v_1(k) \\ v_2(k) \end{bmatrix} \quad (6.4)$$

Therefore, with a state vector $x = [\theta, \omega_r, w]^T$ and input $u(k) = 0$, the state-space model can be written as

$$\begin{aligned} x(k+1) &= Fx(k) + w(k) \\ y(k) &= h(x(k)) + v(k) \end{aligned} \quad (6.5)$$

where

$$F = \begin{bmatrix} 1 & \Delta t_s & 0 \\ 0 & 1 & 1 \\ 0 & 0 & 1 \end{bmatrix} \quad (6.6)$$

and

$$h(x(k)) = \begin{bmatrix} \cos(3 \times \theta_r(k)) \\ \sin(3 \times \theta_r(k)) \end{bmatrix} \quad (6.7)$$

where Δt_s is the sampling time.

The Kalman filter gain can now be significantly simplified, and is given by

$$K = \begin{bmatrix} 0 & k_1 \\ 0 & k_2 \\ 0 & k_3 \end{bmatrix} \begin{bmatrix} \cos(3 \times \theta_r^e) & \sin(3 \times \theta_r^e) \\ -\sin(3 \times \theta_r^e) & \cos(3 \times \theta_r^e) \end{bmatrix} \quad (6.8)$$

where k_1 , k_2 , and k_3 are tuning parameters. From the foregoing analysis, it can be shown that the rotor speed and position can be estimated from the following equations, i.e.

$$\begin{aligned} \varepsilon(k) &= y_2(k) \cos \theta_r^e(k) - y_1(k) \sin \theta_r^e(k) \\ \theta_r^e(k+1) &= [\theta_r^e(k) + T_s \omega_r^e(k) + k_1 \varepsilon(k)]_{-\pi}^{\pi} \\ \omega_r^e(k+1) &= \omega_r^e(k) + w(k) + k_2 \varepsilon(k) \\ w(k+1) &= w(k) + k_3 \varepsilon(k) \end{aligned} \quad (6.9)$$

where θ_r^e and ω_r^e are the estimated position and speed, respectively.

Then the rotor position could be estimated from (6.9) and the block diagram of simplified EKF with third harmonic back-EMF is shown in Fig. 6.1. From the analysis, it shows that the two orthogonal source signals are essential for rotor position estimation.

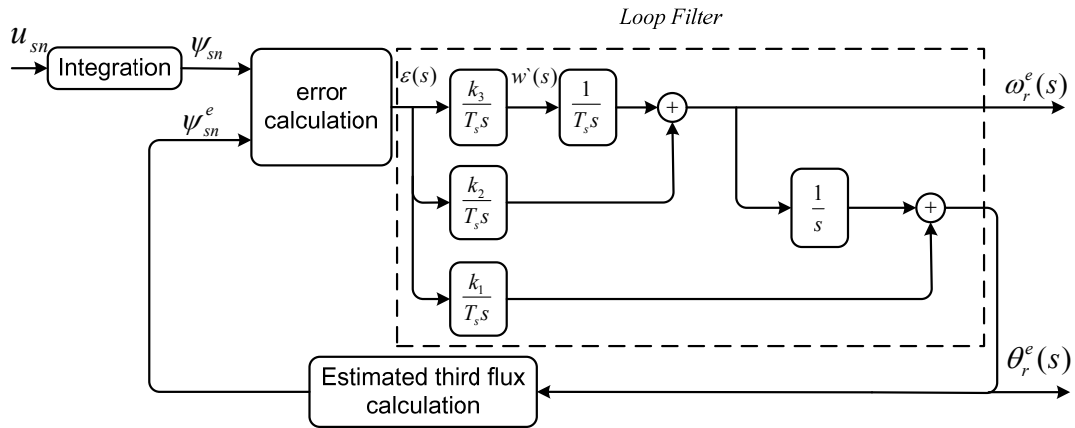


Fig. 6.1. Block diagram of simplified EKF

6.3 Rotor Position Estimation Based on Third Harmonic Back-EMF and Simplified EKF for Single Three-Phase PMSM Operation

Since the resultant third harmonic back-EMF is a voltage signal which is proportional to the rotor speed and may contain certain PWM component noise, the

third harmonic flux-linkage ψ_{sn} which results from the integration of third harmonic back-EMF is usually applied for the rotor position estimation. ψ_{sn} is a smooth continuous signal with constant amplitude and has higher signal quality than u_{sn} , which makes the rotor position estimation much easier and with higher quality than that directly from third harmonic back-EMF. In practice, ψ_{sn} is usually derived by a low cut-off frequency band pass filter (BPF), which may cause unexpected phase delay or poor frequency response. ψ_{sn} can be defined as

$$\psi_{sn} = -A_{mp} \cos(3 \times \theta_r) \quad (6.10)$$

where A_{mp} is the amplitude of ψ_{sn} which could be obtained from the absolute value of ψ_{sn} when its differential is close to zero. To estimate the rotor position by simplified EKF, the required orthogonal signal of ψ_{sn} also should be calculated based on u_{sn} . Since the amplitude of u_{sn} varies with rotor speed, it should be unified as A_{mp} considering the feedback estimated rotor speed ω_r^e as

$$u_{sn_unified} = \frac{K_p}{\omega_r^e} E_3 \sin(3 \times \theta_r) = A_{mp} \sin(3 \times \theta_r) \quad (6.11)$$

where K_p is the unify-ratio of the amplitudes of the third harmonic flux-linkage and back-EMF. Hence, the signals $y(k)$ in (6.3) can be selected as

$$\begin{bmatrix} y_1(k) \\ y_2(k) \end{bmatrix} = \begin{bmatrix} \psi_{sn} \\ u_{sn_unified} \end{bmatrix} \quad (6.12)$$

For the Motor II, the measured ψ_{sn} and $u_{sn_unified}$ which have been shown in Fig. 5.12 of Section 5.3.2, are depicted in Fig. 6.2 for the comparison purpose. It can be found that the measured ψ_{sn} and $u_{sn_unified}$ are sinusoidal of high signal quality.

Then based on the simplified EKF as shown in Fig. 6.1, the simplified EKF based rotor position estimator can be derived as shown in Fig. 6.3. It has the advantage which could eliminate the untracked higher order harmonic components. Hence, these contained high order harmonic components will nearly not affect the accuracy of position estimation.

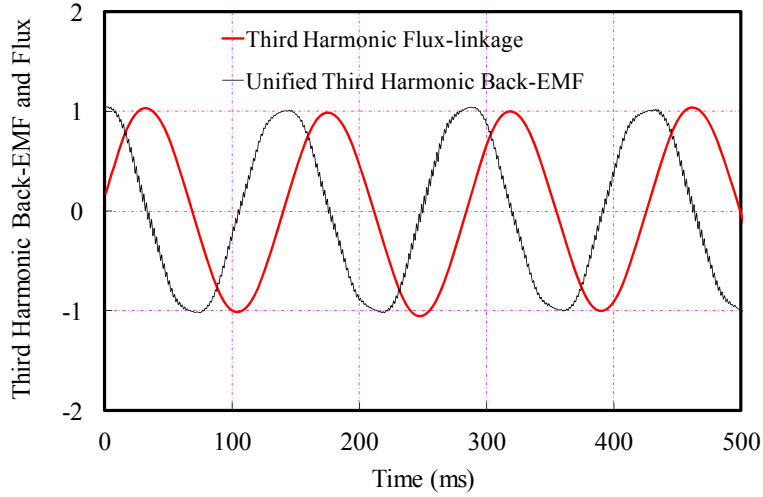


Fig. 6.2. ψ_{sn} and $u_{sn_unified}$ by experiment.

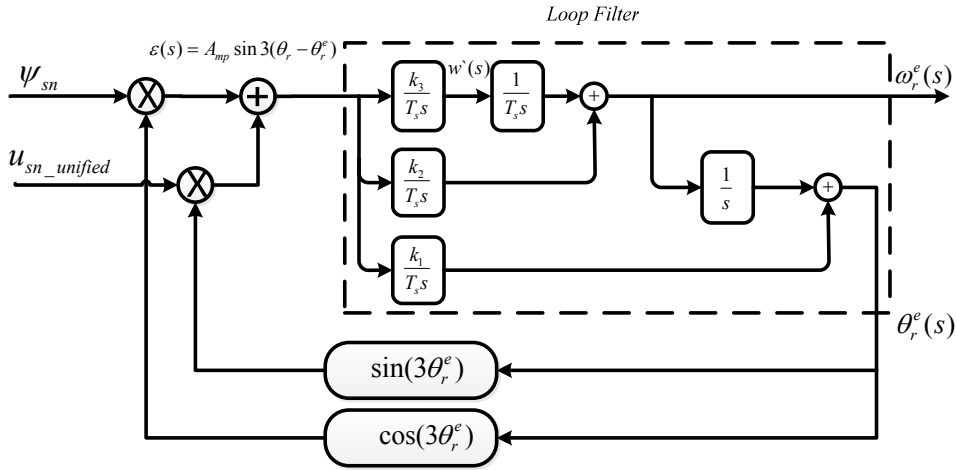


Fig. 6.3. Simplified EKF based rotor position estimator

According to the diagram, the close loop transfer function between the estimated and actual rotor positions can be express as

$$\frac{\theta_r^e}{\theta_r} = \frac{3A_{mp}k_3 \cdot s^2 + 3A_{mp}k_2 \cdot s + 3A_{mp}k_1}{s^3 + 3A_{mp}k_3 \cdot s^2 + 3A_{mp}k_2 \cdot s + 3A_{mp}k_1} \quad (6.13)$$

It could be seen that since A_{mp} is a constant, k_1 , k_2 and k_3 which are covariance matrix gains in the estimator also should be constant to maintain constant bandwidth. The Bode plot of the position estimator are shown in Fig. 6.4, it can be seen that the loop bandwidth is around 24Hz and maintained as constant at different rotor speed.

Fig. 6.5 shows the rotor positions and position errors derived from EKF based rotor position estimator and the rotor position estimation based on compensation of

speed from zero-crossing as introduced in Section 5.3.2, compared with the actual rotor position at the steady-state of 10rpm mechanical rotor speed. It can be found that there is nearly no difference between the two methods since the derived ψ_{sn} and $u_{sn_unified}$ are sinusoidal without disturbance of higher order harmonic components.

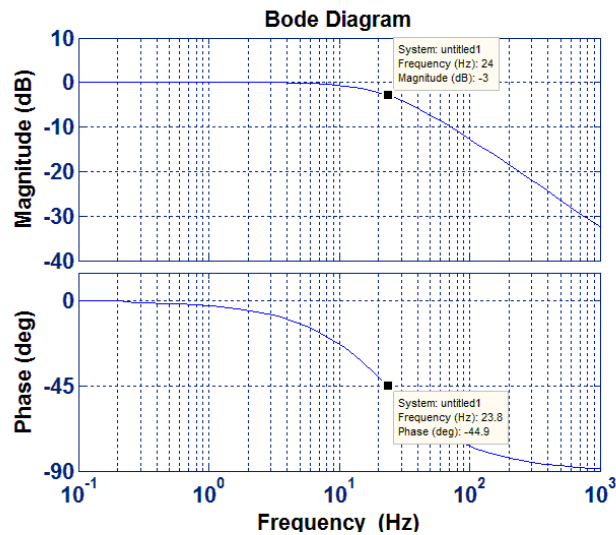


Fig. 6.4. Frequency response of EKF based rotor position estimator

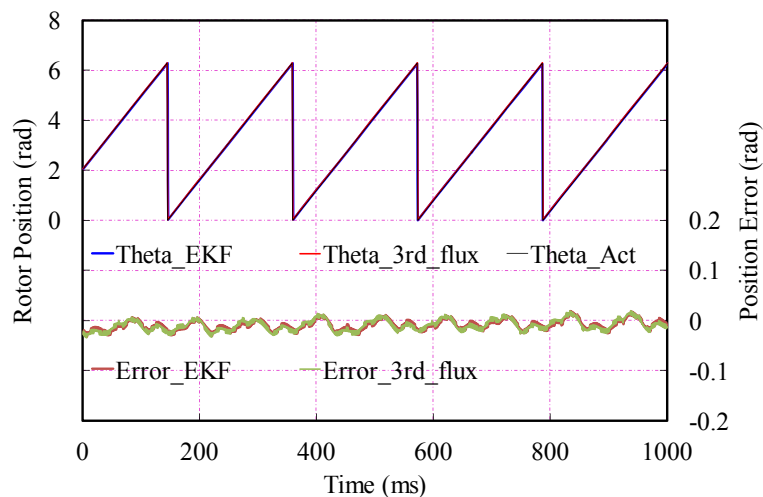
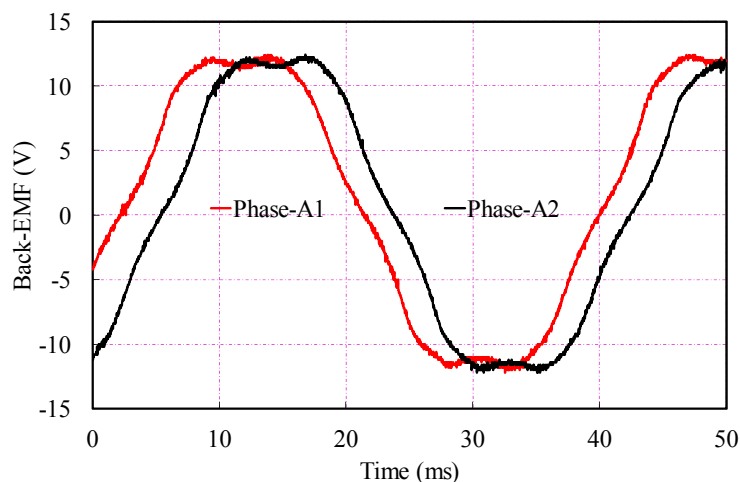
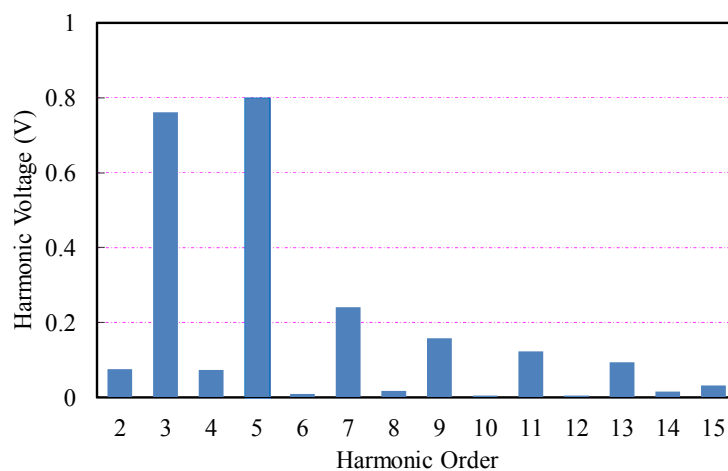


Fig. 6.5. Rotor positions and the error based on the improved estimator and EKF based rotor position estimator (θ_{EKF} : Rotor position estimated by simplified EKF based rotor position estimator, θ_{3rd_flux} : Rotor position estimated based on compensation of speed from zero-crossing, θ_{Act} : Actual rotor position, e_{EKF} : Position error by simplified EKF based rotor position estimator, e_{3rd_flux} : Position error based on compensation of speed from zero-crossing)

The measured Phase-A1 and Phase-A2 back-EMFs of Motor III which is a 230W laboratory dual three-phase PMSM are shown in Fig. 6.6(a) when the windings are open-circuit with 400rpm rotor speed and the FFT analysis of the measured Phase-A1 back-EMF is shown in Fig. 6.6(b). It could be concluded that there are plenty of harmonic components, and the higher order triplen harmonic back-EMF such as ninth and fifteenth are not much smaller than the third harmonic back-EMF.



(a) Back-EMFs



(b) Harmonic spectrum of back-EMF

Fig. 6.6. Back-EMF and harmonic analysis at rated speed

The steady-state tests are carried out with single three-phase operation when the rotor speed is 200rpm with 1A q -axis current, while other set is open circuit. It can be seen that $u_{sn_unified}$ calculated by (6.11) from feedback rotor speed and the measured u_{sn} of one set winding at 200rpm with the aid of 1k Ω sensing resistor network shown in Fig. 6.7 contains too much high order triplen harmonic noise. However, ψ_{sn} derived by

BPF (second order filter with $f_1 = 1\text{Hz}$ and $f_2 = 50\text{Hz}$) are smoother and have better signal quality but still contain certain high frequency components. Hence, the rotor position estimation based on compensation of speed from zero-crossing will be very difficult to be employed especially under dynamic situation, due to the large phase shift of zero-crossings caused by contained higher harmonic components.

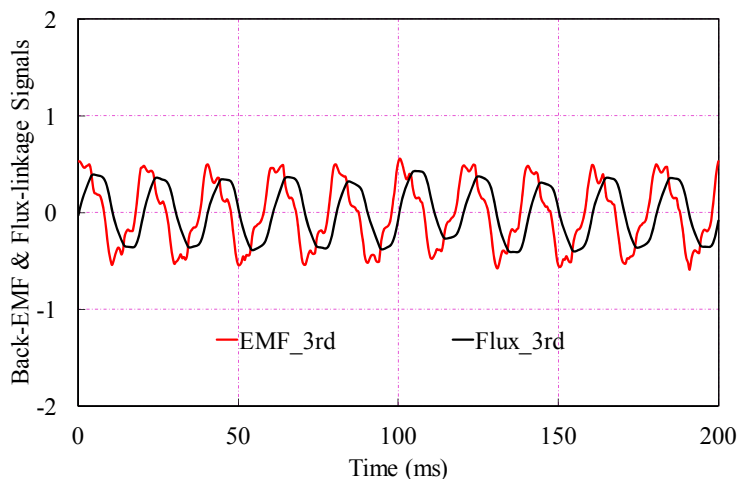


Fig. 6.7. Third harmonic Back-EMF and flux-linkage

(*EMF_3rd*: Third harmonic back-EMF, *Flux_3rd*: Third harmonic flux-linkage)

Fig. 6.8 shows the rotor positions and errors derived from both the estimator based on speed error compensation and EKF based rotor position estimator compared with the actual rotor position at the steady-state of 200rpm mechanical rotor speed. Due to the high order triplen harmonic noise in third harmonic Back-EMF and flux-linkage, the estimated rotor position based on EKF can achieve better performance, since it is less sensitive to these high frequency noises and phase shift of zero-crossings than the speed error compensation based estimator.

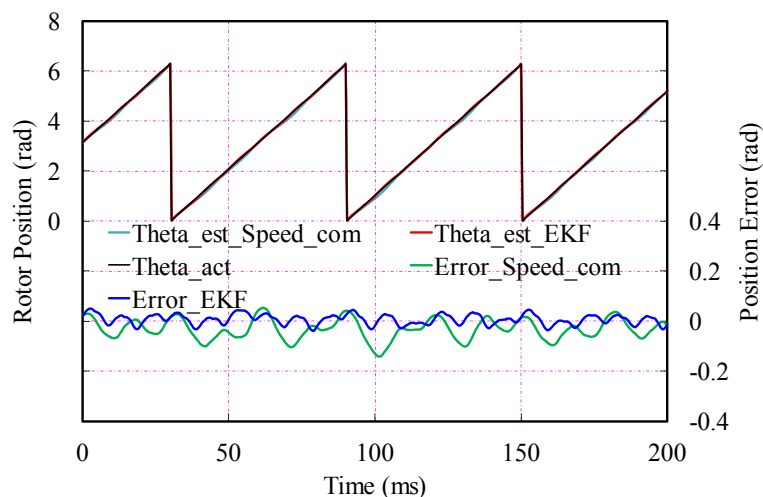


Fig. 6.8. Rotor positions and the error based on EKF based rotor position estimator (θ_{EKF} : Rotor position estimated by simplified EKF based rotor position estimator, θ_{3rd_flux} : Rotor position estimated based on compensation of speed from zero-crossing, θ_{Act} : Actual rotor position, $error_{EKF}$: Position error by simplified EKF based rotor position estimator, $error_{3rd_flux}$: Position error based on compensation of speed from zero-crossing)

The dynamic performance test for the EKF based rotor position estimator is carried out when the rotor initial speed is 200rpm with 1A q -axis current, and the speed reference changes from 200rpm to 320rpm and then the rotor speed response is shown in Fig. 6.9. Then applying the EKF based rotor position estimator as shown in Fig. 6.3, the rotor position can be estimated. From the estimated and actual rotor positions and the error between them shown in Fig. 6.10, it could be found that the peak estimation error can be kept within 0.1rad even under dynamic situation.

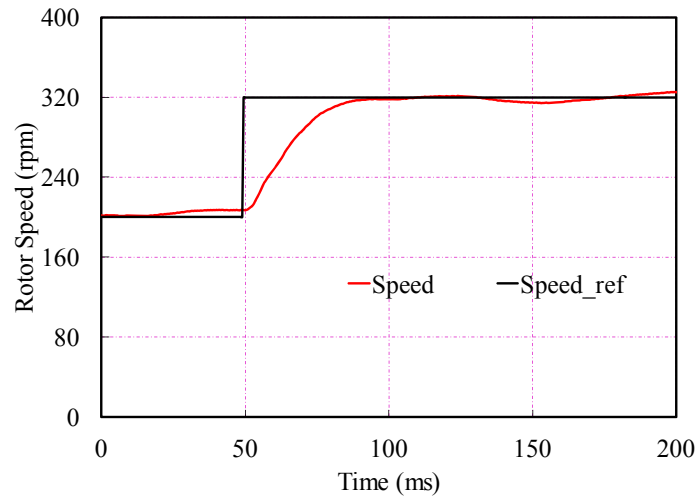


Fig. 6.9. Dynamic test situation

(*Speed_ref*: Speed reference, *Speed*: Actual rotor speed)

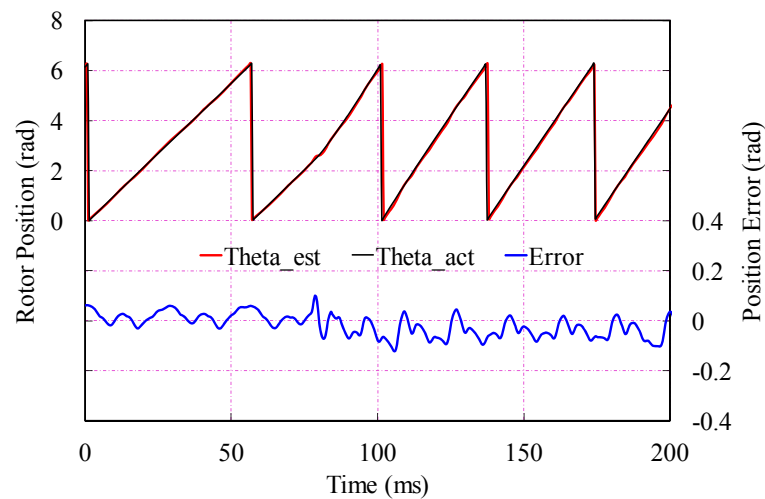


Fig. 6.10. Rotor positions and the error based on EKF based rotor position estimator at dynamic situation. (*Theta_est*: Estimated rotor position, *Theta_act*:

Actual rotor position, *Error*: Rotor position estimation error)

6.4 Rotor Position Estimation Based on Third Harmonic Back-EMF and Simplified EKF for Dual Three-Phase PMSM

Dual three-phase PMSM consists two sets of three-phase winding which are usually displaced by $\pi/6$ elec-rad [NEL74], and has several advantages over

conventional single three-phase systems. Firstly, the predominant frequency has been shifted from six to twelve times than the supply frequency, and the associated sixth harmonic pulsating torque and rotor harmonic losses in conventional three-phase voltage-fed drives are eliminated. Secondly, the required inverter phase current ratings are reduced due to the multiphase inverter instead of a group of devices connected in parallel, and hence, the total system reliability is also improved.

For dual three-phase PMSM, the neutral points of two sets windings are usually isolated as shown in Fig. 6.11. Hence, there is no electrical connection between the two sets of windings.

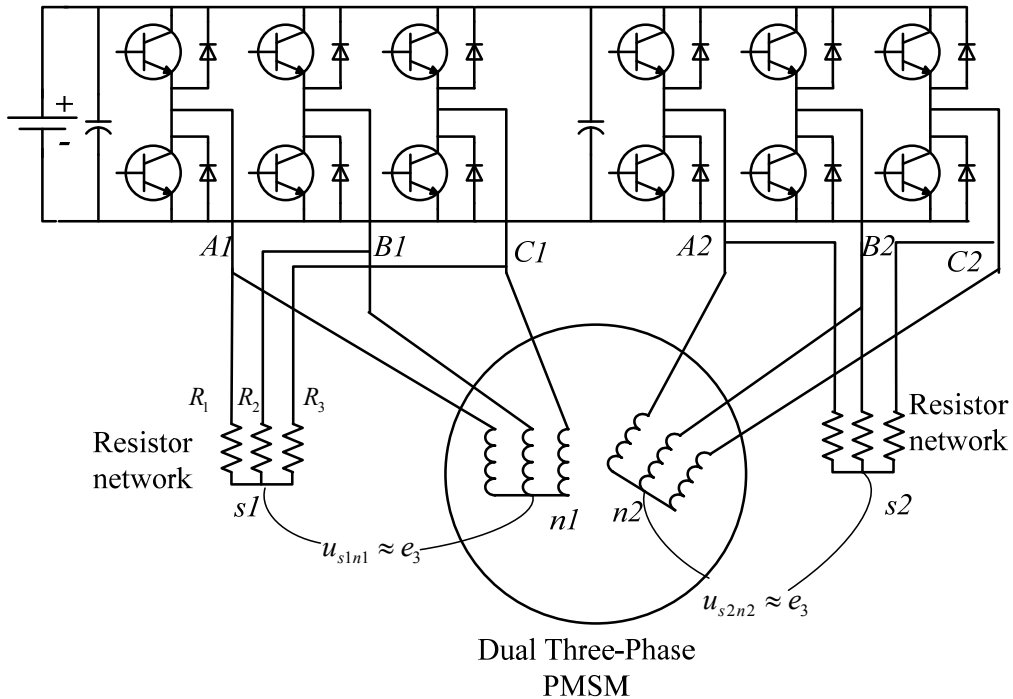


Fig. 6.11. Measurement of third harmonic back-EMF in dual three-phase PMSM

Based on the aforementioned analysis, for the dual three-phase PMSM, the measured voltages between “s1” and “n1”, and between “s2” and “n2”, could represent the two sets of the third harmonic back-EMFs of the two sets of windings as

$$\begin{cases} u_{s1n1} = e_{3_set1} + e_{9_set1} + e_{15_set1} + \dots \approx e_{3_set1} \\ u_{s2n2} = e_{3_set2} + e_{9_set2} + e_{15_set2} + \dots \approx e_{3_set2} \end{cases} \quad (6.14)$$

For most of dual three-phase PMSMs, the two sets winding have a spatial $\pi/6$ elec-rad shift, Fig. 6.12. Hence e_{3_set1} and e_{3_set2} have the same phase shift under

fundamental reference frame as illustrated in Fig. 6.13, i.e.

$$\begin{cases} e_{3_set1} = E_3 \cdot \sin(3\theta_r) \\ e_{3_set2} = E_3 \cdot \sin(3 \times (\theta_r - \pi / 6)) \end{cases} \quad (6.15)$$

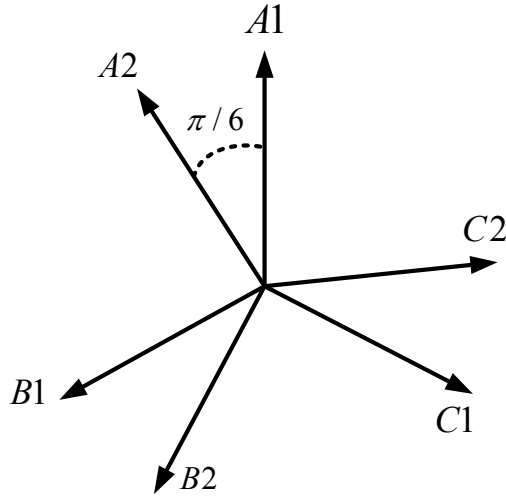


Fig. 6.12. Winding vectors of dual-three-phase PMSM

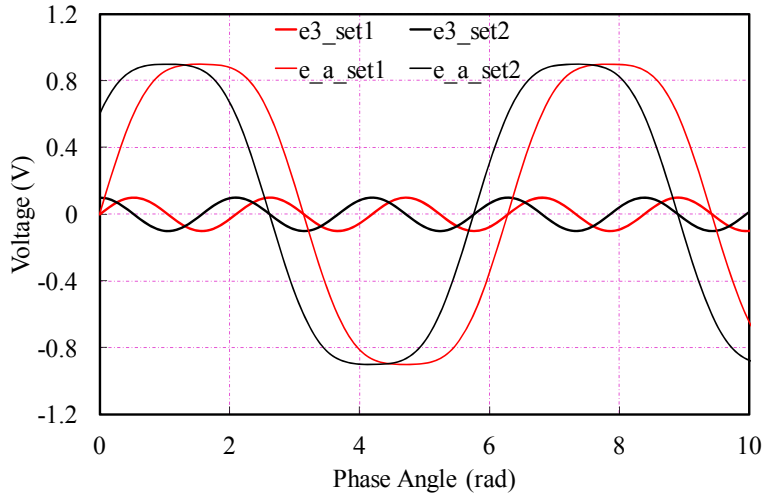


Fig. 6.13. Relationship of fundamental and third harmonic back-EMFs in dual-three-phase PMSM

For single three-phase PMSM, the third harmonic flux-linkage ψ_{sn} which results from the integration of third harmonic back-EMF is usually applied for the rotor position estimation due to its better SNR, and the same for dual three-phase PMSM. Hence, two sets of ψ_{sn} derived by low cut-off frequency BPF orthogonal to each other under third harmonic reference frame, i.e.

$$\begin{cases} \psi_{3_set1} = -\Psi_3 \cdot \cos(3\theta_r) \\ \psi_{3_set2} = -\Psi_3 \cdot \cos(3 \times (\theta_r - \pi / 6)) = -\Psi_3 \cdot \cos(3\theta_r - \pi / 2) = -\Psi_3 \cdot \sin(3\theta_r) \end{cases} \quad (6.16)$$

The steady-state tests are carried out when the rotor speed is 200rpm with 1A q -axis current. It can be seen that the measured u_{sn} of two sets of windings at 200rpm shown in Fig. 6.14 contain too much high order triplen harmonic noise. However, ψ_{sn} of the two sets of windings derived by BPF shown in Fig. 6.15 are smoother and have better signal quality, whilst contain too large error at each zero-crossings which leads the conventional rotor position estimation based on zero-crossing or speed compensation based on zero-crossing very difficult to be employed. However, by applying the simplified EKF based rotor position estimator, the contained triplen, ninth, fifteenth and so forth orders harmonics, could be eliminated.

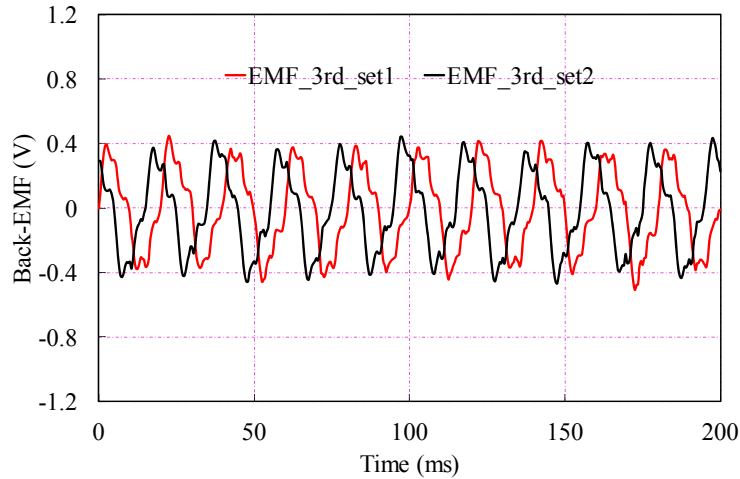


Fig. 6.14. Measured u_{sn} of two sets of windings at 200rpm

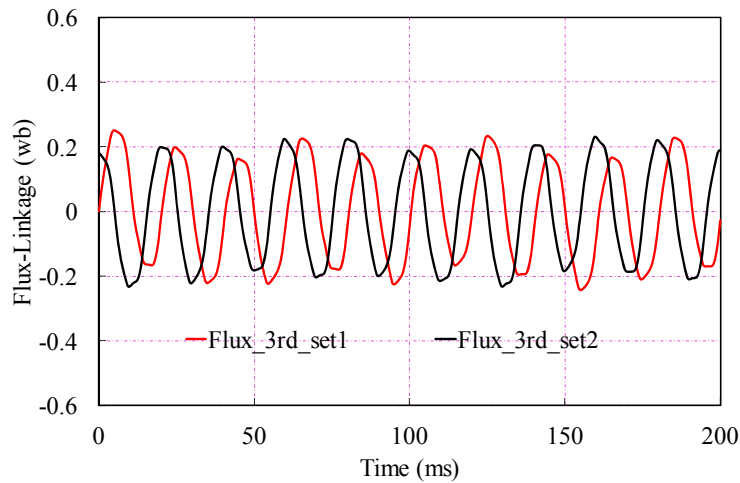


Fig. 6.15. ψ_{sn} of two sets of windings at 200rpm

The overall control scheme of the dual three-phase PMSM is shown in Fig. 6.16, and applying the EKF based rotor position estimator as shown in Fig. 6.3, the rotor position could be estimated from ψ_{sn} . Then, the estimated and actual rotor positions and the error between them estimated from third harmonic flux-linkage at 200rpm rotor speed with 1A q -axis current are shown in Fig. 6.17.

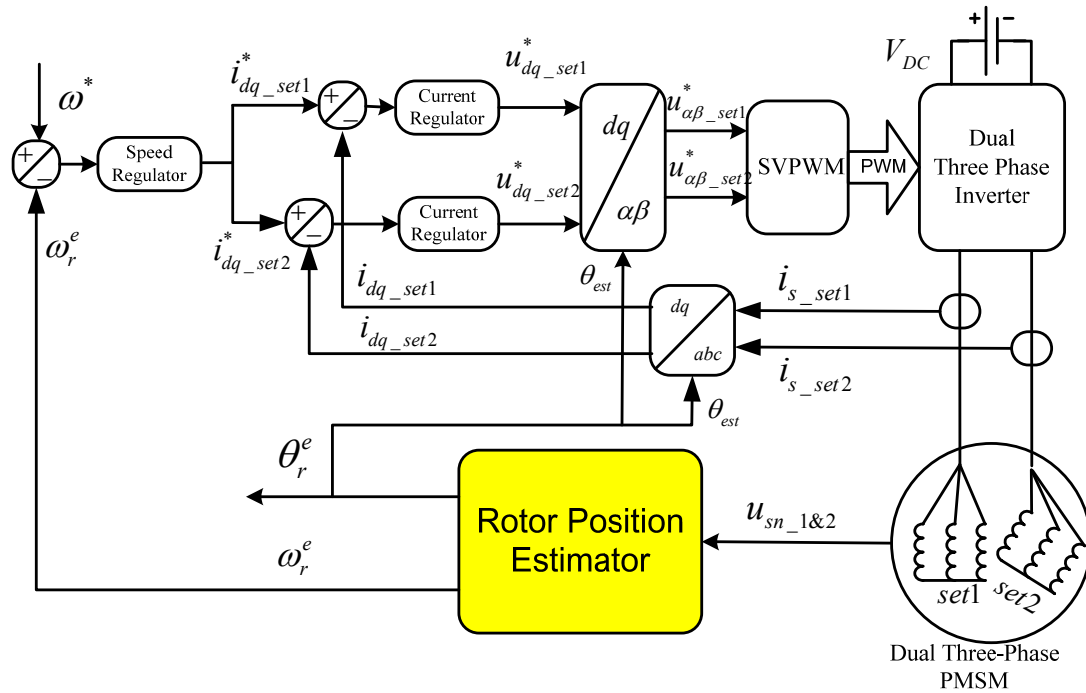


Fig. 6.16. Overall control scheme of dual three-phase PMSM

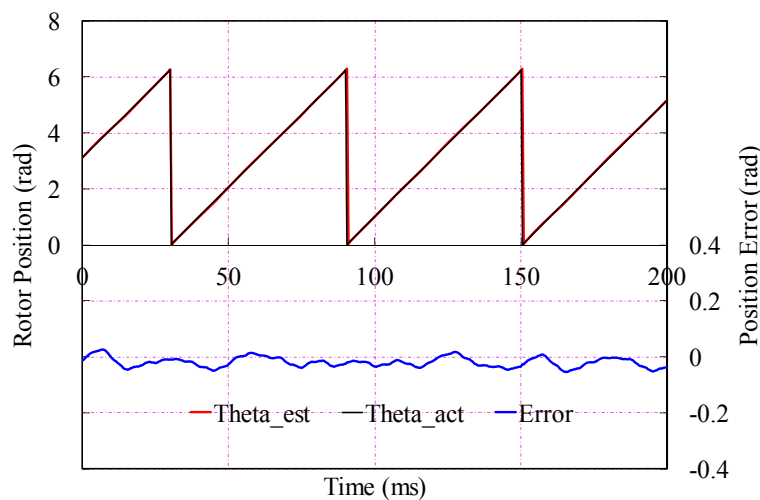


Fig. 6.17. Estimated position and error from third harmonic flux-linkage (θ_{est} : Estimated rotor position, θ_{act} : Actual rotor position, Error: Rotor position estimation error)

Since signal quality of the measured u_{sn} is usually not good enough for the rotor position estimation in the aforementioned strategies, third harmonic flux-linkage ψ_{sn} is usually essential to derive the high accurate rotor position. Due to the constant amplitude of ψ_{sn} , the design of rotor position estimator could be simplified and the bandwidth of estimator could be constant. However, the implementation of BPF for getting the third harmonic flux-linkage may lead unexpected phase delay and poor frequency response, which will deteriorate the performance of the conventional rotor position estimation under dynamic situation.

The dynamic performance tests are carried out when the rotor initial speed is 200rpm with 1A q -axis current, and the speed reference changes from 200rpm to 320rpm and then the rotor speed response which is the same as shown in Fig. 6.9. Then the derived two sets of third harmonic flux-linkage are shown in Fig. 6.18. It is shown that with the change of speed, the amplitude of flux-linkage could be maintained as constant. Then applying the EKF based rotor position estimator as shown in Fig. 6.3, the rotor position can be estimated. From the estimated and actual rotor positions and the error between them shown in Fig. 6.19, it could be found that the estimation error is much larger during speed transit due to the implementation of improper BPF for obtaining the flux-linkage.

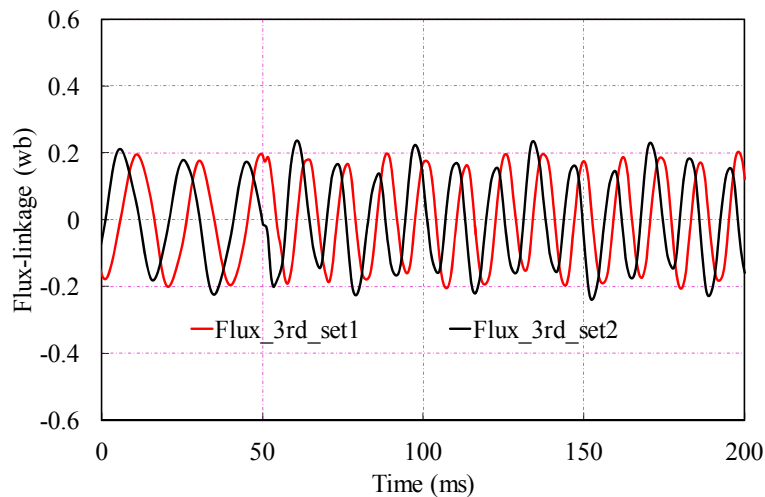


Fig. 6.18. ψ_{sn} of two sets of windings under dynamic situation

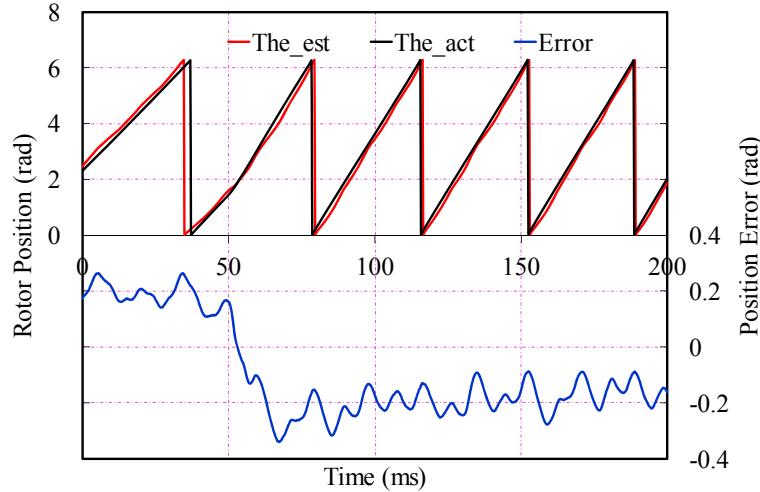


Fig. 6.19. Estimated position and error from third harmonic flux-linkage
 (θ_{est} : Estimated rotor position, θ_{act} : Actual rotor position,
 Error: Rotor position estimation error)

From (6.15), it could be found that e_{3_set1} and e_{3_set2} have a $\pi/6$ rad shift under fundamental reference frame which is equivalent as a $\pi/2$ rad shift under third harmonic reference frame, i.e.

$$\begin{cases} e_{3_set1} = E_3 \cdot \sin(3\theta_r) \\ e_{3_set2} = E_3 \cdot \sin(3 \times (\theta_r - \pi/6)) = -E_3 \cdot \cos(3\theta_r) \end{cases} \quad (6.17)$$

Hence, for dual three-phase PMSM, the two derived third harmonic back-EMFs in (6.17) are orthogonal from each other as illustrated in Fig. 6.13. Hence, the two sets of measured u_{sn} can be directly applied for rotor position estimation by applying the simplified EKF based rotor position estimator as shown in Fig. 6.3 and no filter is needed. Hence, the robustness and accuracy of rotor position estimation could be significantly improved, whilst the phase delay also can be minimized and frequency response in the rotor position estimation can also be enhanced.

However, the amplitude of third harmonic back-EMF E_3 is speed-dependent. Hence, with fixed parameters in PID controller, the bandwidth of the rotor position estimator and frequency response will vary with speed. In practical implementation for simplicity, the PID parameters are set as $k_p=35$ and $k_i=70$, $k_d=40$, based on the value of E_3 as 0.37V at 200rpm which is half rated speed under no-load condition. Although the bandwidth of the estimator changes with speed, the requirement of accuracy can be met. To

improve the frequency response and maintain the constant bandwidth of the estimator, on-line tuning of PID controller with the feedback speed should be considered. Then, the parameters can be derived as $k_p = 35\omega_r^e / 200$, $k_i = 70\omega_r^e / 200$, and $k_d = 40\omega_r^e / 200$. Hence, the loop bandwidth can be maintained around 24Hz at different rotor speed.

Hence, applying this on-line tuning simplified EKF based rotor position estimator, the rotor position could be estimated from the two sets of third harmonic back-EMF directly even when the amplitude varies with speed. Meanwhile, even though the quality of the signals is not good enough, these contaminated high order harmonic back-EMFs such as ninth, fifteenth and so on, will be eliminated and will not affect the rotor position estimation accuracy as shown in Fig. 6.20.

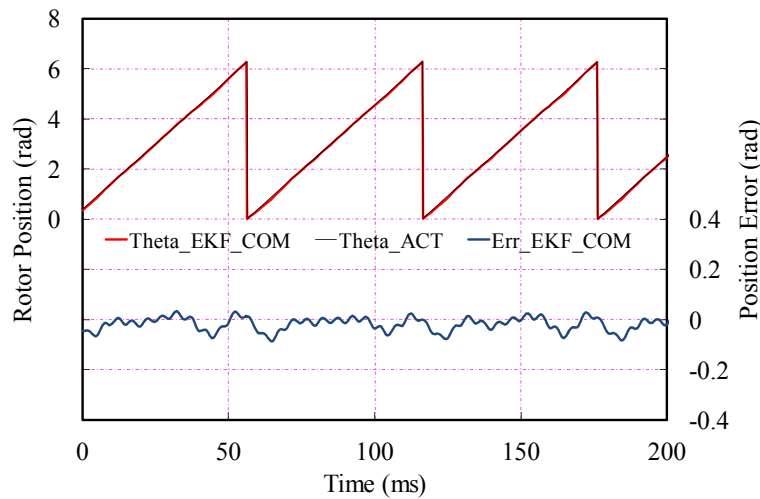


Fig. 6.20. Estimated position and error from third harmonic back-EMF

(*Theta_EKF_COM*: Estimated rotor position from third harmonic back-EMF, *Theta_act*: Actual rotor position, *Error_EKF_COM*: Rotor position estimation error from third harmonic back-EMF)

Compared these results in Fig. 6.17 and Fig. 6.20, it could be found that the accuracy of the two methods are nearly the same, however, the estimation error based on third harmonic back-EMF contains a little more high frequency fluctuation than the one based on flux-linkage due to the higher level of high order triplen harmonic noise.

The same dynamic tests are carried out as shown in Fig. 6.9, the measured two sets

of third harmonic back-EMF are shown in Fig. 6.21 and the amplitudes of them vary with speed. Considering the feedback rotor speed and on-line tuning the parameter of simplified EKF based estimator, the rotor positions and the error can be estimated from third harmonic back-EMF as shown in Fig. 6.22.

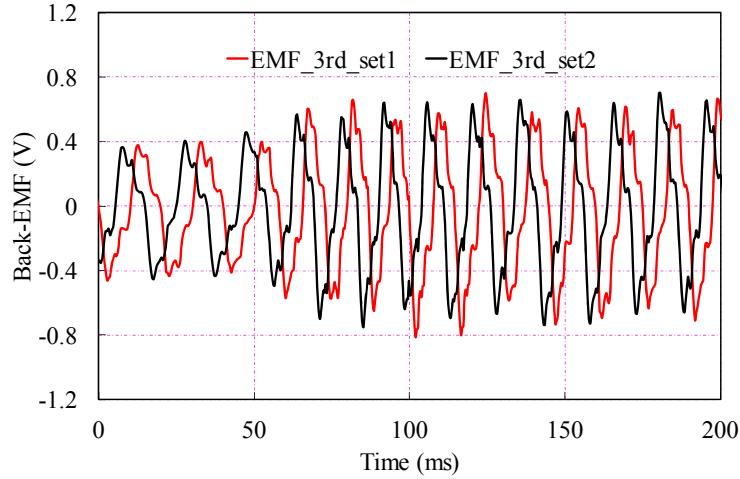


Fig. 6.21. Measured u_{sn} of two sets of windings under dynamic situation

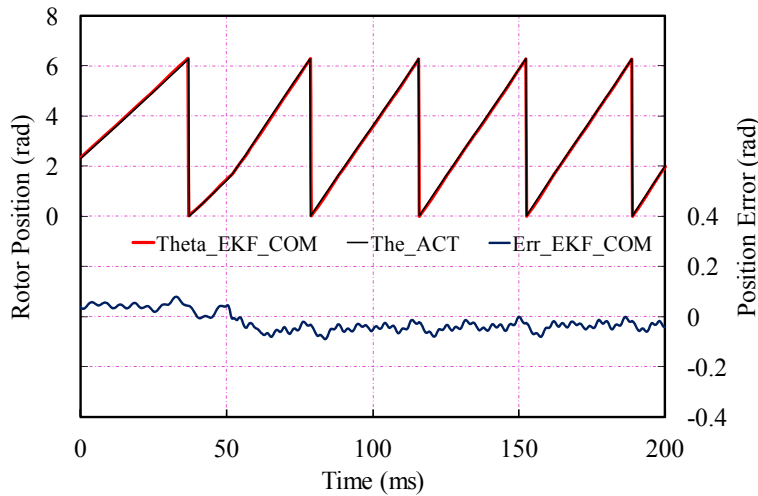


Fig. 6.22. Estimated position and error from third harmonic back-EMF

(θ_{EKF_COM} : Estimated rotor position from third harmonic back-EMF, θ_{act} : Actual rotor position, Err_EKF_COM : Rotor position estimation error from third harmonic back-EMF)

The experimental results demonstrate that the proposed rotor position estimation strategy based on third harmonic back-EMF for dual three-phase PMSM has nearly the same steady-state performance compared with the method based on third harmonic

flux-linkage. Meanwhile, it can significantly improve the dynamic performance of the rotor estimation due to the removal of all filters and the improvement of frequency response.

6.5 Conclusion

In this chapter, simplified EKF which is a recursive optimum-state estimator is applied based on third harmonic back-EMF for sensorless control. For single three-phase PMSM operation, the two essentially orthogonal signals which are third harmonic back-EMF and flux-linkage are applied as references of simplified EKF based rotor position estimator, and then the rotor position can be estimated with high accuracy at steady-state and dynamic situation from triplen harmonic back-EMFs and flux-linkages even though there may contain too much high order harmonic components.

For dual three-phase PMSM, there are two sets of windings, and they usually have a spatial $\pi/6$ elec-rad shift. Hence, the two sets of triplen harmonic back-EMFs are orthogonal under third harmonic reference frame, as well as the triplen harmonic flux-linkages derived from the measured triplen harmonic back-EMFs. By applying the same simplified EKF based rotor position estimator, the rotor position can be estimated from triplen harmonic back-EMFs or flux-linkages. The experimental results prove that both of the proposed strategies have accurate rotor position estimation under steady-state, whilst the strategy based on third harmonic back-EMF with on-line tuning EKF based estimator can achieve much better dynamic performance of rotor estimation due to the elimination of all filters.

CHAPTER 7

INFLUENCE OF MACHINE SALIENCY AND WINDING IMBALANCE ON SENSORLESS CONTROL BASED ON THIRD HARMONIC BACK-EMF

7.1 Introduction

The improvement of dynamic performance of conventional sensorless control and the performance and robustness of flux observer by speed error compensation in Chapter 5, and sensorless control based on simplified EKF based rotor position estimator in Chapter 6, are both highly dependent on the phase angle of the source signal which is third harmonic back-EMF. If the third harmonic back-EMF can precisely reflect the rotor position, then by employing proper estimators, the rotor position definitely can be estimated accurately. As mentioned in Chapter 6, the contained higher order triplen harmonic components can be eliminated by the simplified EKF based rotor position estimator, whereas there are still several cases in which the sensorless control using the u_{sn} derived third harmonic back-EMF will not be applicable, i.e. absence of third harmonic back-EMF, rotor saliency, and imbalanced parameters of three phases.

Hence, in this chapter, the absence of third harmonic back-EMF will be introduced as well as the related alternative sensorless control solution. The influence of the stator current and machine saliency to rotor position estimation based on third harmonic will be investigated. Furthermore, due to the imbalanced machine parameters and sensing resistor network, the measured triplen harmonic back-EMF will contain certain fundamental component distortion which will severely deteriorate the performance of rotor position estimation. Then, an improved rotor position estimation strategy for single and dual three-phase PMSM under imbalanced situation will also be introduced.

7.2 Absence of Third Harmonic Back-EMF

The amplitude of the third harmonic back-EMF E_3 is

$$E_3 \propto \omega_r \cdot B_3 \cdot k_{w3} \quad (7.1)\#$$

where ω_r is the rotor speed and B_3 is the amplitude of the third harmonic component of PM excitation flux density which will change due to the magnetic saturation, whilst k_{w3} is the winding factor for the third harmonic which is calculated as

$$k_{w3} = k_{p3} \cdot k_{d3} \cdot k_{s3} \quad (7.2)$$

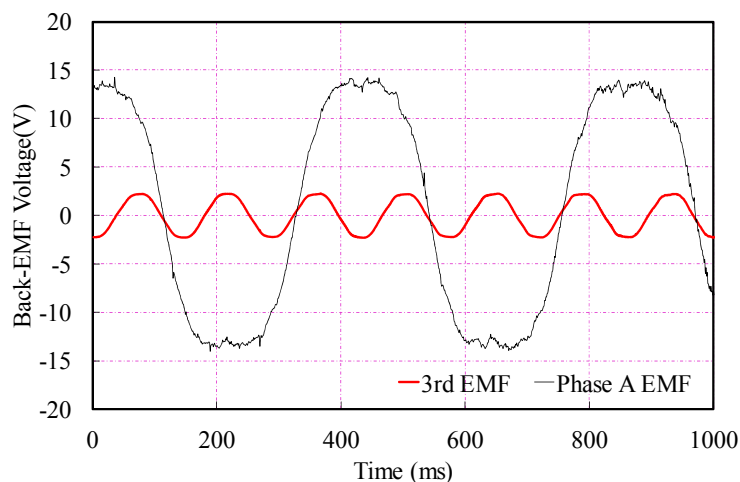
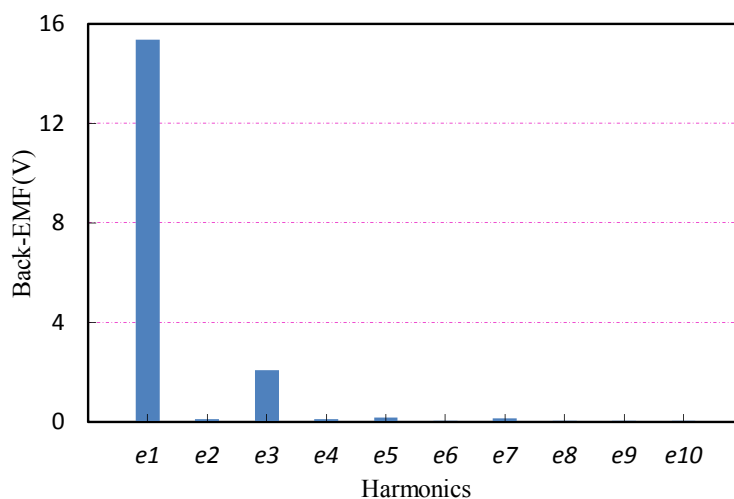
where k_{p3} , k_{d3} and k_{s3} are the coil pitch factor, distribution factor and skew factor, respectively. If either B_3 , k_{p3} , k_{d3} or k_{s3} are zero or very small, the third harmonic back-EMF will be zero or too small to sense. Furthermore, (7.1) also shows that third harmonic back-EMF based sensorless control is also unsuitable for zero or very low speed operation since E_3 is proportional to rotor speed. For simplicity, third harmonic back-EMF can be expressed as

$$e_3 = B_3 \cdot k_{p3} \cdot k_{d3} \cdot k_{s3} \cdot \omega_r \cdot \cos(3\theta_r) = K_3 \cdot \omega_r \cdot \cos(3\theta_r) \quad (7.3)$$

where K_3 represents the third harmonic back-EMF constant [SHE02a].

Motor II has significant third harmonic component in the air gap field, whilst its third harmonic back-EMF constant is approximately 0.1363, which makes the third harmonic back-EMF significant, with amplitude 13% of fundamental back-EMF. The measured waveforms and FFT analysis of the back-EMF are given in Fig. 7.1.

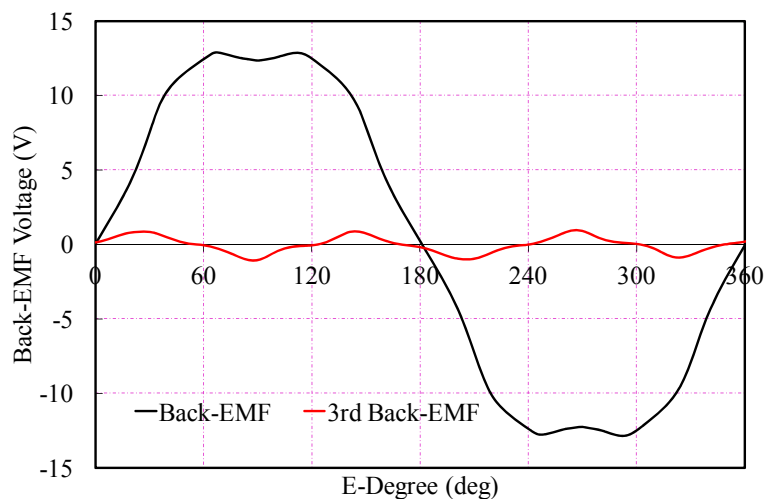
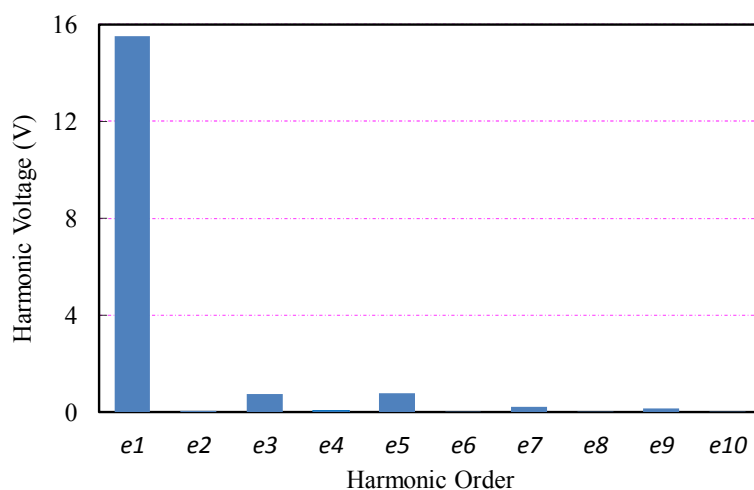
In many PMSMs, the third harmonic excitation field is weak. For example, in Motor III which is dual three-phase PMSM with overlapping windings, the third harmonic EMF constant is approximately 0.0036 and the amplitude of third harmonic EMF is only about 4.9% which is smaller than the ratio of Motor II. The measured waveforms and frequency spectrum of the back-EMF are given in Fig. 7.2. If the ratio of third harmonic back-EMF is smaller than 2%, the sensorless control strategies based on third harmonic back-EMF may not be able to be implemented due to its small SNR. Meanwhile, with serious magnetic saturation, the third harmonic back-EMF may be absent due to the change of third harmonic EMF constant K_3 .

(a) Phase Back-EMF and measured u_{sn} 

(b) Spectrum of phase back-EMF

Fig. 7.1. Back-EMF and spectrum at 10rpm of Motor II

Since the third harmonic back-EMF is proportional to rotor speed, all sensorless controls show the good performance above certain speed but suffering at low speed due to the too small amplitude of third harmonic back-EMF, and cannot be applied with zero speed. Hence, at zero and low speed, sensorless control methods based on high frequency carrier signal injection as introduced in Chapter 3 and Chapter 4 are widely implemented due to the effectiveness in that region. However, when rotor speed is higher than certain speed, which is usually 5% of the rated speed, the back-EMF based sensorless control strategies could be employed, and would be superior to high frequency carrier signal injection based strategy at higher speed range.

(a) Phase Back-EMF and measured u_{sn} 

(b) Spectrum of phase back-EMF

Fig. 7.2. Back-EMF and spectrum at 400rpm of Motor III

7.3 Influence of Stator Current and Machine Saliency to Rotor Position Estimation Based on Third Harmonic Back-EMF

7.3.1 Influence of Stator Current and Machine Saliency

When the machine windings are Y-connected, the third harmonic back-EMF presents in the phase back-EMF rather than line back-EMF irrespective of the operational mode. Then a triplen harmonic back-EMF as shown in (7.4) can be

derived by the measured voltage with the aid of a Y-connected resistor network between the central point “s” of this Y-connected resistor network and the machine winding neutral point “n” as

$$u_{sn} = (u_{an} + u_{bn} + u_{cn}) / 3 = e_3 + e_9 + e_{15} + \dots \approx e_3 \quad (7.4)$$

However, this is correct only when the winding inductance is constant. In salient machines, such as those with interior/inserted PMs, the winding inductance varies with the rotor position [SHE06a]. Thus, the expression of u_{sn} will be affected by stator current. The self and mutual winding inductances can be expressed in (7.5), i.e.

$$\begin{cases} L_{aa} = \sum_k L_k \cos k\theta_r \\ L_{bb} = \sum_k L_k \cos k(\theta_r - 2\pi/3) \\ L_{cc} = \sum_k L_k \cos k(\theta_r + 2\pi/3) \\ M_{bc} = M_{cb} = \sum_k M_k \cos k\theta_r \\ M_{ca} = M_{ac} = \sum_k M_k \cos k(\theta_r - 2\pi/3) \\ M_{ab} = M_{ba} = \sum_k M_k \cos k(\theta_r + 2\pi/3) \end{cases} \quad (7.5)$$

$$k = 0, 2, 4, 6, 8, \dots$$

Whilst the motor voltage equations are

$$\begin{bmatrix} u_{an} \\ u_{bn} \\ u_{cn} \end{bmatrix} = R \begin{bmatrix} i_a \\ i_b \\ i_c \end{bmatrix} + \begin{bmatrix} e_a \\ e_b \\ e_c \end{bmatrix} + p \left\{ \begin{bmatrix} L_{aa} & M_{ab} & M_{ac} \\ M_{ba} & L_{bb} & M_{bc} \\ M_{ca} & M_{cb} & L_{cc} \end{bmatrix} \cdot \begin{bmatrix} i_a \\ i_b \\ i_c \end{bmatrix} \right\} \quad (7.6)$$

Based on (7.5) and (7.6), the measured u_{sn} should be presented as

$$\begin{aligned} u_{sn} &= e_{triplen} + \frac{p}{3} \times \sum_j \{ (L_j - M_j) \times [i_a \cos j\theta_r + i_b \cos j(\theta_r - 2\pi/3) + i_c \cos j(\theta_r + 2\pi/3)] \} \\ &= e_{triplen} + \frac{j\omega_r(L_j - M_j)}{3} \{ (i_d \cos \theta_r - i_q \sin \theta_r)(-\sin j\theta_r) \\ &\quad + [i_d \cos(\theta_r - 2\pi/3) - i_q \sin(\theta_r - 2\pi/3)][-\sin j(\theta_r - 2\pi/3)] \\ &\quad + [i_d \cos(\theta_r + 2\pi/3) - i_q \sin(\theta_r + 2\pi/3)][-\sin j(\theta_r + 2\pi/3)] \} \\ &= -A_{p_3rd} \cos 3\theta_r + \frac{j\omega_r(L_j - M_j)}{2} [-i_d \sin(j \pm 1)\theta_r - i_q \cos(j \pm 1)\theta_r] \\ &j=2,4,8,10, \dots \end{aligned} \quad (7.7)$$

The sign of \pm in $[-i_d \sin(j \pm 1)\theta_r - i_q \cos(j \pm 1)\theta_r]$ is decided by j , where $(j+1)$ or

$(j-1)$ should be a multiple of 3. Clearly, if there is no machine saliency, both L_j and M_j are 0, and u_{sn} will only represent the triplen harmonic back-EMF. However, when the rotor saliency exists, neither L_j nor M_j is 0, nor usually $(L_j - M_j)$ is 0 either. Therefore, if currents flow in the machine, the second part on the right side of (7.7) will cause distortion in the measured u_{sn} .

Ignoring the high frequency components which can be eliminated by EKF based rotor position estimator, only 2nd and 4th harmonic inductances would affect the measurement of u_{sn} , and (7.7) could be rewritten as

$$\begin{aligned}
u_{sn} &\approx -A_{p_3rd} \cos 3\theta_r \\
&\quad + [-\omega_r(L_2 - M_2) + 2\omega_r(L_4 - M_4)] \cdot i_q \cos 3\theta_r \\
&\quad + [-\omega_r(L_2 - M_2) - 2\omega_r(L_4 - M_4)] \cdot i_d \sin 3\theta_r \\
&= -\omega_r [K_3 \cos 3\theta_r \\
&\quad + (L_2 - 2L_4 - M_2 + 2M_4) i_q \cos 3\theta_r \\
&\quad + (L_2 + 2L_4 - M_2 - 2M_4) i_d \sin 3\theta_r] \\
&= -\omega_r [K_3 \cos 3\theta_r + K_{iq} i_q \cos 3\theta_r + K_{id} i_d \sin 3\theta_r]
\end{aligned} \tag{7.8}$$

It could be seen that the measured u_{sn} will mainly contain three parts, viz. third harmonic back-EMF, influence of the q -axis current, and influence of d -axis current, whilst the rotor speed ω_r will not affect the phase angle of the measured u_{sn} . Since the influence of q -axis current is in-phase with third harmonic back-EMF, it will only change the amplitude but not the phase angle of measured u_{sn} . However, the influence of d -axis current is orthogonal to third harmonic back-EMF. Furthermore, the d -axis current also will affect the air gap saturation which will change the third harmonic back-EMF constant and machine inductances. Hence, with larger d -axis current and influence factor K_{id} , and small third harmonic back-EMF constant K_3 , the influence may be too large and has to be compensated.

7.3.2 Experimental Analysis and Estimation Error Compensation

Several experiments have been carried out to analyze the influence of machine saliency and stator current on third harmonic back-EMF and rotor position estimation. The overall control scheme which is same as Fig. 5.8, is shown in Fig. 7.3 for convenience, and has been implemented on the dSPACE platform with Test Rig III.

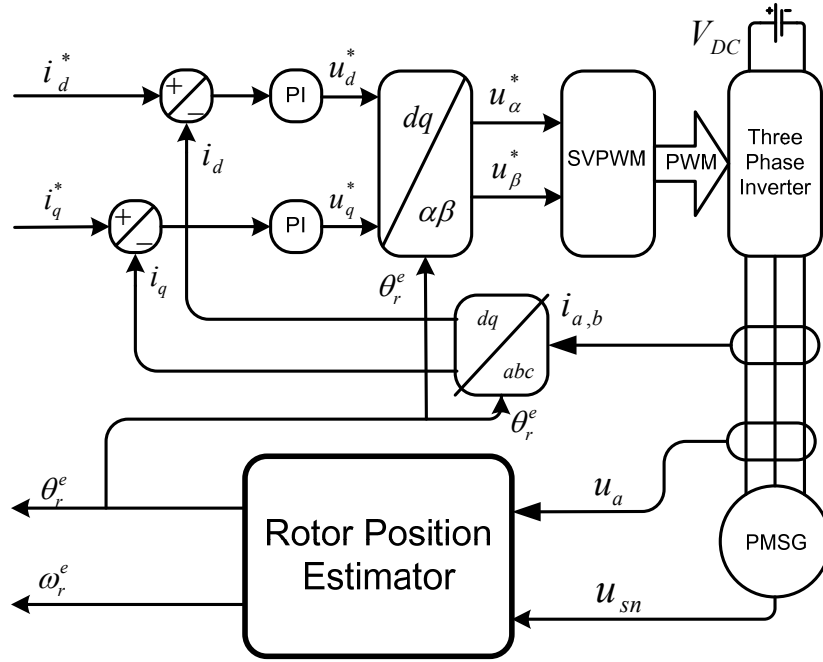


Fig. 7.3. Overall control scheme

The FFT analysis of the measured back-EMF of the implemented Motor III at rated rotor speed has been shown in Fig. 7.2. It could be concluded that the third harmonic back-EMF is identical but not too large, and the higher order triplen harmonic back-EMF such as ninth and fifteenth are not smaller significantly than the third harmonic back-EMF.

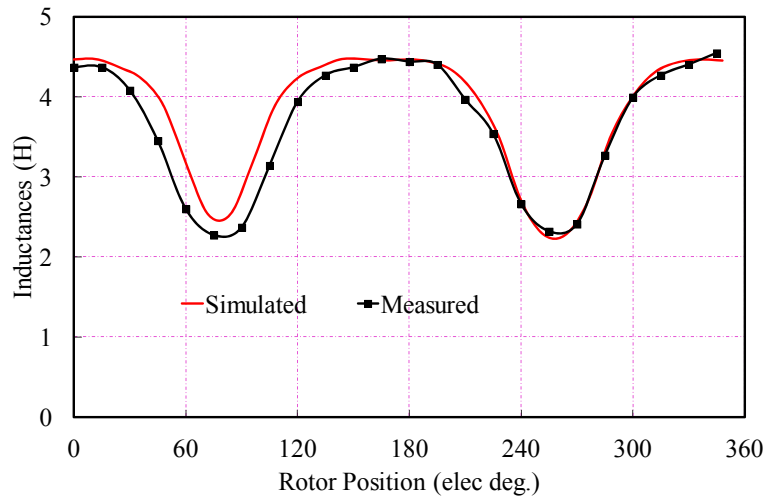
In order to identify the saliency level, the self-inductance against rotor position should be measured. With a controllable voltage source, a fixed sine wave voltage is imposed on the terminals of phase-A1. The frequency of this voltage is chosen to 400 Hz to eliminate the voltage drop due to phase resistance and the influence of iron loss, and the amplitude of voltage is equal to 0.7 V to avoid the magnetic saturation. For each step of stator rotation, the amplitudes of current and the voltage in phase-A1 are read for calculating the self-inductances. Hence, the self-inductance of Phase-A1 could be finally calculated by

$$L_{aa1} = \frac{U_h}{2\pi f I_h} \quad (7.9)$$

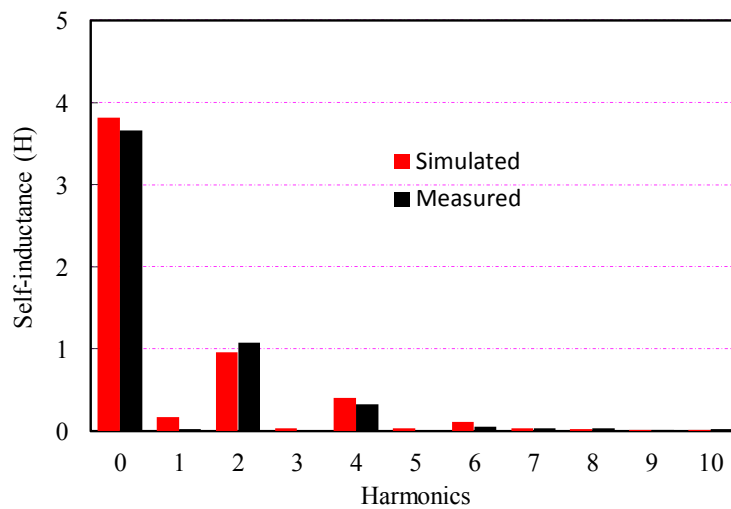
where I_h is the amplitude of phase current measured by current sensor and U_h is the amplitude of injected high frequency voltage.

The simulated and measured self-inductance of Phase-A and their FFT analysis

are shown in Fig. 7.4. It could be seen that, L_2 and L_4 are both large which illustrate the machine saliency is very large. Based on the analysis of (7.8), the influence of d -axis current would be obvious, and the rotor position error would be too large and has to be compensated.



(a) Simulated and measured self inductance



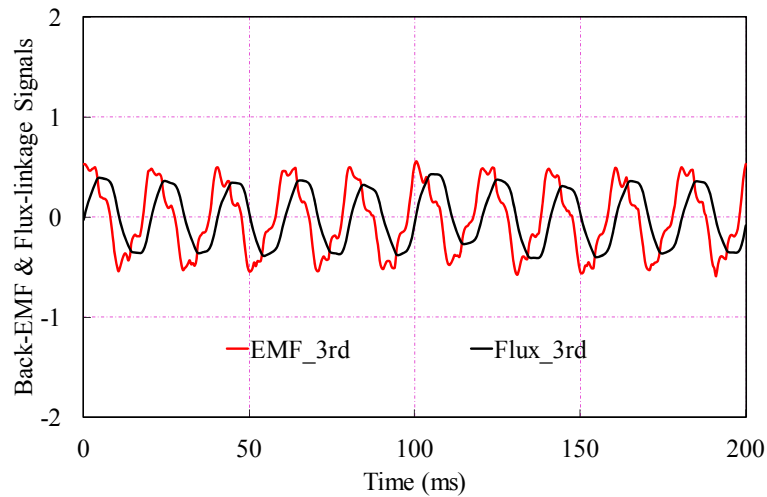
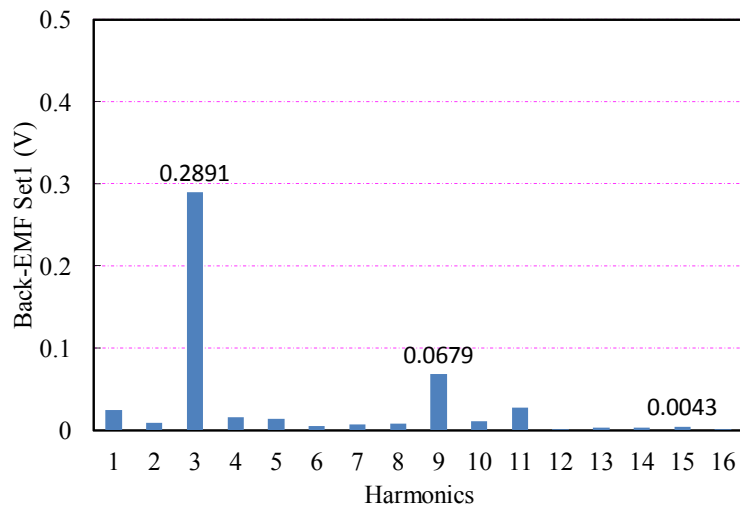
(b) Spectrum of self inductance

Fig. 7.4. Simulated and measured Phase-A self inductance

7.3.2.1 Analysis of q -axis current influence

When the machine windings are open circuit, the measured u_{sn} and ψ_{sn} at 200rpm are shown in Fig. 7.5(a) and the FFT analysis of u_{sn} is shown in Fig. 7.5(b), where the amplitude of u_{sn} is about 0.2891V. If $i_d=0$, then (7.8) could be rewritten as

$$u_{sn} = -\omega_r [K_3 \cos 3\theta_r + K_{iq} i_q \cos 3\theta_r] \quad (7.10)$$

(a) Measured u_{sn} and ψ_{sn} (b) Spectrum of u_{sn} Fig. 7.5. Third harmonic back-EMF and FFT analysis ($i_q=0A$, $i_d=0A$, 200rpm)

The spectrum of measured u_{sn} at different q -axis currents are shown in Fig. 7.6, from which, it could be seen that the amplitude of the measured u_{sn} has a small and linear change to the applied q -axis current since the influence is in-phase with third harmonic back-EMF. Furthermore, the phase angle is kept constant and the rotor position estimation error is also constant to q -axis current. Hence, its influence could be ignored.

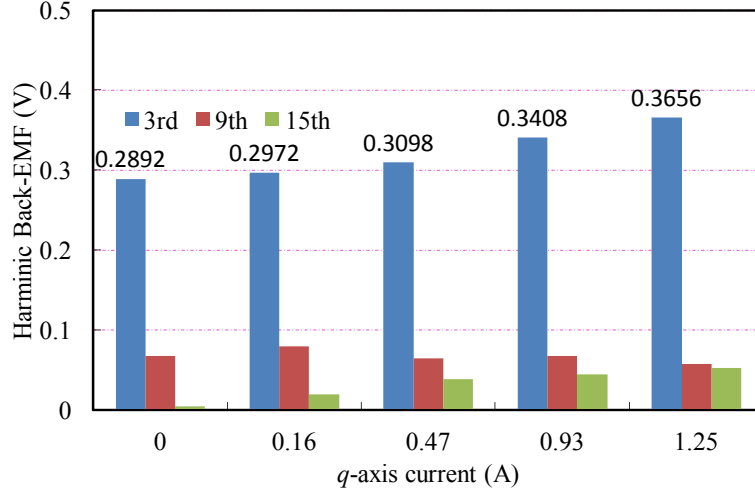


Fig. 7.6. Spectrum of measured u_{sn} at different q -axis currents

7.3.2.2 Analysis of negative d -axis current influence

If i_q is constant, then (7.8) could be rewritten as

$$u_{sn} = -\omega_r [(K_3 + K_{iq}i_q) \cos 3\theta_r + K_{id}i_d \sin 3\theta_r] \quad (7.11)$$

Then, based on the tested machine inductances in Fig. 7.4 and i_q influence factor from Fig. 7.6, the rotor position estimation error should be able to predicted by (7.12) theoretically, i.e.

$$\theta_{err}^e = \frac{1}{3} \arcsin \left[\frac{\omega_r^e K_{id}}{E_3 + \omega_r^e K_{iq} i_q} \right] \quad (7.12)$$

However, when the machine is working with $-5A$ d -axis current, the amplitude of u_{sn} has a significant increase to $0.8183V$ as shown in Fig. 7.7 which is obviously not caused by i_q . It can be determined by analysis that the magnetic saturation effect will change by the applied negative i_d . Hence, the back-EMF constant K_3 will increase and be constant after $-3A$ d -axis current as illustrated in Fig. 7.8 which is the spectrum of u_{sn} at different negative d -axis current.

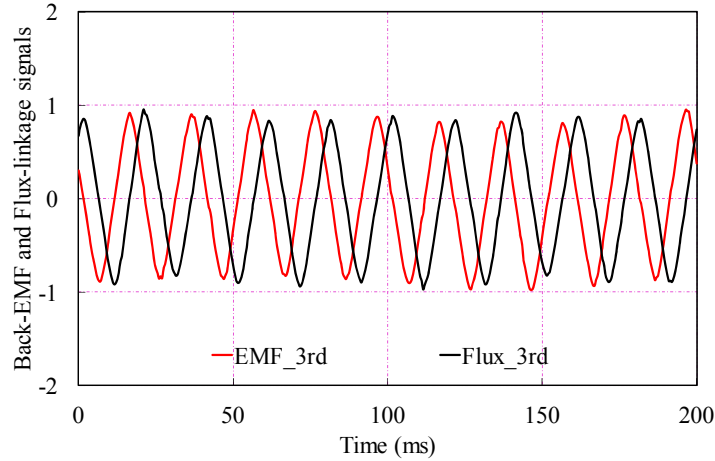


Fig. 7.7. Measured u_{sn} and ψ_{sn} ($i_q=1A$, $i_d=-5A$, 200rpm)

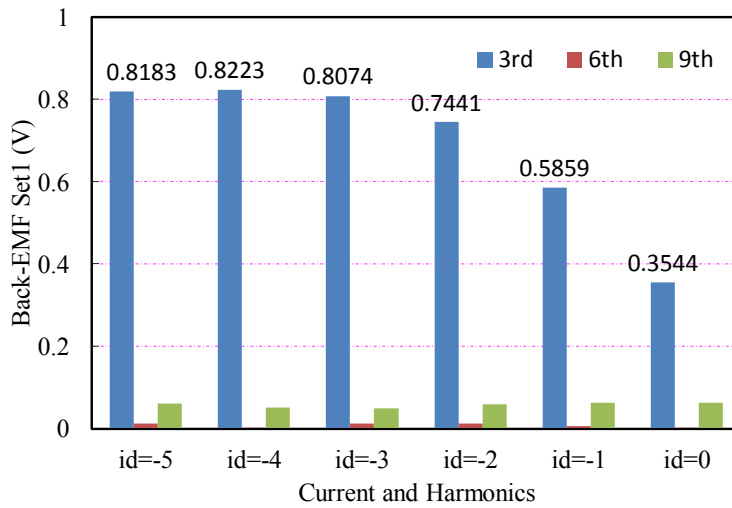


Fig. 7.8. Spectrum of u_{sn} at different negative d -axis current

Then, with measured K_3 and K_{iq} , the phase angle shift caused by d -axis current which is also the rotor position estimation error can be predicted as shown in Fig. 7.9. However, compared with the measured estimation error which is also shown in Fig. 7.9, they do not match well which could be caused by the change of machine inductances due to the air gap saturation effect caused by i_d . Meanwhile, K_{id} seems to be smaller from the experimental results in this case, and phase shift caused by i_d is also limited.

Since the change of machine harmonic inductances and back-EMF constant E_3 is nearly unpredictable, the amplitude and phase shift are both difficult to be predicted. However, the rotor position estimation error which is phase shift of u_{sn} will be

constant with i_d . Hence, the pre-measured estimation error at different i_d in Fig. 7.9 could be compensated easily.

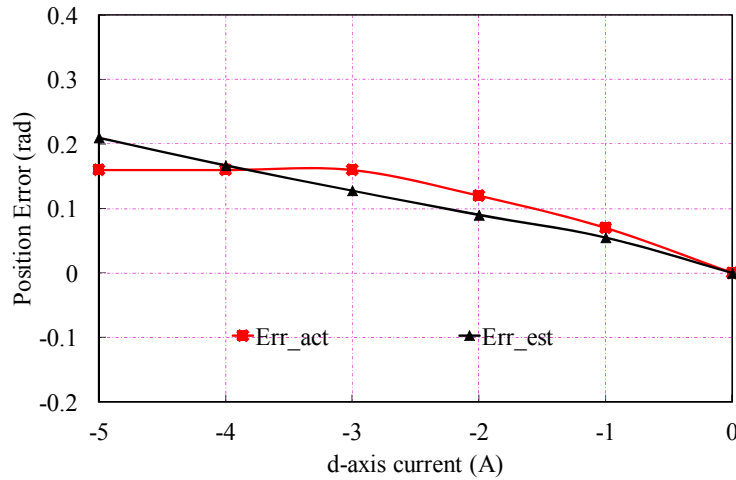


Fig. 7.9. Predicted and measured estimation error (Err_act : Measured rotor position estimation error, Err_est : Predicted rotor position estimation error)

When the d -axis current changes from 0A to -5A, the amplitude of u_{sn} will change as in Fig. 7.10. Meanwhile, the phase angle also changes, which will lead rotor position estimation error.

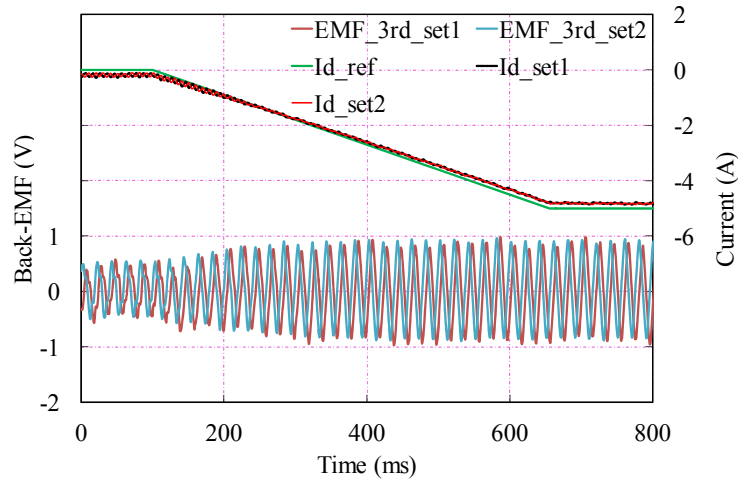


Fig. 7.10. u_{sn} at different d -axis current

($Theta_3rd_set1$: Third harmonic back-EMF of winding set1, $Theta_3rd_set2$: Third harmonic back-EMF of winding set2, Id_ref : d -axis current reference, Id_set1 : d -axis current of winding set1, Id_set2 : d -axis current of winding set2,)

The estimated rotor position and estimation error before and after compensation of the i_d influence are shown in Fig. 7.11. It can be seen that, the estimation error can

be remarkably reduced. However, in this thesis, the third harmonic back-EMF is very small and the machine saliency is very large. Therefore, the influence of machine saliency is significant. In the application with large third harmonic back-EMF constant and small saliency, the estimation error would be limited, and can be ignored.

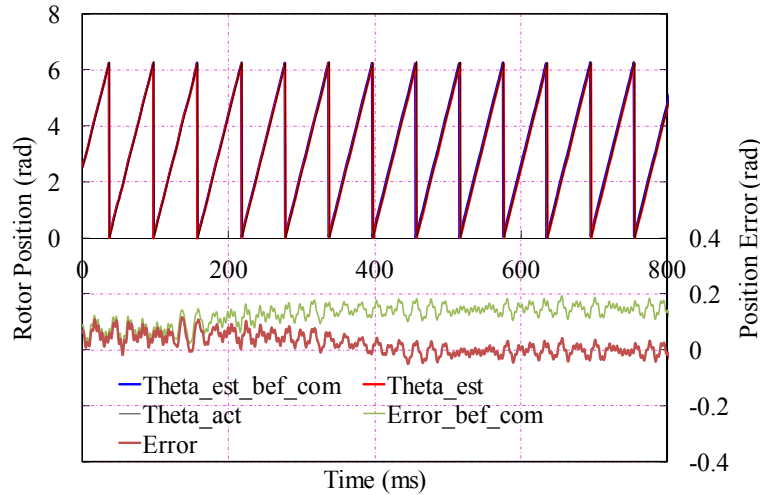


Fig. 7.11. Estimation error before and after compensation

($\Theta_{est_bef_com}$: Estimated rotor position before compensation, Θ_{est} : Estimated rotor position after compensation Θ_{act} : Actual rotor position, $Error_bef_com$: Position estimation error before compensation, $Error$: Position estimation error after compensation)

7.3.2.3 Analysis of positive d -axis current influence

Large positive d -axis current is usually used for flux enhancing and torque boost at low speed. When large positive i_d is applied, the flux density in air gap will be seriously saturated and the measured u_{sn} will be seriously distorted as shown in Fig. 7.12 and have a large phase shift which is measured with 4A d -axis current at 200rpm. Hence, the estimated rotor position will contain large estimation error as illustrated in Fig. 7.13. Therefore, it is important to avoid sensorless control based on third harmonic back-EMF with large positive d -axis current no matter whether there is machine saliency or not. Fortunately, positive d -axis current is usually not used in most cases.

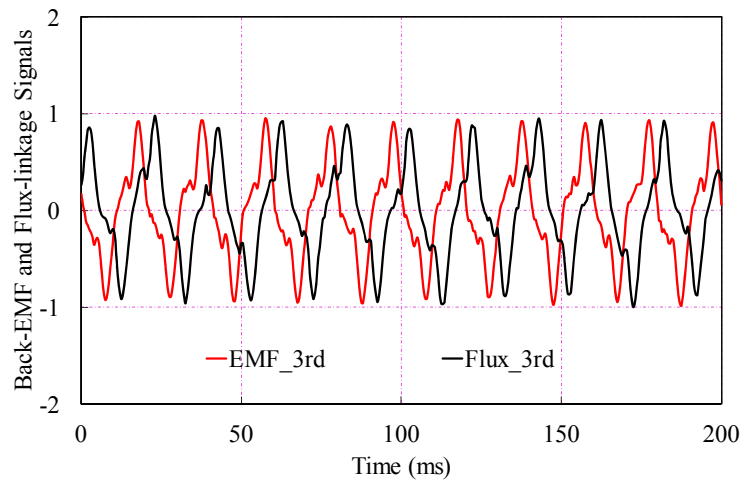


Fig. 7.12. Measured u_{sn} with 4A d -axis currents

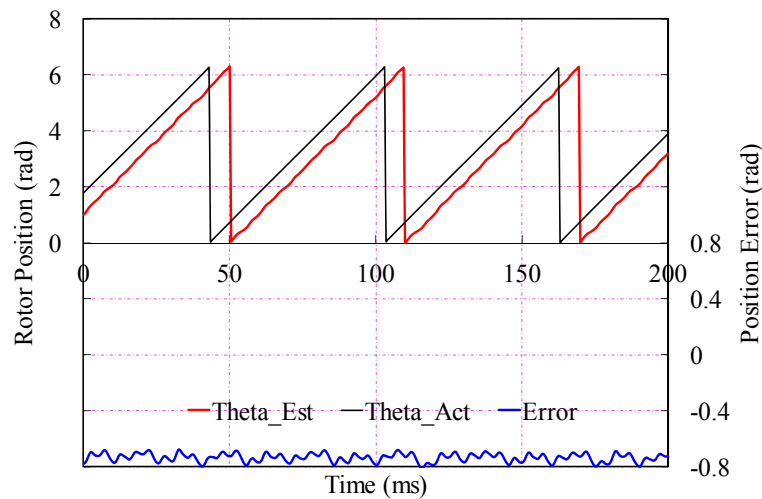


Fig. 7.13. Estimated rotor position and estimation error (θ_{Est} : Estimated rotor position, θ_{Act} : Actual rotor position, $Error$: Position estimation error)

7.3.3 Summary

1. The machine speed and q -axis current will not affect the phase angle of the triplen harmonics.

2. Negative d -axis current will change the amplitude and phase angle of the triplen harmonics due to the machine saliency and variety of magnetic saturation. The estimation error caused by negative d -axis current can be compensated based on pre-measured rotor position error, whilst for the machine with large third harmonic back-EMF constant and small machine saliency, the estimation error would be limited and could just be ignored.

3. Large positive d -axis current which is used for flux enhancing and torque boost at low speed, will cause serious magnetic saturation of flux-linkage leading to large estimation error and failure of sensorless control. Hence, it is better to avoid sensorless control based on third harmonic back-EMF with large positive d -axis current. Fortunately, positive d -axis current is usually not used in most cases.

7.4 Rotor Position Estimation Based on Third Harmonic back-EMF under Imbalanced Situation for Single and Dual Three-Phase PMSM

7.4.1 Detection of Third Harmonic back-EMF under Imbalanced Situation

Without affected by machine saliency, (7.4) will be correct on the condition of balanced phase impedance and fundamental back-EMF. Then, the sum of armature effect of current and fundamental back-EMF should be zero, and the following equation can be derived based on Fourier analysis, i.e.

$$\begin{aligned} u_{an} + u_{bn} + u_{cn} &= [(R_{sa} + pL_{sb}) \cdot i_a + (R_{sb} + pL_{sb}) \cdot i_b + (R_{sc} + pL_{sc}) \cdot i_c] + (e_a + e_b + e_c) \\ &= (R_s + pL_s) \cdot (i_a + i_b + i_c) + (e_{a1} + e_{b1} + e_{c1}) + 3(e_3 + e_9 + e_{15} + \dots) \\ &= 3(e_3 + e_9 + e_{15} + \dots) \end{aligned} \quad (7.13)$$

The voltage between the central point “s” of a Y-connected resistor network and the machine winding neutral point “n” could be expressed as

$$\begin{aligned} u_{sn} &= (u_{an} + u_{bn} + u_{cn})/3 - (u_{as} + u_{bs} + u_{cs})/3 \\ &= (u_{an} + u_{bn} + u_{cn})/3 - (i_{as}R_1 + i_{bs}R_2 + i_{cs}R_3)/3 \end{aligned} \quad (7.14)$$

If the resistor network is also balanced, the second part of (7.14) should be zero as well. Then a triplen harmonic back-EMF which equals the sum of the three phase back-EMF can be derived from the measured voltage between “s” and “n”, i.e.

$$u_{sn} = (u_{an} + u_{bn} + u_{cn})/3 = e_3 + e_9 + e_{15} + \dots = e_{triplen} \quad (7.15)$$

Based on (7.13) and (7.14), (7.15) could be rewritten as

$$\begin{aligned}
u_{sn} &= (u_{an} + u_{bn} + u_{cn})/3 - (i_{as}R_1 + i_{bs}R_2 + i_{cs}R_3)/3 \\
&= [(R_{sa} + pL_{sb}) \cdot i_a + (R_{sb} + pL_{sa}) \cdot i_b + (R_{sc} + pL_{sc}) \cdot i_c]/3 \\
&\quad + (e_{a1} + e_{b1} + e_{c1})/3 \\
&\quad - (i_{as}R_1 + i_{bs}R_2 + i_{cs}R_3)/3 + e_{triplen}
\end{aligned} \tag{7.16}$$

It could be found from (7.16) that the machine impedance, fundamental back-EMF and sensing resistor network will affect the measurement of triplen harmonic back-EMF. Clearly, on the condition of balanced situation, the first three parts in (7.16) will be zero, and u_{sn} will just represent the triplen back-EMF of the machine. However, with imbalanced machine windings, three phase impedances and back-EMFs are usually different. Then the sum of each phase armature effect and back-EMF will result in a fundamental order signal with unknown amplitude and phase angle. With imbalanced resistor network, u_{sn} will also contain certain value fundamental order components. Then the sum of them would be a fundamental order signal whose amplitude and phase angle are very difficult to predict. Hence, (7.16) could be rewritten as (7.17) under imbalanced situation.

$$u_{sn} = A_{p_u} \sin(\omega_r t + \varphi_u) + e_{triplen} = u_f + e_{triplen} \tag{7.17}$$

where A_{p_u} , ω_r and φ_u are the amplitude, angular speed and initial phase angle of fundamental components u_f , respectively. The angular speed ω_r of u_f is already known as it is equal to fundamental rotor speed. However, A_{p_u} and φ_u are both unknown in terms of the different imbalanced situations of phase back-EMF and resistor network.

For Motor III which is a dual three-phase PMSM, the measured u_{sn} will contain fundamental components under imbalanced situation as same as single three-phase PMSM. The measured back-EMF of set1 is shown in Fig. 7.14 when the windings are open circuit with 400rpm rotor speed. A serious imbalance situation was found where the amplitude difference of three phase back-EMF is up to 6.7% due to the winding turn error. Similar situation occurs in set2, whilst two sets of resistor networks are also imbalanced from each other. Hence, the measured u_{sn} of two sets of windings as shown in Fig. 7.15(a) will contain certain fundamental components as validated by the FFT analysis of set1 shown in Fig. 7.15(b) where the fundamental amplitude is about 0.34V, nearly as large as the amplitude of third harmonic back-EMF.

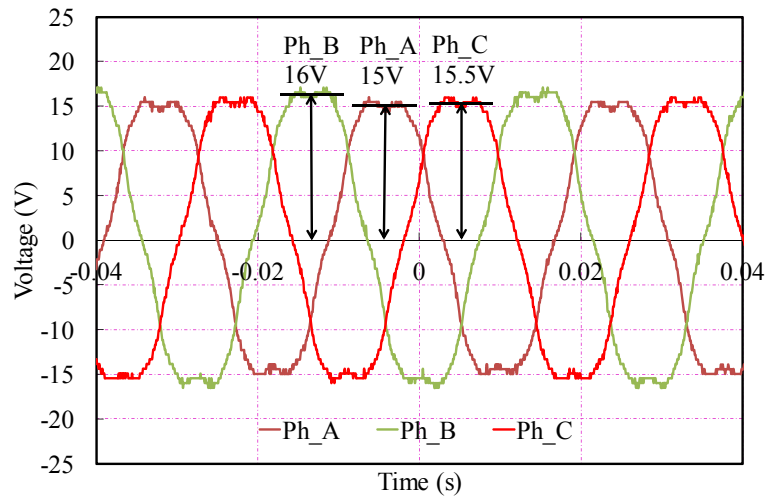
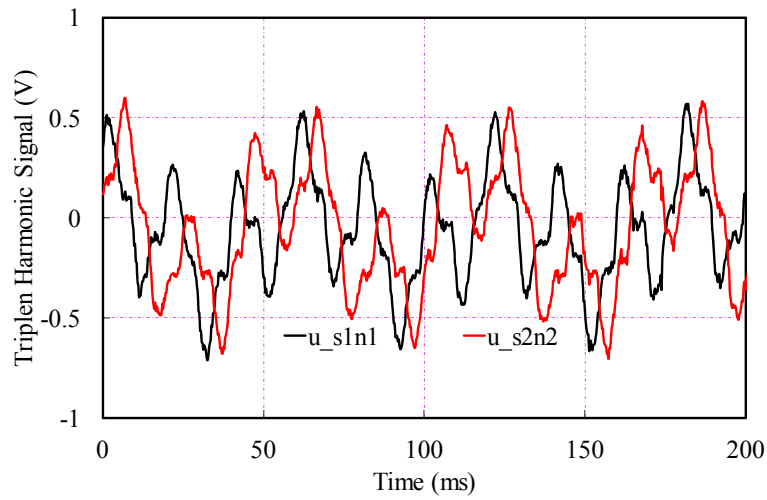
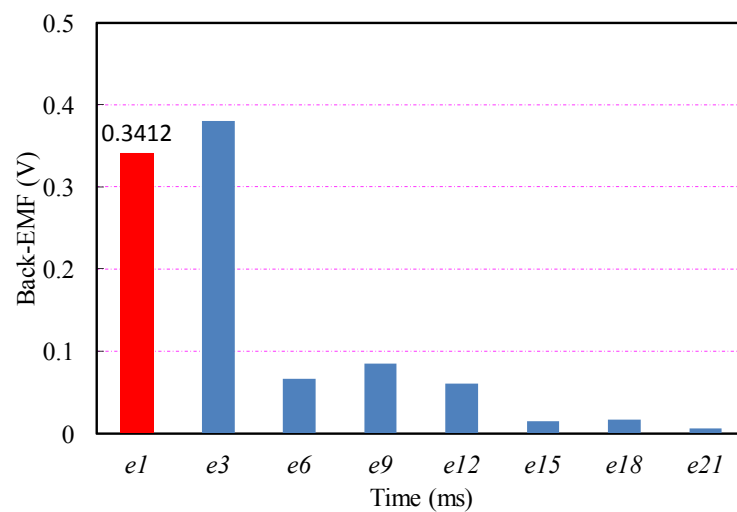


Fig. 7.14. Phase Back-EMFs of set1



(a) Measured u_{sn} of two sets of windings

(u_{s1n1} : Measured u_{sn} of winding set1, u_{s2n2} : Measured u_{sn} of winding set2)



(b) Spectrum of measured u_{sn} of set1

Fig. 7.15. Third harmonic back-EMF and harmonic analysis

7.4.2 Rotor Position Estimation under Imbalanced Situation for Single Three-Phase PMSM operation

7.4.2.1 Rotor position estimation under imbalanced situation

For single three-phase PMSM operation, ψ_{sn} derived by a BPF will be constant amplitude and could be applied as reference to retrieve the rotor position which has been introduced in Section 5.3 and Section 6.3. However, with imbalanced machine impedance, fundamental back-EMF and sensing resistor network, ψ_{sn} should be re-expressed as

$$\psi_{sn} = \psi_f + \psi_{triplen} = -A_{mp} \cos(3 \times \theta_r) + \psi_9 + \psi_{15} + \dots + \psi_f \quad (7.18)$$

where A_{mp} is the amplitude of ψ_{sn} . Since BPF is designed for third harmonic frequency, the frequency response for fundamental components u_f may be different. Hence, the amplitudes and phase angles of u_{sn} and ψ_{sn} would be both different from each other.

To estimate the rotor position, the related orthogonal signal of ψ_{sn} also should be calculated based on u_{sn} . However, since the amplitude of u_{sn} varies with rotor speed, it should be unified as A_{mp} considering the feedback estimated rotor speed ω_r^e as

$$u_{sn_unified} = u_f + \frac{K_p}{\omega_r^e} E_3 \sin(3 \times \theta_r) = A_{mp} \sin(3 \times \theta_r) + e_9 + e_{15} + \dots + u_f \quad (7.19)$$

where K_p is the unify-ratio between the amplitudes of the third harmonic flux-linkage and back-EMF.

When the machine is operating with one set of winding as a single three-phase PMSM, the measured $u_{sn_unified}$ and ψ_{sn} derived by BPF at 200rpm are shown in Fig. 7.16. It can be seen that the measured $u_{sn_unified}$ and ψ_{sn} contain too much high order triplen harmonic noise and therefore exhibits serious fundamental order distortion due to the severe imbalanced situation, and the conventional rotor position estimation cannot be applied with such low quality signals.

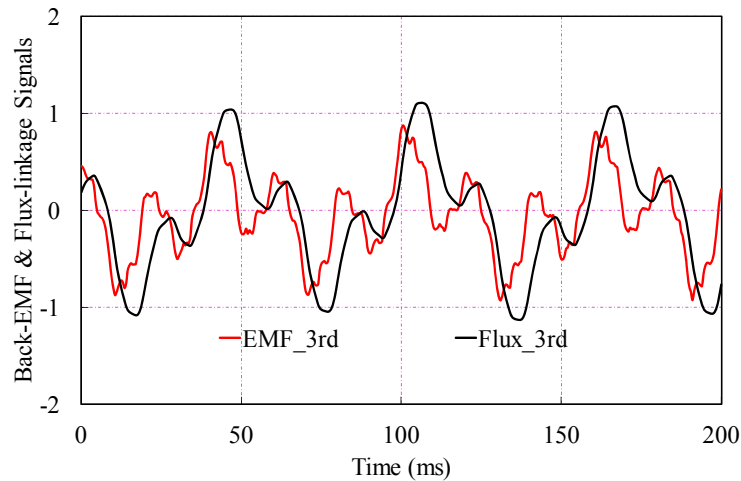


Fig. 7.16. Measured u_{sn} and ψ_{sn}

To obtain the rotor position from (7.18) and (7.19), the rotor position estimator based on simplified EKF which has been demonstrated in Fig. 6.3 is employed. For single three-phase PMSM, the value of Ψ_3 in this work is approximately 0.2Wb, and hence, the amplitude A_{mp} in (7.18) and (7.19) are both 0.2 and the parameters of estimator could be set as $k_p=70$, $k_i=140$, and $k_d=80$. Then, the Bode plot of the position estimator is shown in Fig. 7.17, and it can be seen that the loop bandwidth is around 24Hz.

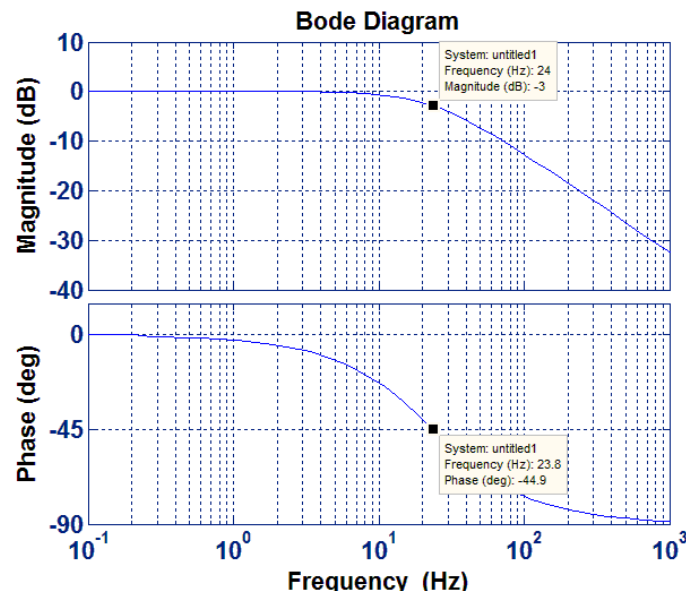


Fig. 7.17. EKF based rotor position estimator

Due to characteristic of applied EKF based rotor position estimator, the high order harmonic components i.e. ninth, fifteenth and so on, could be treated as noise and

eliminated. However, the sub-order harmonic fundamental components cannot be eliminated. The overall control scheme with the proposed rotor position estimation strategy is the same as shown in Fig. 7.3 which has been implemented on the dSPACE platform with Test Rig III, and applying the EKF based rotor position estimator. Then, the rotor position at 200rpm rotor speed with 1A q -axis current is estimated as shown in Fig. 7.18, whereas the estimated error is too large to accept due to the serious fundamental distortion.

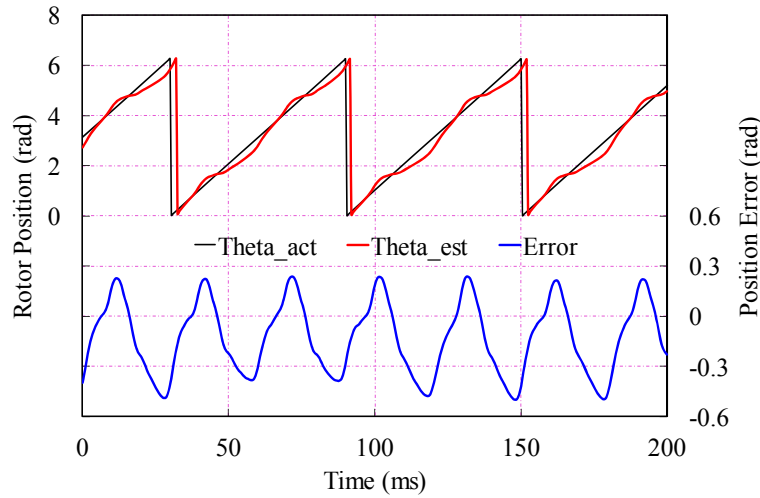


Fig. 7.18. Rotor position estimation under imbalanced situation

(Θ_{est} : Estimated rotor position, Θ_{act} : Actual rotor position, $Error$: Position estimation error)

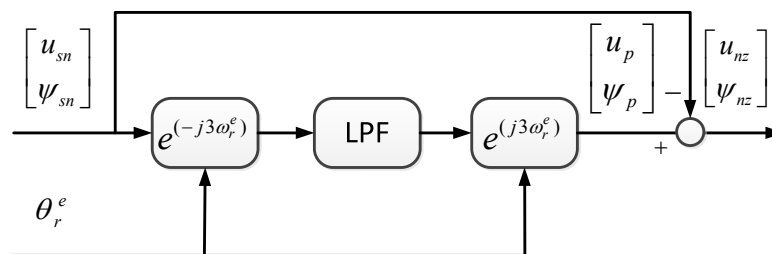
7.4.2.2 Rotor Position Estimation with Imbalanced Situation Compensation

Since the third harmonic back-EMF in (7.19) and the third harmonic flux-linkage in (7.18) are orthogonal from each other and can form a third order circular trace, they could be equivalent as positive sequence signals under third harmonic reference frame, whilst all the other components in (7.18) and (7.19) are negative and zero sequence components and all the contained noise signal, i.e.

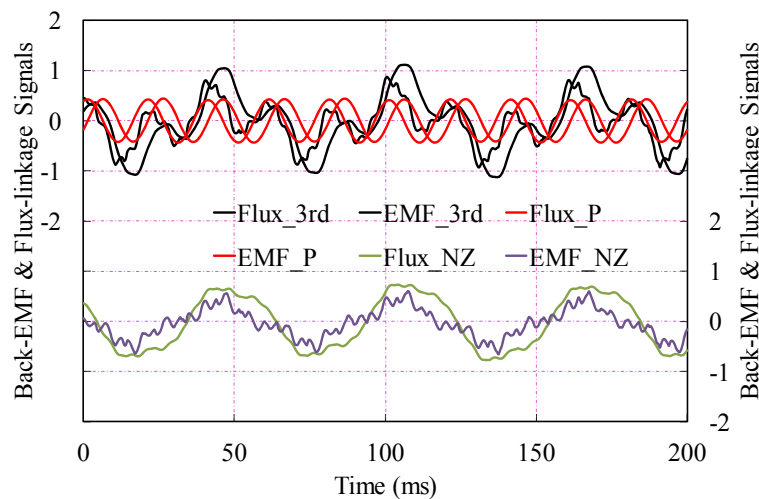
$$\begin{bmatrix} u_{sn} \\ \psi_{sn} \end{bmatrix} = \begin{bmatrix} u_p \\ \psi_p \end{bmatrix} + \begin{bmatrix} u_{nz} \\ \psi_{nz} \end{bmatrix} = \begin{bmatrix} A_{mp} e^{j(3\omega_r t)} \\ \end{bmatrix} + \begin{bmatrix} u_{nz} \\ \psi_{nz} \end{bmatrix} \quad (7.20)$$

In order to separate these components from the original measured signals, SRFF, i.e. synchronous reference frame filter, Fig. 7.19(a), which is applied in signal

demodulation of rotating high frequency carrier voltage injection strategy as introduced in Section 3.2.2 [GAR07] [RAC10] is the typical solution. SRFF uses the frame transformation to centre spectral component of interest at DC. With the aid of a LPF, this DC component can be easily obtained without phase lag. Conversely, applying the frame transformation, the positive sequence voltage is obtained. Then, subtracting from the original signal, the negative and zero sequence components could be derived. With the aid of SRFF and feedback estimated rotor position, the positive sequence components of the measured triplen harmonic signals, and all the other components which contain the relevant fundamental and higher order triplen harmonic components could be derived as shown in Fig. 7.19(b).



(a) Synchronous reference frame filter (SRFF)



(b) Positive, the other contained components

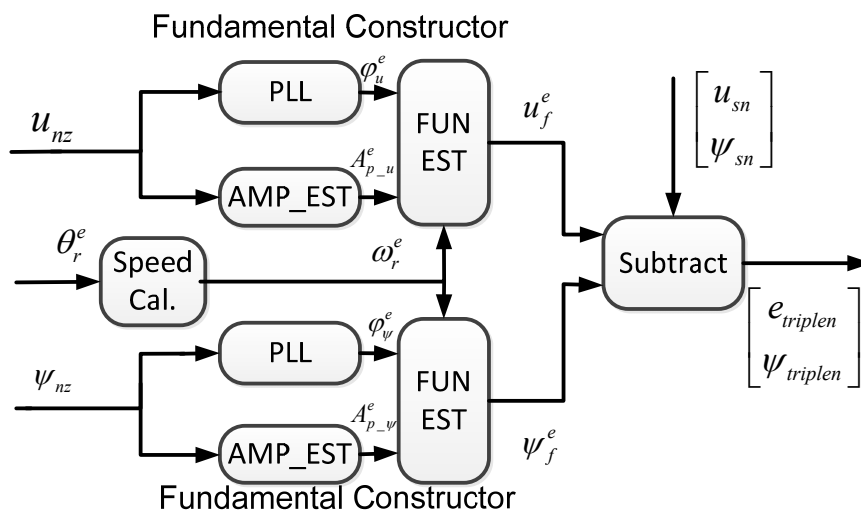
Fig. 7.19. SRFF to separate the fundamental components from the original signals
 (*Flux_3rd/EMF_3rd*: Original third harmonic back-EMF and flux-linkage,
Flux_P/EMF_P: Positive sequence components, *Flux_NZ/EMF_NZ*: All the other
 contained components)

Each derived signal without positive sequence components contains the relevant

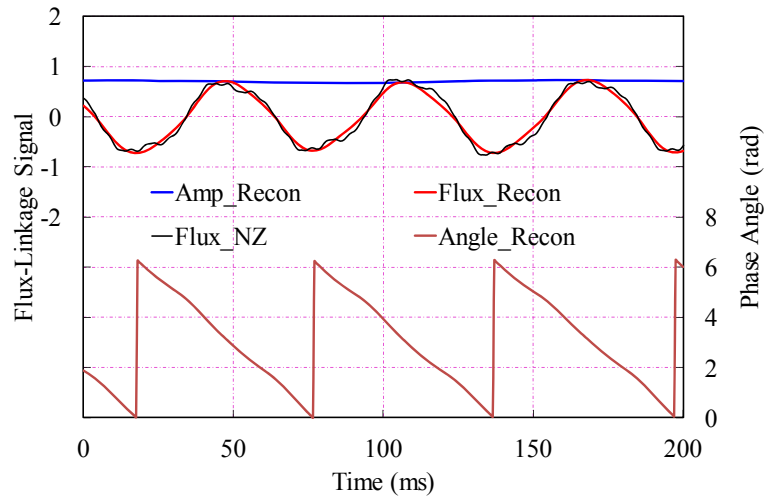
fundamental. By the effect of the EKF based rotor position estimator, the high order triplen harmonic components can be eliminated. However, the most sensitive fundamental component should be compensated in advance.

Hence, the fundamental component compensator as shown in Fig. 7.20(a) will be applied to derive the pure triplen harmonic signals. Treating the higher order components as noise and applying the fundamental component constructor, the initial phase angle φ which is usually constant under the same imbalanced situation could be obtained with the aid of PLL. Meanwhile, the amplitudes A_{p_u} and $A_{p_ψ}$ also can be retrieved by the amplitude estimators. Thus, the fundamental components could be reconstructed through the estimated amplitude $A_{p_u}^e$ and $A_{p_ψ}^e$, initial phase angle and $\varphi_{ψ}^e$, and ω_r^e which is the feedback estimated rotor position.

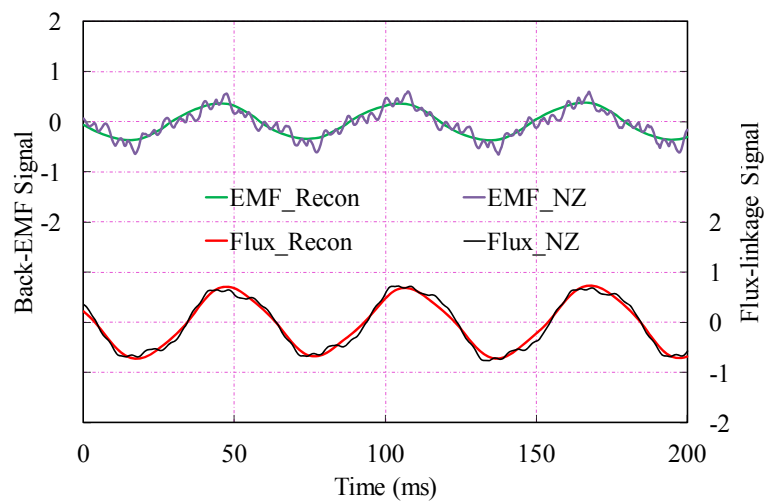
Hence, by applying the fundamental component compensator, e.g. with flux-linkage, the phase angle can be derived by PLL and the feedback estimated rotor angular speed, and the amplitude can also be estimated, Fig. 7.20(b). Hence, the fundamental distortion can be reconstructed. Applying the same compensator to back-EMF, the reconstructed fundamental distortion of back-EMF and flux-linkage are shown in Fig. 7.20(c) compared with the derived negative and zero sequence components, and they can match well.



(a) Fundamental component compensator



(b) Derived amplitude and phase angle, and the reconstructed fundamental components (*Flux_NZ*: All the other contained components in ψ_{sn} , *Amp_Recon*: Estimated amplitude, *Angle_Recon*: estimated phase angle, *Flux_Recon*: Reconstructed fundamental flux-linkage)



(c) Reconstructed fundamental components compared with negative and zero sequence components (*Flux_NZ/EMF_NZ*: All the other contained components, *Flux_Recon/EMF_Recon*: Reconstructed fundamental back-EMF and flux-linkage)

Fig. 7.20. Reconstruction of fundamental components

Then after subtracting the reconstructed fundamental distortions from u_{sn} and ψ_{sn} , the pure triplen harmonic back-EMF and flux-linkage without the fundamental distortion could be derived as shown in Fig. 7.21, compared with the signals before compensation. Then, employing the EKF based rotor position estimator at the same 200rpm rotor speed with 1A q -axis current, the rotor position could be estimated from the pure triplen harmonic back-EMF with high accuracy. Hence, applying the proposed rotor position estimator under imbalanced situation, Fig. 7.22(a), the rotor position can be estimated with much higher accuracy and lower fluctuation as shown in Fig. 7.22(b).

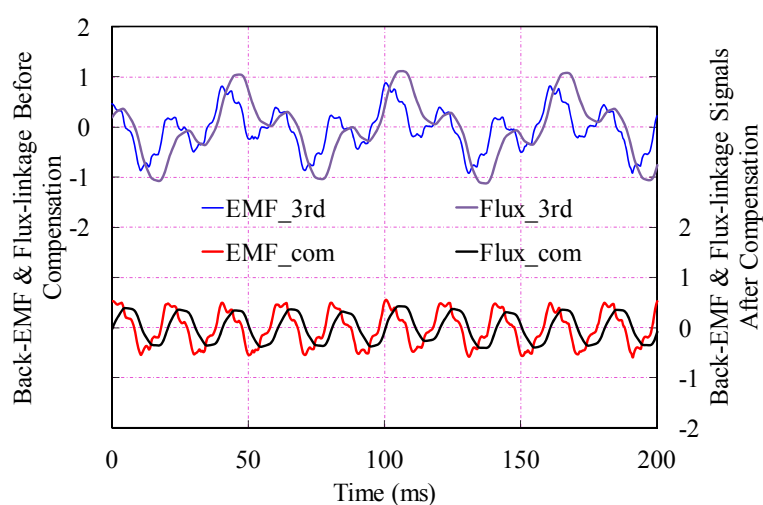
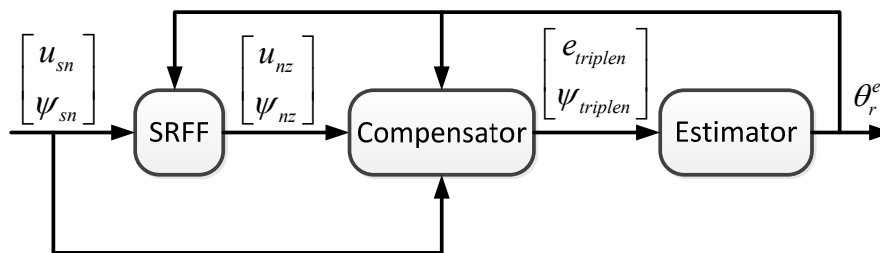
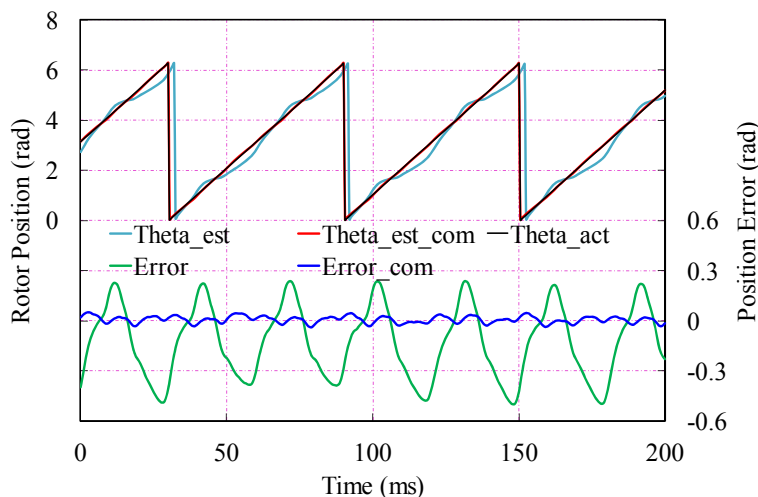


Fig. 7.21. Triplen harmonic back-EMF before and after fundamental components compensation ($Flux_3rd/EMF_3rd$: Original signals of third harmonic back-EMF and flux-linkage, $Flux_com/EMF_com$: Compensated third harmonic back-EMF and flux-linkage)



(a) Rotor position estimator under imbalanced situation



(b) Rotor positions and estimation errors

(*Theta_est*: Estimated rotor position, *Theta_act*: Actual rotor position, *Error*: Rotor position estimation error, *Theta_est_com*: Compensated estimated rotor position, *Error_com*: Compensated rotor position estimation error)

Fig. 7.22. Rotor position estimation before and after fundamental component compensation

The dynamic test is carried out when the rotor speed reference changes from 200rpm to 320rpm as shown in Fig. 7.23. Then applying the proposed rotor position estimation strategy under imbalanced situation, the estimated and actual rotor positions, and the estimation error is shown in Fig. 7.24 compared with the values derived directly from the original signals. It shows that the rotor position estimated after fundamental component compensation can achieve much higher accuracy and lower fluctuation as before compensation. The experimental results demonstrate that the proposed rotor position estimation strategy based on third harmonic back-EMF can significantly improve steady-state and dynamic performance of the rotor estimation under imbalanced situation for single three-phase PMSM operation.

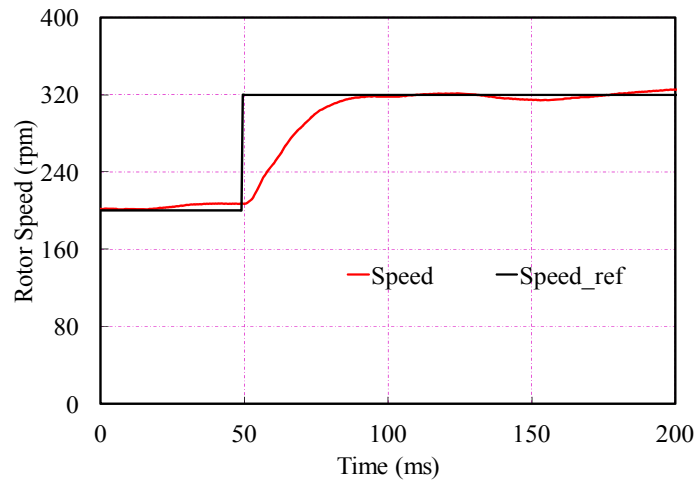


Fig. 7.23. Dynamic test situation

(*Speed_ref*: Speed reference, *Speed*: Actual rotor speed)

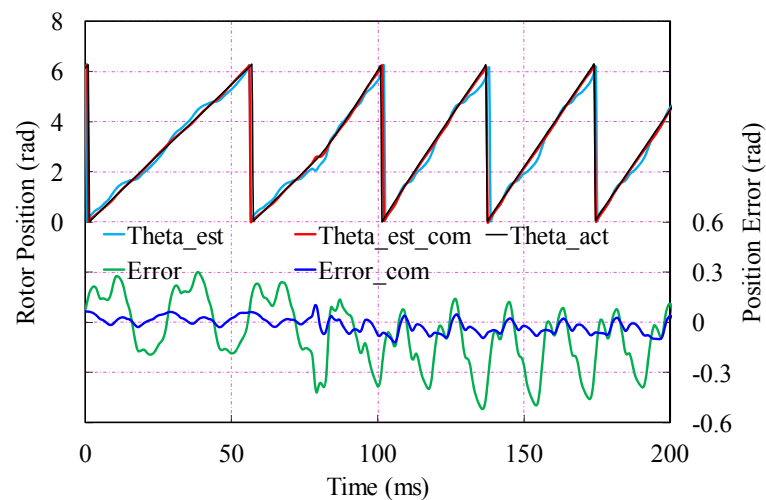


Fig. 7.24. Rotor position estimation before and after fundamental component compensation (*Theta_est*: Estimated rotor position, *Theta_act*: Actual rotor position, *Error*: Rotor position estimation error, *Theta_est_com*: Compensated estimated rotor position, *Error_com*: Compensated rotor position estimation error)

7.4.3 Rotor Position Estimation under Imbalanced Situation for Dual Three-Phase PMSM operation

7.4.3.1 Rotor position estimation under imbalanced situation

For dual three-phase PMSM, the measured voltages between “s1” and “n1”, and between “s2” and “n2”, could represent the two sets of the third harmonic back-EMFs

of the two sets of windings as

$$\begin{cases} u_{s1n1} = e_{3_set1} + e_{9_set1} + e_{15_set1} + \dots = e_{triplen_set1} \approx e_{3_set1} \\ u_{s2n2} = e_{3_set2} + e_{9_set2} + e_{15_set2} + \dots = e_{triplen_set2} \approx e_{3_set2} \end{cases} \quad (7.21)$$

Usually, the two sets of winding have a spatial $\pi/6$ elec-rad shift. Hence, e_{3_set1} and e_{3_set2} orthogonal under third harmonic reference frame i.e.

$$\begin{cases} e_{3_set1} = A_{mp} \sin(3 \times \theta_r) \\ e_{3_set2} = A_{mp} \sin(3 \times (\theta_r - \pi / 6)) = -A_{mp} \cos(3\theta_r) \end{cases} \quad (7.22)$$

However, with imbalanced machine impedance, fundamental back-EMF and sensing resistor network, u_{sn} of the two sets of windings should be re-expressed as

$$\begin{cases} u_{s1n1} = e_{triplen_set1} + u_f = A_{mp} \sin(3 \times \theta_r) + e_9 + e_{15} + \dots + u_{f1} \\ u_{s2n2} = e_{triplen_set2} + u_f = -A_{mp} \cos(3 \times \theta_r) + e_9 + e_{15} + \dots + u_{f2} \end{cases} \quad (7.23)$$

When the Motor III is operating as a dual three-phase PMSM, the measured u_{sn} of the two sets of windings at 200rpm are shown in Fig. 7.25, where the measured u_{sn} both contain too much high order triplen harmonic noise and fundamental order distortion.

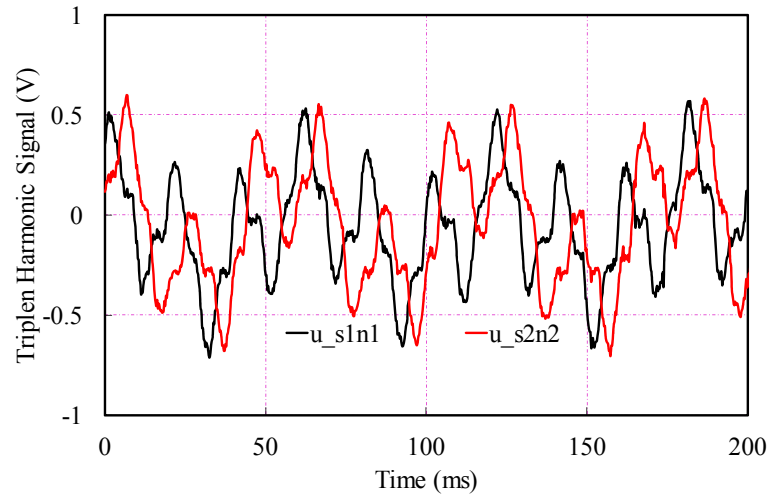


Fig. 7.25. Measured u_{sn} of two sets of windings

(u_{s1n1} : Measured u_{sn} of winding set1, u_{s2n2} : Measured u_{sn} of winding set2)

Applying the simplified EKF based rotor position estimator, these high order harmonic components such as ninth, fifteenth, etc, will be eliminated, and will almost not affect the accuracy of position estimation. However, for dual three-phase PMSM, since A_{mp} is speed-dependent, k_p , k_i and k_d of PI controller should be on-line tuned with speed to maintain the constant bandwidth which has been introduced in details in

Section 6.4. Then, employing the overall control scheme which is same as Fig. 6.16 and shown in Fig. 7.26 for convenience, but with on-line tuned EKF based estimator, the rotor position can be derived at 200rpm rotor speed with 1A q -axis current as shown in Fig. 7.27 but with too large error.

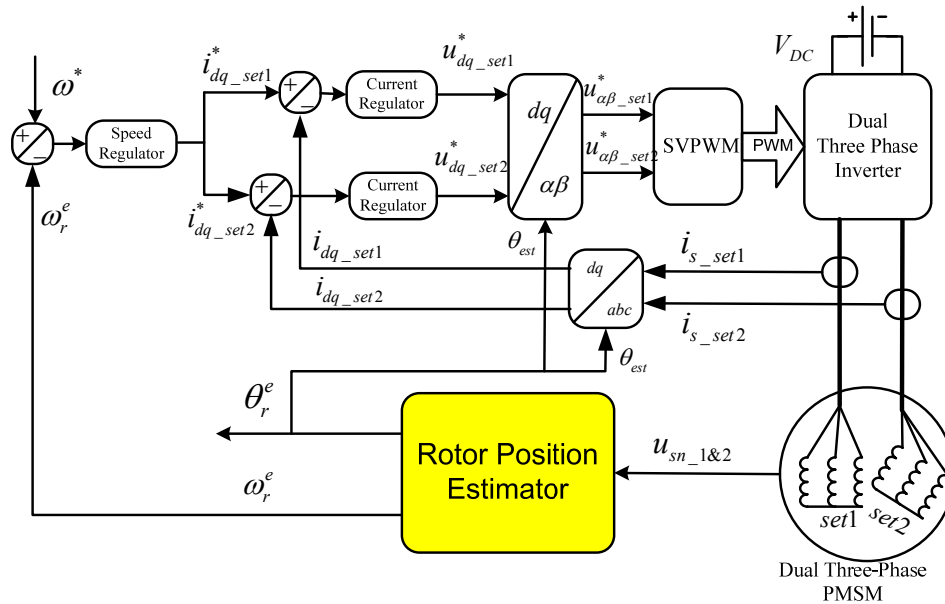


Fig. 7.26. Overall control scheme

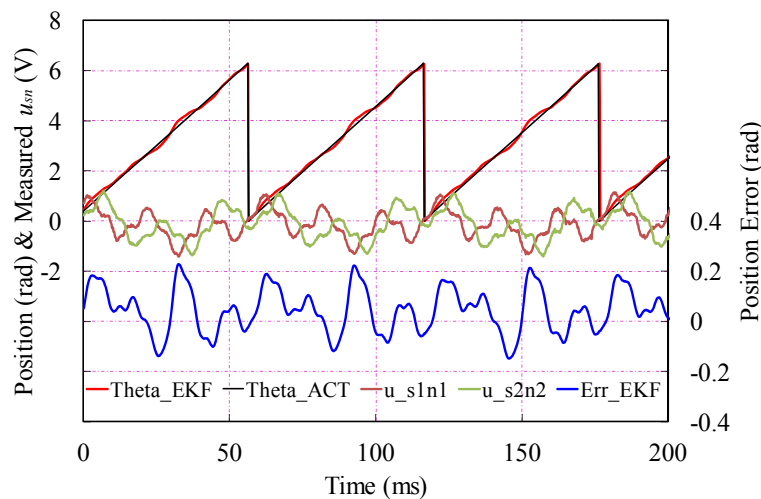


Fig. 7.27. Rotor position estimation under imbalanced situation (u_{s1n1} : Measured u_{sn} of winding set1, u_{s2n2} : Measured u_{sn} of winding set2, θ_{EKF} : Estimated rotor position, θ_{ACT} : Actual rotor position, Err_{EKF} : Position estimation error)

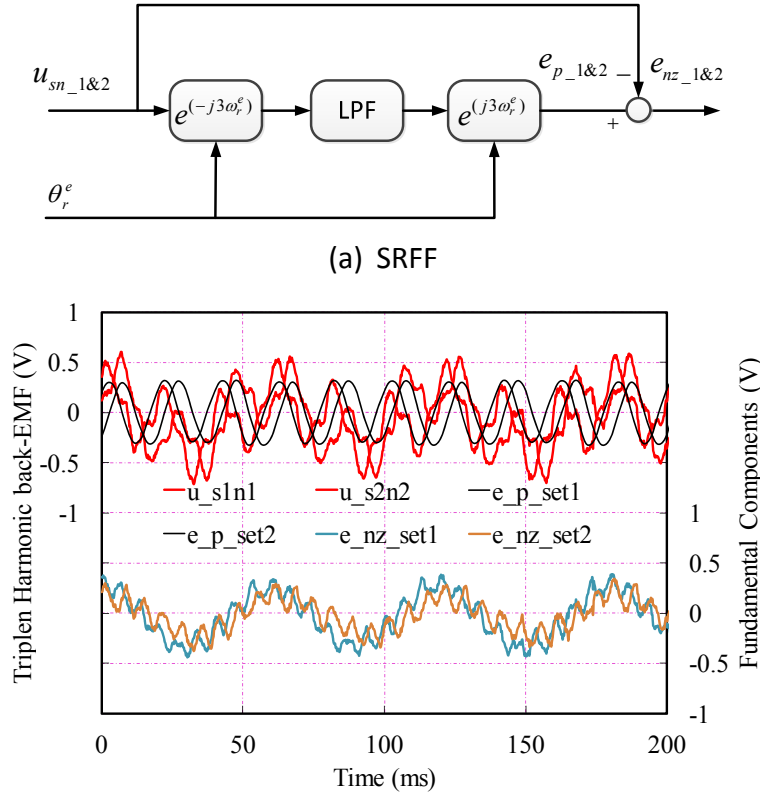
7.4.3.2 Rotor position estimation with imbalanced situation compensation

Since the two sets of third harmonic back-EMF in (7.23) are orthogonal to each

other and can form a third order circular trace, they could be equivalent as positive sequence voltages under third harmonic reference frame, whilst all the other components are negative and zero sequence components and all the contained noise signal, i.e.

$$u_{sn_1\&2} = e_{p_1\&2} + e_{nz_1\&2} = A_{mp}e^{j(3\omega_r t)} + e_{nz_1\&2} \quad (7.24)$$

In order to separate the positive sequence components from the original measured signals, with the aid of feedback estimated rotor position, applying SRFF as shown in Fig. 7.28(a), the positive sequence component, and the other components which contain the relevant fundamental could be derived as shown in Fig. 7.28(b).

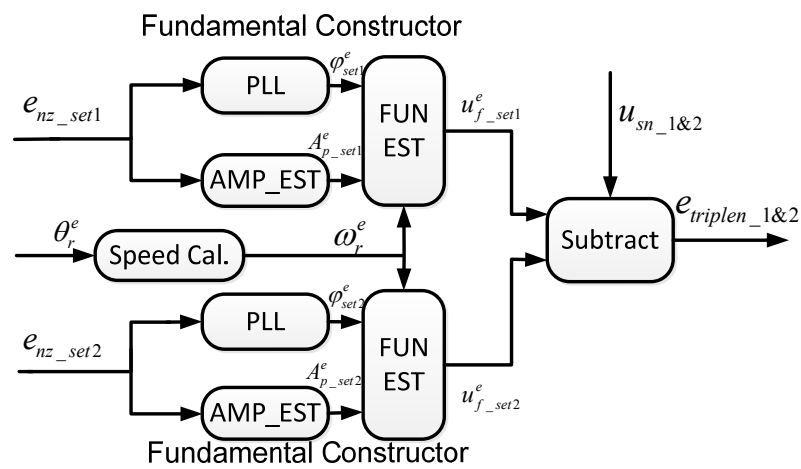


(b) Positive, negative and zero sequence components
 (u_{s1n1}/u_{s2n2} : Measured u_{sn} of winding set1 and set2, e_{p_set1}/e_{p_set2} : Positive sequence components of winding set1 and set2, e_{nz_set1}/e_{nz_set2} : All the other contained components of winding set1 and set2)

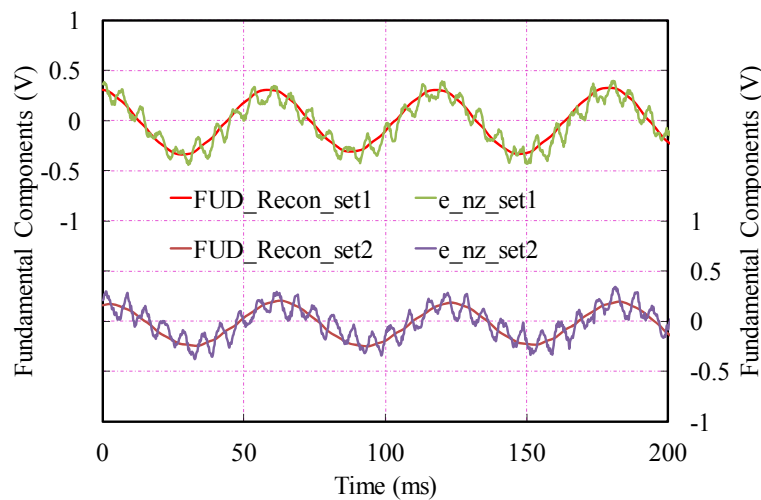
Fig. 7.28. SRFF to separate the fundamental components from the original signals

Then, the fundamental component compensator as shown in Fig. 7.29(a) is applied to derive the pure triplen harmonic signals. Treating the higher order components as noise, the initial phase angle φ could be obtained with the aid of PLL. Meanwhile, the

amplitude A_p also can be retrieved by the amplitude estimators. Thus, the fundamental components could be reconstructed through the estimated amplitude A_p^e and initial phase angle φ^e , and ω_r^e which is the feedback estimated rotor position. Hence, the reconstructed fundamental distortions of back-EMFs are shown in Fig. 7.29(b) compared with the derived negative and zero sequence components, and they can match well. Then subtracting the reconstructed fundamental distortions from $u_{sn_1\&2}$, the pure triplen harmonic back-EMFs could be derived as shown in Fig. 7.30, compared with the ones before compensation.



(a) Fundamental components compensator



(b) Reconstructed fundamental components compared with negative and zero sequence components (e_{nz_set1}/e_{nz_set2} : All the other contained components of winding set1 and set2, $FUD_Recon_set1/FUN_Recon_set2$: Reconstructed fundamental components of winding set1 and set2)

Fig. 7.29. Reconstruction of fundamental components

Then, applying the EKF based rotor position estimator, the rotor position could be estimated from the pure triplen harmonic back-EMF with high accuracy. The overall rotor position estimator is shown in Fig. 7.31(a), and the rotor position can be estimated with much higher accuracy and lower fluctuation as shown in Fig. 7.31(b).

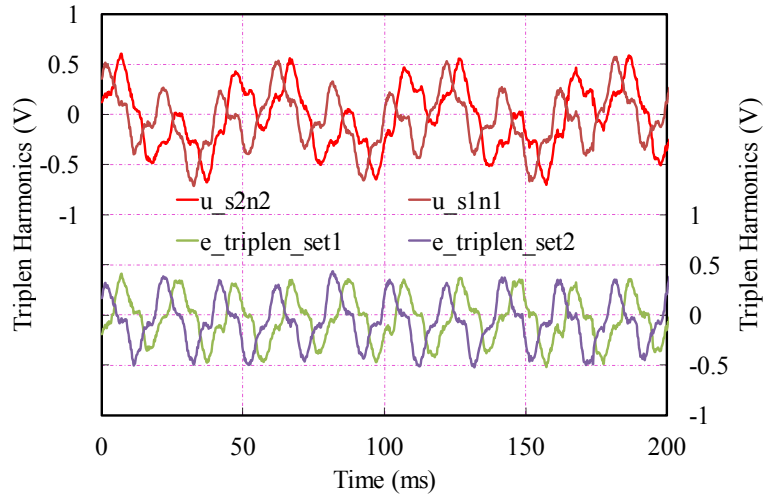
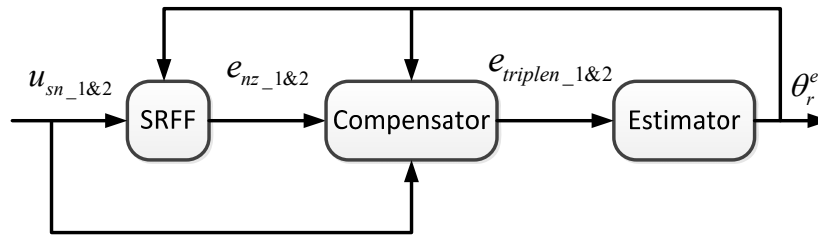
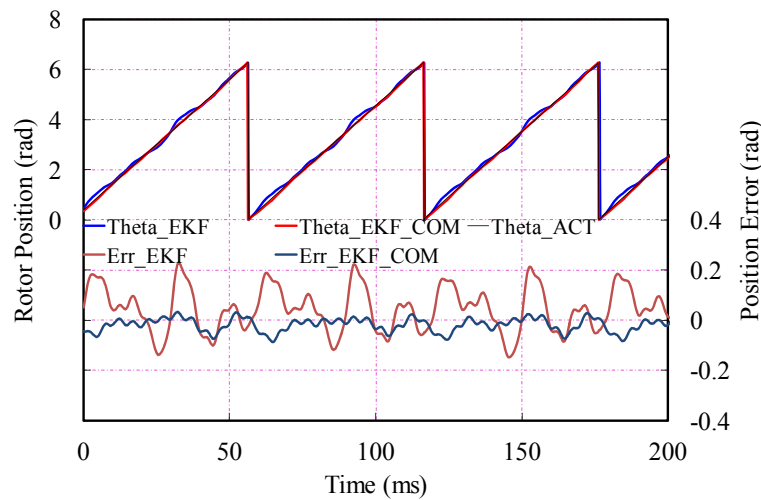


Fig. 7.30. Triplen harmonic back-EMF before and after fundamental compensation (u_{s1n1}/u_{s2n2} : Measured u_{sn} of winding set1 and set2, $e_{triplen_set1}/e_{triplen_set2}$: compensated triplen harmonic back-EMF of winding set1 and set2)

The dynamic test is carried out when the rotor speed reference change from 200rpm to 320rpm, Fig. 7.23. Then applying the rotor position estimation strategy under imbalanced situation, the experimental results for dual three-phase PMSM are shown in Fig. 7.32 compared with the values derived directly from the original signals. The experimental results demonstrate that proposed rotor position estimation strategy based on third harmonic back-EMF can significantly improve steady-state and dynamic performance of the rotor estimation under imbalanced situation with high robustness for dual three-phase PMSM under imbalanced situation.



(a) Rotor Position Estimator under Imbalanced Situation



(b) Rotor position before and after fundamental component compensation (*Theta_EKF*: Estimated rotor position, *Theta_ACT*: Actual rotor position, *Err_EKF*: Rotor position estimation error, *Theta_EKF_com*: Compensated estimated rotor position, *Err_EKF_com*: Compensated rotor position estimation error)

Fig. 7.31. Rotor position estimation under fundamental component compensation

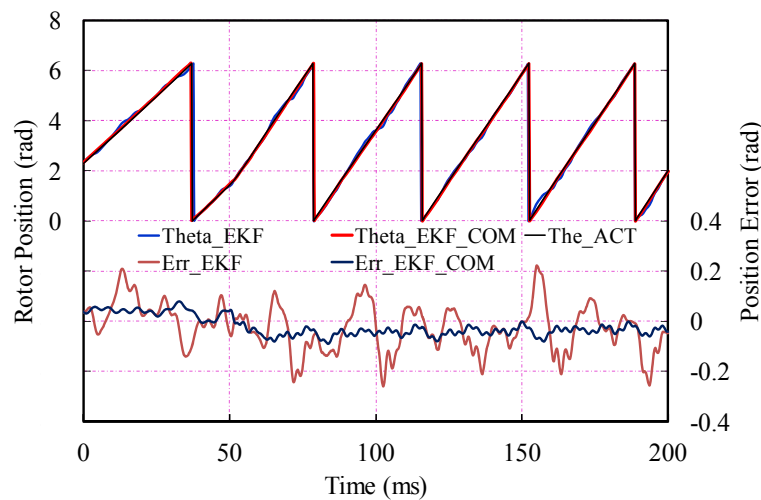


Fig. 7.32. Dynamic performance before and after fundamental components compensation (*Theta_EKF*: Estimated rotor position, *Theta_ACT*: Actual rotor position, *Err_EKF*: Position estimation error, *Theta_EKF_com*: Compensated estimated rotor position, *Err_EKF_com*: Compensated Position estimation error)

7.5 Conclusion

In this chapter, the potential absence of third harmonic back-EMF has been discussed. If the ratio of third harmonic back-EMF to the fundamental is smaller than 2%, the sensorless control strategies based on third harmonic back-EMF may not be able to be implemented due to its smaller amplitude and SNR. Meanwhile, since the third harmonic back-EMF is also proportional to rotor speed, all sensorless controls are usually employed above 5% of the rated speed but suffering at zero and low speed. Hence, sensorless control methods based on high frequency carrier signal injection as introduced in Chapter 3 and Chapter 4 are widely implemented due to the effectiveness in that region.

In salient machines, the winding inductance varies with the rotor position. Thus, u_{sn} will be affected by stator current. After experimental investigation and validation, it can be concluded that: the rotor speed and q -axis current will not affect the phase angle of the third harmonics; negative d -axis current will change the amplitude and phase angle of the triplen harmonics due to the machine saliency and variety of magnetic saturation, and the estimation error can be compensated based on pre-measured data; large positive d -axis current which will cause serious saturation of flux-linkage should be avoided when third harmonic back-EMF based sensorless control is employed no matter there is machine saliency or not.

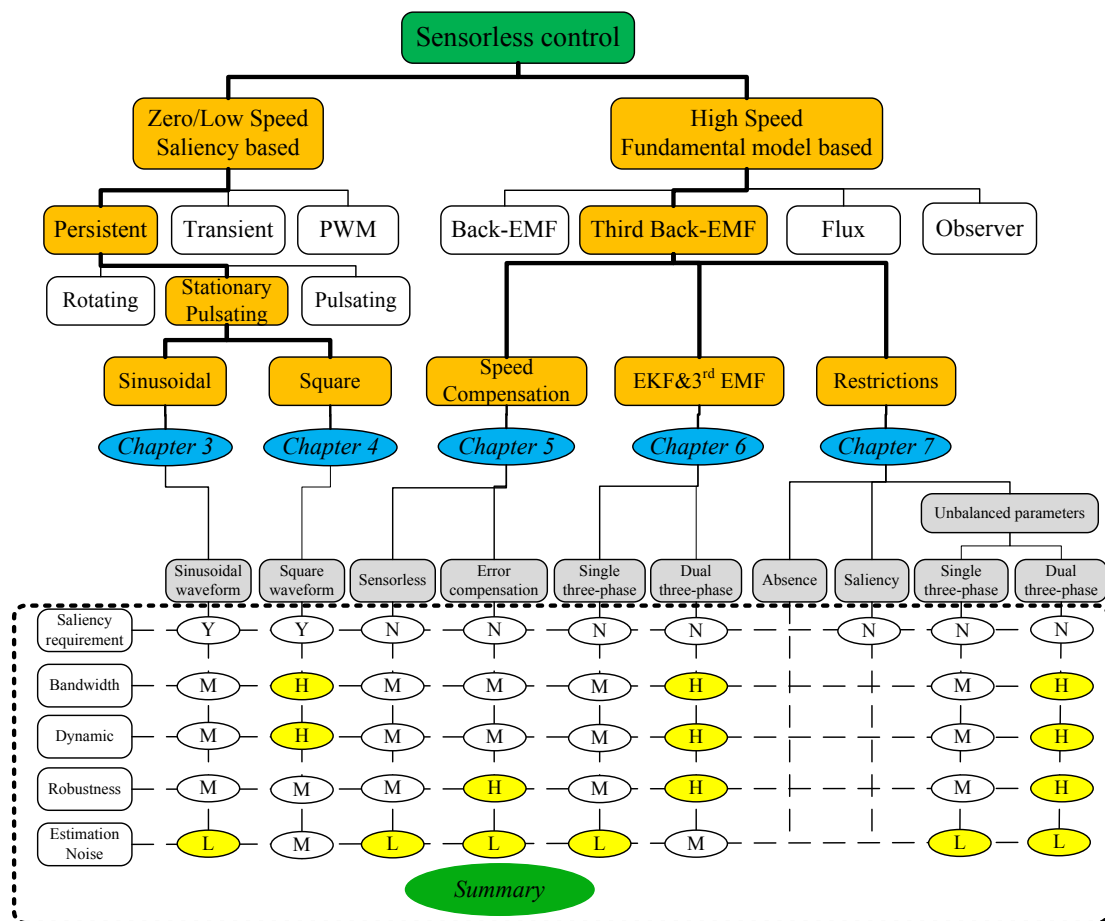
With imbalanced machine parameters, the fundamental back-EMF based sensorless control strategies may not be affected due to the small ratio between imbalanced effects to the fundamental back-EMF. However, for the sensorless control based on third harmonic back-EMF, the measured triplen harmonic back-EMF will contain certain fundamental components which will deteriorate the rotor position estimation. With the aid of fundamental component compensator, the fundamental component distortion in measured u_{sn} due to the imbalanced machine parameters and sensing resistor network can be compensated in advance to improve the performance. The experiments on dual three-phase PMSM with serious imbalanced situation under single and dual three-phase operation prove that the improved rotor position estimation

strategy can significantly compensate the contained fundamental components caused by imbalance situation. Therefore, the steady-state and dynamic performance of single and dual three-phase PMSM can be remarkably improved with high robustness.

CHAPTER 8

GENERAL CONCLUSION AND DISCUSSION

This thesis is focused on the sensorless control of PMSM based on high frequency carrier voltage injection for zero and low speed region and third harmonic back-EMF for higher speed region as illustrated in Fig. 8.1. A brief summary of the each sensorless control methods are shown at the bottom of Fig. 8.1 where the merits of them are highlighted as yellow.



Y=Yes; N=No; H=High; M=Medium; L=Low

Fig. 8.1. Research structure and key features of each investigated method

8.1 Sensorless Control

8.1.1 Sensorless Control Based on Machine Saliency

Machine saliency, resulting from machine geometric anisotropy and magnetic saturation, is essential for saliency based sensorless control techniques, which are well developed due to the effectiveness at zero and low speed region. A high frequency carrier voltage signal (pulsating or rotating conventionally) is persistently superimposed on the fundamental excitation, and then the position-dependant carrier current response, which results from the interaction between the injected carrier voltage signal and the machine saliency, can be used to extract rotor position information.

Based on the detailed discussion on commonly used conventional high frequency carrier signal injection based sensorless control techniques, a new strategy with injection of a pulsating sinusoidal waveform high frequency carrier voltage into α - (or β -) axis of stator stationary reference frame is presented, and then the rotor position information is retrieved from the carrier current response which is amplitude-modulated by rotor position. The new strategy has the advantages of

- (a) Stable performance of signal injection as conventional rotating carrier signal injection method.
- (b) Simple signal demodulation from amplitude-modulated carrier current response as conventional pulsating carrier signal injection method.

Considering the bandwidth of position observer and carrier signal demodulation, the higher the injected carrier voltage frequency, the better. However, it is upper limited by the PWM frequency. Normally, the carrier frequency of the injected sinusoidal voltage is chosen as $1/50 \sim 1/10$ PWM frequency. Regarding to amplitude of injected carrier voltage, it is a compromise between the utilization of DC bus voltage and SNR of the carrier current response. Hence, by employing high frequency square waveform pulsating carrier voltage into stator stationary reference frame, the bandwidth of the position estimation can be significantly improved due to the higher injected frequency

and removal of all filters in the demodulation process. Meanwhile, since the injected frequency is much higher even than the fundamental frequency at rated speed, the square waveform injection method is possible to be applied at wider range of speed and deduce the higher performance.

Since the machine primary saliency undergoes two cycles in single electrical period, the estimated position information from machine saliency behavior suffers from an angle ambiguity of π . Hence, magnetic polarity identification is required for initial rotor position estimation. Then, by the magnetic saturation effect of d -axis fundamental current, the change of the response current magnitude can be used to detect the magnetic polarity. The comparison of the three difference high frequency carrier signal injection strategies is shown in Table 8.1.

TABLE 8.1
COMPARISON OF CARRIER SIGNAL INJECTION STRATEGIES

	Pulsating	Rotating	Proposed
Signal injection			
Reference frame	Estimated synchronous	Stationary	Stationary
Carrier voltage injection	Pulsating carrier voltage	Rotating carrier voltage	Pulsating carrier voltage
Carrier current response	Amplitude-modulated	Phase-modulated	Amplitude-modulated
Stability of signal injection	Medium	Good	Good
Signal demodulation	Simple	Complex	Simple
Square waveform applicability	Applicable	Not applicable	Applicable
Magnetic polarity detection	Required	Required	Required

8.1.2 Sensorless Control Based on Third Harmonic Back-EMF

Since the back-EMF voltage is proportional to rotor speed, when the rotor speed is sufficiently high, the back-EMF component in the high frequency voltage equation cannot be ignored, and will affect the high frequency carrier voltage injection based sensorless control. Then, the back-EMF based sensorless control should be applied due to its good performance at higher speed region. Fundamental back-EMF based sensorless control methods are widely employed. Third harmonic back-EMF in the stator phase back-EMF due to the saturation effect and/or character of designed PM excited flux-linkage which contains third harmonic on purpose is also widely employed for sensorless control, due to its insensitivity to the machine and controller parameters. The comparison of them is shown in Table 8.2.

TABLE 8.2

COMPARISON OF BACK-EMF BASED SENSORLESS CONTROLS

	Fundamental back-EMF	Third harmonic back-EMF
Applicability	SPM/IPM(with extend back-EMF or active flux)	SPM/IPM
Neutral point access	Not required	Required
Sensitivity to parameters	High	Low
Sensitivity to imbalance	Low	Medium
Sensitivity to PWM	Medium	Low
Sensitivity to high order harmonic back-EMF	Low	Medium
Flux weakening	No limit	No limit for SPM/Available for IPM
SNR	High	Medium

The conventional strategy based on third harmonic back-EMF suffers at dynamic situation due to inaccurate average rotor speed calculated from the insufficient precise rotor position reference. To minimize the rotor position error and improve the dynamic performance, a speed error compensation strategy based on the continuous signal of third harmonic flux-linkage is proposed. With the same speed error compensation concept, the performance of flux observer based sensorless control which is sensitive to the machine and controller parameters can be significantly improved. Meanwhile, the robustness can also be enhanced due to the mutually complementary.

For the speed error compensation based sensorless control, the source signal quality is of great importance. With poor quality signals, the speed calculation may fail. Hence, based on EKF, the two essential orthogonal signals which are third harmonic back-EMF and flux-linkage can be directly applied with the simplified EKF based rotor position estimator to derive the rotor position even though there may contain too much high order harmonic components. For dual three-phase PMSM, the two sets of third harmonic back-EMFs are orthogonal under third harmonic reference frame, and can be applied with the same simplified EKF based rotor position estimator to derive the rotor position without any filtering, which can significantly enhance the observe bandwidth and dynamic performance.

Third harmonic back-EMF based sensorless control also have some restrictions as summarized below:

- (a) An adequate third harmonic component must exist in the airgap field, whilst the third harmonic winding factor should not be too low.
- (b) The winding neutral point should be accessible.
- (c) The winding inductance should be constant.
- (d) The three-phase parameters and sensing resistor network should be well balanced.

Without sufficient third harmonic back-EMF nor access of winding neutral, third harmonic back-EMF based sensorless control cannot be employed, and hence, alternative sensorless control should be employed.

In salient machines, the winding inductances vary with the rotor position. Thus,

the measured third harmonic back-EMF will be affected by stator current, and the shifted phase angle is not easy to be predicted due to the nonlinearity of the d -axis current introduced saturation effect. Hence, the estimation error should be compensated based on pre-measured data.

With imbalanced machine impedance, fundamental back-EMF or sensing resistor network, the measured triplen harmonic back-EMF will contain certain fundamental components which will deteriorate the rotor position estimation. With the aid of fundamental components compensator, the fundamental components distortion in measured triplen harmonic back-EMF due to the imbalanced machine parameters and sensing resistor network can be compensated in advance. Then, the steady-state and dynamic performance of single and dual three-phase PMSM can be remarkably improved with high robustness.

Each rotor position estimation algorithm can be equivalently seen as a linear model. With different types of regulator, the equivalent linear model has different order and frequency response. Usually, an equivalent second order linear model with a damping factor ξ of 0.707 is preferred since it has very good dynamic performance without overshooting. However, at different operating condition, the optimum parameters are also different, which makes the optimization process with significant difficulty. Meanwhile, the risk of unstable situation of the whole control system with unsuitable parameters of any regulator is also obvious. Hence, the parameter tuning is of great importance, and should be treated very carefully.

8.2 Future Work: Hybrid Sensorless Control with Proper Designed Motor

Due to extra losses, additional current harmonics, torque ripples and acoustic noise resulting from carrier voltage injection, carrier signal injection based sensorless methods are only accepted for standstill and low speed operation, where fundamental model based sensorless methods fail to effectively estimate the rotor position information.

Back-EMF based sensorless control shows good performance at high speed region but suffers at zero and low speed. However, fundamental back-EMF based strategies including back-EMF based, flux-linkage based and the other entire observer based, nearly all sensitive to the machine parameters. For salient PMSM, further machine model has to be developed. Even the third harmonic back-EMF is also suffering with machine saliency and imbalanced machine and measurement parameters.

As a result, it is desirable to combine different types of sensorless control together to compensate their drawbacks. However, from the analysis in this thesis, it can be found that some essential requirement for certain sensorless may be harmful to the others. Considering the requirement of sensorless control and compromising each conflict in the machine design, it is expected that high performance sensorless position estimation based on the fusion of different strategies could be achieved without complex compensation.

REFERENCES

- [ABA08] G. Abad, M. A. Rodriguez, and J. Poza, "Two-level VSC based predictive direct torque control of the doubly fed induction machine with reduced torque and flux ripples at low constant switching frequency," *IEEE Trans. Power Electron.*, vol. 23, no. 3, pp. 1050-1061, 2008
- [ABB84] M.A. Abbas, R. Christen, and T.M Jahns. "Six-phase voltage source inverter driven induction motor," *IEEE Trans. Ind. Appl.*, vol. 20, no.5, pp. 1251-1259. 1984
- [AIH99] T. Aihara, A. Toba, T. Yanase, A. Mashimo, and K. Endo, "Sensorless torque control of salient-pole synchronous motor at zero-speed operation," *IEEE Trans. Power Electron.*, vol. 14, no. 1, pp.202-208, 1999.
- [ALB12] L. Alberti, and N. Bianchi, "Experimental tests of dual three-phase induction motor under faulty operating condition," *IEEE Trans. Ind. Electron.*, vol. 59, no. 5 pp. 2041 – 2048, 2012
- [AND08] G. D. Andreescu, C. I. Pitic, F. Blaabjerg, and I. Boldea, "Combined flux observer with signal injection enhancement for wide speed range sensorless direct torque control of IPMSM drives," *IEEE Trans. Energy Conversion*, vol. 23, no. 2, pp. 393-402, 2008.
- [APS06] J.M. Apsley, and S. Williamson, "Analysis of multi-phase induction machines with winding faults" *IEEE International Conf. On Electric Machines and Drives*, 2005, pp. 249 – 255
- [BAE03] B.H. Bae, S.K. Sul, J.H. Kwon, and J.S. Byeon, "Implementation of sensorless vector control for super high speed PMSM of turbo compressor," *IEEE Trans. Ind. Appl.*, vol. 39, no. 3, pp. 811-818, 2003
- [BAR09] F. Barrero, M.R. Arahall, R. Gregor, S. Toral, and M.J. Duran, "A proof of concept study of predictive current control for VSI-driven asymmetrical dual three-phase AC machines," *IEEE Trans. Ind. Electron.*, vol. L, no. 6, pp. 1937 – 1954, 2009
- [BAR10a] M. Barcaro, N. Bianchi, and F. Magnussen, "Faulty operations of a PM fractional-slot machine with a dual three-phase winding," *IEEE Trans. Ind. Appl.*, vol. 58, no. 9, pp. 3825-3832, 2011

- [BAR10b] M. Barcaro, N. Bianchi, and F. Magnussen, "Analysis and tests of a dual three-phase 12-slot 10-pole permanent-magnet motor," *IEEE Trans. Ind. Appl.*, vol. 46, no. 6, pp. 2355-2362, 2010.
- [BAR11a] M. Barcaro, N. Bianchi, and F. Magnussen, "Six-phase supply feasibility using a PM fractional-slot dual winding machine," *IEEE Trans. Ind. Appl.*, vol. 47, no. 5, pp. 2042-2050, 2011
- [BAR11b] M. Barcaro, N. Bianchi, and F. Magnussen, "Faulty operations of a PM fractional-slot machine with a dual three-phase winding," *IEEE Trans. Ind. Electron.*, vol. 58, no. 9, pp. 3825 – 3832, 2011
- [BAR12a] M. Barcaro, A. Faggion, N. Bianchi, and S. Bolognani, "Predicted and experimental anisotropy of a dual three-phase interior permanent magnet motor for sensorless rotor position control," *6th IET International Conference on Power Electronics, Machines and Drives, PEMD*, 2012, 2012, pp. 1 – 6
- [BAR12b] M. Barcaro, A. Faggion, N. Bianchi, and S. Bolognani, "Sensorless rotor position detection capability of a dual three-phase fractional-slot IPM machine," *IEEE Trans. Ind. Appl.*, vol.48, no.6, pp. 2068 – 2078, 2012
- [BIA07] N. Bianchi, and S. Bolognani, "Influence of rotor geometry of an interior PM motor on sensorless control feasibility," *Industry Applications Conference*, 2005, vol. 4, pp. 2553 – 2560
- [BOG06] A. Boglietti, R. Bojoi, A. Cavagnino, and A. Tenconi, "Efficiency analysis of PWM inverter fed three-phase and dual three-phase induction machines," *IEEE Industry Applications Conference 2006*. Vol. 1, 2006, pp. 434-440
- [BOJ03] R. Bojoi, M. Lazzari, F. Profumo, and A. Tenconi, "Digital field-oriented control for dual three-phase induction motor drives," *IEEE Trans. Ind. Appl.*, vol. 39, no.3, pp. 752-760, 2003
- [BOJ05] R. Bojoi, F. Farina, G. Griva, F. Profumo, and A. Tenconi, "Direct torque control for dual three-phase induction motor drives," Digital field-oriented control for dual three-phase induction motor drives," *IEEE Trans. Ind. Appl.*, vol. 41, no.6, pp. 1627-1636, 2005
- [BOJ06] R. Bojoi, E. Levi, F. Farina, A. Tenconi, and F. Profumo, "Dual three-phase induction motor drive with digital current control in the

- stationary reference frame,” *IET Electric Power Appl.*, vol. 153, no. 1, pp. 129 – 139, 2006
- [BOL09] I. Boldea, M. C. Paicu, G. D. Andreescu, and F. Blaabjerg, “Active flux DTFC-SVM sensorless control of IPMSM,” *IEEE Trans. Energy Conversion*, vol. 24, no. 2, pp. 314-322, 2009.
- [BOL11] S. Bolognani, S. Calligaro, R. Petrella, and M. Sterpellone, “Sensorless control for IPMSM using PWM excitation: Analytical developments and implementation issues,” *Symposium on Sensorless Control for Electrical Drives*, 2011, pp. 64-73.
- [BOL99] S. Bolognani, R. Oboe, and M. Zigliotto, “Sensorless full-digital PMSM drive with EKF estimation of speed and rotor position,” *IEEE Trans. Ind. Electron.*, vol. 46, no. 1, pp. 184-191, 1999.
- [BOU05] M. Boussak, “Implementation and experimental investigation of sensorless speed control with initial rotor position estimation for interior permanent magnet synchronous motor drive,” *IEEE Trans. Power Electron.*, vol. 20, no. 6, pp.1413–1422, 2005.
- [CHE00a] Z. Chen, M. Tomita, S. Doki, and S. Okuma, “New adaptive sliding observers for position- and velocity-sensorless controls of brushless DC motors,” *IEEE Trans. Ind. Appl.*, vol. 47, no. 3, pp. 582 – 591, 2000
- [CHE00b] Z. Chen, M. Tomita, S. Ichikawa, S. Doki, and S. Okuma, “Sensorless control of interior permanent magnet synchronous motor by estimation of an extended electromotive force,” *Industry Applications Conference*, 2000, vol.3, pp. 1814-1819.
- [CHE03] Z. Chen, M. Tomita, S. Doki, and S. Okuma, “An extended electromotive force model for sensorless control of interior permanent-magnet synchronous motors,” *IEEE Trans. Ind. Electron.*, vol. 50, no. 2, pp. 288-295, 2003.
- [CHE99] Y.S. Chen, “Motor Topologies and Control Strategies for Permanent Magnet Brushless AC Drives,” PhD Thesis, Research Group of Electric Machines and Drives, Department of Electronic and Electrical Engineering, University of Sheffield, 1999.
- [CHI09] S. Chi, Z. Zhang, and L. Xu, “Sliding-mode sensorless control of direct drive PM synchronous motors for washing machine

- applications,” *IEEE Trans. Ind. Appl.*, vol. 45, no. 2, pp. 582 – 590, 2009.
- [CHO07] C.H. Choi, and J.K. Seok, “Compensation of zero-current clamping effects in high-frequency-signal-injection-based sensorless PM motor drives,” *IEEE Trans. Ind. Appl.*, vol. 43, no. 5, pp. 1258 – 1265, 2007
- [COR11] V. Coroban-Schramel, I. Boldea, G.D. Andreescu, and F. Blaabjerg, “Active-flux-based motion-sensorless vector control of biaxial excitation generator/motor for automobiles,” *IEEE Trans. Ind. Appl.*, vol. 47, no. 2, pp. 812 – 819, 2011
- [COR98] M. J. Corley, and R. D. Lorenz, “Rotor position and velocity estimation for a salient-pole permanent magnet synchronous machine at standstill and high speed,” *IEEE Trans. Ind. Appl.*, vol.34, no. 4, pp.784–789, 1998.
- [CUP10] F. Cupertino, P. Giangrande, L. Salvatore, and G. Pellegrino, “Model based design of a sensorless control scheme for permanent magnet motors using signal injection,” *IEEE Energy Conversion Congress and Exposition (ECCE)*, 2010, pp. 3139-3146.
- [DEG98] M.W. Degner, and R.D Lorenz, “Using multiple saliencies for the estimation of flux, position, and velocity in AC machines,” *IEEE Trans. Ind. Appl.*, vol. 34, no. 5, pp. 1097–1104, 1998
- [DEK09] H.W. De Kock, M.J. Kamper, and R.M. Kennel, “Anisotropy comparison of reluctance and PM synchronous machines for position sensorless control using HF carrier injection,” *IEEE Trans. Power Electron.*, vol. 24, no. 8, pp. 1905-1913, 2009.
- [DEP88] M. Depenbrock, “Direct self-control (DSC) of inverter-fed induction machine,” *IEEE Trans. Power Electron.*, vol. 3, no. 4, pp. 420-429, 1988.
- [DSP10] dSPACE, “Hardware installation and configuration reference,” Release 6.6, May 2010
- [DWA08] S. Dwari, and L. Parsa, “Open-circuit fault tolerant control of five-phase permanent magnet motors with third-harmonic back-EMF,” *Industrial Electronics, IECON 2008. 34th Annual Conference of IEEE*, 2008, pp. 3114 - 3119.
- [EMU00] T. Emura, L. Wang, M. Yamanaka, and H. Nakamura, “A high

- precision positioning servo controller based on phase/frequency detecting technique of two-phase-type PLL,” *IEEE Trans. Ind. Appl.*, vol.47, no. 6, pp.1298-1306, Dec. 2000.
- [FAE09] M. Faeq, and D. Ishak, “A new scheme sensorless control of BLDC motor using software PLL and third harmonic back-EMF,” *IEEE Industrial Electronics & Applications ISIEA*, vol. 2, 2009, pp. 861 - 865.
- [FAR06] F. Farina, R. Bojoi, A. Tenconi, and F. Profumo, “Direct torque control with full order stator flux observer for dual-three phase induction motor drives,” *IEEJ Trans. Ind. Appl.*, vol.126, no. 4, pp. 412–419, 2006,
- [FOO09a] G. Foo, and M. F. Rahman, “Direct torque and flux control of an IPM synchronous motor drive using a back stepping approach”, *IET Electric. Power Appl.*, vol. 3, no. 5, pp. 413-421, 2009
- [FOO09b] G. Foo, and M.F. Rahman, “Sensorless adaptive sliding mode control of an IPM synchronous motor drive using a sliding mode observer and HF signal injection,” *Power Electronics and Applications, EPE'09. 2009* , pp. 1 - 11
- [FOO10] G. Foo, and M.F. Rahman, “Sensorless sliding-mode MTPA control of an IPM synchronous motor drive using a sliding-mode observer and HF signal injection,” *IEEE Trans. Ind. Electron.*, vol. 57, no. 4, pp. 1270 – 1278, 2010
- [FUE11] E. Fuentes, and R. Kennel, “Sensorless-predictive torque control of the PMSM using a reduced order extended Kalman filter,” *Symposium on Sensorless Control for Electrical Drives*, 2011, pp. 123-128.
- [FUR92] T. Furuhashi, S. Sangwongwanich, and S. Okuma, “A position and velocity sensorless control for brushless DC motors using an adaptive sliding mode observer,” *IEEE Trans. Ind. Electron.*, vol. 39, no. 2, pp. 89 – 95, 1992
- [GAD10] S. M. Gadoue, D. Giaouris, and J. W. Finch, “MRAS sensorless vector control of an induction motor using new sliding-mode and fuzzy-logic adaptation mechanisms,” *IEEE Trans. Energy Conversion*, vol. 25, no. 2, pp. 394-402, 2010.
- [GAO07] Q. Gao, G. M. Asher, M. Sumner, and P. Makys, “Position estimation

- of AC machines over a wide frequency range based on space vector PWM excitation,” *IEEE Trans. Ind. Appl.*, vol. 43, no. 4, pp. 1001-1011, 2007.
- [GAR07] P. Garcia, F. Briz, M.W. Degner, and D. Diaz-Reigosa, “Accuracy, bandwidth, and stability limits of carrier-signal-injection-based sensorless control methods,” *IEEE Trans. Ind. Appl.*, vol. 43, no. 4, pp. 990 – 1000, 2007.
- [GON11a] L.M. Gong, and Z.Q. Zhu, “A novel method for compensating inverter nonlinearity effects in carrier signal injection-based sensorless control from positive-sequence carrier current distortion,” *IEEE Trans. Ind. Appl.*, vol. 47, no. 3, pp. 1283 – 1292, 2011
- [GON11b] L.M. Gong, and Z.Q. Zhu, “Improved rotating carrier signal injection method for sensorless control of PM brushless AC motors, accounting for cross-saturation effect,” *Power Electronics and ECCE Asia (ICPE & ECCE)*, 2011, pp. 1132 - 1139
- [GON12] L. Gong, “Carrier signal injection based sensorless control of permanent magnet brushless ac machines”, PhD Thesis, Research Group of Electric Machines and Drives, Department of Electronic and Electrical Engineering, University of Sheffield, 2012.
- [GON13] L. Gong, and Z.Q. Zhu, “Robust initial rotor position estimation of permanent magnet brushless AC machines with carrier signal injection-based sensorless control” *IEEE Trans. Ind. Appl.*, vol. PP, no. 99, pp. 1-9, 2013. In press
- [GOP93] K. Gopakumar, V.T. Ranganthan, and S.R. Bhat, “Split-phase induction motor operation from PWM voltage source inverter,” *IEEE Trans. Ind. Appl.*, vol. 29, no. 5, pp. 927 – 932, 1993
- [GRE10] R. Gregor, F. Barrero, S.L. Toral, M.J. Duran, M.R. Arahal, J. Prieto, and J.L. Mora, “Predictive-space vector PWM current control method for asymmetrical dual three-phase induction motor drives,” *IET Electric. Power Appl.*, vol. 4, no. 1, pp. 26 – 34, 2010
- [GRE12] R. Gregor, and J. Rodas, “Speed sensorless control of dual three-phase induction machine based on a luenberger observer for rotor current estimation,” *Annual Conference on IEEE Industrial Electronics Society IECON*, 2012, pp. 3653 – 3658

References

- [GUE05] J.M. Guerrero, M. Leetmaa, F. Briz, A. Zamarron, and R.D. Lorenz, "Inverter nonlinearity effects in high-frequency signal-injection-based sensorless control methods," *IEEE Trans. Ind. Appl.*, vol. 41, no. 2, pp. 618 – 626, 2005
- [GUG06] P. Guglielmi, M. Pastorelli, and A. Vagati, "Cross-saturation effects in IPM motors and related impact on sensorless control," *IEEE Trans. Ind. Appl.*, vol. 42, no. 6, pp. 1516 – 1522, 2006
- [GUY78] W. C. Guyker, W.H. Booth, M.A. Jansen, S.S. Venkata, E.K. Stanek, and N.B. Bhatt, "138-kV six-phase transmission system feasibility," *Proc. Am. Power Conf.* 1978, vol. 40, pp. 1293-1305
- [HA00] J.I. Ha, and S.K. Sul, "Physical understanding of high frequency injection method to sensorless drives of an induction machine," *Ind. Appl. Conf., IEEE*, vol. 3, pp. 1802 – 1808, 2000
- [HA03] J.I. Ha, K. Ide, T. Sawa, and S.K. Sul, "Sensorless rotor position estimation of an interior permanent-magnet motor from initial states," *IEEE Trans. Ind. Appl.*, vol. 39, no. 3, pp. 761–767, 2003.
- [HAD06] D. Hadiouche, L. Baghli, and A. Rezzoug, "Space-vector PWM techniques for dual three-phase AC machine: analysis, performance evaluation, and DSP implementation," *IEEE Trans. Ind. Appl.*, vol. 42, no. 4, pp. 1112 - 1122, 2006
- [HAM10] W. Hammel, and R. M. Kennel, "Position sensorless control of PMSM by synchronous injection and demodulation of alternating carrier voltage," *Symposium on Sensorless Control for Electrical Drives*, 2010, pp. 56-63
- [HAQ03] M.E. Haque, L. Zhong, and M.F. Rahman, "A sensorless initial rotor position estimation scheme for a direct torque controlled interior permanent magnet synchronous motor drive," *IEEE Trans. Power Electron.*, vol. 18, no. 6, pp.1376–1383, 2003.
- [HAR00] L. Harnefors, and H.P. Nee, "A general algorithm for speed and position estimation of AC motors," *IEEE Trans. Ind. Electron.*, vol. 47, no. 1, pp. 77-83, 2000.
- [HAR05] M.C. Harke, D. Raca, and R.D. Lorenz, "Implementation issues for fast initial position and magnet polarity identification of PM synchronous machines with near zero saliency," *Conference on Power*

- Electronics and Applications*, 2005, pp. 1–10
- [HAT05] K. Hatua, V.T. Ranganathan, “Direct torque control schemes for split-phase induction machine,” *IEEE Trans. Ind. Appl.*, vol. 41, no. 5, pp. 1243 – 1254, 2005
- [HE09] Y. He, W. Hu, Y. Wang, J. Wu, and Z. Wang, “Speed and position sensorless control for dual-three-phase PMSM drives,” *Applied Power Electronics Conference and Exposition, APEC 2009, 25th Annual IEEE*, 2009, pp. 945 - 950
- [HE10] Y. He, Y. Wang, J. Wu, Y. Feng, and J. Liu, “A comparative study of space vector PWM strategy for dual three-phase permanent-magnet synchronous motor drives,” *IEEE Applied Power Electronics Conference and Exposition (APEC)*, 2010 , pp. 915 - 919
- [HEN94] J.R. Hendershot, and T.J.E. Miller, “Design of Brushless Permanent-Magnet Motors,” Magna Physics Publishing and Clarendon Press, Oxford, 1994.
- [HOA12] K.D. Hoang, Z.Q. Zhu, and M. Foster, “Optimum look-up table for reduction of current harmonics in direct torque controlled dual three-phase permanent magnet brushless AC machine drives,” *Power Electronics, Machines and Drives (PEMD 2012)*, 2012, PP. 1 - 6
- [HOL05] J. Holtz, and J. Juliet, “Sensorless acquisition of the rotor position angle of induction motors with arbitrary stator windings,” *IEEE Trans. Ind. Appl.*, vol. 41, no. 6, pp. 1675-1682, 2005.
- [HOL08] J. Holtz, “Acquisition of position error and magnet polarity for sensorless control of PM synchronous machines,” *IEEE Trans. Ind. Appl.*, vol. 44, no. 4, pp. 1172–1180, 2008.
- [HOL98] J. Holtz, “Sensorless position control of induction motors – an emerging technology,” *IEEE Trans. Ind. Electron.*, vol. 45, No. 6, pp. 840–852, 1998
- [HOS09] T. Hoshino, and J.I. Itoh, “Output voltage correction of an induction motor drive using a disturbance observer with speed sensor-less vector control method,” *IEEE Power Electronics and Motion Control Conference, IPEMC '09*, 2009, pp. 607 - 612
- [HOS89] G.H. Hostetter, C.J. Savant Jr., and R.T.Stefani, “Design of feedback control systems-2st edition,” Saunders College Publishing, 1989.

- [HU98] J. Hu, and B. Wu, "New integration algorithms for estimating motor flux over a wide speed range," *IEEE Trans. Power Electron.*, vol. 13, no. 5, pp. 969 – 977, 1998
- [HUA11] Y. Hua, M. Sumner, G. Asher, Q. Gao, and K. Saleh, "Improved sensorless control of a permanent magnet machine using fundamental pulse width modulation excitation," *IET Electric Power Appl.*, vol. 5, no. 4, pp. 359-370, 2011.
- [JAH80] T.M. Jahns, "Improved reliability in solid-state AC drives by means of multiple independent phase drive units," *IEEE Trans. Ind. Appl.*, vol. 16, no. 3, pp. 321-331, 1980
- [JAN03] J.H. Jang, S.K. Sul, J.I. Ha, K. Ide, and M. Sawamura, "Sensorless drive of surface-mounted permanent-magnet motor by high-frequency signal injection based on magnetic saliency," *IEEE Trans. Ind. Appl.*, vol. 39, no. 4, pp. 1031 – 1039, 2003.
- [JAN04] J.H. Jang, J.I. Ha, M. Ohto, K. Ide, and S.K. Sul, "Analysis of permanent-magnet machine for sensorless control based on high-frequency signal injection," *IEEE Trans. Ind. Appl.*, vol. 40, pp. 1595-1604, 2004.
- [JAN95] P.L. Jansen, and R.D. Lorenz, "Transducerless position and velocity estimation in induction and salient AC machines," *IEEE Trans., Ind. Appl.*, vol. 31, no. 2, pp. 240 – 247, 1995.
- [JOE05] Y.S. Jeong, R.D. Lorenz, T.M. Jahns, and S.K. Sul, "Initial rotor position estimation of an interior permanent-magnet synchronous machine using carrier-frequency injection methods," *IEEE Trans. Ind. Appl.*, vol. 41, no. 1, pp. 38–45, 2005.
- [KAN10] J. Kang, "Sensorless control of permanent magnet motors," *Control Engineering*, vol. 57, no. 4, pp. 1-4, 2010.
- [KAR12] J. Karttunen, S. Kallio, P. Peltoniemi, P. Silventoinen, and O. Pyrhonen, "Dual three-phase permanent magnet synchronous machine supplied by two independent voltage source inverters," in *Proc. 2012 International Symposium on Power Electronics, Electrical Drives, Automation and Motion (SPEEDAM)*, 2012, pp. 741-747.
- [KIM04] H. Kim, K.K. Huh, and R.D. Lorenz, "A novel method for initial rotor position estimation for IPM synchronous machine drives," *IEEE*

- Trans. Ind. Appl.*, vol. 40, no. 5, pp. 1369–1378, 2004.
- [KIM95] J.S. Kim, and S.K. Sul, “High performance PMSM drives without rotational position sensors using reduced order observer,” *IEEE Industry Applications Conference, 1995*. vol. 1, 1995, pp. 75 - 82
- [KRE93] L. Kreindler, A. Testa, and T.A. Lipo, “Position sensorless synchronous reluctance motor drive using the stator phase voltage third harmonic,” *Conference Record of IEEE Industry Applications Society Annual Meeting, 1993*, vol. 1, pp. 679 – 686.
- [KRE94] L. Kreindler, J.C. Moreira, A. Testa, and T. A. Lipo, “Direct field orientation controller using the stator phase voltage third harmonic,” *IEEE Trans. Ind. Appl.*, vol. 30, no. 2, pp. 441-447, 1994.
- [KWO05] T.S. Kwon, M.H. Shin, and D.S. Hyun, “Speed sensorless stator flux oriented control of induction motor in the field weakening region using Luenberger observer,” *IEEE Trans. Power Electro.*, vol. 20, no. 4, pp. 864 – 869, 2005
- [LAN10] P. Landsmann, D. Paulus, P. Stolze, and R. Kennel, “Saliency based encoderless predictive torque control without signal injection,” in *Power Electronics Conference (IPEC) 2010*, pp. 3029-3034.
- [LEE11] K. Lee, I. Choy, J. Back, and J. Choi, “Disturbance observer based sensorless speed controller for PMSM with improved robustness against load torque variation,” *IEEE Power Electronics and ECCE Asia (ICPE & ECCE)*, 2011, pp. 2537 - 2543
- [LEI11] R. Leidhold, “Position sensorless control of PM synchronous motors based on zero-sequence carrier injection,” *IEEE Trans. Ind. Electron.*, vol. 58, no. 12, pp. 5371-5379, 2011.
- [LI07] Y. Li, Z.Q. Zhu, D. Howe, and C. M. Bingham, “Modelling of cross-coupling magnetic saturation in signal injection based sensorless control of permanent magnet brushless AC motors,” *IEEE Transactions on Magnetics*, vol.43, no.6, June 2007, pp.2552-2554
- [LI09a] Y. Li, “Sensorless control of permanent magnet brushless AC motors accounting for cross-coupling magnetic saturation”, PhD Thesis, Research Group of Electric Machines and Drives, Department of Electronic and Electrical Engineering, University of Sheffield, 2009.
- [LI09b] Y. Li, Z.Q. Zhu, D. Howe, C.M. Bingham, and D. Stone, “Improved

- rotor position estimation by signal injection in brushless AC motors, accounting for cross-coupling magnetic saturation,” *IEEE Trans. Ind. Appl.*, vol.45, no.5, pp.1843-1849, 2009.
- [LIN02] M. Linke, R. Kennel, and J. Holtz, “Sensorless position control of permanent magnet synchronous machines without limitation at zero speed,” *Industrial Electronics Society 28th Annual Conference (IECON 02)*, vol.1, 2002, pp. 674-679.
- [LIN03] M. Linke, R. Kennel, and J. Holtz, “Sensorless speed and position control of synchronous machines using alternating carrier injection,” *Electric Machines and Drives Conference*, vol.2, pp. 1211-1217, 2003.
- [LIP80] T.A. Lipo, “A d-q model for six phase induction machines,” *Proc. Int. Conf. on Electrical Machines ICEM*, 1980, pp. 860–867
- [LIU04] Y. Liu, Z.Q. Zhu, Y.F. Shi, and D. Howe, “Sensorless direct torque control of a permanent magnet brushless AC drive via an extended Kalman filter,” *Power Electronics, Machines and Drives, (PEMD 2004)*, 2004, vol. 1, pp. 303 - 307
- [LIU11a] J. Liu, T.A. Nondahl, P.B. Schmidt, S. Royak, and M. Harbaugh, “Rotor position estimation for synchronous machines based on equivalent EMF,” *IEEE Trans. Ind. Appl.*, vol. 47, no. 3, pp. 1310-1318, 2011.
- [LIU11b] Y. Liu, B. Zhou, Y. Feng, J. Wei, and M. Shi “Sensorless control with two types of pulsating high frequency signal injection methods for SPMSM at low speed,” *Power Electronics Systems and Applications (PESA)*, 2011, pp. 1 - 5
- [LYR02] R.O.C. Lyra, and T.A. Lipo, “Torque density improvement in a six-phase induction motor with third harmonic current injection,” *IEEE Trans. Ind. Appl.*, vol. 38, no. 5, pp. 1351- 1360, 2002
- [MAD95] A. Madani, J.P. Barbot, F. Colamartino, and C. Marchand, “Reduction of torque pulsations by inductance harmonics identification of a permanent-magnet synchronous machine,” *Proc. of the 4th IEEE Conference on Control Applications*, 1995, pp. 787-792.
- [MAT96] N. Matsui, “Sensorless PM brushless DC motor drives,” *IEEE Trans. Ind. Electron.*, vol. 43, no. 2, pp. 300 – 308, 1996
- [MOR02] S. Morimoto, K. Kawamoto, M. Sanada, and Y. Takeda, “Sensorless

- control strategy for salient-pole PMSM based on extended EMF in rotating reference frame,” *IEEE Trans. Ind. Appl.*, vol. 38, no. 4, pp. 1054-1061, 2002.
- [MOR92] J. Moreira, and T.A. Lipo, “Modeling saturated AC machines including air gap flux harmonic components,” *IEEE Trans. Ind. Appl.*, vol. 28, no.2, pp. 343-349, 1992.
- [MOR96] S. Morimoto, M. Sanada, and Y. Takeda, “Inverter-driven synchronous motors for constant power,” *IEEE Trans. Ind. Appl.*, vol. 2, no. 6, pp. 18 – 24, 1996.
- [NAK00] S. Nakashima, Y. Inagaki, and I. Miki, “Sensorless initial rotor position estimation of surface permanent-magnet synchronous motor,” *IEEE Trans. Ind. Appl.*, vol. 36, no. 6, pp. 1598–1603, 2000.
- [NEL74] R.H. Nelson, P.C. Krause, “Induction machine analysis for arbitrary displacement between multiple winding sets,” *IEEE Trans. Power Apparatus and Systems*, vol. 93, no. 3, pp. 841 – 848, 1974
- [NOG98] T. Noguchi, K. Yamada, S. Kondo, and I. Takahashi, “Initial rotor position estimation method of sensorless PM synchronous motor with no sensitivity to armature resistance,” *IEEE Trans. Ind. Electron.*, vol. 45, pp. 118–125, 1998.
- [OVR03] S. Ovrebo, and R. Nilsen, “New self sensing scheme based on INFORM, heterodyning and Luenberger observer,” *IEEE Electric Machines and Drives Conference, IEMDC'03*, vol. 3, 2003 , pp. 1819 - 1825
- [PAC05] M. Pacas, and J. Weber, "Predictive direct torque control for the pm synchronous machine," *IEEE Trans. Ind. Electron.*, vol. 52, no. 5, pp. 1350-1356, 2005.
- [PAU11] D. Paulus, P. Landsmann, and R. Kennel, “Sensorless field-oriented control for permanent magnet synchronous machines with an arbitrary injection scheme and direct angle calculation,” *Symposium on Sensorless Control for Electrical Drives (SLED2011)*, 2011, pp. 41-46.
- [PEI95] Z.M.A. Peixo, F.M. Freitas Sa, P.F. Seixas, B.R. Menezes, P.C. Cortizo, and W.S. Lacerda, “Application of sliding mode observer for induced e.m.f., position and speed estimation of permanent magnet motors,” *Power Electronics and Drive Systems*, 1995, pp. 599 - 604

- [PII08] A. Piippo, M. Hinkkanen, and J. Luomi, "Analysis of an adaptive observer for sensorless control of interior permanent magnet synchronous motors," *IEEE Trans. Ind. Electron.*, vol. 55, no. 2, pp. 570-576, 2008.
- [PRO92] F. Profumo, G. Griva, M. Pastorelli, J. Moreira, and R. DeDoncker, "Universal field oriented controller based on air gap flux sensing via third harmonic stator voltage," *Conference Record of IEEE Industry Applications Society Annual Meeting, 1992*, 1992, pp. 515-523.
- [RAC08a] D. Raca, M.C. Harke, and R.D. Lorenz, "Robust magnet polarity estimation for initialization of PM synchronous machines with near-zero saliency," *IEEE Trans. Ind. Appl.*, vol. 44, no. 4, pp. 1199-1209, 2008.
- [RAC08b] D. Raca, P. Garcia, D. Reigosa, F. Briz, and R. Lorenz, "A comparative analysis of pulsating vs. rotating vector carrier signal injection-based sensorless control," *Applied Power Electronics Conference and Exposition. APEC08*, 2008, pp. 879 - 885
- [RAC10] D. Raca, P. Garcia, D.D. Reigosa, F. Briz, and R.D. Lorenz, "Carrier-signal selection for sensorless control of PM synchronous machines at zero and very low speeds," *IEEE Trans. Ind. Appl.*, vol. 46, no. 1, pp. 167-178, 2010
- [RAU10] R. Raute, C. Caruana, C. S. Staines, J. Cilia, M. Sumner, and G. M. Asher, "Sensorless control of induction machines at low and zero speed by using PWM harmonics for rotor-bar slotting detection," *IEEE Trans. Ind. Appl.*, vol. 46, no. 5, pp. 1989-1998, 2010.
- [REI08] D. Reigosa, P. Garcia, D. Raca, F. Briz, and R.D. Lorenz, "Measurement and adaptive decoupling of cross-saturation effects and secondary saliencies in sensorless-controlled IPM synchronous machines," *IEEE Trans. Ind. Appl.*, vol. 44, no. 6, pp. 1758-1767, 2008.
- [RIV13] J.D. Rivera, A. Navarrete, M. Meza, A. Loukianov, and J. Canedo, "Digital sliding mode sensorless control for surface mounted PMSM," *IEEE Trans. Ind, Informatics*, vol. PP, no. 99, pp. 1, 2013
- [ROB04] E. Robeischl, and M. Schroedl, "Optimized INFORM measurement sequence for sensorless PM synchronous motor drives with respect to minimum current distortion," *IEEE Trans. Ind. Appl.*, vol. 40, no. 2,

- pp. 591–598, 2004.
- [SCH96] M. Schroedl, “Sensorless control of AC machines at low speed and Standstill based on the ‘INFORM’ method,” *Conf. Rec. IEEE-IAS Annual Meeting*, 1996, pp. 270–277.
- [SEN95a] T. Senjyu, and K. Uezato, “Adjustable speed control of brushless DC motors without position and speed sensors,” *Industrial Automation and Control: Emerging Technologies, 1995., International IEEE/IAS Conference on*, 1995, pp. 160 – 164
- [SEN95b] T. Senjyu, M. Tomita, S. Doki, and S. Okuma, “Sensorless vector control of brushless DC motors using disturbance observer,” *IEEE Power Electronics Specialists Conference, PESC '95*, vol. 2, 1995, pp. 772 – 777
- [SHE02a] J.X. Shen, “Sensorless control of permanent magnet brushless drives,” PhD Thesis, Research Group of Electric Machines and Drives, Department of Electronic and Electrical Engineering, University of Sheffield, 2002.
- [SHE02b] J.X. Shen, Z.Q. Zhu, and D. Howe, “Improved speed estimation in sensorless PM brushless AC drives ” *IEEE Trans. Ind. Appl.*, vol. 38, no. 4, pp. 1072-1080, 2002.
- [SHE04] J.X. Shen, Z. Q. Zhu, and D. Howe, “Sensorless flux-weakening control of permanent-magnet brushless machines using third-harmonic back EMF,” *IEEE Trans. Ind. Appl.*, vol. 40, no. 6, pp. 1629-1636, 2004.
- [SHE06a] J.X. Shen, Z.Q. Zhu, and D. Howe, “Practical issues in sensorless control of PM brushless machines using third-harmonic back-EMF,” *IEEE 5th International Power Electronics and Motion Control Conference, IPEMC2006*, 2006, pp. 1 – 5.
- [SHE06b] J.X. Shen, and S. Iwasaki, “Sensorless control of ultrahigh-speed PM brushless motor using PLL and third harmonic back EMF,” *IEEE Trans. Indus. Electron.*, vol. 53 , no. 2, pp. 421 - 428, 2006.
- [SIL06] C. Silva, G. M. Asher, and M. Sumner, “Hybrid rotor position observer for wide speed-range sensorless PM motor drives including zero speed,” *IEEE Trans. Ind. Electron.*, vol. 53, no. 2, pp. 373-378, 2006.

- [SOL96] J. Solsona, M.I. Valla, and C. Muravchik, "A nonlinear reduced order observer for permanent magnet synchronous motors," *IEEE Trans. Indus. Electron.*, vol. 43 , no. 4, pp. 492 – 497, 1996
- [STA06] C. S. Staines, C. Caruana, G. M. Asher, and M. Sumner, "Sensorless control of induction Machines at zero and low frequency using zero sequence currents," *IEEE Trans. Ind. Electron.*, vol. 53, no. 1, pp. 195-206, 2006.
- [TAK86] I. Takahashi, and T. Noguchi, "A new quick-response and high efficiency control strategy of an induction-motor," *IEEE Trans. Ind. Appl.*, vol. 22, no. 5, pp. 820-827, 1986.
- [TAT98] K. Tatematsu, D. Hamada, K. Uchida, S. Wakao, and T. Onuki, "Sensorless permanent magnet synchronous motor drive with reduced order observer," *Applied Power Electronics Conference and Exposition, APEC '98*, 1998, vol. 1, pp. 75 - 80
- [TER01] B. Terzic, and M. Jadric, "Design and implementation of the extended Kalman filter for the speed and rotor position estimation of brushless DC motor," *IEEE Trans. Indus. Electron.*, vol. 48, no. 6, pp. 1065 – 1073, 2001
- [TES00] N. Teske, G.M. Asher, M. Sumner, and K.J. Bradley, "Suppression of saturation saliency effects for the sensorless position control of induction motor drives under loaded conditions," *IEEE Trans. Ind. Electron.*, vol. 47, pp. 1142-150, Oct. 2000.
- [TES03] N. Teske, G.M. Asher, M. Sumner, and K.J. Bradley, "Analysis and suppression of high-frequency inverter modulation in sensorless position-controlled induction machine drives," *IEEE Trans. Ind. Appl.*, vol. 39, no. 1, pp. 10–18, 2003.
- [TES94] A. Testa, A. Consoli, M. Coco, and L. Kreindler, "A new stator voltage third-harmonic based direct field oriented control scheme," in *Conf. Rec. IEEE-IAS Annu. Meeting*, 1994, pp. 608–615.
- [VAS03] P. Vas, "Sensorless vector and direct torque control," Oxford University Press, 2003
- [WAN10] H. Wang, C. Wang, Y. Deng, Z. Wang, and H. Liu, "Rotor position estimation method of permanent magnet synchronous motor based on high frequency signal injection and sliding mode observer,"

- Informatics in Control, Automation and Robotics (CAR), 2010 2nd International Asia Conference on*, vol. 1, 2010, pp. 392 - 395
- [WAN10] H. Wang, M. Yang, L. Niu, and D. Xu, "Current-loop bandwidth expansion strategy for permanent magnet synchronous motor drives," *the 5th IEEE Conference on Industrial Electronics and Applications (ICIEA2010)*, pp. 1340-1345, 2010.
- [WAN12a] G. Wang, G. Zhang, R. Yang, and D. Xu, "Robust low-cost control scheme of direct-drive gearless traction machine for elevators without a weight transducer," *IEEE Trans. Ind. Appl.*, vol. 48, no. 3, pp. 996-1005, 2012.
- [WAN12b] Z. Wang, K. Lu, and F. Blaabjerg, "A Simple startup strategy based on current regulation for back-EMF-based sensorless control of PMSM," *IEEE Trans. Power Electron.*, vol. 27, no. 8, pp. 3817 – 3825, 2012
- [WAR69] E.E. Ward, and H. Harer, "Preliminary investigation of an inverter-fed 5-phase induction motor," *Electrical Engineers, Proc. of the Institution*, 1969, vol. 116, no. 6, pp. 980 - 984
- [WU91] R. Wu, and G.R. Slemon, "A permanent magnet motor drive without a shaft sensor," *IEEE Trans. Ind. Appl.*, vol.27, no.5, pp. 1005–1011, 1991
- [XU95] L. Xu, and L. Ye, "Analysis of a novel stator winding structure minimizing harmonic current and torque ripple for dual six-step converter-fed high power AC machines," *IEEE Trans. Ind. Appl.*, vol. 31, no. 1, pp. 84 - 90, 1995
- [XU98] L. Xu, and C. Wang, "Implementation and experimental investigation of sensorless control schemes for PMSM in super-high variable speed operation," *IEEE Thirty-Third IAS Annual Meeting on Industry Applications Conference, 1998*, vol. 1, pp. 483- 489, 1998.
- [YAN11] S.C. Yang, T. Suzuki, R.D. Lorenz, and T.M. Jahns, "Surface permanent magnet synchronous machine design for saliency tracking self-sensing position estimation at zero and low speeds," *IEEE Trans. Ind. Appl.*, vol. 47, no. 5, pp. 2103-2116, 2011.
- [YOO09] A. Yoo, and S.K. Sul, "Design of flux observer robust to interior permanent-magnet synchronous motor flux variation," *IEEE Trans. Ind. Appl.*, vol. 45, no. 5, pp. 1670-1677, 2009.

- [YOO11] Y.D. Yoon, S.K. Sul, S. Morimoto and K. Ide, "High bandwidth sensorless algorithm for AC machines based on square-wave type voltage injection," *IEEE Trans. Ind. Appl.*, vol. 47, no. 3, pp. 1361-1370, 2011
- [ZHA06] Z. Zhang, H. Xu, L. Xu, and L.E. Heilman, "Sensorless direct field oriented control of three-phase induction motors based on "Sliding Mode" for washing-machine drive applications," *IEEE Trans. Ind. Appl.*, vol. 42, no. 3, pp. 694 – 701, 2006
- [ZHA11] Y.C. Zhang, J.G. Zhu, W. Xu, and Y.G. Guo, "A simple method to reduce torque ripple in direct torque-controlled permanent-magnet synchronous motor by using vectors with variable amplitude and angle," *IEEE Trans. Ind. Electron.*, vol. 58, no. 7, pp. 2848-2859, 2011.
- [ZHA95] Y. Zhao, and T.A. Lipo, "Space vector PWM control of dual three-phase induction machine using vector space decomposition," *IEEE Trans. Ind. Appl.*, vol. 31, no. 5, pp. 1100- 1109, 1995
- [ZHO97] L. Zhong, M.F. Rahman, W.Y. Hu, and K.W. Lim, "Analysis of direct torque control in permanent magnet synchronous motor drives," *IEEE Trans. Power Electron.*, vol. 12, no. 3, pp. 528-536, 1997.
- [ZHU07] Z.Q. Zhu, Y. Li, D. Howe, and C.M. Bingham, "Compensation for rotor position estimation error due to cross-coupling magnetic saturation in signal injection based sensorless control of PM brushless AC motors," *IEEE Electric Machines & Drives Conference, IEMDC '07*. 2007, vol. 1, pp. 208 - 213
- [ZHU12] Z.Q. Zhu, and J.H. Leong, "Analysis and mitigation of torsional vibration of pm brushless AC/DC drives with direct torque controller," *IEEE Trans. Ind. Appl.*, vol. 48, no. 4, pp. 1296-1306, 2012.

APPENDICES

Appendix I Specification of Prototype Machines

Motor I

Rated voltage (peak)	158 V
Rated current (peak)	4.0 A
Rated power	0.6 kW
Rated speed	1000 rpm
Rated torque	4.0 Nm
Pole number	6
Slot number	18
Number of series connected conductors/pole/phase	152 turns
Wire diameter (2 wires stranded)	0.36 mm + 0.51 mm
Winding coil pitch	3 slots
Winding resistance per phase	6.0 Ω (20°C)
Skew	1 slot-pitch
Stator outer radius	53.30 mm
Stator inner radius	31.00 mm
Rotor outer radius	30.25 mm
Core length (stator)	32.00 mm
Core length (rotor)	30.00 mm
Shaft diameter	25.00 mm
Air gap length	0.75 mm
Magnet	UGIMAX 35HC1 ($B_r=1.17T$, $\mu_r=1.07$)
Stator Steel	Transil 310-50
Rotor Steel	Transil 310-50 (Surface-mounted PM motor) Transil 300-35 (Inset and interior PM motors)

Motor II

Rated DC voltage	600 V
Rated phase current (RMS)	5.83A
Rated output power	3194.48W
Total number of coils	42
Open circuit Phase EMF (RMS) @ 170rpm 60°c	
1 st	199.44V
3 rd	26.78V
5 th	0.62V
7 th	0.46V
Cogging torque p-p 60C	1.24Nm
Cogging torque 60C	0.31%
Pole number	28
Mechanical rated speed	170rpm
Current density	4.06A mm ⁻²
Rated torque (current source)	195.84Nm
Rated input power	3486.41W
Phase resistance DC 20°C	1754.9mΩ
Phase resistance DC 95°C	2272.1mΩ
Copper losses (fundamental)	231.97W
iron losses full load based on SPEED	59.96W
Rated efficiency	91.63%
Rated power factor	99.48
Ld (exclude the end winding)	13.04mH
Lq (exclude the end winding)	13.04mH
PM flux per pole	1.1315Wb

Motor III

Supply DC voltage	36V
Rated torque	5.5 Nm
Rated speed	400 rpm
Rated power	260W
Slot number	12
Pole number	10
Stator outer radius	50 mm
Stator inner radius	28.5 mm
Yoke height	3.7 mm
Tooth body width	7.1 mm
Slot opening	2 mm
Stack length	50 mm
Airgap length	1 mm
Rotor outer radius	27.5 mm
Magnet thickness	3 mm
Magnet remanence	1.2 T
Number of series turns per phase	132
Phase resistances ($R_{A1}, R_{B1}, R_{C1}, R_{A2}, R_{B2}, R_{C2}$)	1.11, 1.10, 1.11, 1.10, 1.10, 1.14 Ω

Appendix II Transformation of Phase Vector with Harmonics

Assuming a phase vector $f(\delta)$ with harmonics can be expressed in station reference frame, as

$$\begin{bmatrix} f_a(\delta) \\ f_b(\delta) \\ f_c(\delta) \end{bmatrix} = \begin{bmatrix} k_1 \cos \delta \\ k_1 \cos(\delta - \frac{2\pi}{3}) \\ k_1 \cos(\delta + \frac{2\pi}{3}) \end{bmatrix} + \begin{bmatrix} k_3 \cos 3\delta \\ k_3 \cos 3(\delta - \frac{2\pi}{3}) \\ k_3 \cos 3(\delta + \frac{2\pi}{3}) \end{bmatrix} + \begin{bmatrix} k_5 \cos 5\delta \\ k_5 \cos 5(\delta - \frac{2\pi}{3}) \\ k_5 \cos 5(\delta + \frac{2\pi}{3}) \end{bmatrix} + \begin{bmatrix} k_7 \cos 7\delta \\ k_7 \cos 7(\delta - \frac{2\pi}{3}) \\ k_7 \cos 7(\delta + \frac{2\pi}{3}) \end{bmatrix} \dots \quad (\text{A2.1})$$

It can be re-written as

$$\begin{bmatrix} f_a(\delta) \\ f_b(\delta) \\ f_c(\delta) \end{bmatrix} = \begin{bmatrix} k_1 \cos \delta \\ k_1 \cos(\delta - \frac{2\pi}{3}) \\ k_1 \cos(\delta + \frac{2\pi}{3}) \end{bmatrix} + \begin{bmatrix} k_3 \cos 3\delta \\ k_3 \cos 3\delta \\ k_3 \cos 3\delta \end{bmatrix} + \begin{bmatrix} k_5 \cos 5\delta \\ k_5 \cos(5\delta + \frac{2\pi}{3}) \\ k_5 \cos(5\delta - \frac{2\pi}{3}) \end{bmatrix} + \begin{bmatrix} k_7 \cos 7\delta \\ k_7 \cos(7\delta - \frac{2\pi}{3}) \\ k_7 \cos(7\delta + \frac{2\pi}{3}) \end{bmatrix} + \dots \quad (\text{A2.2})$$

With coordinate transformation, the phase vector $f(\delta)$ can be transformed to synchronous reference frame

$$\begin{bmatrix} f_d \\ f_q \end{bmatrix} = \frac{2}{3} \begin{bmatrix} \cos \theta_r & \cos(\theta_r - 2\pi/3) & \cos(\theta_r + 2\pi/3) \\ -\sin \theta_r & -\sin(\theta_r - 2\pi/3) & -\sin(\theta_r + 2\pi/3) \end{bmatrix} \begin{bmatrix} f_a \\ f_b \\ f_c \end{bmatrix} \quad (\text{A2.3})$$

Then,

$$\begin{bmatrix} f_d \\ f_q \end{bmatrix} = \begin{bmatrix} k_1 \cos(\theta_r - \delta) \\ k_1 \sin(\theta_r - \delta) \end{bmatrix} + \begin{bmatrix} k_5 \cos(\theta_r + 5\delta) \\ k_5 \sin(\theta_r + 5\delta) \end{bmatrix} + \begin{bmatrix} k_7 \cos(\theta_r - 7\delta) \\ k_7 \sin(\theta_r - 7\delta) \end{bmatrix} + \dots \quad (\text{A2.4})$$

If the fundamental component of $f(\delta)$ is synchronous to the d -axis, i.e., $\delta = \theta_r + \varphi$ where φ is a constant phase shift. Then the above equation can be simplified to be,

$$\begin{bmatrix} f_d \\ f_q \end{bmatrix} = \begin{bmatrix} k_1 \cos(\theta_r - \delta) \\ k_1 \sin(\theta_r - \delta) \end{bmatrix} + \begin{bmatrix} (k_5 + k_7) \cos 6\delta \\ (-k_5 + k_7) \sin 6\delta \end{bmatrix} \cos \varphi + \begin{bmatrix} (k_5 - k_7) \cos 6\delta \\ (k_5 + k_7) \sin 6\delta \end{bmatrix} \sin \varphi + \dots \quad (\text{A2.5})$$

It shows that only 6th, 12th ... harmonics exist in the synchronous reference frame.

Appendix III Rotating Carrier Signal Injection into the Estimated Synchronous Reference Frame

Considering the types of carrier injection signal, pulsating and rotating, and the injected reference frames, estimated synchronous reference frame and stationary reference frame, there should be four different high frequency carrier signal injection based sensorless controls, as shown in Table A1.

TABLE A1

HIGH FREQUENCY CARRIER SIGNAL INJECTIONS

	Pulsating carrier voltage	Rotating carrier voltage
Estimated synchronous reference frame	Conventional pulsating carrier signal injection	Rotating carrier signal injection into estimated synchronous reference frame (To be introduced)
Stationary reference frame	Pulsating carrier signal injection into stationary reference frame (Proposed in Chapter 3)	Conventional rotating carrier signal injection

Two conventional pulsating carrier signal injection based sensorless control have been widely researched and employed. The pulsating carrier signal injection into stationary reference frame is also proposed in Chapter 3. However, the fourth type, i.e., rotating carrier signal injection into estimated synchronous reference frame has not been researched. In this appendix, it will be introduced.

Rotating carrier signal injection into estimated synchronous reference frame method injects a balanced three phase voltage carrier signal into the estimated reference frame to form a rotating excitation superimposed on the fundamental excitation as demonstrated in Fig. A1. The rotor position information can be obtained from the carrier current response which is phase-modulated by rotor position.

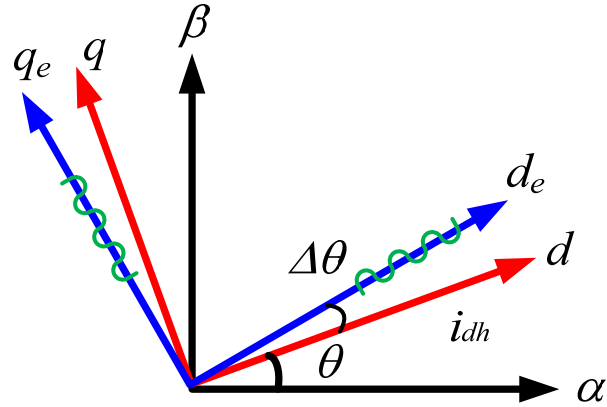


Fig. A1. Conventional rotating signal injection

A balanced rotating carrier voltage vector (A2.6) which is shown in Fig. A2 is injected into estimated synchronous reference frame,

$$\begin{bmatrix} u_{dh}^e \\ u_{qh}^e \end{bmatrix} = U_c \begin{bmatrix} \cos \alpha \\ \sin \alpha \end{bmatrix}, \alpha = \omega_c t + \varphi \quad (\text{A2.6})$$

where U_c , ω_c and φ are the amplitude, angular speed and the initial phase angle of the injected pulsating high frequency voltage, respectively. Then the Phase-A current response is shown in Fig. A3, whilst the rotor position is contained in the carrier current response.

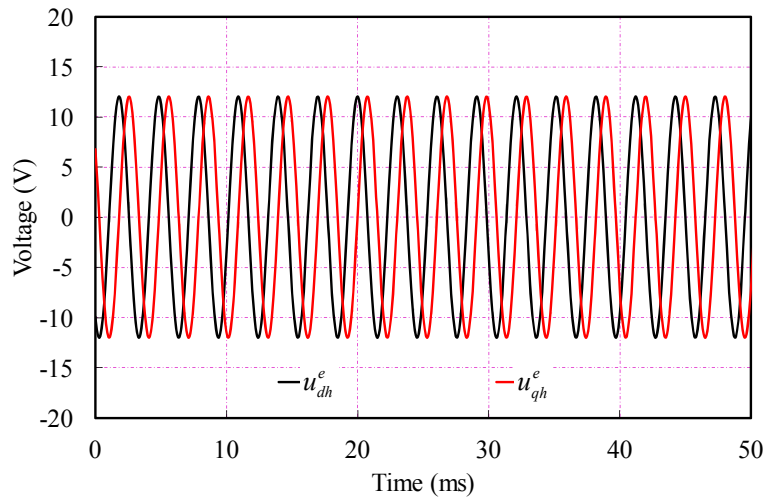


Fig. A2. Injected rotating carrier voltage ($U_c=12V, f=330Hz$)

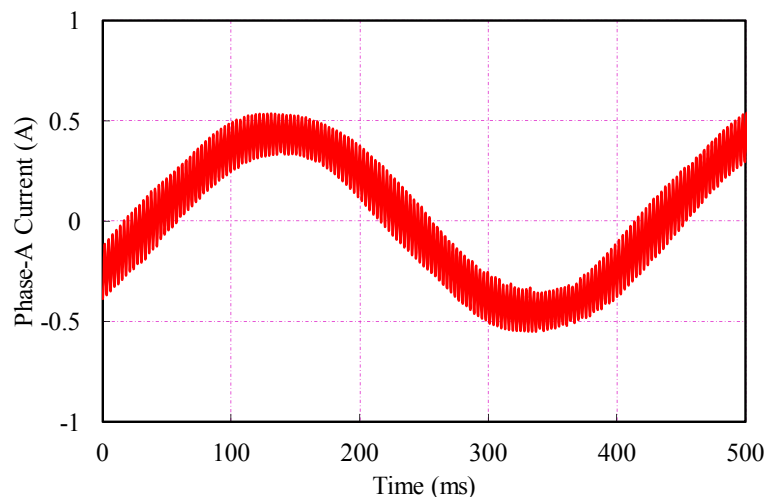


Fig. A3. Phase-A current response

The differential of the carrier current in the estimated synchronous reference frame as shown in (3.9) can be re-expressed as

$$p \begin{bmatrix} i_{dh}^e \\ i_{qh}^e \end{bmatrix} = \begin{bmatrix} \frac{1}{L_p} + \frac{1}{L_n} \cos(2\Delta\theta + \theta_m) & \frac{1}{L_n} \sin(2\Delta\theta + \theta_m) \\ \frac{1}{L_n} \sin(2\Delta\theta + \theta_m) & \frac{1}{L_p} - \frac{1}{L_n} \cos(2\Delta\theta + \theta_m) \end{bmatrix} \cdot U_c \begin{bmatrix} \cos \alpha \\ \sin \alpha \end{bmatrix} \quad (\text{A2.7})$$

Then, the resultant carrier current response in the estimated synchronous reference frame will be shown in (A2.8) and Fig. A4.

$$\begin{aligned} \begin{bmatrix} i_{dh}^e \\ i_{qh}^e \end{bmatrix} &= \frac{U_c}{\omega_c} \begin{bmatrix} \frac{1}{L_p} + \frac{1}{L_n} \cos(2\Delta\theta + \theta_m) & \frac{1}{L_n} \sin(2\Delta\theta + \theta_m) \\ \frac{1}{L_n} \sin(2\Delta\theta + \theta_m) & \frac{1}{L_p} - \frac{1}{L_n} \cos(2\Delta\theta + \theta_m) \end{bmatrix} \cdot \begin{bmatrix} \sin \alpha \\ -\cos \alpha \end{bmatrix} \\ &= \begin{bmatrix} I_p \cos(\alpha - \frac{\pi}{2}) \\ I_p \sin(\alpha - \frac{\pi}{2}) \end{bmatrix} + \begin{bmatrix} I_n \cos(-\alpha + 2\Delta\theta + \theta_m + \frac{\pi}{2}) \\ I_n \sin(-\alpha + 2\Delta\theta + \theta_m + \frac{\pi}{2}) \end{bmatrix} \end{aligned} \quad (\text{A2.8})$$

and by using complex vector as

$$i_h = I_p \cdot e^{j(\alpha - \pi/2)} + I_n \cdot e^{j(-\alpha + 2\Delta\theta + \theta_m + \pi/2)} \quad (\text{A2.9})$$

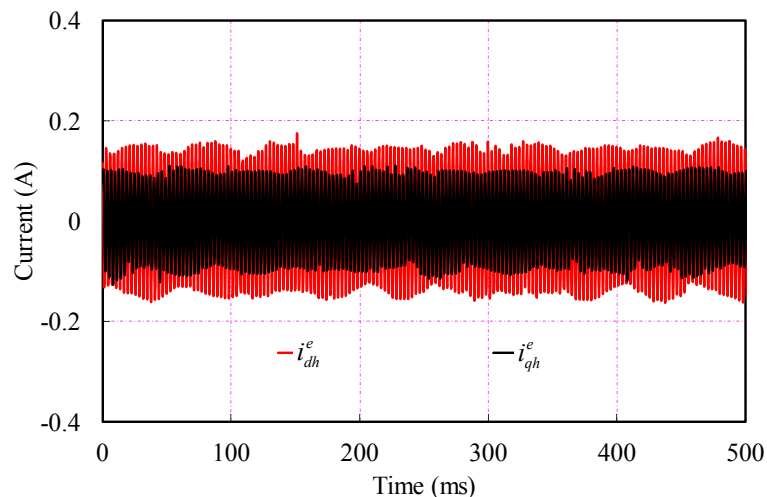


Fig. A4. Carrier current response of rotating signal injection

Clearly, the carrier current response consists of two components. The first term is a positive sequence component, which has the same angular speed as the injected carrier voltage vector, and the second term is referred to as the negative sequence component, which contains the rotor position information in phase angle.

In order to extract the position dependent negative sequence carrier current from the total current response, SRFF which is exactly the same as the one in conventional rotating carrier signal injection method is employed. Firstly, SRFF uses the frame transformation based on feedback estimated rotor position to transform the fundamental current to DC. With the aid of a LPF, this DC component is obtained without phase lag. Then with the reverse frame transformation, this fundamental current can be easily obtained. By employing the same procedure with the phase angle of the injected carrier voltage, the positive sequence current can be derived. The employed demodulation procedure is shown in Fig. A5. Then subtracting them from the total current response, the negative sequence current can be obtained as

$$i_n = I_n \cdot e^{j(-\alpha + 2\Delta\theta + \theta_m + \pi/2)} \quad (\text{A2.10})$$

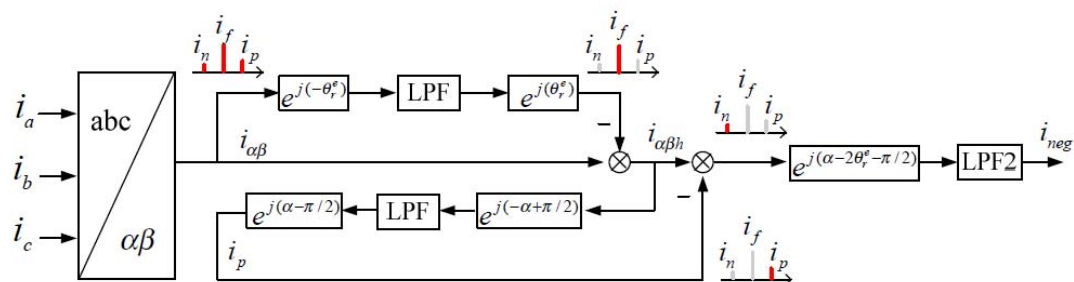


Fig. A5. Signal demodulation for rotating injection [GON12]

Then i_n in the reference frame synchronous with estimated negative sequence carrier frequency, can be expressed as shown in (A2.11) and Fig. A6.

$$i_{neg} = I_n \cdot e^{j(-\alpha+2\Delta\theta+\theta_m+\pi/2)} \cdot e^{j(\alpha-\pi/2)} = I_n \cdot e^{j(2\Delta\theta+\theta_m)} = I_n \cdot e^{j\theta_{neg}} \quad (\text{A2.11})$$

which is identical to (3.30) in conventional rotating carrier signal injection method. Normally, the q -axis component is regarded as the error signal $f(\Delta\theta)$ input to the position observer as shown in Fig. 3.14, i.e.

$$f(\Delta\theta) = i_{neg_q} = I_n \sin(2\Delta\theta + \theta_m) \quad (\text{A2.12})$$

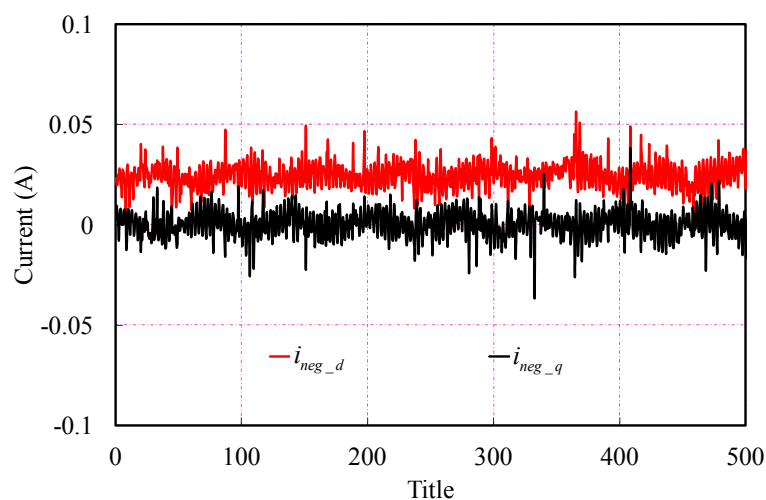


Fig. A6. Demodulated negative sequence carrier current response in estimated negative sequence reference frame

Therefore, the rotor position with the cross-saturation error ($-\theta_m/2$) can be estimated. With cross-saturation effect compensation which is the same as the one in conventional rotating carrier signal injection method, the accurate rotor position can be derived. The block diagram of rotating carrier voltage signal injection into the

estimated synchronous reference frame based sensorless control is shown in Fig. A7.

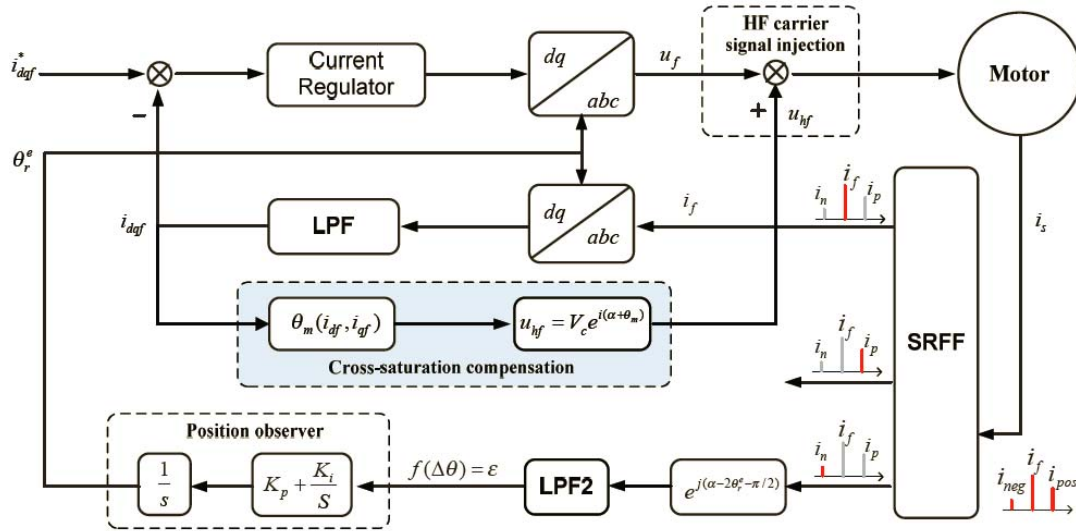


Fig. A7. Block diagram of rotating injection into the estimated synchronous reference frame based sensorless control

Compared with this strategy with conventional rotating carrier signal injection, it can be found that, except the injected reference frame, the whole signal demodulation process is nearly the same as conventional rotating method. It is also expected that this method could achieve the same steady-state and dynamic performances.

The steady-state tests for the rotating carrier signal injection into estimated synchronous reference frame method is carried out at the condition of 50rpm rotor speed with about 1A q -axis current, and the estimated rotor positions considering the cross-saturation effect are shown in Fig. A8 compared with the actual value from encoder. It can be seen that the estimation error is sufficiently small and the estimated rotor position is with high accuracy. The dynamic performance tests are carried out when the rotor mechanical initial speed is zero and step change to 25rpm and then 50rpm as demonstrated in Fig. 3.16, and the estimated and actual rotor positions, as well as the estimation error are shown in Fig. A9. The experimental results prove that the two conventional high frequency injection methods have outstanding dynamic performances. Compared with the steady-state, Fig. 3.15 (b), and dynamic performances, Fig. 3.17(b), this method can achieve the similar experimental results

as expected.

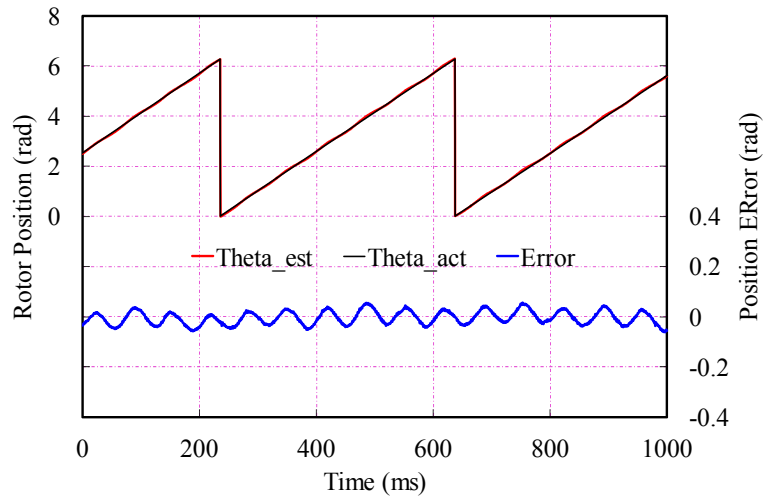


Fig. A8. Steady-state performance (*Theta_est*: Estimated rotor position, *Theta_act*: Actual rotor position, *Error*: Position estimation error)

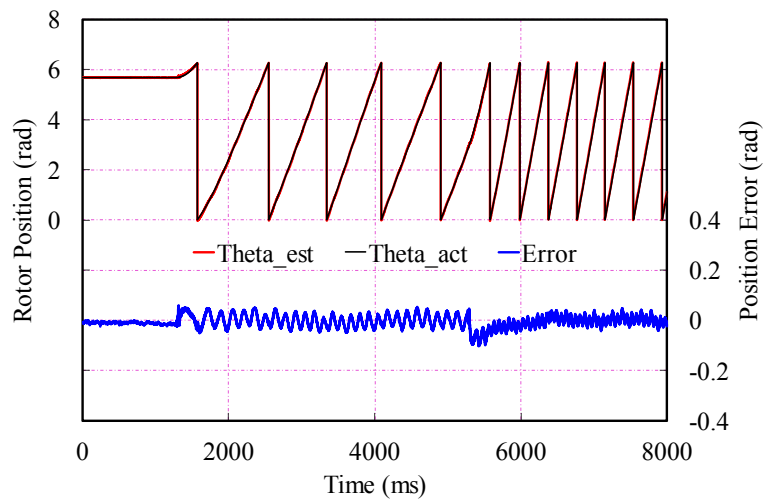


Fig. A9. Dynamic performance (*Theta_est*: Estimated rotor position, *Theta_act*: Actual rotor position, *Error*: Position estimation error)

Appendix IV Patents and Papers during This PhD Study

Patents

1. **J.M. Liu**, Z.Q. Zhu, “System for correcting an estimated position of a rotor of an electrical machine” Siemens plc. SWP Ref. 2012E13219 GB PTT/REI, European Patent application no/Patent no: 12183314.9 – 1242, application date: 6 Sept. 2012
2. **J.M. Liu**, Z.Q. Zhu, and Zhan-Yuan Wu “Estimation method of generator initial rotor position for wind power application,” Siemens plc. SWP Ref. 2012E16745 GB PTT/BKT, application date: 12 Jul. 2012
3. **J.M. Liu**, Z.Q. Zhu, and Zhan-Yuan Wu “Rotor position estimation for dual-three-phase PM machine under imbalanced situation,” Siemens plc. SWP Ref. 2012E28198 GB PTT/BKT, application date: 21 Dec. 2012

Papers

Journal Papers:

1. **J.M. Liu**, Z.Q. Zhu, “Improved sensorless control of permanent magnet synchronous machine based on third-harmonic back-EMF,” *IEEE Trans. Ind. Appl.* in press.
2. **J.M. Liu**, Z.Q. Zhu, “Novel sensorless control strategy with injection of high-frequency pulsating carrier signal into stationary reference frame,” *IEEE Trans. Ind. Appl.* Under revision.
3. **J.M. Liu**, and Z.Q. Zhu, “Rotor position error compensation based on third harmonic back-EMF in flux observer based sensorless control,” *IET-Electric Power Appl.* Submitted.
4. **J.M. Liu**, and Z.Q. Zhu, “High-bandwidth sensorless control strategy by square waveform high frequency pulsating signal injection into stationary reference frame,” *Special Issue on Advanced Control of Electric Motor Drives in Journal of Emerging and Selected Topics in Power Electronics*, Under revision
5. **J.M. Liu**, and Z.Q. Zhu, “Sensorless control based on third harmonic back-EMF

- and PLL for permanent magnet synchronous machine,” *Journal of International Conference on Electrical Machines and Systems, JICEMS*, Submitted.
6. **J.M. Liu**, and Z.Q. Zhu, “Rotor position estimation for dual-three-phase permanent magnet synchronous machine based on third harmonic back-EMF,” Drafted, waiting for patent processing, to be submitted to *IEEE Trans. Ind. Electron.*
 7. **J.M. Liu**, and Z.Q. Zhu, “Rotor position estimation for dual-three-phase permanent magnet synchronous machine under imbalanced situation,” Drafted, waiting for patent processing, to be submitted to *IEEE Trans. Ind. Electron.*
 8. T.C. Lin, L.M. Gong, **J.M. Liu**, and Z.Q. Zhu “Investigation of saliency in switched-flux permanent magnet machine using high-frequency signal injection,” *IEEE Trans. Ind. Electron.* In press.
 9. Y. Ren, Z.Q. Zhu, and **J.M. Liu**, “torque regulator to reduce steady-state error of torque response for direct torque control of permanent magnet synchronous machine drives,” *IET-Electric Power Applications*, Accepted.
 10. Y. Ren, Z.Q. Zhu, and **J.M. Liu**, “Direct torque control of permanent magnet synchronous machine drives with simple duty ratio regulator,” *IEEE Trans. Ind. Electron.*, Submitted.

Conference Papers:

1. **J.M. Liu**, Z.Q. Zhu, “Improved sensorless control of permanent magnet synchronous machine based on third-harmonic back-EMF,” *IEEE International Electric Machines and Drives Conference, IEMDC2013*, 2013, pp. 1180-1187.
2. **J.M. Liu**, Z.Q. Zhu, “A new sensorless control strategy by high-frequency pulsating signal injection into stationary reference frame,” *IEEE International Electric Machines and Drives Conference, IEMDC2013*, 2013, pp. 505-512.
3. **J.M. Liu**, and Z.Q. Zhu, “Sensorless control based on third harmonic back-EMF and PLL for permanent magnet synchronous machine,” *International Conference on Electrical Machines and Systems 2013, ICEMS2013*, Accepted.
4. **J.M. Liu**, and Z.Q. Zhu, “Investigation of stator current and machine saliency influence on sensorless control based on third-harmonic back-EMF,” *IET int. conf. on Power Electronics, Machines and Drives, PEMD, 2014*, Submitted

5. J.H. Leong, Z.Q. Zhu, and **J.M. Liu**, “Space-vector PWM based direct torque control of PM brushless machine drives having non-ideal characteristics,” *8th International Conference and Exhibition on Ecological Vehicles and Renewable Energies, EVER`13*, 2013, pp. 1-6.
6. J.H. Leong, Z.Q. Zhu, and **J.M. Liu**, “Minimization of steady-state torque tracking error in direct-torque controlled pm brushless AC drives,” *8th International Conference and Exhibition on Ecological Vehicles and Renewable Energies, EVER`13*, 2013, pp. 1-4.